Experimental and Numerical Modelling of Boundary Effects on Internal Solitary Waves

Samuel George Hartharn-Evans

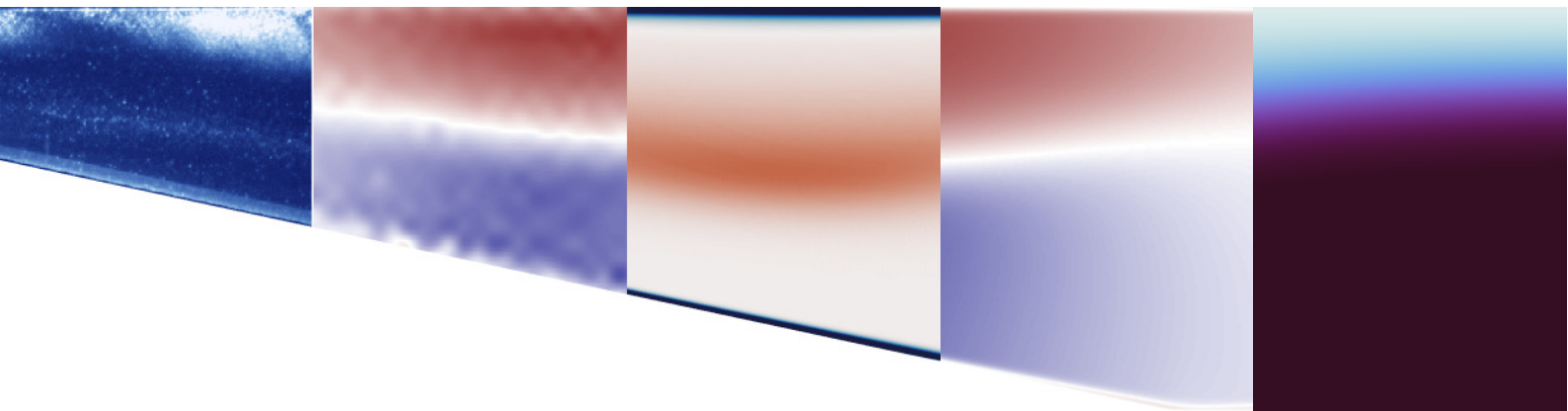
Supervisors:
Dr. Magda Carr,
Prof. Andrew Willmott,
Prof. Adrian Jenkins.

Thesis submitted for the degree of
Doctor of Philosophy



School of Mathematics, Statistics & Physics
Newcastle University
Newcastle upon Tyne
United Kingdom

September 2023



Abstract

In the ocean, waves exist not just at the surface, but also on internal density interfaces. Driven by energy from the tide and wind, these internal waves are responsible for horizontal transport, and vertical mixing of heat, nutrients, and water properties. Large Internal Solitary Waves (ISW) can travel long distances without significantly changing. Until that is they interact with boundaries. This thesis explores two such cases of boundary effects on ISWs, firstly when ISWs travel up slopes (shoaling), and secondly when they interact with floating bodies, such as sea ice. Numerical and laboratory methods are utilised in the thesis.

The first two chapters of this thesis investigate shoaling ISWs, and the effects of stratification on this process. Whilst previous studies have identified that ISWs shoal via one of four mechanisms (namely plunging, collapsing, surging and fission), depending on a combination of the slope, and wave steepness (wave amplitude/wavelength), here it is identified that the presence of density gradients in the upper layer and lower layer suppress the plunging and collapsing dynamics respectively. In Chapter 4, it is discussed how dense pulses produced by shoaling over a shallow (geophysically representative) slope compare under different stratifications. Chapter 5 presents a new diagnostic tool for understanding mixing in these numerical models, by tagging water parcels based on their fluid properties.

The final chapter investigates ISW-sea ice interactions using laboratory experiments with floats of varying sizes. The motion of these floats are successfully modelled simply as the average velocity of fluid under the float, and the relationship between float motion, float length and wavelength is explored. Flow features induced by larger floats form a pair of counter-rotating vortices, which are explained with the relative velocity of the flow, relative to the float. This indicates a complex dynamic in a system with many non-stationary components.

Acknowledgements

I would like to begin by thanking my supervisory team, both formal and informal, for their support and guidance throughout my PhD. Adrian Jenkins and Andrew Willmott, as my supervisory team, provided advice and support through the process; Peter Davies supported improving my writing skills, and shared his expertise on experimental fluid dynamics; and Marek Stastna for all his contributions during my PhD, in particular the support in setting up SPINS during COVID, better understanding numerical modelling, and for hosting me at the University of Waterloo in 2022. I am also grateful to Marek's research group for their warm welcome during my visit, an experience I will remember with great fondness. Most of all, I thank my main supervisor Magda, for offering her world-class expertise in laboratory ISWs, guidance, encouragement, opportunities and support throughout my PhD, especially during the difficult times of the pandemic.

This work was supported by the Natural Environment Research Council (NERC) funded ONE Planet Doctoral Training Partnership (S.H.E., grant number [NE/S007512/1]). My six week research placement at the University of Waterloo was made possible by a Turing Global Fellowship under the Turing Scheme, and by the Natural Science and Engineering Research Council of Canada grant RGPIN-311844-37157. Use of the Rocket High Performance Computing service at Newcastle University, the Math Faculty Computing Facility at the University of Waterloo, and laboratory resources in the Novak Laboratory are gratefully acknowledged.

A laboratory-based PhD would go nowhere without the technical support of many individuals, and I would like to thank David Dick, Stuart Patterson, and Paul Watson (and their teams) for their support at various stages. I extend special thanks to Jonathan Bell for his management of the Novak Laboratory, ensuring we could enjoy carrying out our experiments. IT and computing technical support, in particular from John Richardson and Michael Beatty have also been invaluable.

A PhD is a long journey, and would not have been possible without the support of friends going through the same process. My thanks to everybody who shaped my PhD experience especially those who frequented the MSP common room, lived with me in Brandon Grove, worked with me in office 4.15, and the fellow students of ONE Planet DTP. And of course, to my parents, who have supported me from the start. Finally, to Charlotte, for her love and support as I pursue becoming a nerd.

Covid-19 Impact Statement

The main component of this PhD is experimental research, which requires access to the Novak Laboratory in the university. From 9th March - 3rd August 2020 (midway through my first year), access to the laboratory, and therefore the ability to carry out experiments, was revoked due to the COVID-19 lockdown. As a mitigation, early in the pandemic, the decision was made to switch the focus for this initial stage of the project to numerical modelling, and this represented a significant change in the project direction, to an area (numerical modelling, computing) outside of my existing expertise at a time when face to face support was unavailable. However, the significant delay involved in changing to the alternative plan for data collection, as well as the remaining need to carry out further laboratory experiments upon the lab reopening delayed my project timeline by at least 6 months, for which a 6 month funded extension has mitigated many of those impacts.

The experimental campaign was additionally delayed due to reduced IT support during the pandemic. On-campus technicians were required for PC repairs, but the availability of this was limited, due to prioritisation of online teaching support, limited on-campus staff, and a university-wide cyber attack.

There have also been additional impacts relating to the pandemic. Working from home was slowed by software/hardware availability (e.g. DigiFlow, the lab-based image processing, analysis and capture software; and high power and storage laboratory PCs), for which remote/home working access was not provided.

It is worth noting positive aspects of these impacts. Success with the numerical model yielded results during lockdown and reduced the number of laboratory experiments required upon return, and later shaped the project by becoming the basis for the second chapter, and a research trip to the University of Waterloo, Canada.

However, an under-anticipated impact was the social/community aspect of lockdown. Discussions and informal support in person around the department are a bedrock of academic research, and yet this was simply not available during a crucial period of my project and skills development. Such impacts only became apparent once the research community returned to campus after the summer of 2021.

Declaration

Each chapter within this thesis represent work completed in collaboration with colleagues, led by the thesis author. The contributions from authors are noted for each chapter below. All published papers (where published) are published Open Access (CC-BY 4.0 Licence) and the author retains the right to publish, reproduce or distribute the work.

Chapter 3. This chapter is a modification of Hartharn-Evans et al. (2022), published in Journal of Fluid Mechanics with minor (formatting) changes. Details of the numerical model have been moved from this chapter to chapter 2. The paper was co-authored by Sam Hartharn-Evans, Magda Carr, Marek Stastna and Peter Davies. Author contributions are as follows: S.H.E. performed and analysed the numerical simulations and experiments, and was responsible for visualisation and writing of the original draft. M.C. supervised the project, and was responsible for the experimental methodology, was responsible for resource provision and funding acquisition. M.S. was responsible for the DJL and WNL simulations/calculations, and for providing the numerical model (SPINS). All authors contributed to study conceptualisation and design, reviewed and edited the manuscript.

Hartharn-Evans, S. G., Carr, M., Stastna, M. & Davies, P. A. 2022 Stratification effects on shoaling internal solitary waves *Journal of Fluid Mechanics*, **933** (A19).

Chapter 4. This chapter is a modification of Hartharn-Evans et al. (2023) published in Environmental Fluid Mechanics with minor (formatting) changes. Details of the numerical model have been moved from this chapter to chapter 2. The paper was co-authored by Sam Hartharn-Evans, Marek Stastna and Magda Carr. Author contributions are as follows: S.H.E. performed and analysed the numerical simulations, was responsible for visualisation and writing of the original draft. M.C. supervised the project, and was responsible for resource provision and funding acquisition. M.S. supported the numerical model usage (SPINS) and associated analysis. All authors contributed to study conceptualisation and design, reviewed and edited the manuscript

Hartharn-Evans, S. G., Stastna, M. & Carr, M. 2023 Dense Pulses formed from fissioning internal waves *Environ. Fluid Mech*, **23**, 389-405.

Chapter 5. This chapter is a modification of Hartharn-Evans et al. (2024b) published in Nonlinear Processes in Geophysics with minor changes. The paper was co-authored by Sam Hartharn-Evans, Marek Stastna and Magda Carr. Author contributions are as follows: S.H.E and M.S. performed, analysed, and curated data from the numerical simulations, produced the analysis code, and were responsible for study conceptualisation and design and writing the original draft. S.H.E was responsible for visualisation, M.C. and M.S were responsible for resource acquisition and

supervision, and all authors reviewed and edited the manuscript, and contributed to funding acquisition.

Hartharn-Evans, S. G., Stastna, M., and Carr, M.: A new approach to understanding fluid mixing in process-study models of stratified fluids, *Nonlinear Processes in Geophysics* **31**, 61-74

Chapter 6. This chapter is a modification of Hartharn-Evans et al. (2024) published in JGR Oceans with minor (formatting) changes. The paper was co-authored by Sam Hartharn-Evans, Magda Carr and Marek Stastna. Author contributions are as follows: S.H.E. designed, performed and analysed the experiments, validated and curated the data, and was responsible for the visualisations and writing of the original draft. M.C. was responsible for funding acquisition, and supervision of the project. S.H.E and M.C. were responsible for study conceptualisation and methodology, resource provision. All authors contributed to study conceptualisation and design, reviewed and edited the manuscript.

Hartharn-Evans, S. G., Carr, M. & Stastna, M. 2024 Interactions between internal solitary waves and sea ice. *Journal of Geophysical Research: Oceans*, **129**, e2023JC020175

In line with UKRI/NERC Open Data policies, the data and code that supports this thesis is available open access in FAIR data repositories linked to in the data availability statements at the end of each chapter.

Contents

1 Introduction **1**

1.1 Motivation 1

1.2 Aims & Objectives 4

1.3 Summary of Methodology 4

2 Background and Key Concepts **13**

2.1 Internal Waves 13

2.2 Mixing and Instabilities in ISWs 15

2.3 Interactions with an obstacle 18

2.3.1 Weakly and Fully nonlinear theory of obstacle interaction 18

2.3.2 Blocking and parameterisations 20

2.4 Assumptions & Simplifications 21

2.5 Non dimensional parameters and scaling 23

2.6 Numerical Model 23

3 Stratification effects on shoaling Internal Solitary Waves (ISWs) **32**

3.1 Introduction 32

3.2 Experimental Methods 36

3.2.1 Laboratory set-up 36

3.2.2 Flow Measurement and Visualisation 38

3.3 Numerical Model 40

3.4 Weakly Nonlinear Theory (WNL) 41

3.5 Results 43

3.5.1 Wave on approach . . . 46
3.5.2 Surging . . . 48
3.5.3 Collapsing . . . 50
3.5.4 Plunging . . . 52
3.5.5 Surging in the Broad Tanh Profile Stratification . . . 54
3.5.6 Fission . . . 57
3.6 Discussion . . . 60
3.6.1 Relevance at the Ocean Scale . . . 60
3.7 Conclusion . . . 64
3.A Supplementary Figures . . . 68
3.B Supplementary Tables . . . 69

4 Dense Pulses formed from fissioning internal waves 83
4.1 Introduction . . . 83
4.2 Methods . . . 86
4.3 Results . . . 88
4.3.1 Initial pulse formation . . . 88
4.3.2 Pulse Evolution and Degeneration . . . 93
4.4 Discussion & Conclusion . . . 95

5 A new approach to understanding fluid mixing in process-study models of stratified fluids 106
5.1 Introduction . . . 106
5.2 Methods . . . 109
5.2.1 Paired Histograms . . . 109
5.2.2 Numerical model . . . 111
5.3 Results . . . 113
5.3.1 Fissioning Internal Solitary Waves & the newly-mixed layer . . . 113
5.3.2 Cold shear instability . . . 118
5.3.3 Cold shear instability with passive tracers . . . 120
5.4 Discussion . . . 123
5.5 Conclusions . . . 124
5.A Supplementary Figures . . . 126

6 Interactions between Internal Solitary Waves and Sea Ice 135
6.1 Introduction . . . 135

6.2 Methods . . . 138
6.2.1 Laboratory Experiments . . . 138
6.2.2 Flow and Float Quantification . . . 141
6.2.3 Float Motion Model (FMM) . . . 142
6.3 Results . . . 144
6.3.1 Motion of floats . . . 144
6.3.2 Observations of float interactions with internal wave-induced flow 149
6.4 Discussion . . . 150
6.4.1 Application of theory to understand the flow and floats . . . 150
6.4.2 Field Scale . . . 156
6.4.3 Roughness and Shape of floats . . . 157
6.5 Conclusion . . . 158

7 Conclusions **167**
7.1 Summary of Key Findings . . . 167
7.2 Future work . . . 169

List of Figures

1.1 Generic Tank Schematic 5

2.1 Mode 1 and Mode 2 Wave structures 16
2.2 Schematic of Boundary Layer Instability 17
2.3 Schematic of four scenarios considered for obstacle interactions in Weakly and Fully nonlinear theories. Black lines indicate the location of the upper and lower boundaries, and the pycnocline depth is shown in blue 19
2.4 Effect of changing depth on KdV and DJL Solutions 20
2.5 Variation of blocking parameters 22

3.1 Schematic of laboratory experimental setup 37
3.2 Coefficients of KdV theory for three stratifications as a function of total depth 42
3.3 ISW breaker types as a function of wave steepness ($a/L\lambda$) and slope steepness (s) 46
3.4 Wave form for each stratification prior to interaction with slope 47
3.5 Raw experimental images for experiment Surf_s0.2_S_lab (surging) 49
3.6 Numerical Simulation and Experimental PIV for surging experiments Surf_s0.2_S_num and Surf_s0.2_S_lab 50
3.7 Raw experimental images for experiment Surf_s0.2_L_lab (collapsing) . . 51
3.8 Numerical Simulation and Experimental PIV for collapsing experiments Surf_s0.2_L_num and Surf_s0.2_L_lab 52
3.9 Numerical Simulations for plunging experiment in thin tanh stratification, and equivalent wave in broad tanh stratification 53
3.10 Richardson number plots of surging in the broad stratification 56

3.11 Side and transverse plane plots of 3-D shoaling simulations in broad stratification . . . 57
3.12 3-D plots of shoaling simulations in broad stratification . . . 58
3.13 Numerical Simulation for fissioning simulation Surf_s0.033_M_num and Broa_s0.033_M_num . . . 59
3.14 Experimental snapshot of fissioning-like experiment Surf_s0.067_L_lab . 60
3.15 Time series of energetics measures for a selection of simulations . . . 63
3.16 Vertical structures of N^2 (black) and ϕ (blue) of each stratification in this chapter, thin tanh (left), surface stratification (centre) and broad tanh stratification (right). Each normalised by the maximum value. . . . 68

4.1 Schematics for fissioning internal wave simulations . . . 87
4.2 Example fissioning wave in surface stratification (Exp. Surface-10L) . . . 90
4.3 Turbulent fissioning wave in surface stratification (Exp. Surface-30L) . . 91
4.4 Example fissioning wave in broad stratification (Exp. Broad-10L) . . . 92
4.5 Along-slope Hovmoller plots of near-bed horizontal velocity and volume of dense fluid . . . 94
4.6 Number of pulses formed as a function of wave amplitude a . . . 95
4.7 Relationship between wave and pulse parameters . . . 96
4.8 Plot of $u - c_p$ for pulses formed in two simulations . . . 97
4.9 Time-evolution of pulse properties a_p, c_p and λ_p . . . 98
4.10 Time series of normalised density and kinetic energy at the bottom for the point where the slope intersects with the pycnocline location . . . 99

5.1 Schematic of the creation of USP Diagrams . . . 110
5.2 Schematics for USP case study simulations . . . 114
5.3 Time sequence of collapsing shoaling with USP . . . 115
5.4 Late time step comparisons of USPs for ISW breaking types . . . 117
5.5 Time sequence of cold shear instability with USP . . . 119
5.6 Cold shear instability Regions of Interest . . . 120
5.7 Passive dye comparison for cold shear instabilities . . . 121
5.8 Region of Interest plots for cold shear instability with less diffusive tracer (K-H dye 1) . . . 122
5.9 Region of Interest plots for cold shear instability with more diffusive tracer (K-H dye 2) . . . 123
5.10 SM1: Time sequence of surging shoaling wave with USP . . . 127

5.11 SM2: Time sequence of plunging shoaling wave with USP 128
5.12 SM3: Time sequence of fissioning shoaling wave with USP 129

6.1 Schematic of laboratory experimental setup 138
6.2 Hovmoller time series of horizontal velocity 143
6.3 Time series of float motion 145
6.4 Time series of float velocities for experiments, and Float Motion Model . 146
6.5 Histograms of fluid velocities impacting the float 148
6.6 Relationships between float length, wave parameters and float speed . . . 149
6.7 Time sequences showing medium float experiments 151
6.8 Time sequences showing long float experiments 152
6.9 Time sequences showing medium curved edge float experiments 153
6.10 Time series evolution of streamlines of flow around medium floats 155

List of Tables

3.1 Summary table of parameters for example experiments and simulations in chapter 3 44
3.2 Complete table of parameters for simulations in chapter 3 70
3.3 Complete table of parameters for experiments in chapter 3 73

4.1 Summary of simulation parameters for chapter 4 88

6.1 Table of experimental parameters in chapter 6 140

List of Notation

Symbol	Description
a	Wave Amplitude
a_p	Pulse Amplitude
b_{0-5}	ICW Parameterisation Coefficients
$B(x,t)$	Temporal and horizontal structure of the velocity field
c	Measured Wave Propagation Speed
c_0	Linear Longwave Speed
c_{DJL}	Wave propagation speed from DJL
c_p	Pulse Speed
d	Slope Transition distance
dx, dy, dz	Resolution in x, y, z
Fr	Froude Number
g	Gravity
h	Local Bottom Depth
h'	Derivative of bottom depth
h_1	Thickness of Lower Layer
h_2	Thickness of Upper Layer
h_i	Thickness of affected layer
$h_{adj-pyc}$	Behind-gate Depth
h_f	Step Height
h_{pyc}	Pycnocline thickness
h_{mix}	Transition Deepness
h_r	Obstacle thickness
H	Tank Depth
H_s	Slope height
I	USP Cartesian grid cell weighting
Ir	Iribarren Number (internal)
$\boldsymbol{k}$	Unit vector
L	Characteristic length scale

Symbol	Description
L_f	Float Length
L_s	Slope Length
L_x, L_y, L_z	Tank Length, width and depth
N^2	Buoyancy Frequency
N_x, N_y, N_z	Number of x, y, z gridpoints
n_{ij}	Unit tangent vector
$\boldsymbol{P}$	Pressure
Re	Reynolds Number = cH/ν
Re_w	IW Reynolds Number = cA/ν
Ri	Richardson Number
Ri_0	Bulk Ri
t	Time
T	Temperature
T_0	Reference temperature
s	Topographic Slope
S_w	Wave steepness
(u, w)	Velocity Field in (x, y, z) directions
$\boldsymbol{u}$	Velocity vector
U	Float Velocity
$u_{DJL}(x, z)$	DJL Velocity
u_{PIV}	PIV Velocity
V	Total volume of tank
W_{ij}	USP Weighting per cell
x_f	Float Location
x	Cartesian coordinate in horizontal direction along tank
y	Cartesian coordinate in horizontal direction across tank
z	Cartesian coordinate in vertical direction
z_{mix}	Interface Depth
z_{pyc}	Pycnocline Depth
α	Nonlinear KdV term
β	Dispersion parameter in KdV
ε	Viscous dissipation
η	Isopycnal Displacement

Symbol	Description
θ	Variable 2 in USP
κ	Scalar Diffusivity
λ	Wavelength
λ_p	Pulse Wavelength
ν	Shear viscosity
Ξ	Passive tracer
ρ	Density
ρ_0	Feeder Bucket Density
ρ_1	Upper layer density & reference density
ρ_2	Lower Layer Density
ρ'	Density Anomaly
ρ_f	Float Density
$\Delta\rho$	$\rho_2 - \rho_1$
$\bar{\rho}$	Background Density Profile
$\boldsymbol{\tau}$	Viscous force on BBL
τ_{ij}	Stress tensor
ϕ	Vertical Structure for KdV
ϕ_d	Rate of change of BPE
ϕ_i	rate of conversion of energy from internal to PE
ϕ_m	Rate of conversion of energy to mixing
Φ	Variable 1 in USP
ω	Vorticity
Ω	Enstrophy
APE	Available Potential Energy
AW	Atlantic Water
BBL	Bottom/Benthic Boundary Layer
BPE	Background Potential Energy
DJL	Dubreil-Jacotin-Long equation
EOF	Empirical Orthogonal Function
ISW	Internal Solitary Wave
KdV	Korteweg–De Vries equation
KE	Kinetic Energy
K-H	Kelvin-Helmholtz

Symbol	Description
PDF	Probability Density Function
PIV	Particle Image Velocimetry
PTV	Particle Tracking Velocimetry
ROI	Region of Interest
SPINS	Spectral Parallel Incompressible Navier-Stokes Solver
WCS	World Coordinate System
WNL	Weakly Non-linear

Chapter 1

Introduction

1.1. Motivation

The ocean is always in motion, driven at the largest scales by energy from the wind, tides, and heat from the sun. Such motions can be characterised at all scales from global circulation at the size of the planet $O(10,000$ km) to dissipation at molecular scales $O(1$ mm), and energy cascades from these largest scales to the smallest scales where they dissipate as heat. The oceans deliver practical utility to human society, as a major food source (FAO, 2020), a source of recreation, and as a major component of the climate system, buffering the impacts of greenhouse gas emissions (McKinley *et al.*, 2017), producing oxygen, and redistributing heat, nutrients and water. As each of these (and the entire Earth system) relies on the processes involved in this cascade of energy it is important to understand the processes at all scales. Of these motions, most people are familiar with surface gravity waves in the ocean. These waves formed at the free surface of the ocean occur due to gravity acting to restore water (the denser fluid of air and water) to a horizontal level. Similarly, beneath the ocean's surface internal waves occur in a water column where two layers with differing densities occur (Cushman-Roisin & Beckers, 2011), and buoyancy acts to restore displaced water parcels to their equilibrium state. These internal waves were first identified scientifically by Nansen (1897) via the dead-water effect, and following those observations the first experimental studies soon followed (Ekman, 1904).

Under certain circumstances, these internal waves can be "internal solitary waves" (ISWs) similar to the surface solitary waves discovered by John Scott Russell (1844). They are described as behaving in a solitary manner; that is, their propagation speed is

proportional to amplitude, and their form is preserved on interaction with other internal solitary waves (at least to leading order (see Lamb, 1998)). Formally, these waves exist as a balance between non-linear wave steepening and linear wave dispersion, and this balance enables the waves to travel long distances without change of form (Apel *et al.*, 1985). As a result, stable ISWs are effective mechanisms for transporting energy and scalar properties (including sediment) (Boegman & Stastna, 2019). The waves themselves are able to induce horizontal currents $O(0.1 - 1\ \mathrm{m\,s^{-1}})$ (Boegman & Stastna, 2019), and are found commonly in the stratified coastal seas.

ISWs propagating over a flat bed exist in effectively steady state, and can be understood analytically. Such theories can provide us with insight into the form and behaviour of these waves. Weakly nonlinear theories valid for small ISWs (e.g. Korteweg–De Vries (KdV), Lamb & Yan, 1996) can be solved analytically, whilst fully nonlinear theory, valid for large amplitude waves (e.g. Dubriel-Jacotin–Long (DJL), Turkington *et al.*, 1991; Stastna & Lamb, 2002) need to be solved numerically (e.g. Dunphy *et al.*, 2011). However, when ISWs interact with boundaries, either due to shallowing topography, or obstacles at the surface, they transform in a manner that can only be fully understood by time-resolving simulations incorporating viscous dissipation, or through observations (in the laboratory or field).

This stage in the evolution of an ISW is of particular oceanographic interest. After transporting energy and mass long distances, the waves produce vertical (diapycnal) mixing (Carr *et al.*, 2012). Benthic ecosystems such as mangroves and coral reefs benefit from upwelling of cold, nutrient-rich deep waters as a result of internal bores produced by ISWs propagating upslope (shoaling) (Green *et al.*, 2019), whilst the change to the thermal environment they produce may increase reef resilience to climate change (Reid *et al.*, 2019). Shoaling ISWs are also implicated as a major component of the global cascade of energy, the process by which internal tides degenerate (Munk, 1966; Lamb, 2014; Sarkar & Scotti, 2017), whilst shoaling ISWs have been linked to large sedimentary structures and sediment transport processes (Reeder *et al.*, 2011).

One region of the planet where non-linear internal waves (such as ISWs) are particularly important is the Arctic Ocean. It can be shown that poleward of the critical latitude (where the period of the principal tidal constituent exceeds the local inertial period), linear internal tides cannot freely propagate and develop, and so their non-linear counterparts (of which ISWs form a major component) become far more important (Rippeth *et al.*, 2017). Such ISWs have been recently observed in newly ice-free regions (at the Marginal Ice Zone) (Kozlov *et al.*, 2017), and are known to interact with sea ice (e.g. Czipott *et al.*, 1991;

Marchenko *et al.*, 2010), indicating another important scenario of ISW-obstacle interaction.

In the Arctic Ocean, thin, cold, fresh surface waters (freshened by the high river discharge into the basin (Carmack *et al.*, 2016)) are separated from a warm salty Atlantic Water layer by the Cold Halocline Layer; a layer of increasing salinity with depth, but more or less constantly cold temperatures (Bluhm *et al.*, 2015). The deep Atlantic Water layer contains enough heat to melt the entire sea ice cap (a characteristic feature of the Arctic) within a few years (Rudels *et al.*, 1996; Turner, 2010; Carmack *et al.*, 2016; Polyakov *et al.*, 2017). Currently, strong haline stratification suppresses vertical mixing in the Arctic Ocean (Turner, 2010), but sea ice thickness and extent are sensitive to modest $O(1\,\mathrm{W\,m^{-2}})$ increases in ocean heat flux (Maykut & Untersteiner, 1971). These low rates of vertical mixing, and the critical sensitivity to changes in those rates make the modest transfers of energy from the tide to turbulence by tidally generated internal waves particularly significant in this region (Rippeth *et al.*, 2017). This is despite low internal wave energy in the Arctic compared to lower latitudes (Munk, 1966; Morison *et al.*, 1985; Guthrie *et al.*, 2013). Although the exact mechanism is not fully understood, this lower internal wave energy is thought to be linked to weak tidal forcing, and the inability for M2 internal tides to freely propagate north of the critical latitude (Guthrie *et al.*, 2013). Additionally, the presence of sea ice, which forms a lid over the ocean, may play an important role in dampening internal wave energy, both by increasing the dissipation at the surface boundary layer (Morison *et al.*, 1985), and by reducing the input of energy from surface forcing (e.g. wind) (Lincoln *et al.*, 2016). Such mixing rates are also important in the fate of heat in the larger-scale circulation; the observed flux of heat from Atlantic Water (AW) boundary currents cannot be explained from double diffusive fluxes alone (Holloway & Proshutinsky, 2007; Lenn *et al.*, 2009).

However, in recent years, rapid changes to the Arctic have taken place, being one of the fastest warming regions on the planet with a 12.7 % decade^{-1} decline in September Sea Ice extent from the 1979 to 2021 (Meier & Stroeve, 2022), warming of surface waters by 4 °C–5 °C compared to the 1981 to 2010 climatology (Cohen *et al.*, 2014) and so-called "Atlantification" with expansion of the Atlantic Water layer (Polyakov *et al.*, 2017). With a rapidly changing Arctic Ocean, and in particular dramatic losses of sea ice extent, the internal wave energy is, in theory, expected to change in relation to these factors. Yet, Guthrie *et al.* (2013) found no evidence for significant increases in internal wave energy during recent years. As each of these processes interact, and further changes become inevitable, it becomes ever more important to understand the processes mixing the Arctic Ocean in order to determine the overall heat budgets and how this will impact on climate.

1.2. Aims & Objectives

This thesis aims to improve understanding of two processes where ISWs of depression encounter obstacles at the boundary. Firstly, the impact of different stratification types on the breaking of ISWs as they propagate upslope will be investigated. Such interactions with slopes are globally important as a crucial step in the global cascade of energy from tidal to dissipation scales (Munk, 1966), and locally are an important source of mixing, including in the Arctic Ocean, where turbulent heat fluxes associated with conversion of tidal energy to internal tides/waves and mixing can reach over 100 times background levels (Meyer *et al.*, 2017; Fer *et al.*, 2020).

Then, the role of ISWs in the Arctic Ocean will be investigated through a study into how ISWs interact with floating obstacles at the surface, representative of sea ice, and to work towards an understanding of how these waves, and the oceanographic consequences of them, will change in a rapidly changing Arctic.

Chapter 2 introduces key concepts that are important to the thesis, including some exploratory work which helps frame the results in later chapters. Across four research chapters, the interactions of ISWs of depression with obstacles at the boundaries are explored in detail. Chapters 3 and 4 investigate the interaction of ISWs with a slope, identifying for the first time the role of stratification in these processes. The mixing induced by these processes, is further investigated through a new mixing tool presented in chapter 5. Finally, the interaction of ISWs with surface floating obstacles, representing sea-ice, are studied in chapter 6. Whilst there are similarities with this final scenario and the earlier scenarios of ISWs propagating over an obstacle, three key differences are evident: firstly, the floats move; secondly the floats are at the surface, and are therefore more similar to an ISW of elevation passing over an obstacle; and finally the edge effects induced by the presence of a straight-edged step. A final chapter (chapter 7) draws together key conclusions from the thesis, and outlines suggestions for further work. Each of the results chapters includes a more comprehensive introduction to that topic, and the methodology.

1.3. Summary of Methodology

All this is done through process studies at the experimental scale, both laboratory experiments and numerical simulations. This combined numerical and experimental approach allows controlled, systematic studies of the processes and dynamics at play, and for them to be isolated in a way that is impractical for field studies (Dauxois *et al.*, 2021). Whilst

laboratory experiments are able to access regimes that are challenging for analytical and numerical models, numerical modelling provides an excellent counterpart with more complex analysis/diagnostics available such as energetics.

This project uses laboratory experiments, in a 7 m long (ISW) tank (figure 1.1), using the lock release (or step pool) technique, similar to previous ISW experiments (e.g. Kao *et al.*, 1985; Grue *et al.*, 1999; Carr & Davies, 2006; Sutherland *et al.*, 2013; Carr *et al.*, 2019). These experiments involve setting up a salinity stratification, and creating a discontinuity in the pycnocline behind a gate. Upon removal of the gate, a disturbance propagates along the pycnocline as an ISW. Wave propagation and breaking will be recorded using video cameras filming overlapping sections of the tank. The fluid is seeded with 150 µm–300 µm neutrally-buoyant tracer particles of two densities, applied such that seeding particles are dispersed roughly evenly across the water column, and a thin sheet of light along the central axis of the tank illuminates these particles, and against a black backdrop the contrast provided allows visualisation of the flow through the camera (and by direct observation). The DigiFlow software (Dalziel *et al.*, 2007) is used to visualise the flow and carry out Particle Image Velocimetry (PIV) to measure the synoptic flow field.

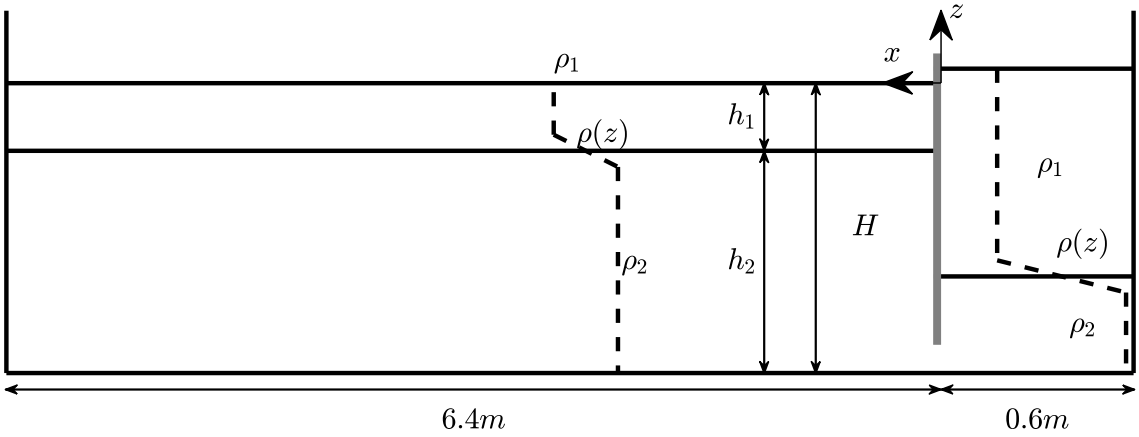


Figure 1.1: Schematic of generic tank setup used throughout this thesis

Alongside the laboratory experiments, numerical modelling with the Spectral Parallel Incompressible Navier-Stokes Solver (SPINS) (Subich *et al.*, 2013) supplements the laboratory work and aids analysis of the dynamics. The combined approach allows for the explanation of the features observed in the laboratory, whilst ensuring the model output is physically realistic. Both methods are discussed in further detail in chapter 3 (§§3.2 and 3.3), with specific methods for each study further described in those chapters. Quantification of the flow field via PIV is an involved method, requiring considerable setup and post-processing computation time, but gives valuable quantitative visualisation of the

flow features throughout the water column, including the boundary layers and pycnocline. Combining laboratory experiments with numerical simulations in this way, allows the mixing and energetics associated with flow features to be identified, whilst also dynamically and visually explained.

Chapter 1

References

Apel, J., Holbrook, J., Liu, A. & Tsai, J. 1985 The Sulu Sea Internal Soliton Experiment. *Journal of Physical Oceanography* **15** (12), 1625–1651, https://doi.org/10.1175/1520-0485(1985)015¡1625:TSSISE¿2.0.CO;2.

Bluhm, B. A., Kosobokova, K. N. & Carmack, E. C. 2015 A tale of two basins: An integrated physical and biological perspective of the deep Arctic Ocean. *Progress in Oceanography* **139**, 89–121, https://doi.org/10.1016/j.pocean.2015.07.011.

Boegman, L. & Stastna, M. 2019 Sediment Resuspension and Transport by Internal Solitary Waves. *Annual Review of Fluid Mechanics* **51** (1), 129–154, https://doi.org/10.1146/annurev-fluid-122316-045049.

Carmack, E. C., Yamamoto-Kawai, M., Haine, T. W. N., Bacon, S., Bluhm, B. A., Lique, C., Melling, H., Polyakov, I. V., Straneo, F., Timmermans, M.-L. & Williams, W. J. 2016 Freshwater and its role in the Arctic Marine System: Sources, disposition, storage, export, and physical and biogeochemical consequences in the Arctic and global oceans. *Journal of Geophysical Research: Biogeosciences* **121** (3), 675–717, https://doi.org/10.1002/2015JG003140.

Carr, M. & Davies, P. A. 2006 The motion of an internal solitary wave of depression over a fixed bottom boundary in a shallow, two-layer fluid. *Physics of Fluids* **18** (1), 016601, https://doi.org/10.1063/1.2162033.

Carr, M., King, S. E. & Dritschel, D. G. 2012 Instability in internal solitary waves with trapped cores. *Physics of Fluids* **24** (1), https://doi.org/10.1063/1.3673612.

Carr, M., Sutherland, P., Haase, A., Evers, K. U., Fer, I., Jensen, A., Kalisch, H., Berntsen, J., Parau, E., Thiem, O. & Davies, P. A. 2019 Laboratory Experiments on Internal Solitary Waves in Ice-Covered Waters. *Geophysical Research Letters* https://doi.org/10.1029/2019GL084710.

Cohen, J., Screen, J. A., Furtado, J. C., Barlow, M., Whittleston, D., Coumou, D., Francis, J., Dethloff, K., Entekhabi, D., Overland, J. & Jones, J. 2014 Recent Arctic amplification and extreme mid-latitude weather. *Nature Geoscience* **7** (9), 627–637, https://doi.org/10.1038/ngeo2234, arXiv: 1204.5445.

Cushman-Roisin, B. & Beckers, J. 2011 *Introduction to Geophysical Fluid Dynamics : Physical and Numerical Aspects*. Academic Press.

Czipott, P. V., Levine, M. D., Paulson, C. A., Menemenlis, D., Farmer, D. M. & Williams, R. G. 1991 Ice flexure forced by internal wave packets in the Arctic Ocean. *Science* **254** (5033), 832–835, https://doi.org/10.1126/science.254.5033.832.

Dalziel, S. B., Carr, M., Sveen, J. K. & Davies, P. A. 2007 Simultaneous synthetic schlieren and PIV measurements for internal solitary waves. *Measurement Science and Technology* **18** (3), 533–547, https://doi.org/10.1088/0957-0233/18/3/001.

Dauxois, T., Peacock, T., Bauer, P., Caulfield, C. P., Cenedese, C., Gorlé, C., Haller, G., Ivey, G. N., Linden, P. F., Meiburg, E., Pinardi, N., Vriend, N. M. & Woods, A. W. 2021 Confronting Grand Challenges in environmental fluid mechanics. *Phys. Rev. Fluids* **6** (2), 020501, https://doi.org/10.1103/PhysRevFluids.6.020501.

Dunphy, M., Subich, C. & Stastna, M. 2011 Spectral methods for internal waves: Indistinguishable density profiles and double-humped solitary waves. *Nonlinear Processes in Geophysics* **18** (3), 351–358, https://doi.org/10.5194/npg-18-351-2011.

Ekman, V. W. 1904 On Dead-Water: Being a description of the so-called phenomenon often hindering the headway and navigation of ships in Norwgian Fjords and elsewhere, and an experimental investigation of its causes etc. In *The Norwegian North Polar Expedition 1893-1896: Scientific Results* (ed. F. Nansen), , vol. 5, pp. 1–150. London: Fridtjof Nansen Fund for the Advancement of Science, Longmans, Green, and Co.

FAO 2020 *The State of World Fisheries and Aquaculture 2020: Sustainability in Action*. *The State of World Fisheries and Aquaculture (SOFIA)* 2020 - SOFIA 2020. Rome, Italy: FAO.

Fer, I., Koenig, Z., Kozlov, I. E., Ostrowski, M., Rippeth, T. P., Padman, L., Bosse, A. & Kolås, E. 2020 Tidally Forced Lee Waves Drive Turbulent Mixing Along the Arctic Ocean Margins. *Geophysical Research Letters* **47** (16), e2020GL088083, https://doi.org/10.1029/2020GL088083.

Green, R. H., Jones, N. L., Rayson, M. D., Lowe, R. J., Bluteau, C. E. & Ivey, G. N. 2019 Nutrient fluxes into an isolated coral reef atoll by tidally driven internal bores. *Limnology and Oceanography* **64** (2), 461–473, https://doi.org/10.1002/lno.11051.

Grue, J., Jensen, A., Rusas, P. & Sveen, J. K. 1999 Properties of large-amplitude internal waves. *Journal of Fluid Mechanics* **380**, 257–278, https://doi.org/10.1017/S0022112098003528.

Guthrie, J. D., Morison, J. H. & Fer, I. 2013 Revisiting internal waves and mixing in the Arctic Ocean. *Journal of Geophysical Research: Oceans* **118** (8), 3966–3977, https://doi.org/10.1002/jgrc.20294.

Holloway, G. & Proshutinsky, A. 2007 Role of tides in Arctic ocean/ice climate. *Journal of Geophysical Research: Oceans* **112** (C4), https://doi.org/10.1029/2006JC003643.

Kao, T. W., Pan, F. & Renouard, D. 1985 Internal solitons on the pycnocline: Generation, propagation, and shoaling and breaking over a slope. *Journal of Fluid Mechanics* **159**, 19–53, https://doi.org/10.1017/S0022112085003081.

Kozlov, I. E., Zubkova, E. V. & Kudryavtsev, V. N. 2017 Internal Solitary Waves in the Laptev Sea: First Results of Spaceborne SAR Observations. *IEEE Geoscience and Remote Sensing Letters* **14** (11), 2047–2051, https://doi.org/10.1109/LGRS.2017.2749681.

Lamb, K. G. 1998 Are Solitary Internal Waves Solitons? *Studies in Applied Mathematics* **101** (3), 289–308, https://doi.org/10.1111/1467-9590.00094.

Lamb, K. G. 2014 Internal Wave Breaking and Dissipation Mechanisms on the Continental Slope/Shelf. *Annual Review of Fluid Mechanics* **46** (1), 231–254, https://doi.org/10.1146/annurev-fluid-011212-140701.

Lamb, K. G. & Yan, L. 1996 The evolution of internal wave undular bores: Comparisons of a fully nonlinear numerical model with weakly nonlinear theory. *Journal of Physical Oceanography* **26** (12), 2712–2734, https://doi.org/10.1175/1520-0485(1996)026¡2712:TEOIWU¿2.0.CO;2.

Lenn, Y. D., Wiles, P. J., Torres-Valdes, S., Abrahamsen, E. P., Rippeth, T. P., Simpson, J. H., Bacon, S., Laxon, S. W., Polyakov, I. V., Ivanov, V. & Kirillov, S. 2009 Vertical mixing at intermediate depths in the Arctic boundary current. *Geophysical Research Letters* **36** (5), L05601, https://doi.org/10.1029/2008GL036792.

Lincoln, B. J., Rippeth, T. P., Lenn, Y. D., Timmermans, M. L., Williams, W. J. & Bacon, S. 2016 Wind-driven mixing at intermediate depths in an ice-free Arctic Ocean. *Geophysical Research Letters* **43** (18), 9749–9756, https://doi.org/10.1002/2016GL070454.

Marchenko, A. V., Morozov, E. G., Muzylev, S. V. & Shestov, A. S. 2010 Interaction of short internal waves with the ice cover in an Arctic fjord. *Oceanology* **50** (1), 18–27, https://doi.org/10.1134/S0001437010010029.

Maykut, G. A. & Untersteiner, N. 1971 Some results from a time-dependent thermodynamic model of sea ice. *Journal of Geophysical Research (1896-1977)* **76** (6), 1550–1575, https://doi.org/10.1029/JC076i006p01550.

McKinley, G. A., Fay, A. R., Lovenduski, N. S. & Pilcher, D. J. 2017 Natural Variability and Anthropogenic Trends in the Ocean Carbon Sink. *Annual Review of Marine Science* **9** (1), 125–150, https://doi.org/10.1146/annurev-marine-010816-060529.

Meier, W. N. & Stroeve, J. 2022 An Updated Assessment of the Changing Arctic Sea Ice Cover. *Oceanography* **35** (3/4), 10–19, arXiv: 27182690.

Meyer, A., Fer, I., Sundfjord, A. & Peterson, A. K. 2017 Mixing rates and vertical heat fluxes north of Svalbard from Arctic winter to spring. *Journal of Geophysical Research: Oceans* **122** (6), 4569–4586, https://doi.org/10.1002/2016JC012441.

Morison, J. H., Long, C. E. & Levine, M. D. 1985 Internal wave dissipation under sea ice. *Journal of Geophysical Research* **90** (C6), 11959, https://doi.org/10.1029/jc090ic06p11959.

Munk, W. H. 1966 Abyssal recipes. *Deep-Sea Research and Oceanographic Abstracts* **13** (4), 707–730, https://doi.org/10.1016/0011-7471(66)90602-4.

Nansen, F. 1897 *Farthest North: Being the Record of a Voyage of Exploration of the Ship "Fram" 1893-96 and of a Fifteen Months' Sleigh Journey by Dr. Nansen and Lieut. Johansen*, , vol. 1. London, UK: Constable.

Polyakov, I. V., Pnyushkov, A. V., Alkire, M. B., Ashik, I. M., Baumann, T. M., Carmack, E. C., Goszczko, I., Guthrie, J., Ivanov, V. V., Kanzow, T., Krishfield, R., Kwok, R., Sundfjord, A., Morison, J., Rember, R. & Yulin, A. 2017 Greater role for Atlantic inflows on sea-ice loss in the Eurasian Basin of the Arctic Ocean. *Science (New York, N.Y.)* **356** (6335), 285–291, https://doi.org/10.1126/science.aai8204.

Reeder, D. B., Ma, B. B. & Yang, Y. J. 2011 Very large subaqueous sand dunes on the upper continental slope in the South China Sea generated by episodic, shoaling deep-water internal solitary waves. *Marine Geology* **279** (1-4), 12–18, https://doi.org/10.1016/j.margeo.2010.10.009.

Reid, E. C., DeCarlo, T. M., Cohen, A. L., Wong, G. T., Lentz, S. J., Safaie, A., Hall, A. & Davis, K. A. 2019 Internal waves influence the thermal and nutrient environment on a shallow coral reef. *Limnology and Oceanography* **64** (5), 1949–1965, https://doi.org/10.1002/lno.11162.

Rippeth, T. P., Vlasenko, V., Stashchuk, N., Scannell, B. D., Green, J. A. M., Lincoln, B. J. & Bacon, S. 2017 Tidal Conversion and Mixing Poleward of the Critical Latitude (an Arctic Case Study). *Geophysical Research Letters* **44** (24), 12,349–12,357, https://doi.org/10.1002/2017GL075310.

Rudels, B., Anderson, L. G. & Jones, E. P. 1996 Formation and evolution of the surface mixed layer and halocline of the Arctic Ocean. *Journal of Geophysical Research* **101** (C4), 8807, https://doi.org/10.1029/96JC00143.

Sarkar, S. & Scotti, A. 2017 From Topographic Internal Gravity Waves to Turbulence. *Annual Review of Fluid Mechanics* **49** (1), 195–220, https://doi.org/10.1146/annurev-fluid-010816-060013.

Scott Russell, J. 1844 The Wave of Translation in the Oceans of Water, Air and Ether. In *Report of The*, pp. 311–390. York: John Murray.

Stastna, M. & Lamb, K. G. 2002 Large fully nonlinear internal solitary waves: The effect of background current. *Physics of Fluids* **14** (9), 2987–2999, https://doi.org/10.1063/1.1496510.

Subich, C. J., Lamb, K. G. & Stastna, M. 2013 Simulation of the Navier-Stokes equations in three dimensions with a spectral collocation method. *International Journal for Numerical Methods in Fluids* **73** (2), 103–129, https://doi.org/10.1002/fld.3788.

Sutherland, B. R., Barrett, K. J. & Ivey, G. N. 2013 Shoaling internal solitary waves. *Journal of Geophysical Research: Oceans* **118** (9), 4111–4124, https://doi.org/10.1002/jgrc.20291.

Turkington, B., Eydeland, A. & Wang, S. 1991 A Computational Method for Solitary Internal Waves in a Continuously Stratified Fluid. *Studies in Applied Mathematics* **85** (2), 93–127, https://doi.org/10.1002/sapm199185293.

Turner, J. S. 2010 The Melting of Ice in the Arctic Ocean: The Influence of Double-Diffusive Transport of Heat from Below. *Journal of Physical Oceanography* **40** (1), 249–256, https://doi.org/10.1175/2009JPO4279.1.

CHAPTER 2

Background and Key Concepts

2.1. Internal Waves

Many physical phenomena can be described in terms of wave motion, and in the special case of waves generated by the the balance of gravity as a restoring force (bringing the system to it's undisturbed state) and inertia (which causes the system to overshoot this undisturbed state) they are termed are gravity waves. Where they occur at the interface of two fluids of different density they are internal gravity waves (IWs). Due to the much smaller relative density difference between the layers than surface gravity waves, IWs typically have lower frequency and propagation speeds than surface waves, but for an equal energy input, have much larger amplitude than surface waves. IWs in the ocean are generated at a range of spatial and temporal scales, but away from boundaries, surprisingly converge onto spectra that apply universally, such as Garrett & Munk (1972, 1975), that describes the distribution of waves between the buoyancy frequency (the highest possible frequency set by the stratification) and the lowest stable frequency at the inertial frequency (set by rotational constraints). This indicates that instabilities and wave-wave interactions rapidly transfer energy from newly-generated waves across this spectrum.

Under certain circumstances, IWs become nonlinear internal solitary waves (ISWs). Where ISWs exist and have small amplitude (specifically, $a \ll H$, where a is wave amplitude and H water depth), the system can be assumed to be weakly nonlinear (WNL), an assumption that gives way to the Korteweg-de-Vries theory (KdV), which is used in this thesis as an analysis tool. The KdV theory expands the equations in terms of two small parameters, the wave amplitude (or nonlinear parameter) and aspect ratio (or dispersion

parameter). The structure of the perturbation velocity and buoyancy fields is assumed to be separable, with the vertical structure, $\phi(z)$, determined by the solution of a linear eigenvalue problem:

$$\phi_{zz} + \frac{N^2(z)}{c_0^2}\phi = 0 \tag{2.1}$$

where $\phi(0) = \phi(H) = 0$. Here c_0 is the linear, longwave phase speed for each mode, and in this study focus is on mode–1 waves, or those waves with the largest value of c_0 for a given stratification.

The temporal and horizontal structure, $B(x,t)$, of the velocity field is governed by the KdV equation

$$B_t = -c_0 B_x + \alpha B B_x + \beta B_{xxx} \tag{2.2}$$

where subscripts denote partial derivatives, and the non-linearity, α, and dispersion, β, parameters are determined from the eigenvalue problem via integration (Lamb & Yan, 1996; Helfrich & Melville, 2006).

Various other WNL models have been derived, a number of which are reviewed and compared to laboratory experiments in Ostrovsky & Stepanyants (2005). Each of these have the advantage of having exact solutions which providing insight into the form and behaviour of ISWs. In many situations, laboratory, numerical and field observations produce ISWs for which the WNL assumption is clearly invalid, i.e. the waves are large amplitude. Fully nonlinear theories offer an exact model of large ISWs, but unfortunately solutions do not exist analytically and instead must be computed numerically. However, doing so remains much less computationally expensive than time-resolved Navier-Stokes solvers. Examples of these fully nonlinear equations are the DJL equation (Turkington *et al.*, 1991; Stastna & Lamb, 2002) and Miyata-Choi-Camassa (MCC) (Choi & Camassa, 1999; Miyata, 1985). For a two layer system, the MCC system is in excellent agreement with both lock gate experiments similar to those presented here, and DJL solutions (Camassa *et al.*, 2006). The DJL equation is used as a wave model throughout this thesis, and is a nonlinear, elliptic eigenvalue problem for the isopycnal displacement $\eta(x,z)$,

$$\nabla^2\eta + \frac{N^2(z-\eta)}{c^2}\eta = 0 \tag{2.3}$$

where $N^2(z-\eta)$ is the square of the buoyancy frequency evaluated at the height of the isopycnal far upstream $z - \eta(x,z)$ (the upstream height), and c the wave propagation speed. The equation was solved by a pseudospectral method with a version of the software used publicly available at `https://github.com/mdunphy/DJLES`.

In a frame of reference moving with the wave $\rho(x - ct, z) = \bar{\rho}(z - \eta)$, where $\bar{\rho}$ is the background density profile, and is chosen for use here due to the simplicity of applying it to the range of continuous stratifications in the laboratory.

ISWs therefore belong to a family of internal waves, and in themselves can be categorised in a variety of ways. They are closely related to lee waves, and are a subset of Nonlinear Internal Waves (NLIWs), and these terms can be used interchangeably (although they have different formal definitions). The primary classification of an ISW is the mode of the wave, referring to the vertical velocity function (shown for the first two modes for comparison in figure 2.1). ISWs of mode-1 displace isopycnals in one direction only, whilst mode-2 ISWs displace isopycnals in opposing directions (figure 2.1) (Yang *et al.*, 2010). Within those first two modes, up to 90 % of the baroclinic energy is captured, whilst higher modes account for the remaining energy. The fastest propagating mode, mode-1 waves are further classified into ISWs of depression and elevation, depending if isopycnals are displaced vertically downward or upward respectively from rest, and further still where considerably different dynamics arise where there is a linear stratification reaching the surface, and the wave can be described as having a trapped core. Such stable trapped cores of fluid can be analytically derived for ISW mode-1 waves of depression (Derzho & Grimshaw, 1997; Lamb, 2003; Lien *et al.*, 2012; Luzzatto-Fegiz & Helfrich, 2014), and have been observed in numerical experiments (e.g. Lamb, 2003; Helfrich & White, 2010; King *et al.*, 2011; He *et al.*, 2019), in the laboratory (Grue *et al.*, 2000; Carr *et al.*, 2008*b*), as well as in limited field observations in the South China Sea (Lien *et al.*, 2012). Likewise, these trapped cores can occur at the lower boundary for an ISW of elevation, where the linear stratification meets the lower boundary.

2.2. Mixing and Instabilities in ISWs

In various locations ISWs, and specifically the mixing induced by ISW-induced instabilities, have been identified as the primary mixing mechanism, including the Scotian Shelf break (Sandstrom & Elliott, 1984), the Australian North West Shelf (Holloway, 1991), and the Portuguese Shelf (Jeans & Sherwin, 2001). The various instability mechanisms, often induced by the interactions with topography or obstacles which will be explored later in this thesis, are briefly introduced and reviewed here. Instabilities that form in waves can generally be understood as stratified shear instabilities, boundary layer instabilities or convective instabilities.

Behind the trough of an ISW of depression over a smooth fixed bottom boundary exists

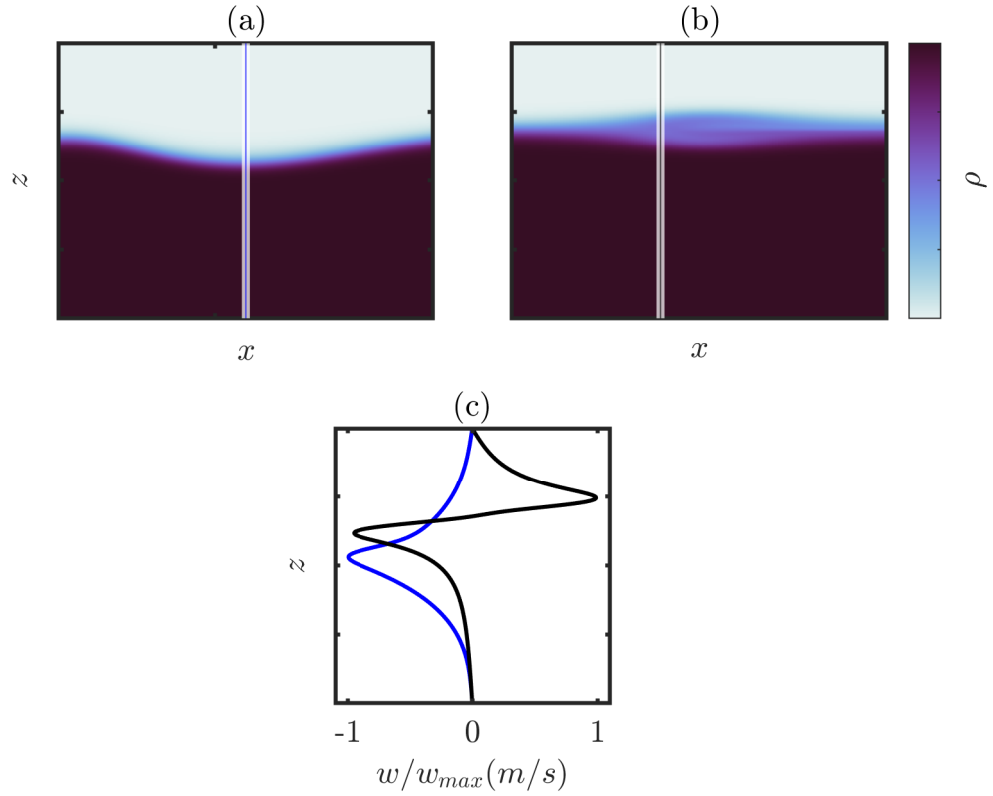


Figure 2.1: Schematic of modal structures for Internal Solitary Waves, showing (*a*) density of mode-1 wave, (*b*) density of a mode-2 wave, and (*c*) profile of vertical velocity through centre of mode-1 wave (blue) and mode-2 wave (black). Each quantity normalised by the maximum.

an adverse pressure gradient region, where the separation of the wave-induced velocity produces a separation bubble (figure 2.2). Where the ISW is large enough, and the fluid shallow enough, the separation bubble can become an unsteady boundary layer jet in the direction of wave motion (figure 2.2) (Carr & Davies, 2006; Diamessis & Redekopp, 2006). The formation of this boundary layer jet soon after the passage of the ISW indicates its existence is due to the adverse pressure gradient formed as the fluid at the rear of the wave decelerates (Carr & Davies, 2006) (figure 2.2). When wave amplitude exceeds a critical wave amplitude (itself dependent on the wave Reynolds number, $Re_w = \frac{c_0 H}{\nu}$), the passage of large amplitude ISWs over a Bottom Boundary can further result in vortex shedding, where the boundary layer jet becomes unstable (Diamessis & Redekopp, 2006; Carr *et al.*, 2008*a*; Ellevold & Grue, 2023). These vortexes, which can extend high up into the water column (Diamessis & Redekopp, 2006), can be an effective means of fluid and sediment mixing from the near-bottom layer to higher in the water column (Bogucki & Redekopp,

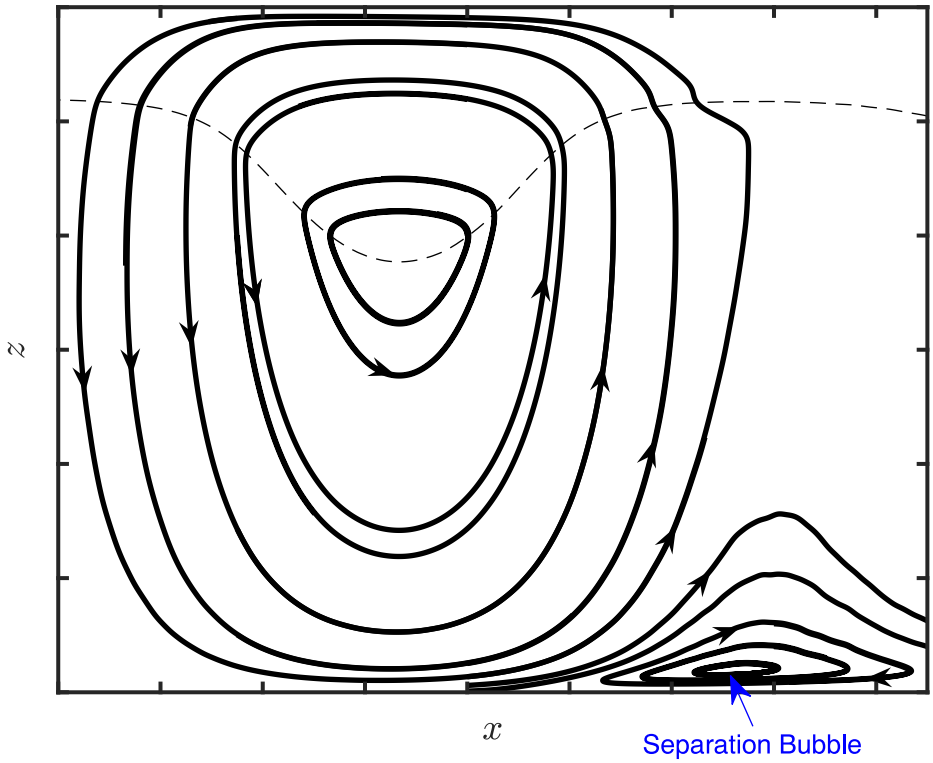


Figure 2.2: Schematic of a boundary layer separation for an ISW of depression propagating right to left. Dashed line indicates the location of the pycnocline, and solid black lines are streamlines, with the direction indicated with arrows. Boundary layer separation is visible in the rear of the wave. A supplementary movie of an experiment from Carr & Davies (2006) (Movie) is provided for additional clarity.

1999; Stastna & Lamb, 2002). This has been described as a global instability meaning that it is strongly coherent in space and time (e.g. Bogucki & Redekopp, 1999; Carr *et al.*, 2008*a*). The global instability manifests itself as coherent patches of vorticity which are shed upwards from the separation bubble and follow the wave form, and has been linked to sediment transport as an important mechanism by which ISWs can enhance sediment re-suspension (Bogucki *et al.*, 2005; Stastna & Lamb, 2008). Such features are enhanced by the shoaling process (Aghsaee *et al.*, 2012; Xu & Stastna, 2020).

The stratified shear instability is another mechanism for mixing in ISWs, which occur where the velocity shear is aligned with the density gradient, and results in mixing. Specifically for ISWs, the shear instability only occurs when both the minimum Richardson number, $Ri = -\frac{g}{\rho_0}\frac{d\rho/dz}{(du/dz)^2}$ in the pycnocline is less than about 0.1, and the horizontal extent that this minimum criteria is met exceeds around 80 % of the wavelength (Fructus *et al.*, 2009; Lamb & Farmer, 2011). These instabilities produce the familiar Kelvin-Helmholtz (K-H) instability across the pycnocline, and as a result are effective at mixing fluid between

the two layers, and have been identified in field observations of ISWs in numerous locations (Farmer & Dungan Smith, 1980; Moum *et al.*, 2003; Orr & Mignerey, 2003; Lamb & Farmer, 2011).

Convective instabilities can also occur in internal waves where the fluid velocity exceeds the wave propagation speed. Small scale convective instabilities have been reported in laboratory experiments (with a lower homogeneous layer and a linearly stratified upper layer) (Carr *et al.*, 2008*b*), and at the field scale (Lien *et al.*, 2012). Larger scale plunging Taylor-Rayleigh like instabilities have been reported in various studies of shoaling internal solitary waves (e.g. Lamb, 2003; Sutherland *et al.*, 2013), where the fluid velocity exceeds the wave speed (which is slowing as the wave changes depth), and the rear face of the wave overturns. These are both examples of a convective instability formed from the fluid velocity exceeding the wave propagation speed, leading to overturning of denser fluid above less dense fluid.

2.3. Interactions with an obstacle

2.3.1. *Weakly and Fully nonlinear theory of obstacle interaction*

The evolution of an ISW as it propagates around a boundary obstacle can, at a basic level, be investigated through the evolution of terms in the weakly nonlinear KdV theory (equation (2.1)), and the wave parameters in fully nonlinear DJL (equation (2.3)) as the depth of the wave is changed. Whilst theory-specific studies apply more complex analysis to these scenarios, (e.g. Grimshaw *et al.*, 2014), and the exact nature of these changes can only be interpreted via time-resolving simulations or experiments, such simple analysis can yield useful insights into expected wave behaviours that will be explored fully in later chapters. A similar analysis is applied to each of the stratifications in chapter 3 (§3.4).

Four scenarios are considered (see figure 2.3), each over a range of obstacle heights, h_r removed from the upper or lower layer. The Surface Narrowing Depression wave scenario (figure 2.3*a*) has the pycnocline above mid depth (and so ISWs of depression would form), and the 'obstacle' is at the surface. This scenario is identical to the Bottom narrowing elevation case (figure 2.3*d*), but upside down. Likewise, the bottom narrowing depression wave scenario (figure 2.3*b*) as the 'obstacle' is at the surface, and is identical (but upside down) to the surface narrowing elevation case (figure 2.3*c*). All calculations are in a thin tanh stratification (or the version flipped in the z axis). Where the obstacle is at the top boundary, it is seen to represent a shelf at the surface (named surface narrowing), and when at the bottom boundary it is seen to represent a step on the bottom (named bottom

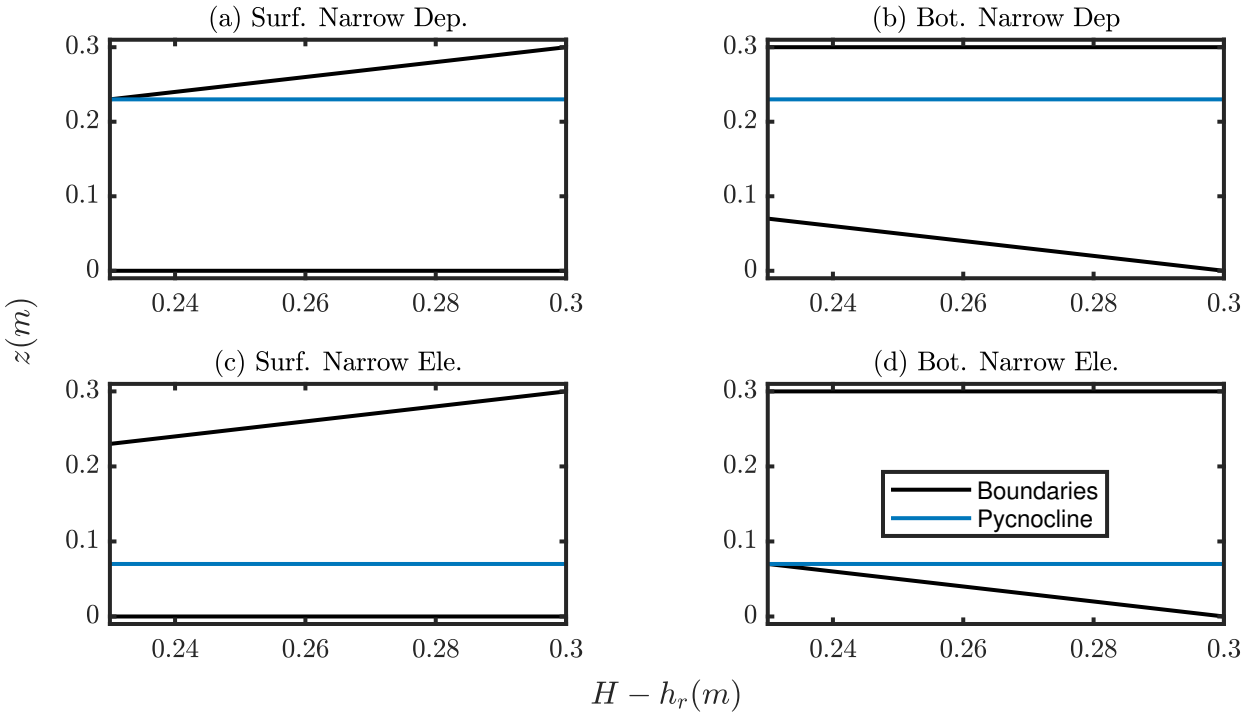


Figure 2.3: Schematic of four scenarios considered for obstacle interactions in Weakly and Fully nonlinear theories. Black lines indicate the location of the upper and lower boundaries, and the pycnocline depth is shown in blue

narrowing). Note that for KdV this assumes the wave has fully re-adjusted to a given stratification, whilst for DJL, it assumes a wave with the same Available Potential Energy at all stages. In both cases, energy transfers or temporary states as the wave adjusts are not considered.

For KdV, in all cases, as $H - h_r$ decreases (i.e. as the step size increases), linear wave speed c_0 and α (the nonlinearity coefficient) decrease (figure 2.4*a, b*), whilst β (the dispersion coefficient) is increasing (figure 2.4*c*). As h_r reaches h_i (where h_i, the depth of the affected layer is 0.07 m) the nonlinearity coefficient, α reaches 0, and undergoes a polarity change. This is the fission process discussed in greatest detail in chapter 4. The fastest changes occur for surface narrowing (depression) or bottom narrowing (elevation), in each case where the thinner layer is the one being compressed further.

DJL also provides insights here. In agreement with KdV, the wave speed, c decreases with decreasing $H - h_r$ (figure 2.4*d*), but the evolution of amplitude and wavelength is dependent on the boundary which layer is narrowing (figure 2.4*e, f*). In the case of a bottom narrowing ISW of depression/surface narrowing ISW of elevation, amplitude reduces slightly as $H - h_r$ decreases, whilst λ increases (figure 2.4*e, f*), indicating a flattening of

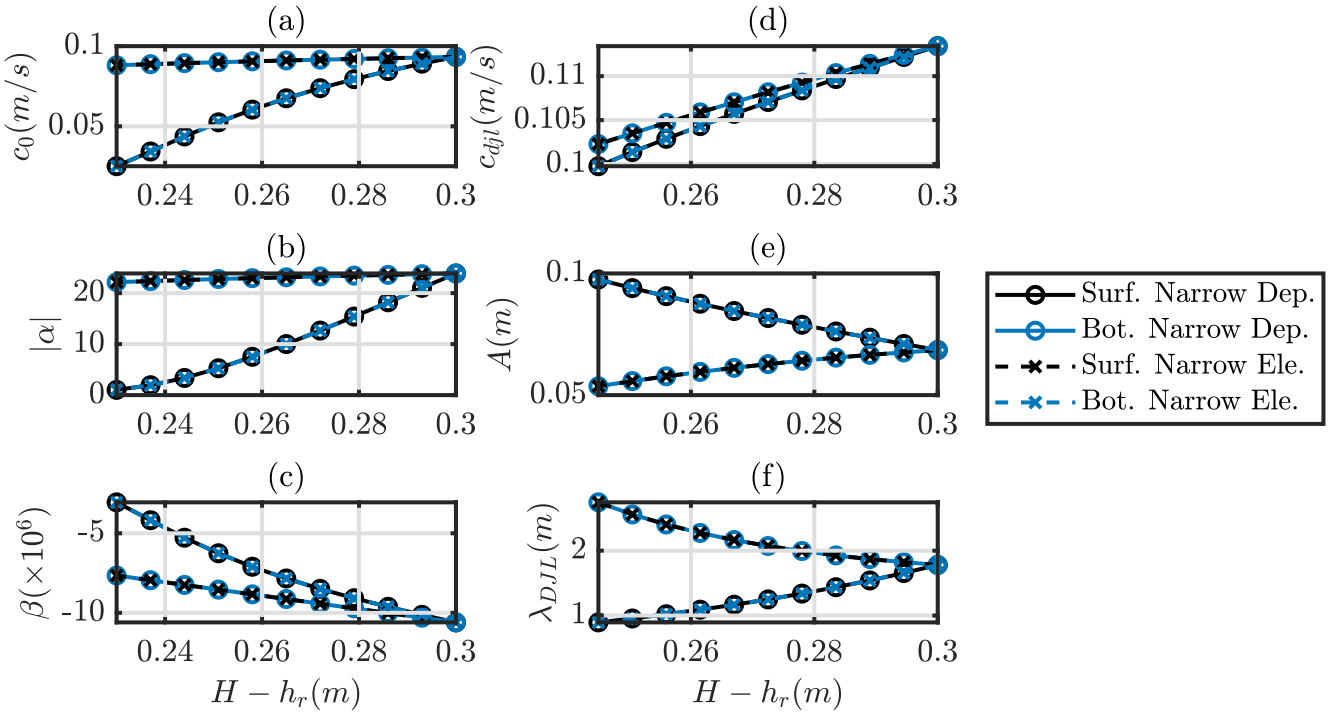


Figure 2.4: Effect of changing depth on (left) KdV solution with linear wave speed, c_0, (top), nonlinearity coefficient, α, (middle), and dispersion coefficient, β (bottom). Effect of changing depth on (right) DJL solution, with wave speed, c_{djl} (top), wave amplitude, a (middle), and wavelength, λ (bottom). Note the limits of $H - h_r$ axis extents differ slightly due to constraints of the models.

waves as they pass over a step. Conversely, an ISW of depression passing under a shelf would instead increase in amplitude, whilst the wavelength decreases indicating steepening of waves. The process is not linear, and so the wave steepness also changes in a non-linear fashion. Such calculations make the clearly incorrect assumption that energy is conserved fully during the process of passing over a step.

The same results for both models occur if the system is flipped, e.g. a bottom narrowing for an ISW of depression is flipped to a surface narrowing for an ISW of elevation. Whilst not employed here, this opens a potential avenue for future ISW-ice interaction work, drawing on the existing literature, and future experimental setups for an ISW of elevation interacting with a step at the bottom.

2.3.2. *Blocking and parameterisations*

ISWs approaching and interacting with an obstacle are affected in a way that force the wave to adapt to the new boundary conditions. The extent and nature of this interaction

between any flow and an obstacle is often considered in the context of a blocking parameter (or dimensionless obstacle size), describing the extent to which the flow is interrupted by the obstacle. In the internal wave literature, a number of blocking parameters have been proposed (e.g. Vlasenko & Hutter, 2001; Zhang *et al.*, 2022; Talipova *et al.*, 2013). Whilst Vlasenko & Hutter (2001) use $B = h_r/h_i$, both Talipova *et al.* (2013) and Zhang *et al.* (2022) instead use $B = \frac{h_r - h_i}{a}$, thus incorporating the wave amplitude, a, too. By re-formulating this as $B = \frac{h_r}{h_i + a}$, a blocking parameter is derived that considers the effective layer depth at maximum pycnocline displacement ($h_i + a$), so that B represents the percentage of that effective layer depth blocked by the flow (0 for a flow with no obstacle, and 1 for a fully blocked wave).

The distribution of energy in the system can be split into energy transmitted onto the obstacle (as a wave), reflected from it (as a wave), or dissipated. However B is defined, as it increases, so does the level to which the wave is reflected, or dissipated, and less of the wave can be transmitted over the obstacle. Such features are reported not only for ISWs propagating onto a shelf, but for flow under an ice keel, indicating a universality to this relationship, with remarkable similarity between situations (figure 2.5), despite the differences in scale and application.

Beyond this, assuming an interaction does occur, a variety of literature has explored the interaction of ISWs and a linearly sloping bottom boundary. In these situations, $B \geq 1$ and the obstacle is fully blocking further wave propagation. At this stage, wave behaviours are further declassified based on the slope, and wave steepness, the nature of which is discussed in chapters 3 & 4. An conceptual understanding of blocking is further useful for understanding results in chapter 6.

2.4. Assumptions & Simplifications

Process-based experiments make assumptions which are part of these simplifications of the real world. Within the experiments presented here, the assumptions of a smooth bottom, the absence of surface waves, and the Boussinesq approximation (that density variability is small compared to the absolute density) are all made.

A further assumption is made that rotation can be neglected. This can be justified through a parameter ϵ, which relates the time of one revolution of the Earth, T, and an indicative flow timescale (calculated as the time taken by a particle to cover distance L at speed U). Where $\epsilon = T\frac{U}{L} \lesssim 1$, rotation is important, if not then it can be neglected. At the laboratory scale, $L = 7\,\text{m}$, $U \sim 0.1\,\text{m}\,\text{s}^{-1}$, and T =86 164.1 s, such that $\epsilon = 1231$. As

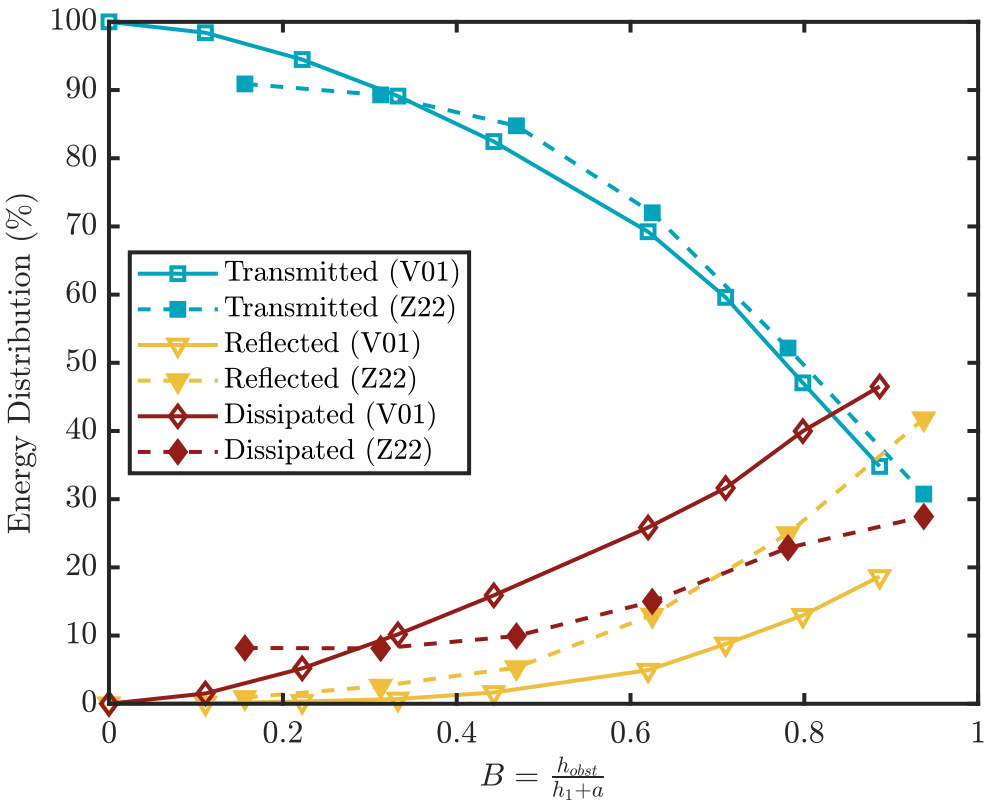


Figure 2.5: Effects of varying the internal wave blocking parameter, $B = \frac{h_r}{h_i+a}$ on the distribution of internal wave energy after interaction with the obstacle for two past studies Vlasenko & Hutter (2001) (V01) and Zhang *et al.* (2022) (Z21)

such, rotation in the laboratory experiments can be neglected. To consider the applicability of this assumption at the field scale, $L \sim 100 - 20000$ m, $U \sim 0.05 - 0.5$ m s^{-1}. Over the length scales of ISW propagation therefore, rotation becomes important (as indicated by curved wavefronts in SAR imagery), but the processes explored in this thesis take place over shorter timescales, where $\epsilon > 1$, and so the assumption that rotation can be neglected remains valid.

Most simulations throughout this thesis are two-dimensional. Such a simplification considerably improves computational efficiency, however results in the assumption that variability and instabilities in the third (x, y) dimension are not significant. The impact of the 2-D assumption is not fully agreed upon (Rivera-Rosario *et al.*, 2023). Whilst spanwise structures that only exist in three dimensions can generate potential vorticity (Winters & D'Asaro, 1994), mixing and dissipation (Arthur & Fringer, 2014); there is evidence that such spanwise structures only become significant once the wave has become unstable. Therefore, and so the leading order effects (driven by 2-D instabilities) can be investigated

in two dimensions. The effects of these three-dimensional effects are explored further in chapter 3 §3.5.5, and chapter 5 §5.3.2.

The effects of no slip lower and upper boundary conditions in driving boundary layer instability is discussed in 2.2. Whilst a fixed lower boundary is a necessity in the laboratory, the upper boundary condition can be changed from free slip to no slip by adding a rigid lid. The effects of this choice are discussed in Carr *et al.* (2008*b*). In this thesis a rigid lid is employed for the experiments in chapter 3 to aid comparison with simulations. In chapter 6 floats are used in the laboratory experiments giving rise to a mixed upper boundary condition that cannot be directly compared with the numerical simulations (which are limited to fixed boundary conditions). Boundary layers at the side walls are assumed to be negligible in the laboratory, with visualisation of the flow taken at the centre of the tank (with $Ly = 0.4$m, the visualisation plane is ≈ 0.2m from the boundary) to ensure this is the case.

2.5. Non dimensional parameters and scaling

In fluid dynamics, dimensionless numbers derived from governing equations can be a useful reference in identifying how phenomenon may scale up or down. For stratified flows such as those in this thesis, the Reynolds number Re, which is a ratio of inertial to viscous effects, is particularly relevant. From this, one can infer the tendency of the flow towards turbulence. A flow with low Re is typically dominated by laminar flow, whilst a flow with high Re is typically dominated by turbulence. This draws an important distinction between flows at the laboratory scale (which are similar between the laboratory and numerical simulations), which typically have low Re (in this thesis $Re_w \approx O10^2 - 10^4$)) and flows in the field, where Re can be much higher ($Re_w \approx O10^6 - 10^8$).

Elsewhere in the thesis, variables are scaled by a representative reference value, for example velocities are commonly scaled by a measure of wave speed. Such scaling (producing variables that are dimensionless) is valuable in assessing how these behaviours may be represented at different scales, from the laboratory to the ocean scale.

2.6. Numerical Model

Throughout this thesis, the direct numerical simulations (DNS) are carried out with the pseudospectral code SPINS (Spectral Parallel Incompressible Navier Stokes Solver) developed by (and fully documented in) Subich *et al.* (2013). The model solves the full

stratified Navier–Stokes equations subject to the Boussinesq approximation:

$$\frac{\partial \boldsymbol{u}}{\partial t} + \boldsymbol{u} \cdot \boldsymbol{\nabla} \boldsymbol{u} = -\frac{1}{\rho_1} \boldsymbol{\nabla} P + \nu \nabla^2 \boldsymbol{u} - \frac{\rho g}{\rho_1} \hat{k}, \tag{2.4}$$

$$\boldsymbol{\nabla} \cdot \boldsymbol{u} = 0, \tag{2.5}$$

$$\frac{\partial \rho}{\partial t} + \boldsymbol{u} \cdot \boldsymbol{\nabla} \boldsymbol{\rho} = \kappa \nabla^2 \rho, \tag{2.6}$$

where $\boldsymbol{u}$ is the velocity, P is the pressure, ρ is the density and where the reference density of the fluid is ρ_1. The physical parameters are gravity g (set at 9.81 ms^{-2}), the shear viscosity ν (set at 10^{-6} $\mathrm{m}^2\mathrm{s}^{-1}$, chosen to be consistent with the physical value) and scalar diffusivity κ (set at 10^{-7} $\mathrm{m}^2\mathrm{s}^{-1}$). The unit vector in the vertical direction is denoted by $\hat{k}$. The pressure term is solved implicitly, and the boundaries are considered solid (so there are no free surface effects).

The solver uses a spectral collocation method, time stepped by an Adams-Bashforth adaptive three level time discretisation. This combines some key features of higher order models in terms of accuracy at the range of scales needed for such simulations, with efficient scaling that benefits users of modern high performance computing capabilities, and crucially for the purposes of this thesis, the ability to implement 1-D topography using global coordinate mapping. The accuracy is third order in time, and spectral accuracy in space (order of accuracy increases with the number of grid points), the ability to achieve this accuracy in the presence of topography is the key achievement of SPINS. Finally, pseudo-spectral methods (as used by SPINS) do not suffer from spurious diffusion and dispersion, an important factor when comparing with laboratory experiments. Instead, an exponential numerical filter is applied in SPINS (this is discussed in detail in (Deepwell, 2018)).

The code has been thoroughly validated in a number of different configurations (e.g. boundary layer instabilities (e.g. Harnanan *et al.*, 2017), internal wave generation, internal solitary wave propagation, interaction with topography (e.g. Deepwell *et al.*, 2017)) and is available for download and open access use through its online manual:

https://wiki.math.uwaterloo.ca/fluidswiki/index.php?title=SPINS_User_Guide

The code is implemented via a combination of the primary code (which manages the evolution of the simulation), casefiles (which formulate the setup of each experimental setup), and configuration files (which specify specific problem parameters, changed for each experiment). The first two of these are compiled, whilst the configuration files spins.conf)

is the one the user interacts with most. The simplest setup for generating an ISW via the lock gate method can be found in the mode1_mode2 casefile at the SPINS_main GitLab repository. Throughout this thesis, the casefiles and configuration files specific to each chapter and simulation are available within the data shared for that chapter.

Chapter 2

References

Aghsaee, P., Boegman, L., Diamessis, P. J. & Lamb, K. G. 2012 Boundary-layer-separation-driven vortex shedding beneath internal solitary waves of depression. *Journal of Fluid Mechanics* **690**, 321–344, https://doi.org/10.1017/jfm.2011.432.

Arthur, R. S. & Fringer, O. B. 2014 The dynamics of breaking internal solitary waves on slopes. *Journal of Fluid Mechanics* **761** (2), 360–398, https://doi.org/10.1017/jfm.2014.641.

Bogucki, D. J. & Redekopp, L. G. 1999 A mechanism for sediment resuspension by internal solitary waves. *Geophysical Research Letters* **26** (9), 1317–1320, https://doi.org/10.1029/1999GL900234.

Bogucki, D. J., Redekopp, L. G. & Barth, J. 2005 Internal solitary waves in the Coastal Mixing and Optics 1996 experiment: Multimodal structure and resuspension. *Journal of Geophysical Research C: Oceans* **110** (2), 1–19, https://doi.org/10.1029/2003JC002253.

Camassa, R., Choi, W., Michallet, H., Rusås, P.-O. & Sveen, J. K. 2006 On the realm of validity of strongly nonlinear asymptotic approximations for internal waves. *Journal of Fluid Mechanics* **549**, 1–23, https://doi.org/10.1017/S0022112005007226.

Carr, M. & Davies, P. A. 2006 The motion of an internal solitary wave of depression over a fixed bottom boundary in a shallow, two-layer fluid. *Physics of Fluids* **18** (1), 016601, https://doi.org/10.1063/1.2162033.

Carr, M., Davies, P. A. & Shivaram, P. 2008*a* Experimental evidence of internal solitary wave-induced global instability in shallow water benthic boundary layers. *Physics of Fluids* **20** (6), 066603, https://doi.org/10.1063/1.2931693.

Carr, M., Fructus, D., Grue, J., Jensen, A. & Davies, P. A. 2008*b* Convectively induced shear instability in large amplitude internal solitary waves. *Physics of Fluids* **20** (12), 126601, https://doi.org/10.1063/1.3030947.

Choi, W. & Camassa, R. 1999 Fully nonlinear internal waves in a two-fluid system. *Journal of Fluid Mechanics* **396**, 1–36, https://doi.org/10.1017/S0022112099005820.

Deepwell, D. 2018 High resolution simulations of mode-2 internal waves : Transport , shoaling , and the influence of rotation by. PhD thesis, University of Waterloo.

Deepwell, D., Stastna, M., Carr, M. & Davies, P. A. 2017 Interaction of a mode-2 internal solitary wave with narrow isolated topography. *Physics of Fluids* **29** (7), 076601, https://doi.org/10.1063/1.4994590.

Derzho, O. G. & Grimshaw, R. 1997 Solitary waves with a vortex core in a shallow layer of stratified fluid. *Physics of Fluids* **9** (11), 3378–3385, https://doi.org/10.1063/1.869450.

Diamessis, P. J. & Redekopp, L. G. 2006 Numerical investigation of solitary internal wave-induced global instability in shallow water benthic boundary layers. *Journal of Physical Oceanography* **36** (5), 784–812, https://doi.org/10.1175/JPO2900.1.

Ellevold, T. J. & Grue, J. 2023 Calculation of internal-wave-driven instability and vortex shedding along a flat bottom. *Journal of Fluid Mechanics* **966**, A40, https://doi.org/10.1017/jfm.2023.476.

Farmer, D. M. & Dungan Smith, J. 1980 Tidal interaction of stratified flow with a sill in Knight Inlet. *Deep Sea Research Part A. Oceanographic Research Papers* **27** (3), 239–254, https://doi.org/10.1016/0198-0149(80)90015-1.

Fructus, D., Carr, M., Grue, J., Jensen, A. & Davies, P. A. 2009 Shear-induced breaking of large internal solitary waves. *Journal of Fluid Mechanics* **620**, 1–29, https://doi.org/10.1017/S0022112008004898.

Garrett, C. & Munk, W. 1972 Space-Time scales of internal waves. *Geophysical Fluid Dynamics* **3** (3), 225–264, https://doi.org/10.1080/03091927208236082.

Garrett, C. & Munk, W. 1975 Space-time scales of internal waves: A progress report. *Journal of Geophysical Research (1896-1977)* **80** (3), 291–297, https://doi.org/10.1029/JC080i003p00291.

Grimshaw, R., Guo, C., Helfrich, K. & Vlasenko, V. 2014 Combined Effect of Rotation and Topography on Shoaling Oceanic Internal Solitary Waves. *Journal of Physical Oceanography* **44** (4), 1116–1132, https://doi.org/10.1175/JPO-D-13-0194.1.

Grue, J., Jensen, A., Rusås, P. O. & Sveen, J. K. 2000 Breaking and broadening of internal solitary waves. *Journal of Fluid Mechanics* **413**, 181–217, https://doi.org/10.1017/S0022112000008648.

Harnanan, S., Stastna, M. & Soontiens, N. 2017 The effects of near-bottom stratification on internal wave induced instabilities in the boundary layer. *Physics of Fluids* **29** (1), 016602, https://doi.org/10.1063/1.4973502.

He, Y., Lamb, K. G. & Lien, R. C. 2019 Internal solitary waves with subsurface cores. *Journal of Fluid Mechanics* **873**, 1–17, https://doi.org/10.1017/jfm.2019.407.

Helfrich, K. R. & Melville, W. K. 2006 Long nonlinear internal waves. *Annual Review of Fluid Mechanics* **38** (1), 395–425, https://doi.org/10.1146/annurev.fluid.38.050304.092129.

Helfrich, K. R. & White, B. L. 2010 A model for large-amplitude internal solitary waves with trapped cores. *Nonlinear Processes in Geophysics* **17** (4), 303–318, https://doi.org/10.5194/npg-17-303-2010.

Holloway, P. E. 1991 On dissipation of internal tides. In *Tidal Hydrodynamics* (ed. B.B. Parker), pp. 449–466. John Wiley & Sons, Ltd.

Jeans, D. & Sherwin, T. 2001 The evolution and energetics of large amplitude nonlinear internal waves on the Portuguese shelf. *Journal of Marine Research* **59** (3), https://doi.org/10.1357/002224001762842235.

King, S. E., Carr, M. & Dritschel, D. G. 2011 The steady-state form of large-amplitude internal solitary waves. *Journal of Fluid Mechanics* **666**, 477–505, https://doi.org/10.1017/S0022112010004301.

Lamb, K. G. 2003 Shoaling solitary internal waves: On a criterion for the formation of waves with trapped cores. *Journal of Fluid Mechanics* **478**, 81–100, https://doi.org/10.1017/S0022112002003269.

Lamb, K. G. & Farmer, D. 2011 Instabilities in an Internal Solitary-like Wave on the Oregon Shelf. *Journal of Physical Oceanography* **41** (1), 67–87, https://doi.org/10.1175/2010JPO4308.1.

Lamb, K. G. & Yan, L. 1996 The evolution of internal wave undular bores: Comparisons of a fully nonlinear numerical model with weakly nonlinear theory. *Journal of Physical Oceanography* **26** (12), 2712–2734, https://doi.org/10.1175/1520-0485(1996)026¡2712:TEOIWU¿2.0.CO;2.

Lien, R. C., D'Asaro, E. A., Henyey, F., Chang, M. H., Tang, T. Y. & Yang, Y. J. 2012 Trapped core formation within a shoaling nonlinear internal wave. *Journal of Physical Oceanography* **42** (4), 511–525, https://doi.org/10.1175/2011JPO4578.1.

Luzzatto-Fegiz, P. & Helfrich, K. R. 2014 Laboratory experiments and simulations for solitary internal waves with trapped cores. *Journal of Fluid Mechanics* **757**, 354–380, https://doi.org/10.1017/jfm.2014.501.

Miyata, M. 1985 An internal solitary wave of large amplitude. *La mer* **23**, 43–48.

Moum, J. N., Farmer, D. M., Smyth, W. D., Armi, L. & Vagle, S. 2003 Structure and generation of turbulence at interfaces strained by internal solitary waves propagating shoreward over the continental shelf. *Journal of Physical Oceanography* **33** (10), 2093–2112, https://doi.org/10.1175/1520-0485(2003)033¡2093:SAGOTA¿2.0.CO;2.

Orr, M. H. & Mignerey, P. C. 2003 Nonlinear internal waves in the South China Sea: Observation of the conversion of depression internal waves to elevation internal waves. *Journal of Geophysical Research* **108** (C3), 3064, https://doi.org/10.1029/2001JC001163.

Ostrovsky, L. A. & Stepanyants, Y. A. 2005 Internal solitons in laboratory experiments: Comparison with theoretical models. *Chaos: An Interdisciplinary Journal of Nonlinear Science* **15** (3), 037111, https://doi.org/10.1063/1.2107087.

Rivera-Rosario, G., Diamessis, P. J., Lien, R.-C., Lamb, K. G. & Thomsen, G. N. 2023 Three-dimensional perspective on a convective instability and transition to turbulence in an internal solitary wave of depression shoaling over gentle slopes. *Environ Fluid Mech* **23** (5), 1015–1035, https://doi.org/10.1007/s10652-022-09844-7.

Sandstrom, H. & Elliott, J. A. 1984 Internal tide and solitons on the Scotian Shelf: A nutrient pump at work. *Journal of Geophysical Research: Oceans* **89** (C4), 6415–6426, https://doi.org/10.1029/JC089iC04p06415.

Stastna, M. & Lamb, K. G. 2002 Vortex shedding and sediment resuspension associated with the interaction of an internal solitary wave and the bottom boundary layer. *Geophysical Research Letters* **29** (11), 1512, https://doi.org/10.1029/2001GL014070.

Stastna, M. & Lamb, K. G. 2008 Sediment resuspension mechanisms associated with internal waves in coastal waters. *Journal of Geophysical Research: Oceans* **113** (C10), https://doi.org/10.1029/2007JC004711.

Subich, C. J., Lamb, K. G. & Stastna, M. 2013 Simulation of the Navier-Stokes equations in three dimensions with a spectral collocation method. *International Journal for Numerical Methods in Fluids* **73** (2), 103–129, https://doi.org/10.1002/fld.3788.

Sutherland, B. R., Barrett, K. J. & Ivey, G. N. 2013 Shoaling internal solitary waves. *Journal of Geophysical Research: Oceans* **118** (9), 4111–4124, https://doi.org/10.1002/jgrc.20291.

Talipova, T., Terletska, K., Maderich, V., Brovchenko, I., Jung, K. T., Pelinovsky, E. & Grimshaw, R. 2013 Internal solitary wave transformation over a bottom step: Loss of energy. *Physics of Fluids* **25** (3), 032110, https://doi.org/10.1063/1.4797455.

Turkington, B., Eydeland, A. & Wang, S. 1991 A Computational Method for Solitary Internal Waves in a Continuously Stratified Fluid. *Studies in Applied Mathematics* **85** (2), 93–127, https://doi.org/10.1002/sapm199185293.

Vlasenko, V. I. & Hutter, K. 2001 Generation of second mode solitary waves by the interaction of a first mode soliton with a sill. *Nonlinear Processes in Geophysics* **8** (4/5), 223–239, https://doi.org/10.5194/npg-8-223-2001.

Winters, K. B. & D'Asaro, E. A. 1994 Three-dimensional wave instability near a critical level. *Journal of Fluid Mechanics* **272**, 255–284, https://doi.org/10.1017/S0022112094004465.

Xu, C. & Stastna, M. 2020 Instability and cross-boundary-layer transport by shoaling internal waves over realistic slopes. *Journal of Fluid Mechanics* **895**, R6, https://doi.org/10.1017/jfm.2020.389.

Yang, Y. J., Fang, Y. C., Tang, T. Y. & Ramp, S. R. 2010 Convex and concave types of second baroclinic mode internal solitary waves. *Nonlinear Processes in Geophysics* **17** (6), 605–614, https://doi.org/10.5194/npg-17-605-2010.

Zhang, P., Xu, Z., Li, Q., You, J., Yin, B., Robertson, R. & Zheng, Q. 2022 Numerical Simulations of Internal Solitary Wave Evolution Beneath an Ice Keel. *Journal of Geophysical Research: Oceans* **127** (2), e2020JC017068, https://doi.org/10.1029/2020JC017068.

CHAPTER 3

Stratification effects on shoaling Internal Solitary Waves (ISWs)

3.1. Introduction

Across the world's oceans, variations in seawater temperature and salinity stratify the water column, producing conditions where density disturbances can propagate as internal waves. A key aim in physical oceanography is the untangling of processes responsible for the global cascade of energy from planetary-scale mechanical energy inputs (wind and the tides), to dissipation at the Kolmogorov scale. The generation and subsequent degeneration of these internal waves is a key process in this global cascade (Lamb, 2014; Sarkar & Scotti, 2017).

Internal solitary waves (ISWs) are a particular form of internal waves that have amplitude comparable to the pycnocline thickness, and often the overall depth of the water column (e.g. Grue *et al.*, 1999). They are characterised by a balance of nonlinear steepening and wave dispersion, and as a result are able to travel large distances without significant change of form or magnitude. ISWs are found commonly across the world's oceans, and they maintain high levels of research interest due to their effectiveness in transporting energy and scalar properties (Helfrich & Melville, 2006), and for mixing in the ocean (e.g. Huang *et al.*, 2016; Boegman & Stastna, 2019). Typically, internal waves are generated on density interfaces in stably stratified fluids by barotropic motion over topography such as sills, slopes and the shelf edge (e.g. Grue, 2005; da Silva *et al.*, 2015; Rayson *et al.*, 2019), with the evolution of the barotropic internal tide motion into far-field baroclinic mode 1 and higher-mode ISWs being determined by nonlinear steepening mechanisms (Rayson *et al.*, 2019).

Whilst ISWs can travel considerable distance over a flat bottom without change of form, under certain conditions, such as when shoaling, their form can change considerably. As they do so, dissipation produced by the motion of breaking waves, both in the benthic boundary layer (BBL) and the pycnocline, is identified as a key process in the global cascade of energy from global-scale mechanical forcing to dissipation (St Laurent *et al.*, 2011; Sarkar & Scotti, 2017). Yet, these breaking processes remain poorly parameterised and understood (Lamb, 2014; Boegman & Stastna, 2019). Breaking ISWs are also known to induce considerable vertical mixing of heat, nutrients and other scalar properties. Benthic ecosystems such as coral reefs benefit from upwelling of cold, nutrient-rich deep waters as a result of internal bores produced by the ISWs (Green *et al.*, 2019), whilst the change to the thermal environment these waves produce may increase reef resilience to climate change (Reid *et al.*, 2019).

In the field, ISWs of depression shoaling over gentle slopes have frequently been observed evolving into a train of ISWs of elevation (e.g. Orr & Mignerey, 2003; Shroyer *et al.*, 2009; St Laurent *et al.*, 2011). Although these same geophysically realistic slopes are typically difficult to replicate in the laboratory, or in numerical models, laboratory experiments in an 18 m wave tank identified the formation of boluses propagating up-slope from the evolution of periodic waves propagating over gentle slopes (Wallace & Wilkinson, 1988). Additionally, Xu & Stastna (2020) recently identified the role of boundary layer instability in fissioning waves propagating over realistic slopes in a high resolution model. When shoaling, energy transported by the ISWs has been observed to dissipate at rates at least 100 times background levels (Lien *et al.*, 2005), and is used to enhance turbulent mixing (Moum *et al.*, 2003). ISWs induce currents and turbulence at the BBL, enhanced by the shoaling process, which drive sediment re-suspension and transport (Bogucki *et al.*, 1997; Boegman & Stastna, 2019; Deepwell *et al.*, 2020; Zulberti *et al.*, 2020).

Sedimentary transport processes induced by very large episodic shoaling ISWs in the South China Sea have been linked to large sedimentary structures, such as sub-aqueous sand dunes over 16 m in amplitude and 350 m in wavelength (Reeder *et al.*, 2011), with important implications for coastal structures. Ma *et al.* (2016) observed flow structures up-slope of the turning point where ISWs of depression change polarity and where convergence of wave-induced oscillatory currents produced sand waves. Such waves were associated with asymmetrical up-slope transport of sediment and consequent asymmetrical dune form and migration by currents under these ISWs of elevation. Boluses associated with the front of ISWs that have broken are associated with enhanced up-slope sediment and nutrient transport, both as a result of strong up-slope velocities and fluid transport, and re-suspension

by a rotor at the leading edge of the bolus (Hosegood *et al.*, 2004). Such field observations document the complexity of real-world dynamics, providing evidence for the existence of dynamical features identified in laboratory and numerical modelling (e.g. Boegman & Stastna, 2019). However, due to practical and technological constraints field observations cannot obtain the suite of measurements with high temporal and spatial resolution that allow idealised modelling studies to fully understand the underlying fluid dynamics. For this reason, some studies (Walter *et al.*, 2012; Masunaga *et al.*, 2016; Davis *et al.*, 2020) combine field observations with semi-idealised two-dimensional (2-D) models at the field scale to attempt to build a more complete picture of the dynamics. However, fully idealised, laboratory-scale experimental and modelling studies are also capable of sweeping parameter spaces, identifying trends and regimes that represent specific dynamical characteristics.

Numerous efforts have been made to study the breaking processes of shoaling mode-1 ISWs of depression on a linear slope in laboratory experiments (e.g Michallet & Ivey, 1999; Boegman *et al.*, 2005; Sutherland *et al.*, 2013), and numerical models (e.g. Aghsaee *et al.*, 2010; Arthur & Fringer, 2014; Nakayama *et al.*, 2019; Xu & Stastna, 2020). These studies have created a coherent classification scheme for the key breaking processes, namely plunging, collapsing, surging and fission, as the waves shoal (Boegman *et al.*, 2005; Aghsaee *et al.*, 2010; Sutherland *et al.*, 2013; Lamb, 2014; Nakayama *et al.*, 2019). Analogous to studies on surface wave breaking, these studies used an adapted internal wave Iribarren number (Ir) as the ratio between wave steepness (S_w) and slope steepness (s) (Boegman *et al.*, 2005; Sutherland *et al.*, 2013), and an internal wave Reynolds number (Nakayama *et al.*, 2019) to delineate the classifications. In these studies, the validity of 2-D simulations for identifying breaker classification has been shown, with good agreement with corresponding laboratory experiments (e.g. Aghsaee *et al.*, 2010). However, in all of these studies, attention has been restricted to a three-layer stratification of a homogeneous surface and bottom layer, separated by a thin pycnocline, resembling an idealised three-layer ocean. Within the literature, authors have adopted different analytical functions to represent generically the ocean stratification, to describe the variation of density ρ, with depth, z. For example, recent work by Rayson *et al.* (2019) and Manderson *et al.* (2019) has shown that stratification on the Australian NW Shelf can be represented well by a double hyperbolic function. Here, we adopt a hyperbolic tangent function that has been widely used in numerical and laboratory modelling studies (e.g. Maderich *et al.*, 2001; Allshouse & Swinney, 2020; Vieira & Allshouse, 2020),

$$\rho(z) = \rho_1 + \frac{\Delta\rho}{2}\left(1 - \tanh\left(\frac{z + z_{pyc}}{h_{pyc}}\right)\right), \tag{3.1}$$

where ρ_1 is the density of the upper layer, $\Delta\rho$ the change in density through the water column, z_{pyc} the depth of the centre of the pycnocline, and h_{pyc} the pycnocline half thickness.

The idealised three-layer (hereafter named the thin tanh profile) system represents a lower limit of h_{pyc}. Yet, stratification varies across the globe, with associated variability in h_{pyc}, from 50 m in the Labrador Sea (total depth not provided) approaching the three-layer idealised system, to 459 m in the East China Sea, where density varies linearly (or approximated as linearly) with depth over the full water column (Vieira & Allshouse, 2020). With such a variation in pycnocline thickness in the real ocean, it is reasonable to question what impact changing stratification may have on the shoaling dynamics. In simulations with a pycnocline centred at the mid-depth, Vieira & Allshouse (2020) found internal wave bolus size and transport distance to be larger where pycnocline thickness was larger, whilst Arthur *et al.* (2017) investigated the effect of pycnocline thickness on shoaling energetics and mixing. However, no studies to date have investigated the effect of this on the shoaling dynamics of ISWs in the context of breaker type.

In this chapter, the effect of different forms of stratification on ISW shoaling is studied. This is the first time such an investigation has been undertaken where the form of stratification is varied. Combined use of laboratory experiments and numerical simulations is made to investigate the propagation of a mode-1 ISW of depression propagating over a uniformly sloping solid boundary. Three different kinds of stratification are considered (figure 3.1*b*), namely, (i) a system like that studied previously in the literature consisting of a thin, approximately linearly stratified pycnocline sandwiched between homogeneous layers, here referred to as 'thin tanh stratification', (ii) a stratification consisting of a homogeneous bottom layer and an approximately linearly stratified top layer, here referred to as 'surface stratification' as the density gradient is close to the surface and (iii) a water column in which the density varies approximately linearly with depth throughout the full water depth, here referred to as 'broad tanh stratification' due to the large value of h_{pyc}. It is found that the form of the stratification affects both the breaking characteristics of the waves as they shoal and the wave induced BBL, each of which, in turn, affects rates of energy transfer and sediment transport. Moreover, in the broad tanh profile case, it is shown that billows resulting from Kelvin-Helmholtz instabilities can occur on surging breakers. This is the first time such dynamics has been reported in the literature. The combined use of laboratory experiments and 3-D simulations to compare with 2-D simulations is used to validate the use of 2-D simulations for classifying wave breakers in the broad tanh and surface stratifications.

The chapter is organised as follows. In § 3.2 and 3.3 the experimental and numerical methods are described, respectively. In § 3.5, the overall effect of stratification on breaker type is described, followed by a description of the dynamics of each of the breaker types observed in the surface stratification and broad tanh stratification systems. Finally, a discussion of these results, and their relevance to the ocean scale, is given in § 3.6, with a conclusion in § 3.7. An appendix on weakly nonlinear theory places this work in the context of the theoretical framework.

3.2. Experimental Methods

3.2.1. *Laboratory set-up*

The experiments were carried out in a wave tank 7 m long, 0.4 m wide and 0.6 m high with a removable vertical gate situated 0.6 m from one end of the flume separating it into two sections (see figure 3.1*a*). This gate when inserted sat 0.03 m from the base of the tank, separating the main flume ($x > 0$) and the wave generating region ($x < 0$). A rigid acrylic slope was installed with varying height H_s, and base length 1.5 m to form a sloping boundary at the opposite end of the channel to the gate.

The background stratification of the main part of the flume consisted of two layers of miscible brine solution, and represents the surface stratification system. The lower layer was a homogeneous layer of prescribed density $\rho_2 = 1045.5 \pm 0.5\ \mathrm{kg\,m^{-3}}$ with a target depth (once the tank was fully filled) of $h_2 = 0.23$ m, whilst the upper layer was linearly stratified with depth, towards a surface density of $\rho_1 = 1025 \pm 1\ \mathrm{kg\,m^{-3}}$, and target thickness of $h_1 = 0.07$ m. Densities ρ_1 and ρ_2 were measured using a hydrometer, and micro-conductivity sensors were used to determine the depths of each layer and the overall water column structure (see §3.2.2 and Carr *et al.* (2015) for further details). This stratification was set up through the initial filling of the lower layer with ρ_2 density brine, and filling the top linearly stratified layer using the double-bucket and filling sponge system. Two buckets were set up in hydrostatic balance, with ρ_2 brine in a mixer bucket, and fresh water of density $\rho_0 = 999\,\mathrm{kgm^{-3}}$ in a feeder bucket. Brine was slowly drained from the mixer bucket through an array of sponges to ensure laminar flow into the main tank, and therefore prevent mixing into the lower layer. As the mixer bucket drained, water from the feeder bucket (which was connected to the mixer bucket via a valve) was drawn through, diluting the brine solution. The tank was filled to a prescribed depth in this manner. The depth of the mixer and feeder buckets in the present set-up limited the thickness of the stratified layer, thus preventing experiments being carried out for the broad tanh profile

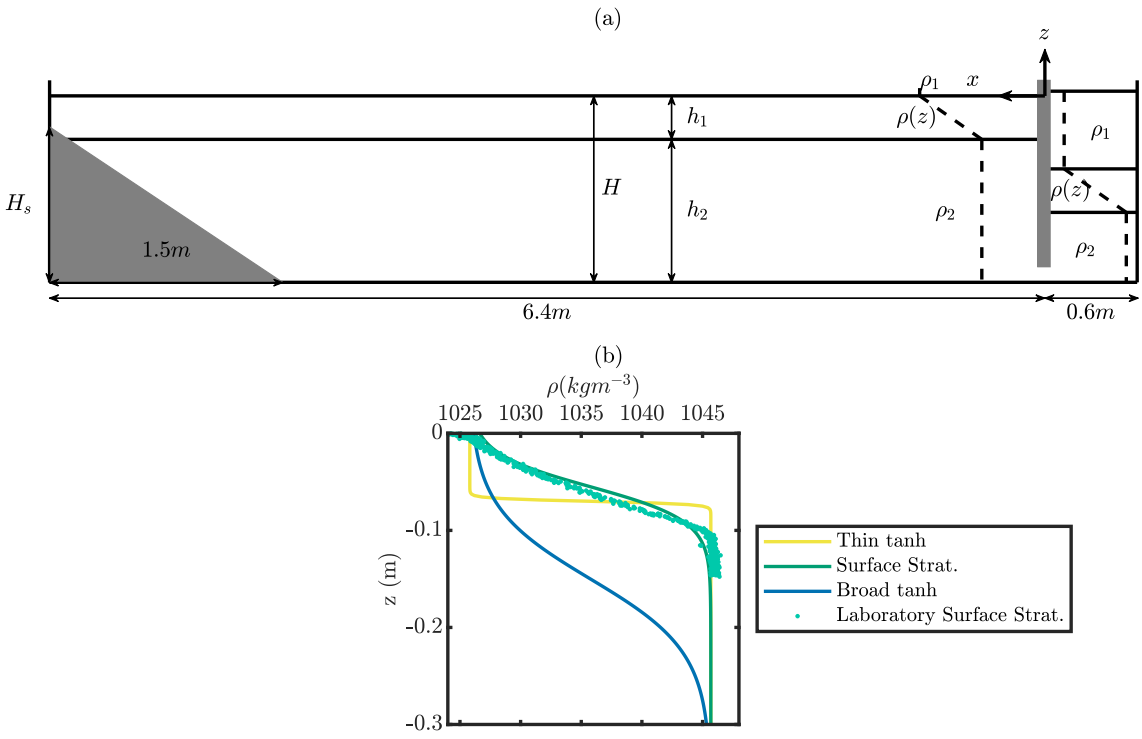


Figure 3.1: (*a*) Schematic diagram of laboratory experiment used throughout this study, and (*b*) profiles from each of the three stratification types used in the corresponding numerical models (solid lines), overlaid with an example stratification profile measured in the laboratory (blue points).

stratification.

To generate a mode-1 ISW, the gate was inserted, and through a single sponge behind the gate, a further volume of ρ_1 density brine added, causing a downwards displacement of the pycnocline and linearly stratified layer behind the gate. The volume of brine added behind the gate was varied to alter wave amplitude, and was determined by the change in total fluid depth, measured before and after filling behind the gate. The total fluid depth after filling behind the gate was fixed at $H = 0.3$ m throughout the study. Due to practical constraints, the density of the lower layer (ρ_2) and that added behind the gate (ρ_1) differed slightly from prescribed values between runs, but the values were measured before the initiation of each run.

The experiment was initiated by the vertical removal of the gate, which by producing a discontinuity and displacement of the pycnocline resulted in the generation of a mode-1 ISW. To aid comparison with numerical studies, and to avoid free surface effects (such as capillary effects which are non-negligible at the laboratory scale) a rigid Styrofoam lid was placed on top of the water column prior to initiation of the experiment (Carr *et al.*, 2008*b*; Grue *et al.*, 2000).

A total of 13 experiments were carried out for a selection of five different starting volumes propagating over three different slopes (with steepness $s = 0.4, 0.2$ and 0.067). This gave a range of wave amplitudes of 0.022 m–0.104 m, and corresponding incident wave steepness $S_w = 0.029 - 0.162$, where $S_w = a/\lambda$, and a and λ were the incident wave's amplitude and wavelength, respectively (details of how these measures were made are given in §3.2.2). The parameters for each wave are shown in table 3.2, and a summary for the waves presented in figures 3.5, 3.6, 3.7, 3.8 and 3.14 is presented in table 3.1. The naming of experiments presented in this chapter is according to the stratification ('Thin', 'Surg', or 'Broa'), slope steepness (e.g. s0.2 a slope of 0.2), an indication of wave amplitude (Small (S), Medium (M), Large (L) or extra large (XL)), along with if the experiment was a numerical simulation ('num') or experiment ('lab').

3.2.2. *Flow Measurement and Visualisation*

Once filled, the density profile of the main tank (e.g. figure 3.1*b*) was measured using high precision micro-conductivity probes (Munro & Davies, 2006), with the surface and bottom densities fixed as measurements of the lower layer and mixing bucket, respectively, made using a hydrometer. These sensors were moved vertically through the water column along a rigid rack and pinion traverse system fitted with a potentiometer to simultaneously measure travel distance (which was converted to depth). Density profiles were measured for the downcast only, and each cast was repeated at least three times to ensure consistency. To match the density profile of the numerical model, the hyperbolic tangent profile (equation (3.1)) was fitted to the laboratory measurements. For the laboratory experiments, z_{pyc} and h_{pyc} were 0.072 ± 0.019 m and 0.033 ± 0.013 m respectively.

The tank was described within a Cartesian coordinate system (x, y, z) (hereafter the world coordinate system, WCS), where the x and z directions denote the horizontal direction of wave propagation (from right to left) and vertical direction against gravity respectively. The WCS origin was chosen so that $x = 0$ is at the horizontal location of the removable gate, and $z = 0$ was at the surface of the water column.

The continuous synoptic velocity and vorticity fields ((u, w) and ω respectively) in a given two-dimensional vertical slice (x, z) of the flow was quantified and visualised using particle image velocimetry (PIV) in the DigiFlow software package (Dalziel *et al.*, 2007). In order to carry out this PIV, a vertical section in the mid-plane of the tank was illuminated by a continuous collimated light sheet from an array of light boxes placed beneath the transparent base of the tank, and three fixed digital video cameras recorded the motions within the light sheet. The cameras (UNIQ UP-1830CL-12B) were set up outside the tank,

synchronised in time and positioned to have overlapping fields of view. They were centred in the vertical direction on the pycnocline to avoid distortion and perspective errors, and maximise visibility of the BBL. The cameras recorded at 30 f.p.s. at 1024×1024 pixels resolution, and were labelled from 1 to 3, with 1 and 3 being, respectively, the cameras closest to and furthest from the top of the slope. Fluid motion was viewed through the movement of light-reflecting neutrally buoyant tracer particles within the vertical light sheet (e.g. figure 3.14*b*). These tracer particles were made of inert "pliolite" 150 µm–300 µm in diameter, and by using two types with different densities had neutral buoyancy over the density range throughout the water column. Past experiments found the settling velocities of these particles to be two orders of magnitude lower than the wave-induced vertical velocities (Dalziel *et al.*, 2007). PIV was then carried out in DigiFlow using the most recent algorithm (2017a) with window size and spacing of 18×18, and 12×12 pixels squared, respectively.

Wave properties were measured using the method described in Carr *et al.* (2019) (their figure 2). The time series function of DigiFlow, which tracks changes of pixel values in a given column, row or defined line over time, was used to measure wave speed, c, and amplitudes, a. Tracing of the streamline coinciding with the pycnocline is possible through these time series due to the high concentration of seeding particles that collects at the density interface. Due to practical considerations, it was not always possible to trace the exact same streamline based on height between runs, however, the closest available streamline to the pycnocline centre was always chosen. Horizontal time series (constructed by stacking a given row of pixels at each frame) from the row corresponding to the maximum streamline displacement allowed wave speed to be measured by calculating the gradient of the line that tracked the wave trough. This method allowed for the identification of regions of the tank where the wave was influenced by the slope, as the gradient being measured became non-linear at this point (and the wave speed non-constant). Vertical time series (constructed from a given column of pixels from each frame) were also used to measure wave amplitude; the maximum displacement of a chosen streamline, with this process repeated at three vertical cross-sections in order to measure variance. Wavelength was determined by calculating the wavelength for a Dubriel-Jacotin-Long (DJL) wave (equation (2.3) see §2.1) with an amplitude corresponding to the experimental determination.

Given η, a wavelength can be estimated by finding the location of the maximum isopycnal displacement (e.g. the location of the wave crest), and following the isopycnal from this point until the vertical distance from the upstream height is halved. Doubling the horizontal distance of this point from the wave crest provides the estimated wavelength.

Fully non-linear DJL solutions have previously been shown to be in good agreement with laboratory waves (Luzzatto-Fegiz & Helfrich, 2014).

3.3. Numerical Model

Simulations were carried out with the pseudospectral code SPINS (Subich *et al.*, 2013) (see chapter 1 §2.6) using the same set-up and generation mechanism as the laboratory experiments in two dimensions. Instead of a physical gate, a hyperbolic smoothing function produced the numerical step in density. To account for this difference, the width of the gate region was 0.3 m in the model (compared with 0.6 m in the laboratory).

Here, the reference density, $\rho_1 = 1026\,\mathrm{kgm}^{-3}$). No-slip boundary conditions (tangential components of $\boldsymbol{u} = 0$ at the boundary) were applied at the flat upper, and mapped lower boundaries to satisfy model requirements for mapped grids. A mapped Chebyshev grid is employed in the vertical, implying a clustering of points near both the upper and lower boundaries that scales with the number of points in the vertical squared, and that vertical resolution improves over the slope. Free-slip boundary conditions (tangential components of $\boldsymbol{u'} = 0$ at the boundary) were applied at the vertically oriented left and right ends of the computational domain, the grid spacing of which was regularly spaced. Grid resolution was 4096 points in the x and 256 grid points in the z coordinate, giving $dx = 1.7$ mm (for simulations in the 7 m tank, this reduces to $dx = 3.5$ mm in the extended tank length simulations), and away from the slope, dz varies between 0.124 mm in the BBL and 1.8 mm near mid-depth.

A total of 59 model runs were carried out for this study spanning a range of values of wave and slope steepness (figure 3.3, Table S1), of which 12 were in the broad tanh profile stratification, 14 in the previously explored thin tanh profile stratification and 33 were from the surface stratification regime. A range of slope steepness values were investigated for each stratification, with a range of wave amplitudes (and therefore wave steepness) in each stratification. For investigations on slopes where $s < 0.2$, simulations were carried out with an extended numerical domain which allowed the slope to reach the surface. In these experiments, the total domain length was $(5.5 + H/s)$ m (5.5 m being the distance waves propagated before meeting the slope in a standard 7 m long tank). In the numerical model, the bottom boundary follows the form of Lamb & Nguyen (2009):

$$z = s\,(\mathrm{itanh}(x, L_x - L_s, d) - \mathrm{itanh}(x, L_x, d)) \tag{3.2}$$

where

$$\text{itanh}(x, \alpha, d) = \frac{1}{2}\left(x - \alpha + d \ln\left(2\cosh\left(\frac{x-\alpha}{d}\right)\right)\right) \tag{3.3}$$

where d represents a characteristic distance for the transition from 0 to a constant slope of 1, and L_s the length of the slope. α in (3.3) is an input variable, as indicated in (3.2). The function smooths the transition from the flat bed to the slope, which is necessary for the spectral code, but small values for d (0.01-0.03) make the topography practically similar to the laboratory slope.

A further three simulations in the broad tanh profile stratification (simulations 3.9R, 3.10L, 3.10C) were extended into three dimensions using $N_y = 64$ points in the transverse over $L_y = 0.128$ m. Free-slip boundary conditions were applied at the transverse ends of the computation domain, and grid spacing was regular. These simulations were restarted from their corresponding 2-D simulation just prior to the emergence of instabilities when 3-D effects become important. Each output field was expanded to three dimensions, with a small random perturbation added to each of the velocity fields in order to trigger any 3-D instabilities.

It has been shown in previous works that excellent agreement can be obtained between the laboratory and numerical model techniques (see Carr *et al.* (2019); Deepwell *et al.* (2020)), and will be further shown here (e.g. figures 3.5, 3.6, 3.7, 3.8)

3.4. Weakly Nonlinear Theory (WNL)

While the focus of this manuscript is on large waves for which perturbation theoretic approaches may not give quantitatively accurate information (Lamb & Yan, 1996), we provide a brief summary of KdV theory (see §2.1, equations (2.1) and (2.2)) for the context of the shoaling behaviour. This theory has been used for a variety of purposes in the literature, most pertinently to classify shoaling (Nakayama *et al.*, 2019). A discussion of the validity of the KdV approach for the large amplitude ISWs of interest here can be found in Grue *et al.* (1999).

Assuming the stratification is fixed (see figure 3.16 for reference), as waves shoal they effectively move into an environment with different relative strengths of the nonlinear and dispersive terms in the KdV equation. Figure 3.2 shows the linear longwave speed, the non-linearity and dispersion parameters for the three stratifications used in this study. The depths shown range from the total depth away from the slope to a 50 % reduction of the total depth. It can be seen that the nonlinearity parameter experiences the largest changes, followed by the propagation speed, with relatively smaller changes in the dispersion

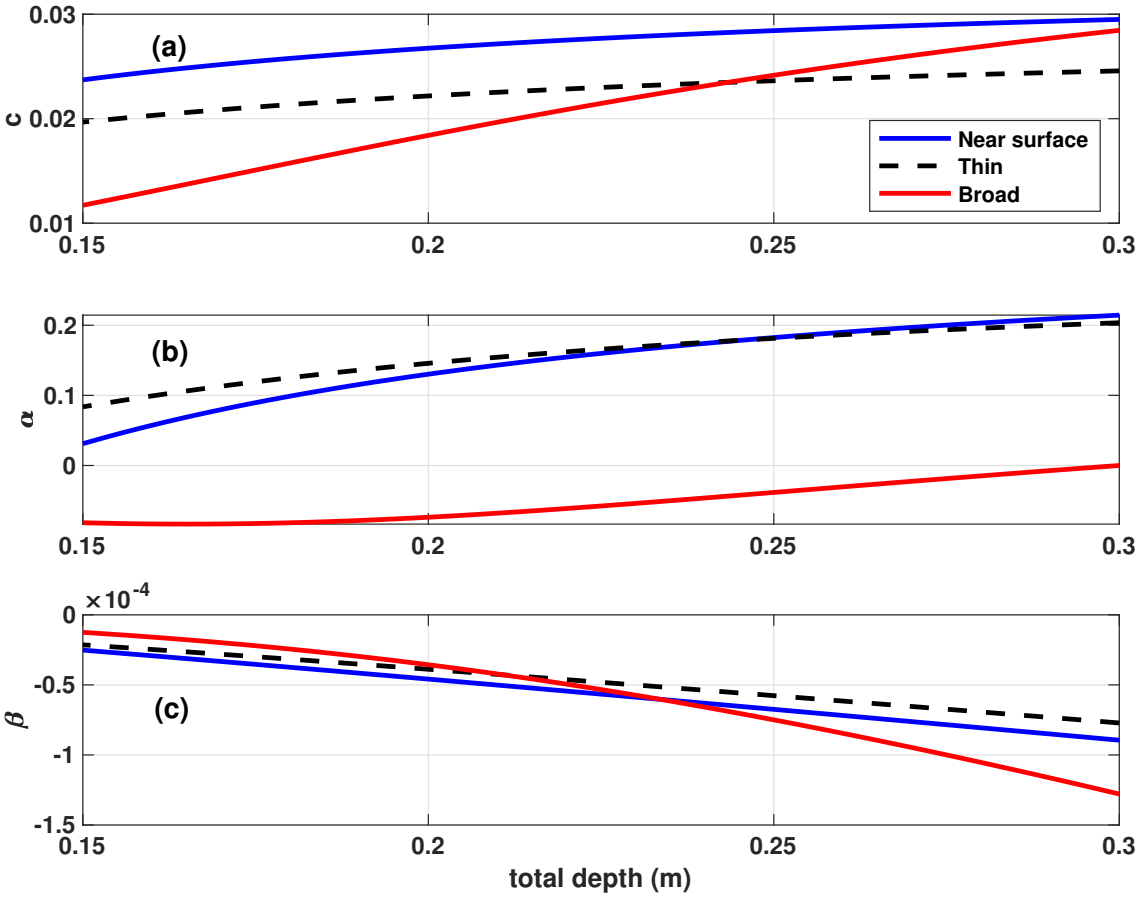


Figure 3.2: The coefficients of KdV theory for the three stratifications discussed for simulations as a function of total depth; (a) the linear long wave speed c_0, (b) the nonlinearity coefficient α, (c) the dispersion coefficient β.

parameter. In particular the nonlinearity parameter is zero away from the slope for the broad stratification. This means that solitary waves cannot be computed from KdV theory, and indeed this is confirmed by the exact DJL theory (not shown). As waves shoal, WNL predicts that they slow down and the dispersion parameter decreases for all three stratifications. However, the change in the nonlinearity parameter suggests that the broad stratification will yield qualitatively different behaviour than the two others, and the $\alpha < 0$ condition indicates that upon shoaling the wave will immediately begin transitioning to a wave of elevation. The exact manifestation of this difference will only become evident through time-dependent numerical simulations.

3.5. Results

The effect of stratification on the shoaling characteristics of ISWs is presented in this section. Four different types of shoaling, namely, fission, surging, collapsing and plunging, which have previously been identified in the literature in the thin tanh profile stratification (Sutherland *et al.*, 2013), are investigated for different stratification types (thin and broad tanh profiles, and surface stratification). Throughout figures 3.4 - 3.14 where horizontal velocity is shown, positive velocity (red) indicates flow in the up slope horizontal direction, and negative horizontal velocity (blue) is in the downslope horizontal direction. To aid comparison, slope and wave steepness are held fixed (within practical limits) in the displayed collapsing (§ 3.5.3), plunging (§ 3.5.4) and surging in the broad tanh profile stratification (§ 3.5.5) examples shown, whilst the surging wave example (§3.5.2) in the surface stratification is for the same slope (see table 3.1 for a summary of parameters for the example waves). A combination of numerical results and laboratory measurements is given. For reference, two internal wave Reynolds numbers are shown in Supplementary Table S3.2, namely $Re = cH/\nu$ and $Re_w = ca/\nu$ (also shown in table 3.1), where ν is the kinematic viscosity of the fluid. Note that these parameters differ in an important respect from their respective counterparts in (i) Diamessis & Redekopp (2006) and (ii) Boegman & Ivey (2009) and Nakayama *et al.* (2019) through the inclusion of the measured wave speed c and not the linear long wave speed, c_0. Although the adoption of c_0 as the characteristic external velocity scale in the definitions of wave Reynolds number is attractive in order to specify a prescribed wave, c_0 is commonly taken to be given by the two-layer formula, which is only appropriate for the thin pycnocline stratification. In order to preserve generality across all density configurations, the local values of Re (table S3.2 only) and Re_w (table 3.1 and S3.2) (defined using the measured wave speed, c) are adopted.

Table 3.1: Summary table of parameters for example experiments and simulations presented in figures of this chapter. Classifications denoted as follows, R = Reflected, F = Fission, S = Surging, C = Collapsing, P = Plunging, IS = Surging with instabilities on bolus (bracketed classification indicating some elements of that breaking dynamic present). $Re_w = ca/\nu$ and $Ir = \frac{s}{\sqrt{a/\lambda}}$

Exp. Name	Laboratory / Numerics	Stratification Type	Slope	Slope Length (m)	a (m)	λ (m)	S_w	c (m/s)	Ir	Class.	L_x (m)	Re
Thin_s0.2_XL_num	Numerics	Thin	0.200	1.50	0.076	0.491	0.154	0.111	0.509	P	7.00	8100
Surf_s0.2_S_num	Numerics	Surface	0.200	1.50	0.011	0.529	0.022	0.077	1.358	S	7.00	879
Surf_s0.2_S_lab	Laboratory	Surface	0.200	1.50	0.024	0.686	0.035	0.075	1.076	S	7.00	–
Surf_s0.033_M_num	Numerics	Surface	0.033	9.00	0.045	0.504	0.090	0.092	0.111	F	14.50	4180
Surf_s0.067_L_lab	Laboratory	Surface	0.067	1.50	0.104	0.895	0.117	0.101	0.195	C(F)	7.00	–
Surf_s0.2_L_num	Numerics	Surface	0.200	1.50	0.083	0.634	0.131	0.099	0.552	C	7.00	8200
Surf_s0.2_L_lab	Laboratory	Surface	0.200	1.50	0.089	0.708	0.126	0.103	0.564	C	7.00	–
Broa_s0.2_L_num	Numerics	Broad	0.200	1.50	0.054	0.427	0.126	0.079	0.563	IS	7.00	4240
Broa_s0.033_M_num	Numerics	Broad	0.033	9.00	0.035	0.386	0.092	0.081	0.110	F	14.50	2860
Broa_s0.2_S_num	Numerics	Broad	0.200	1.50	0.010	0.356	0.027	0.082	1.212	S	7.00	796
Broa_s0.2_L_num	Numerics	Broad	0.200	1.50	0.038	0.388	0.097	0.080	0.642	IS	7.00	3030

In each of the three stratification types studied here, the range of wave and slope properties span the domains in S_w/s space studied by Aghsaee *et al.* (2010) (see figure 3.3). Figure 3.3 shows how the breaker type for a given wave and slope steepness changes in each stratification, in line with previous work on mode-1 ISWs by Aghsaee *et al.* (2010), and on mode-2 ISWs (see Carr *et al.* (2019) and references therein), the classification of breaking types is presented in terms of s and S_w. Classification of wave breaker type was performed visually based on the following criteria. Breakers were classified as fissioning where the incoming wave fissioned into one or more ISWs of elevation travelling up-slope. Breakers were classified as surging where the incoming wave evolves into a single surge of fluid up-slope, without significant formation of global instability. Collapsing breakers were classified where a global instability forms and the resulting vortex arrests the propagation of the wave trough, such that the pycnocline on the rear of the wave 'collapses'. Finally, breakers were classified as plunging where the top of the rear face of the wave overtakes the trough of the wave before significant global instability has formed. The boundary between each wave breaker type is transitional, however, classifications have been given based on the dominant dynamics.

Figure 3.3 (*a*) shows that the numerical model employed here is in excellent agreement, in the thin tanh profile stratification, with the results of Aghsaee *et al.* (2010) for the majority of parameter space investigated. However, at the highest wave steepnesses investigated in this study, plunging waves would be predicted by extending the delineations of Aghsaee *et al.* (2010), but instead collapsing waves are identified based on the simulations and experiments. This indicates a possible need to adjust the definitions of the delineations to apply at steeper slopes.

In the surface stratification regime (figure 3.3*b*), waves in the fission, surging and collapsing regimes continue to break as would be predicted by the Aghsaee *et al.* (2010) classification for a thin tanh profile stratification. However, waves that fall within the predicted plunging regime instead shoal as collapsing type breakers (figure 3.3*b*). This appears to be due to the density gradient throughout the upper layer in the surface stratification regime impeding the formation of overturning of the rear face of the wave (see §3.5.4). Laboratory results in this stratification are in good agreement with corresponding numerical results.

The broad tanh stratification case (figure 3.3*c*) changes the classification scheme further, with only two regimes being observed, namely fission and surging. In this stratification, on slopes steeper than the critical steepness for fission ($s = 0.5S_w + 0.1$), breaker type is independent of Ir, unlike in the other stratifications. This appears to be due to the

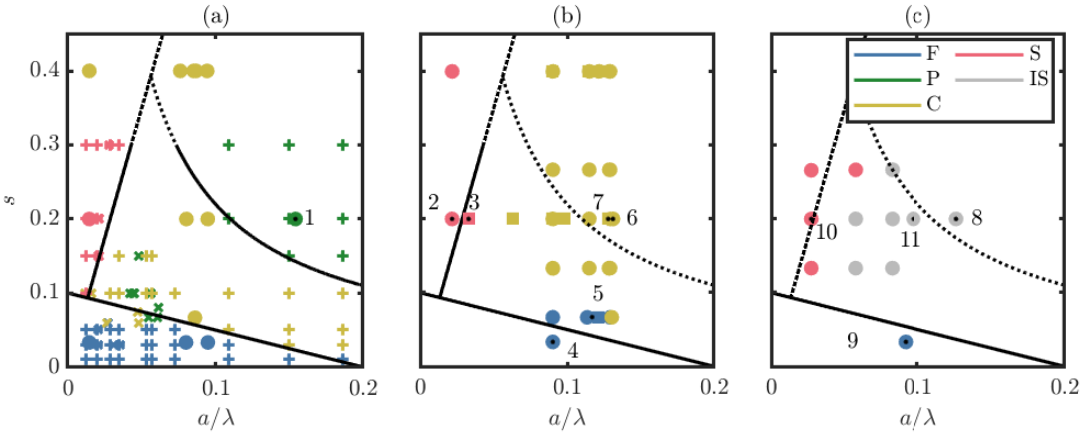


Figure 3.3: ISW breaker types (colour coded) as a function of wave steepness (a/λ) and slope steepness (s). Shown for (a) the thin tanh stratification with data from the present numerical study (large filled circles), alongside those from the studies of Nakayama *et al.* (2019) (X) and Aghsaee *et al.* (2010) (+); (b) numerical results (large filled circles) and laboratory results (large filled squares) in the surface stratification; and (c) numerical results in the broad tanh stratification. 'F', 'C', 'P' 'S' and 'IS' denote fission, collapsing, plunging surging and surging with instabilities on the bolus, respectively. Labelled markers represent the example cases presented in later figures: (1) Thin_s0.2_XL_num, (2) Surf_s0.2_S_num, (3) Surf_0.2_S_lab, (4) Surf_s0.033_M_num, (5) Surf_s0.067_L_lab, (6) Surf_s0.2_L_num, (7) Surf_s0.2_L_lab, (8) Broa_s0.2_L_num, (9) Broa_s0.033_M_num, (10) Broa_s0.2_S_num, and (11) Broa_s0.2_M_num. Black lines indicate delineations between breaking regimes from Aghsaee *et al.* (2010), with dotted black lines indicating locations where these delineations no longer apply in the new stratification.

stabilising effect of the density gradient at the lower boundary suppressing the formation of vortex shedding and global instability (see § 3.5.5).

3.5.1. *Wave on approach*

In both the thin tanh and the surface stratifications waves propagate above the flat bed portion of the domain as large amplitude ISWs of depression, with small amplitude trailing waves, which on approaching the slope are considerably downstream of the leading solitary wave (figure 3.4*a, b*). The passage of such ISWs has been shown to form an unsteady boundary layer jet in the direction of wave motion (adverse to the local flow) (Bogucki *et al.*, 1997; Carr & Davies, 2006; Diamessis & Redekopp, 2006). This boundary layer jet, (associated with a separation bubble, and hereafter designated a flow reversal) forms soon after the passage of the ISW and can be identified in figures 3.4 (*a*) and 3.4 (*b*) by the thin layer of positively signed (red) horizontal velocity at the bed under the rear half of the wave. Its existence is due to the adverse pressure gradient formed as the fluid at the rear of

the wave decelerates (Carr & Davies, 2006). This reverse flow is observed along the flat bed in all simulations, with increasing strength as wave amplitude increases. However, in all these cases, the flow remains laminar and near-bed vortices (which can exist over the flat bed (Carr *et al.*, 2008*a*)) do not form.

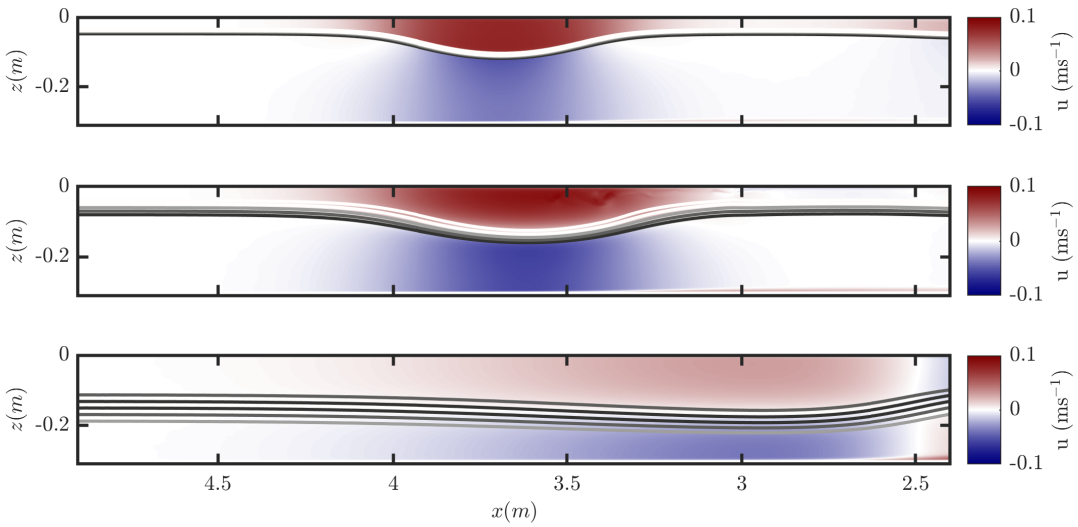


Figure 3.4: Typical wave form propagating right to left over the flat bed portion of the tank in the (*a*) thin tanh profile, (*b*) surface and (*c*) broad tanh stratifications respectively. Plots show the numerically computed horizontal velocity field (*u*) as background, overlaid with isopycnals (in black).

The waveform is qualitatively in good agreement with the theoretical DJL waveform for the surface and thin tanh stratifications, both in the model and laboratory. However, in the surface stratification regime, for larger waves in the numerical model and laboratory, some instability in the rear of the wave core exists (a darker red region in the wave in figure 3.4*b*), representing the transition towards a trapped core regime. These cores are described as "leaky", as fluid is continually lost from the rear of the wave, but become stable on approach to the slope. Wave steepness is dependent on amplitude, with increasing steepness with wave amplitude until a critical amplitude, beyond which steepness begins to reduce again, as the wave broadens. These results are closely matched between the numerical results and DJL theory (not shown here).

Waves in the broad tanh stratification have an undular bore profile (a series of wave disturbances), rather than the solitary waves observed in the other stratification types. This can be explained by the fact that the nonlinear (α) term in the Korteweg-De Vries (KdV) equation is nearly zero, preventing the leading-order balance between nonlinear and

dispersive terms in the KdV description (Horn *et al.*, 2001). For a longer domain, a modified balance is possible, provided one uses a higher-order extension such as the Gardner equation (Helfrich & Melville, 2006) or MCC (Barros *et al.*, 2020) which contains a higher-order nonlinear term whose coefficient would be non-zero. This detailed reclassification is beyond the present manuscript, and provides an avenue for future work. As a result, ISWs are prevented from forming (figure 3.2*b*), instead producing an undular bore profile with alternating regions of positive and negative horizontal velocity at the bottom and upper boundaries, which enhances the flow reversal usually found at the rear of the wave. Under certain conditions (e.g. experiment Broa_s0.2_L_num), this boundary layer flow reversal becomes unstable and produces a shed vortex whilst the wave propagates over the flat bed.

3.5.2. *Surging*

In this section, the numerical simulation of a surging wave in the surface stratification case (experiment Surf_s0.2_S_num) with wave steepness of $S_w = 0.0217$ propagating over the middle slope ($s = 0.2$) is presented, alongside the corresponding laboratory experiment (experiment Surf_s0.2_S_lab) (figures 3.5, 3.6). Surging was observed for very small amplitude waves, with comparatively long wavelengths, resulting in a very low wave steepness. Due to the very small amplitude of these waves, flow velocities are also very small.

As the wave propagates over a slope, the propagation speed slows, as the water depth decreases. However, during this process, as the water depth is different at different parts of the wave, the front face of the wave shallows, becoming parallel to the slope, forcing water down-slope from beneath it, whilst the rear face steepens, as the wave speed here remains faster than the trough (figure 3.5*b*, 3.6*b*, *f*, Supp. Movie 1). At the point of maximum steepening, boundary layer reverse flow catches up with the wave trough and intensifies (figure 3.5*c*, 3.6*c, g*). In doing so, this bolus of lower layer fluid surges through the rear face of the wave and up-slope as a single bolus of fluid with negative vorticity at the head, and a region of positive vorticity at the bed (figure 3.5*d*, 3.6*d, h*). This bolus, and the associated vorticity field, results in resuspension of material at the bed, seen as a peak in light intensity in raw images (figure 3.5*c, d*). The process occurs high up the slope, as the small wave amplitude means the trough of the wave interacts with the slope only after propagating along it for a considerable distance. Intensification of the boundary layer reverse flow is a dominant mechanism for this form of wave breaker. This dynamics is seen across all three types of stratification. Dynamics in the laboratory is in strong agreement with the corresponding simulation, and is in strong agreement with past studies of the thin

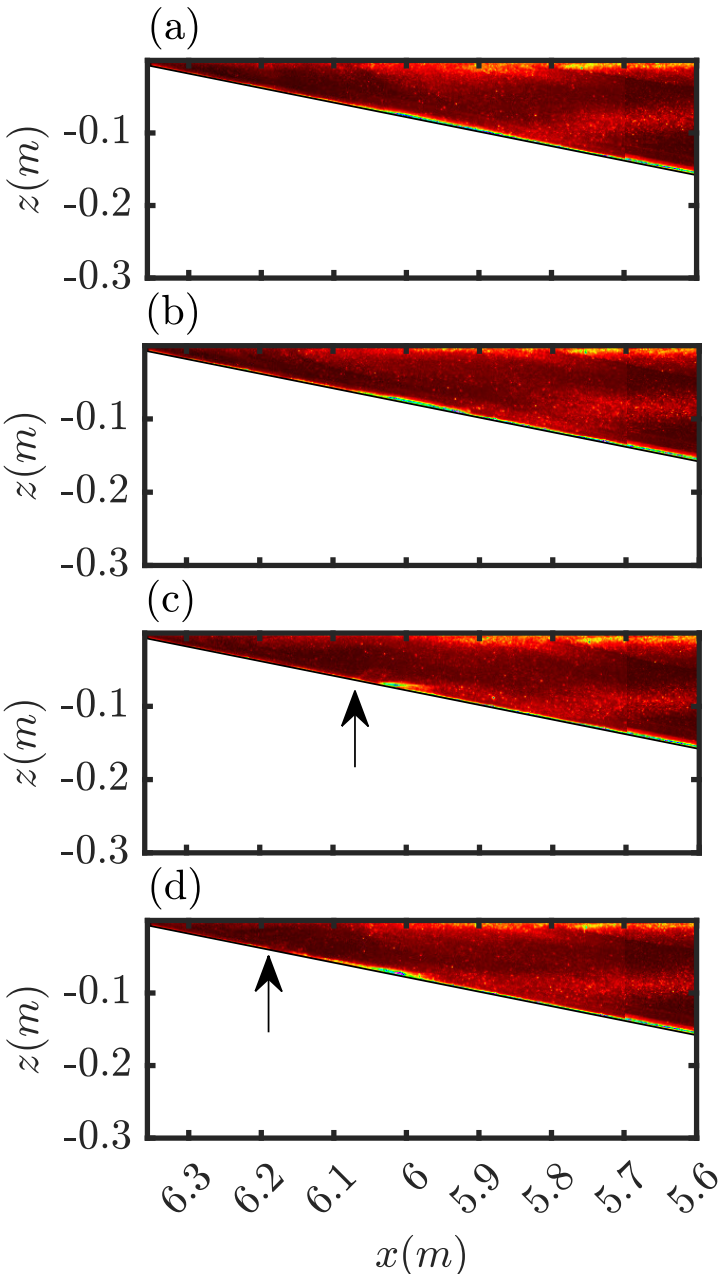


Figure 3.5: Time sequences of raw images showing light intensity (in false colour) for experiment Surf_s0.2_S_lab of the surging example (corresponding to same velocity images as in figure 3.6*e-h*). Black arrows in (*c, d*) indicate the location of the head of the bolus. Time interval between images is $\Delta t = 5$ s. Note that images are made up of images from two cameras merged to form a single image. Corresponding movie of the experiment (Supplementary Material Movie 1) is provided for additional clarity.

tanh profile stratification (Boegman *et al.*, 2005; Aghsaee *et al.*, 2010; Nakayama *et al.*, 2019; Sutherland *et al.*, 2013).

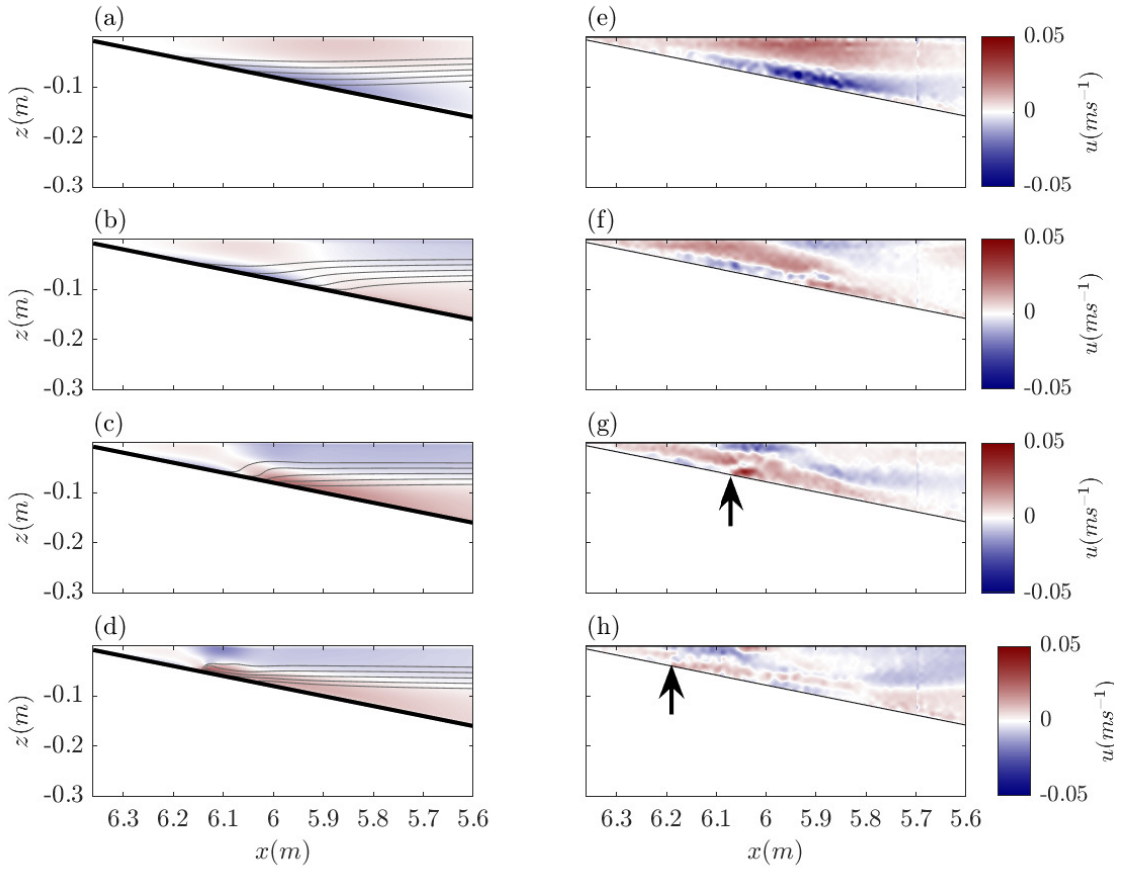


Figure 3.6: Time sequences showing numerical simulation Surf_s0.2_S_num (*a-d*), and corresponding experiment Surf_s0.2_S_lab (*e-h*) of the surging example. The colour scheme displays horizontal velocity, u, and in the numerical simulations u is overlaid with isopycnals (in black). Black arrows in (*g, h*) indicate the location of the head of the bolus. Time interval between images is $\Delta t = 5$ s. Note that experimental images are made up of images from two cameras merged to form a single image. Corresponding movie of the simulation is provided in supplementary material as Movie 2.

3.5.3. *Collapsing*

In this section, the numerical simulation of the collapsing wave in the surface stratification regime (experiment Surf_s0.2_L_num) with wave steepness of $S_w = 0.131$ propagating over the middle slope ($s = 0.2$) is presented alongside the corresponding laboratory experiment (experiment Surf_s0.2_L_lab) (figure 3.7, 3.8). In the thin tanh counterpart case, the work of Aghsaee *et al.* (2010) suggests a plunging wave would be anticipated (see figure 3.3*a*, green data points compared with figure 3.3*b*).

As the wave approaches the slope, as described in §3.5.2 the front face of the wave

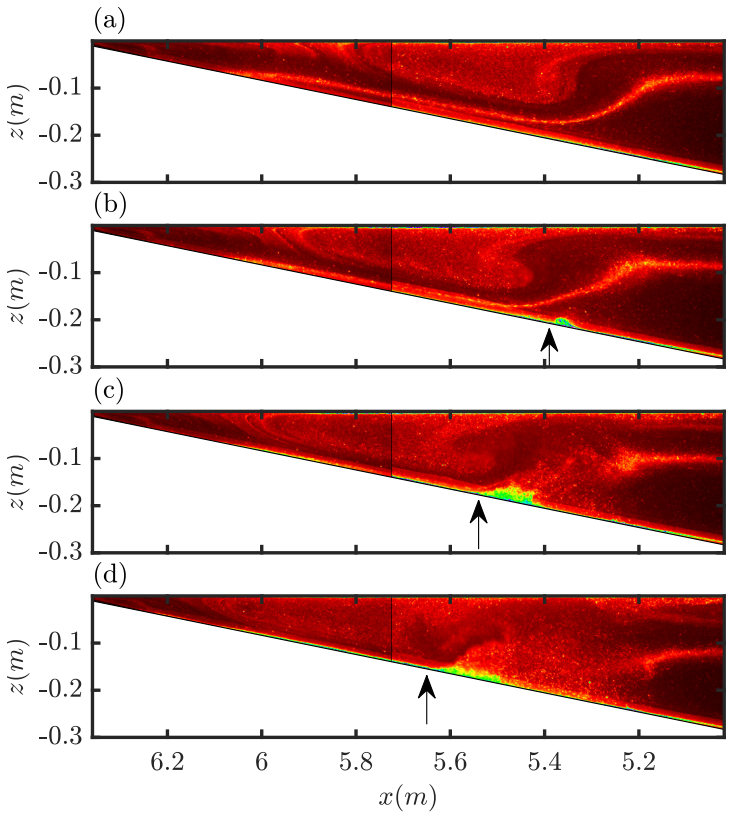


Figure 3.7: Time sequences of raw images showing light intensity (in false colour) for experiment Surf_s0.2_L_lab of the collapsing example (corresponding to same velocity images in figure 3.8*e-h*). Black arrows in (*b-d*) indicate the location of the head of the boundary layer vortex. Time interval between images is $\Delta t = 2$ s. Note that images are made up of images from two cameras merged to form a single image. Corresponding movie of the experiment is provided in supplementary material as Movie 3.

flattens against the slope, becoming parallel to it and forcing the lower layer fluid down-slope out from underneath it whilst the rear face steepens (figure 3.7*a-b*, 3.8*a-b, e-f*). This produces a region of strong down-slope velocity beneath the wave trough, and front face of the wave. Meanwhile, the boundary layer reverse flow moves up-slope along with the wave's rear face, intensifying as it moves into shallower water (figure 3.7*b*, 3.8*b, f*). Under these conditions, shear at the top of the flow reversal is known to produce vortices through the process of global instability (Diamessis & Redekopp, 2006; Carr *et al.*, 2008*a*). These vortices, which can extend high up into the water column (Diamessis & Redekopp, 2006), can be an effective means of fluid and sediment mixing from the near-bottom layer to higher in the water column (Bogucki & Redekopp, 1999; Stastna & Lamb, 2002). The vortices serve to distort the trough of the wave and the lower parts of the wave's rear face in such a manner that the pycnocline collapses on itself (figure 3.8*c, g*, 3.7*c*). After causing

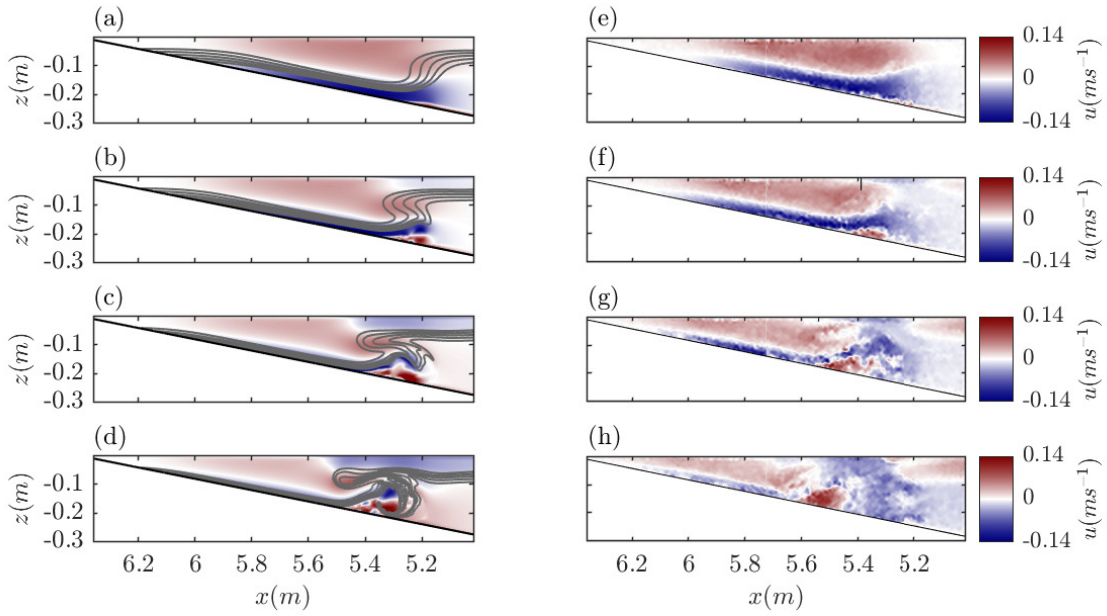


Figure 3.8: Same as figure 3.6, but for the collapsing wave example, numerical simulation Surf_s0.2_L_num (*a-d*), and corresponding laboratory experiment Surf_s0.2_L_lab (*e-h*). Black arrows in (*f-h*) indicate the location of the head of the boundary layer vortex. Time interval between images is $\Delta t = 2$ s. Corresponding movie of the simulation is provided in supplementary material Movie 4.

the pycnocline to collapse, the vortex propagates up-slope along the bottom boundary as a bolus, bringing with it a parcel of denser lower layer fluid (figure 3.8*d, h*, 3.7*d*), and resuspension of material from the bed (seen in figure 3.7*c, d*, as a region of high light intensity). The dominant mechanism in this form of breaking wave is the intensification of the boundary layer reverse flow producing the boundary layer vortex. Discrepancy between figure 3.8*d* and figure 3.8*h* at the toe of the slope is due to a trailing wave in the experiments not present in the simulation. This dynamics is in strong agreement with collapsing shoaling waves in the thin tanh profile stratification, both in this present study and in past studies using the thin tanh profile stratification (Aghsaee *et al.*, 2010; Sutherland *et al.*, 2013; Nakayama *et al.*, 2019).

3.5.4. *Plunging*

In this section, a numerical simulation of the plunging wave in the thin tanh profile stratification (experiment Thin_s0.2_XL_num) is presented for comparison with the comparable wave examples in the surface and broad tanh profile stratifications. The example wave

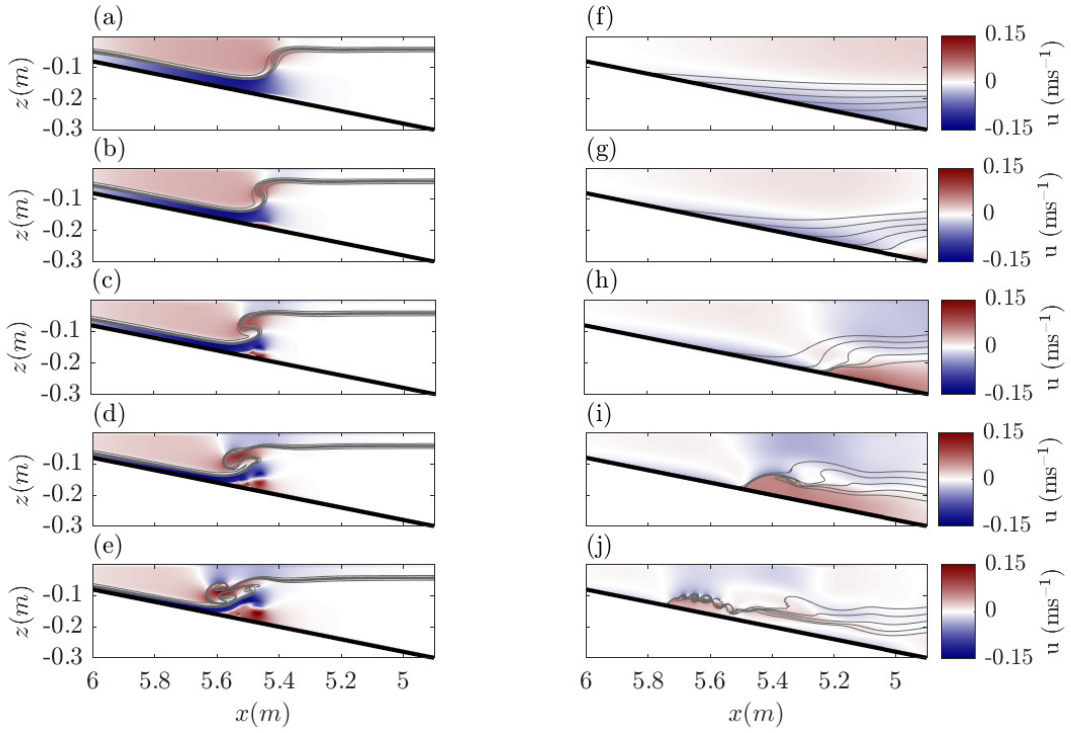


Figure 3.9: Same as figure 3.6, but for numerical simulation Thin_s0.2_XL_num (*a-e*), representing the plunging dynamics in the thin tanh profile stratification, and numerical simulation Broa_s0.2_L_num (*f-j*) representing the same wave in the broad tanh profile stratification. Time interval between images is $\Delta t = 0.8$ s and 5 s for the left- and right-hand columns, respectively. Corresponding movies of the simulations are provided in supplementary material as Movie 5 and Movie 6.

propagating over the middle slope ($s = 0.2$), with $S_w = 0.154$ is equivalent to Simulation 51 of Aghsaee *et al.* (2010) and designated therein as the plunging breaker type, scaled to the wave tank used in the present experiments.

In the thin tanh stratification, plunging is observed as described in past studies (e.g. Aghsaee *et al.*, 2010; Sutherland *et al.*, 2013; Nakayama *et al.*, 2019) (figure 3.9*a-e*). Unlike in the surging and collapsing regimes, plunging is dominated by a dynamics occurring on the pycnocline, rather than BBL dynamics which goes on to impact the pycnocline. In this case, as with the collapsing and surging waves, steepening of the rear face of the wave continues as the wave shoals (figure 3.9*a-b*), but at a faster rate than in those waves, with lower layer fluid being lifted upwards and then advected in the same direction as the wave as it reaches the pycnocline. At a critical point, the horizontal velocity exceeds the local wave speed, and a bulge of lower layer fluid at the top of the rear face of the wave protrudes

forward above the trough of the wave (figure 3.9*c*), and therefore above the upper layer fluid. The resulting convective instability produces an anvil shaped feature that plunges forward (figure 3.9*d-e*), and spreads whilst undergoing Rayleigh-Taylor instability as it does so.

Comparison of experiments Surf_s0.2_L_num and Thin_s0.2_XL_num shows that stratification throughout the upper layer in the surface stratification regime appears to impede the formation of the overturning and surging forward of the rear face of the wave. Where this does occur, it is sufficiently late in the breaking process that the collapsing dynamics has already become dominant and, as such, the wave is classified as a collapsing breaker.

3.5.5. *Surging in the Broad Tanh Profile Stratification*

In this section, numerical simulations of a surging wave in the broad tanh profile stratification (experiment Broa_s0.2_L_num) is presented (figure 3.9*f-j*). The example wave propagates over the middle slope ($s = 0.2$), with leading wave steepness of $S_w = 0.152$.

In the broad tanh profile stratification, the surging breaker type is observed across the full range of wave steepness investigated where the slope is steeper than that required to sustain fission-type breakers (figure 3.3*c*). Where collapsing-type breakers are observed in the surface stratification regime (c.f. figures 3.3 (*b, c*)), in the broad tanh stratification regime, intensification of the boundary layer reverse flow is not sufficient to trigger vortex shedding and global instability. This is due to the destabilising horizontal velocity gradient in the boundary layer remaining small in comparison with the stabilising effect of stratification. As the wave shoals, steepening is able to occur, since $h_1 \neq h_2$ (figure 3.9*f, g*). As it does so the density gradient across the pycnocline also increases (as the pycnocline is reduced in thickness) at the front of the bore-like feature that is shown to form (figure 3.9*g, h*). Resulting from this, a single bolus of fluid travels up-slope (figure 3.9*i, j*), similar to that observed in the previously described surging cases. This dynamics is comparable to the surging dynamics seen in the surface and thin tanh stratifications, with the defining characteristics of formation of a single bolus, and lack of global instability characteristic of collapsing breakers. However, the nonlinear steepening of the pycnocline as the wave hits the slope and coherence of the formed bolus represent a newly revealed dynamics unique to surging waves in the broad tanh profile stratification.

Under certain conditions, as the bolus propagates up-slope, billows resulting from Kelvin-Helmholtz instabilities form along the upper surface (figure 3.9*j*). The Richardson number, *Ri*, is a useful indicator of whether shear instability can (but not necessarily will) occur. It is given as the ratio of stabilising buoyancy and destabilising shear, namely,

$Ri = N^2/(du/dz)^2$, where $N^2 = -\frac{g}{\rho_0}\frac{d\rho}{dz}$. The case $Ri < 1/4$ can be shown to be a critical value, below which shear instabilities can form and grow (Miles, 1961). Note, however, that the presence of regions in which the value of Ri is less than this critical value does not indicate that instabilities will definitely form, and their formation may depend on additional criteria (Fructus *et al.*, 2009). It was observed that, as wave steepness (and therefore wave-induced velocities) increased, the upper surface of the bolus initially formed approximately perpendicular to the slope, but for waves with increasing incident wave steepness, this upper surface curled around, growing in length along the down-slope direction (figure 3.10*a, c, e*). This upper surface was unstable where it formed, and at low wave steepnesses billows formed at the tip only. As the upper surface length grew, the bolus was able to sustain a greater number of billows. Simultaneously, as can be seen in figure 3.10, the region of the flow for which $Ri < 1/4$ increases, suggesting that shear instability is responsible for these features. The bolus that forms without billows (figure 3.10*a, b*) lacks a region where $Ri < 1/4$, whilst the region where $Ri < 1/4$ grows with correspondingly stronger billow formation (figure 3.10*c-f*).

The finding that collapsing breaker types cannot be formed in this broad tanh profile stratification can be attributed to the stabilising effect of stratification at the bottom boundary, suppressing shear instabilities that would otherwise produce the global instability characteristic of the collapsing breaker form. Crucially, the density gradient (and therefore the buoyancy frequency term of Ri) at the boundary is increased in this stratification (i.e. $\delta\rho > 0$), acting to increase Ri and stabilise the fluid, and preventing shear instabilities from growing. Bottom shear stress additionally does not experience a considerable peak as the wave shoals for this stratification, as is observed in other wave breaking events (figure 3.15d). The shear instabilities resemble instabilities described by Xu *et al.* (2016) for the boluses formed by ISWs of elevation shoaling onto a shelf.

Past studies have identified the stable surging breaker in a similar stratification for both laboratory and numerical experiments (e.g. Venayagamoorthy & Fringer, 2007; Arthur *et al.*, 2017; Allshouse & Swinney, 2020; Vieira & Allshouse, 2020). In those works, as pycnocline thickness increased, bolus transport increased (Allshouse & Swinney, 2020; Vieira & Allshouse, 2020) and mixing efficiency also increased (Arthur *et al.*, 2017). For low wave steepnesses, these simulations are in good agreement with those past studies for comparable pycnocline thickness. However, this study systematically shows that, in the parameter space where collapsing and plunging breaker types would be found in the thin tanh profile stratification, the surging breakers in the broad tanh profile stratification become unstable.

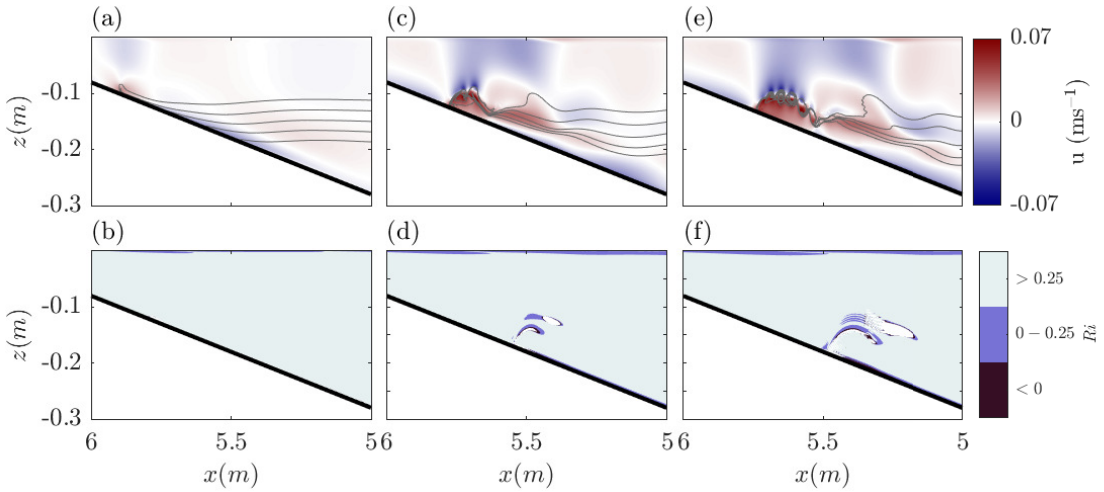


Figure 3.10: Comparison of Richardson number (bottom row), *Ri*, in broad tanh profile stratification simulations with increasing S_w for numerical simulations Broa_s0.2_S_num (*a, b*, $S_w = 0.03$), Broa_s0.2_L_num (*c, d*, $S_w = 0.12$) and Broa_s0.2_L_num (*e, f*, $S_w = 0.15$)). Top panels show horizontal velocity, *u* overlaid with isopycnals for the same simulation 5 seconds later (once any instability has formed). Vertical scale exaggerated for clarity. Corresponding movie of simulation Broa_s0.2_L_num is provided in supplementary material as Movie 7.

Three-dimensional simulations

In this section, 3-D numerical simulations of the surging waves in the broad tanh profile stratification presented in §3.5.5 are investigated (figure 3.11, 3.12) to test the validity of the 2-D simulations for a stratification where laboratory data are not available.

For the lowest incident wave steepness simulation (Broa_s0.2_S_num), the dynamics is in line with that seen in the 2-D simulations. Lateral variability only develops after the bolus forms, primarily in the form of small flow features characteristic of lobe-cleft instability at the head of the bolus (figure 3.11*d*, 3.12*a*). As in the 2-D simulations, as wave steepness increases, further instabilities form, primarily in the form of billows resulting from Kelvin-Helmholtz instabilities on upper surface of the bolus formed (figure 3.11*a-c*). As such, the overall flow dynamics is well captured by the previous 2-D simulations, in line with Xu *et al.* (2019). However, in the 3-D simulations, the extent of lateral variability of these features increases (figure 3.12*b, c*). Not only are these in the form of more prominent

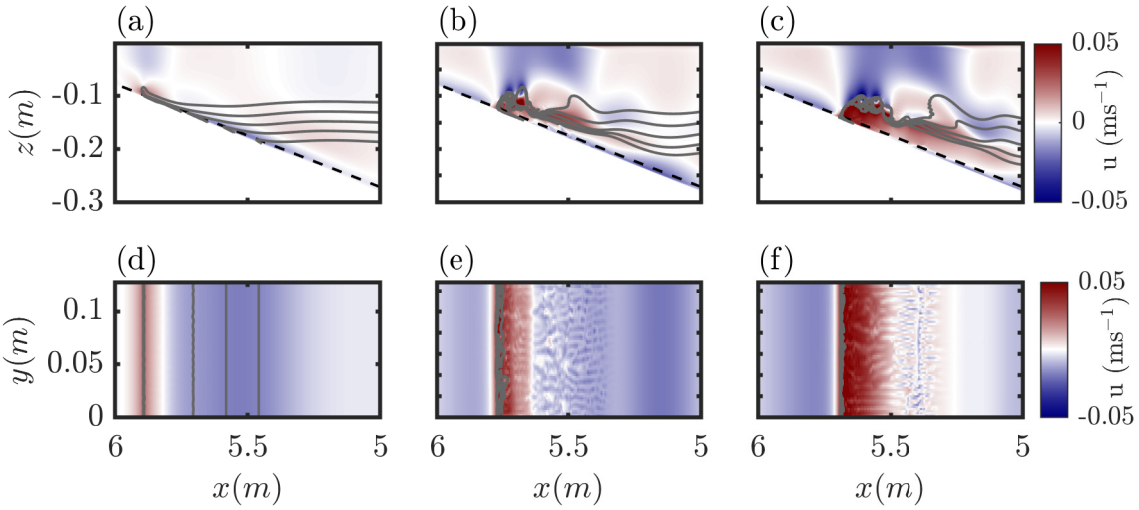


Figure 3.11: Top panels (*a-c*) same as in figure 3.6, but for the corresponding 3-D simulations (Broa_s0.2_S_num, Broa_s0.2_L_num and Broa_s0.2_L_num)) at the same time step, bottom panels (*d-f*) show the transverse plane corresponding to the dashed line. Vertical scale exaggerated for clarity.

features characteristic of lobe-cleft instabilities on the bolus head (figure 3.11*e, f*), but with additional transverse features forming as the billows resulting from Kelvin-Helmholtz instabilities are formed (figure 3.12*b, c*).

3.5.6. *Fission*

In this section, numerical simulation Surf_s0.033_M_num in the surface stratification regime is presented for the wave with wave steepness of $S_w = 0.0871$ in an extended domain propagating over the shallowest slope ($s = 0.03$). This dynamics is in good agreement with fission described in past studies (e.g Aghsaee *et al.*, 2010; Xu & Stastna, 2020).

In these numerical simulations, as the wave propagates over the slope the rear face slowly steepens, and the pycnocline at the rear of the wave is displaced upward from its resting level (figure 3.13*a*). In the lower layer beneath this upward displacement, the boundary layer flow reversal gradually grows in magnitude and height (figure 3.13*b*). This evolves into a bolus at the lower boundary, and an associated wave of elevation forms, which propagates forward through the wave of depression (figure 3.13*b*). As the rear of this wave of elevation clears the rear face of the incident wave, a second ISW of elevation forms, which again overtakes the incident wave (figure 3.13*c, d*). In these numerical simulations, the BBL dynamics and formation of a bolus are dominant processes in the transition from

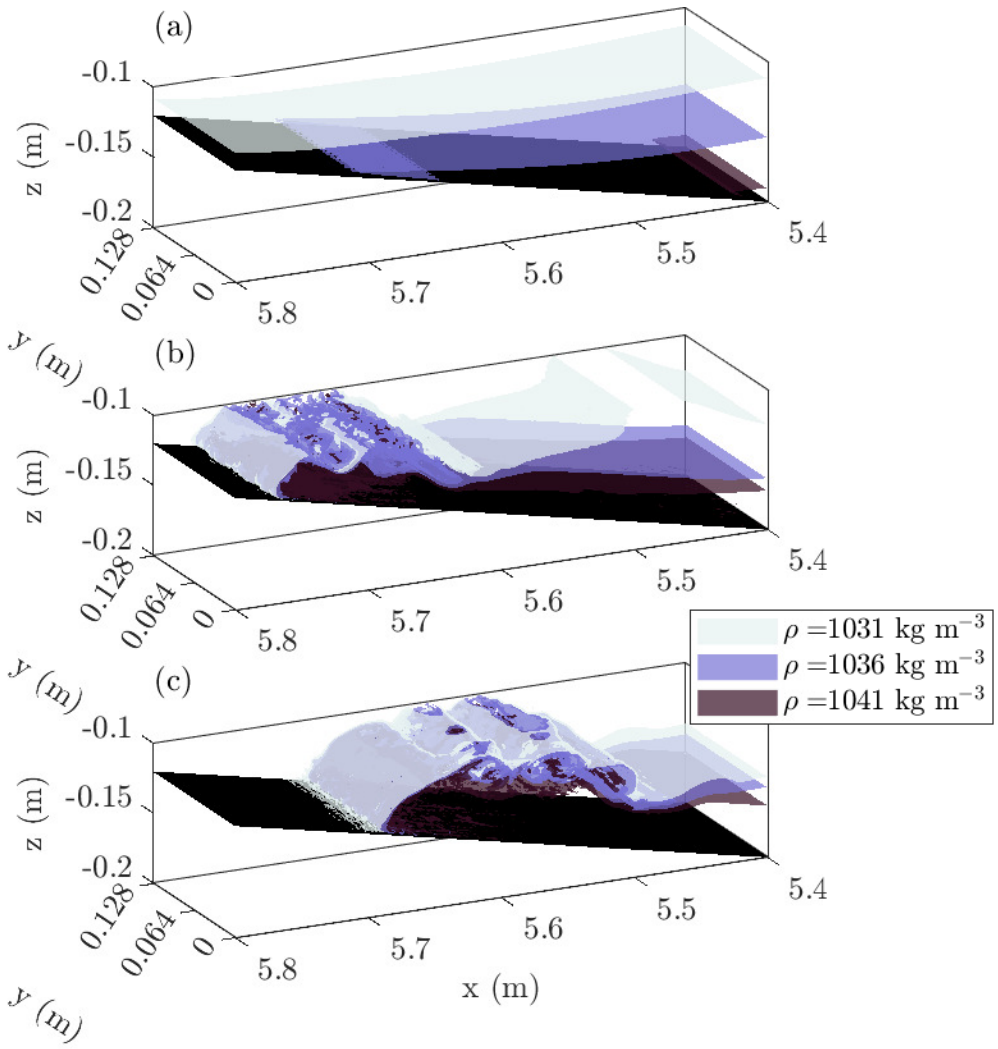


Figure 3.12: Three-dimensional view of isopycnal surfaces of the bolus formed during the surging of waves presented in figure 3.11: Broa_s0.2_S_num (*a*), Broa_s0.2_L_num (*b*) and Broa_s0.2_L_num (*c*). Panels at same time step as in the corresponding panel of figure 3.11

an ISW of depression to a train of ISWs of elevation, processes not reflected in weakly nonlinear theory (WNL) theory. In the thin tanh profile similar dynamics is observed to the surface stratification case presented, and in this case, this process is repeated so that a train of five small waves of elevation undergo fission and travel up-slope.

The slope of steepness $s = 0.03$ could not be replicated in the laboratory where the slope reached the surface, since doing so would require a 15.5 m long tank. However, in one laboratory experiment a shoaling ISW propagating over a slope of $s = 0.067$, prior to reflection, displayed fission dynamics in the BBL (figure 3.14) with a train of boundary layer reverse flows forming, each associated with particle resuspension and as a result

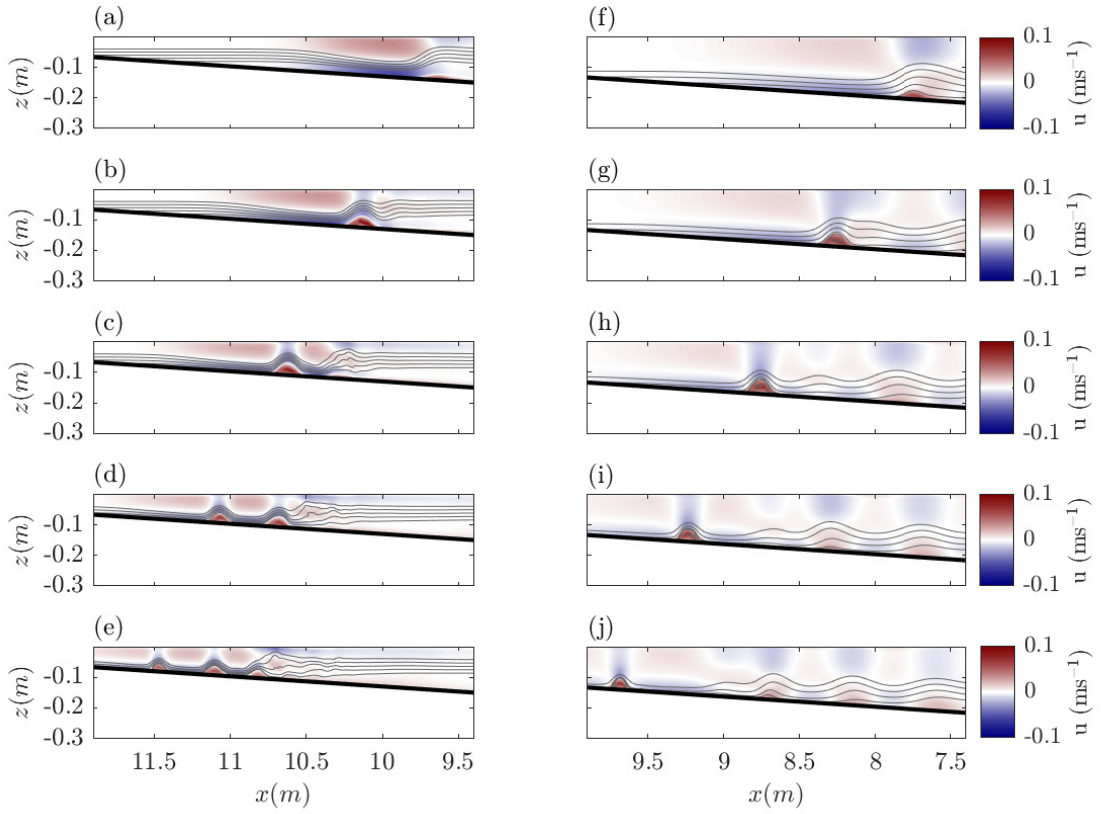


Figure 3.13: Same as figure 3.6, but for numerical simulation Surf_s0.033_M_num (*a-e*), representing the fission dynamics in the surface stratification, and numerical simulation Broa_s0.033_M_num (*f-j*) representing the same wave and dynamics in the broad tanh profile stratification. Time interval between images is Δt = 10s. Vertical scale exaggerated for clarity. Corresponding movies of the simulations are provided in supplementary material as Movie 8 and Movie 9 respectively.

increased light intensity (figure 3.14*a*).

In the broad tanh profile stratification case (figure 3.13*f-j*), the wave approaches the slope propagating as a train of periodic waves. As in the thin tanh and surface stratification regimes, slow changes to the KdV terms allow for gradual adjustment of the wave to changing depth (figure 3.13*f, g*). Behind the passage of the first depression wave, the same boundary layer feature forms and moves forward in the wave, before breaking ahead as a wave of elevation (figure 3.13*h-j*). This wave travels up-slope as a single parcel of fluid, but unlike in the thin tanh profile and surface stratification cases, repeated waves of elevation are not produced (figure 3.13*j*), since pursuing waves in the undulating bore disrupt the process.

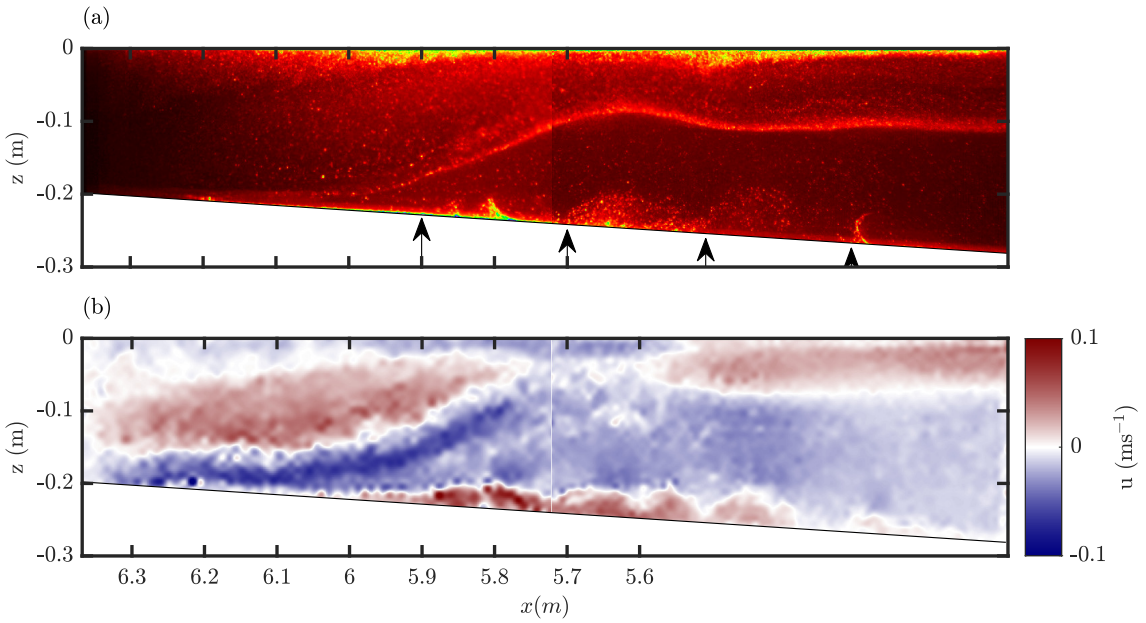


Figure 3.14: Snapshot of experiment Surf_s0.067_L_lab, showing the emergence of fission dynamics in the BBL as the (*a*) raw experimental image in false colour scheme, and (*b*) horizontal velocity plot, as in previous figures. Black arrows in (*a*) indicate the location of the head of each boundary layer vortex. Note that experimental images are made up of images from two cameras merged to form a single image. Corresponding movie of the experiment is provided in supplementary material as Movie 10.

3.6. Discussion

3.6.1. *Relevance at the Ocean Scale*

The majority of slopes investigated in this study far exceed typical slopes in the coastal ocean ($s \approx 0.001$) and lakes ($s \approx 0.01$). However, the shallower slopes here fall within the margin for average continental slopes ($s = 0.03 - 0.07$) (Cacchione *et al.*, 2002). Consistent with past studies at the laboratory scale (Aghsaee *et al.*, 2010; Nakayama *et al.*, 2019; Xu & Stastna, 2020), all waves propagating over these realistic slopes form fission breakers. This process of ISWs of depression evolving into a train of ISWs of elevation has been widely observed in the field (e.g. Orr & Mignerey, 2003; Shroyer *et al.*, 2009; St Laurent *et al.*, 2011) in conditions resembling the thin tanh profile and surface stratification cases investigated here. This process was responsible for inducing dissipation $1 - 2$ orders of magnitude higher than background levels (St Laurent *et al.*, 2011).

Due to scaling differences, it is difficult to compare rates of dissipation and mixing in relation to the field. Instead, here, the rates of mixing and dissipation and bottom stress

are compared between breaker types in figure 3.15, to identify which waves are expected to induce the greatest amount of mixing and dissipation, and to make inferences about sediment re-suspension. Estimates of energy conversions calculated by SPINS (Deepwell, 2018) (based on the sorting algorithm of Winters *et al.* (1995)) were processed using Matlab code publicly available at `https://github.com/ddeepwel/SPINSmatlab`.

Energy converted through mixing into background potential energy is given as:

$$\phi_m = \phi_d - \phi_i \tag{3.4}$$

where ϕ_d is the rate of change of background potential energy, and ϕ_i the rate of conversion from internal energy to potential energy through diffusion. For comparison between simulations with varying initial energetic configurations, mixing and dissipation are presented as percentages of the initial available energy.

The viscous force on the bottom boundary due to fluid motion is $\boldsymbol{\tau} = \tau_{ij} n_j$, where τ_{ij} is the Cauchy stress tensor, and n_j the unit tangent vector. The along-bottom (shear) component of that force the dot product with the unit tangent vector

$$t_x = \boldsymbol{\tau} \cdot (\hat{s}_x, \hat{s}_y) \tag{3.5}$$

From this, bed shear stress can be calculated as

$$t_x = \frac{\nu \rho_1}{1 + h'(x)^2} \left[2h'(x) \left(\frac{\partial w}{\partial z} - \frac{\partial u}{\partial x} \right) + (1 - h'(x)^2) \left(\frac{\partial u}{\partial z} - \frac{\partial w}{\partial x} \right) \right] \tag{3.6}$$

Where h' is the derivative of the bottom depth, h. As a general picture, wave energy is dissipated at a low, constant rate on approach to the slope, indicating the waves are stable on approach. As waves reach the slope, and begin to break, the rate of dissipation increases, before gradually levelling off again to a lower rate than on approach. There is very little mixing prior to the onset of breaking, again indicating the wave is stable on approach in most cases, and even after breaking, most energy converted goes to dissipation, rather than to mixing. In the surface stratification regime, the surging and fission breakers upon reaching the slope and breaking do not dissipate energy at a considerably higher rate than the wave on approach, and very little energy is converted to mixing (figure 3.15*a, e*). Occurrence of Taylor-Rayleigh and global instabilities in the plunging and collapsing breaker waves respectively are likely responsible for enhanced rate of dissipation as the wave breaks (figure 3.15*b,c*). The breaking of ISWs by plunging is anticipated to be dominated by convective instability (specifically the Rayleigh-Taylor gravitational instability), whilst ISW

breaking by collapsing is anticipated to be shear dominated (from the boundary layer). Higher mixing efficiencies are anticipated for flows dominated by convection-driven mixing than shear-driven mixing (Ivey *et al.*, 2021), however, overall rates of mixing were much higher for the collapsing wave than the plunging wave, with approximately 14 % and 4 % of initial available energy going to irreversible mixing, respectively (despite comparable dissipation). To what extent the mixing is affected by variation of stratification, rather than by changing breaker type, would be an interesting area of future study, and is partially considered in chapter 5.

The dissipation profile of the surging breaker in the broad tanh profile stratification is very similar to that seen in the surface stratification system (figure 3.15*d*), although the presence of Kelvin-Helmholtz instabilities brings about considerably higher mixing after $t = 90$ s. These results indicate the impact of both stratification and breaker type on the transport of energy and mixing by shoaling ISWs. Waves that dissipate energy more slowly are anticipated to transport energy further up-slope. These results are restricted to the 2-D simulations; investigation of mixing in 3-D simulations is beyond the scope of the current chapter. Past studies have indicated wave breaking is qualitatively similar in two and three dimensions during the approach to the slope, breaking event, and beginning of the surge up-slope, with differences forming as lateral variability and instabilities (which form only in three dimensional simulations) cause billows on the bolus to break down (Arthur & Fringer, 2014; Xu *et al.*, 2019). These 3-D effects typically occur away from the leading wave or bolus, and so, although important to mixing, are unlikely to impact the leading-order behaviour of the wave (Xu *et al.*, 2019). The presence of lobe-cleft instabilities, and lateral variability at the site of Kelvin-Helmholtz billow generation in 3-D simulations indicates that the underestimation of dissipation and overestimation of mixing would be strongest at the highest wave steepnesses in the broad tanh profile stratification.

Bed stress indicates the degree of sediment re-suspension brought about by the shoaling wave, compared with that as the wave travels over a flat bed. The bolus formed in the surface stratification surging breaker causes relatively high stress, which is anticipated to be associated with high sediment re-suspension and transport up-slope (figure 3.15*a*). This is in stark contrast with that seen in the broad tanh profile case (figure 3.15*d*), where wave-induced velocities in general are much smaller, and the increase in bed stress as the wave shoals and bolus forms, is negligible. This indicates the key importance of stratification type in understanding shoaling-induced sediment transport, even where the dynamics are qualitatively similar. However, Xu *et al.* (2016) showed that, in 3-D simulations, the bolus formed by shoaling ISW of elevation produced more bed stress than in 2-D simulations

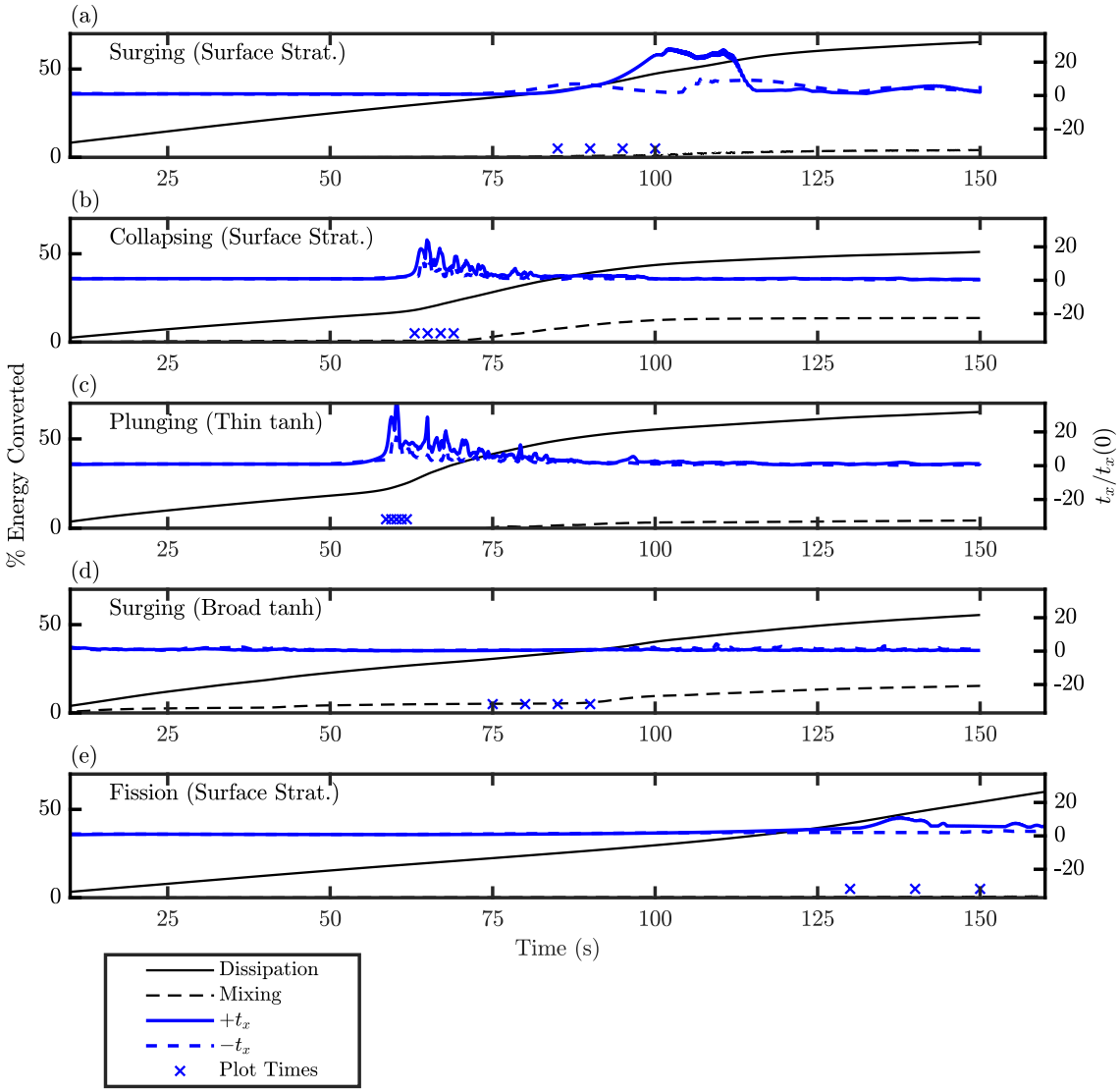


Figure 3.15: Time series of energy dissipated, energy used for mixing and maximum bed stress in positive and negative directions ($+t_x$ and $-t_x$, respectively), for each of the numeric simulations Surf_s0.2_S_num (surging), Surf_s0.2_L_num (collapsing), Thin_s0.2_XL_num (plunging), Broa_s0.2_L_num (broad tanh profile stratification surging with instability) and Surf_s0.033_M_num (fission) respectively. Data normalised by initial total available energy for energy dissipated and energy to mixing, and by average bed stress over $t = 10$ s–20 s (representing the fully formed wave propagating over the flat bed). Blue crosses represent the times at which frames were plotted in the respective figures.

due to the formation of lobe-cleft instabilities. This indicates the need for 3-D simulations to effectively estimate bed stress.

The real-world ocean's topography is not always represented well by a linear slope, the gradient of the slope changes along it's length, there are patches of roughness, and 3-D features such as canyons which have been shown to be important locally. To help answer the question as to how the results of these process-based studies can be applied to these complex topographies, laboratory and numerical experiments should incorporate more of these complexities. This would be easy for roughness, and changing slopes, but is challenging to incorporate 3-D topographical features in part given the current lateral extent of laboratory setups and simulations (which typically are still in 2-D).

Background flow (and in particular background shear) plays an important role in the shoaling process in the real world (Rayson *et al.*, 2019; Jones *et al.*, 2020). Therefore, there is a need for future investigations into shoaling to incorporate these effects. Whilst there would be challenges associated with producing these background currents both in the numerical model and laboratory where there is also a sloping boundary, further modelling studies to investigate such effects would be very valuable. One suggestion would be to incorporate a ridge, separating a volume of fluid (beyond the slope) from the main tank from which background currents could be fed.

3.7. Conclusion

The combination of laboratory experiments and numerical modelling is used here to investigate how the dynamics of shoaling ISWs is affected by the form of the background stratification in which they propagate, for otherwise identical initial conditions. In the thin tanh profile stratification, our numerical experiments are in good agreement with both past numerical studies (Aghsaee *et al.*, 2010; Nakayama *et al.*, 2019), and past laboratory studies in similar stratification regimes (Sutherland *et al.*, 2013). Within the parameter space previously investigated by Aghsaee *et al.* (2010) ($s = 0.01 - 0.3, S_w = 0.0125 - 0.186$), the shoaling dynamics in a thin tanh profile stratification produced in this study was as anticipated for given s and S_w. Although the results of Sutherland *et al.* (2013) were unable to delineate fission-type breakers (as such waves were not observed in the laboratory experiments), these results also follow the Iribarren number-based classifications of past studies for surging, collapsing and plunging breakers in the thin tanh profile stratification.

Laboratory experiments are an effective means of ensuring the validity of numerical model results, and allow a description of the physical breaking processes, whilst numerical

models offer a more complete suite of observations of the dynamics, with the opportunity to investigate density, velocity, vorticity, dissipation and stresses, as well as their derivatives. In this new surface stratification regime, the laboratory experiments are in strong agreement with the results of the numerical experiments. This result, alongside agreement with past studies of shoaling ISWs in the thin tanh profile stratification, gives good confidence in the validity of the numerical model used for this study.

Confidence in the validity of the numerical model for this study allowed its extension further into a new broad tanh profile stratification. The formation of a bolus as a wave in the broad tanh profile stratification is well documented in previous numerical and laboratory studies (e.g. Venayagamoorthy & Fringer, 2007; Allshouse & Swinney, 2020; Vieira & Allshouse, 2020). Vieira & Allshouse (2020) studied the formation of coherent boluses as waves in a range of similar broad tanh profile stratification where total pycnocline thickness varied, and the stratification in this study represents an extreme of pycnocline thickness. The bolus observed in the broad tanh profile stratification surging-type breakers correspond in polarity to the vortices described by Vieira & Allshouse (2020), and are of the same form as described previously (Venayagamoorthy & Fringer, 2007). Here, the formation of Kelvin-Helmholtz instabilities along the upper boundary of these boluses are reported for the first time, features previously described for the boluses formed by shoaling ISWs of elevation (Xu *et al.*, 2016). Whilst transverse variability and lobe-cleft instabilities form on these boluses, the leading-order behaviour is broadly the same in 2-D simulations as in 3-D simulations (similar to that previously observed by Xu *et al.* (2019)). These Kelvin-Helmholtz instabilities induce considerable mixing (figure 3.15*d*). In other stratification forms, such steep waves would yield other breaking types (figure 3.3), and the resulting surging bolus therefore would not form.

As the pycnocline thickness increases, and therefore progressively covers a wider part of the water column (the upper layer and then the BBL), the range of shoaling dynamics the wave can take decreases; convective overturning of the plunging breaker type, and collapsing breaker types which arise due to shear instability at the bottom boundary, are both impeded by stratification stabilising the flow above and below the pycnocline respectively. In the surface stratification, the presence of a density gradient throughout the upper layer inhibits the ability for the wave to plunge forward. Instead, the collapsing breaker type is prevalent across the regimes identified in the thin tanh stratification as plunging and collapsing by Aghsaee *et al.* (2010). Meanwhile, in the broad tanh profile stratification, the density gradient at the bed also prevents the occurrence of shear-induced global instability and vortices that are responsible for collapsing dynamics when the lower layer is homogeneous.

The up-slope bolus produced in the broad tanh profile stratification, where the wave is steep enough, is found to support Kelvin-Helmholtz instabilities on the upper boundary. This is a new dynamics observed here, and not observed in other stratifications, where bolus formation would be prevented by the faster formation of collapsing or plunging breaker types. Previous studies have identified that as pycnocline thickness increases, so too do bolus size and transport (Allshouse & Swinney, 2020; Vieira & Allshouse, 2020). The extreme of pycnocline thickness in the broad tanh profile stratification therefore can be anticipated to produce larger boluses than in the thinner pycnocline stratifications, thus enabling the observed instabilities to form.

It should be borne in mind that several previous studies with thin tanh profiles have identified the influence of internal wave Reynolds number in the classification of breaking ISWs on uniform slopes (see Nakayama *et al.* (2019) for a recent summary). For reasons presented earlier, such findings are difficult to compare with the classifications for the broad tanh and surface stratification profiles in the present investigation, primarily because of the different wave speed scales required to formulate the relevant Reynolds number. In the studies here, however, values of the internal wave Reynolds numbers based upon the measured wave speed are relatively small (see Table 1) compared with those based upon the (external) long wave speed c_0 in the thin tanh studies summarised by Nakayama *et al.* (2019). It is noted that the wave amplitude a appears in both S_w and Re_w and there is insufficient evidence in the data to justify ascribing changes in the behaviour of the shoaling waves to Reynolds number effects. Further investigations of this aspect should be pursued for the broad tanh and surface stratification density configurations studied here (by changing the model viscosity, for example).

The SPINS numerical model has previously been successfully used in conjunction with laboratory experiments, and here is shown to be in good agreement with past studies (both numerical and laboratory) in the thin tanh profile system, and in the new surface stratification, is in good agreement with the laboratory experiments. As previously identified (Xu *et al.*, 2019), the leading-order behaviour of these waves is well captured by 2-D simulations. These results show the importance of representing the stratification of a system in laboratory-scale experiments and models, whilst at the ocean scale, recognising that the form of the stratification may be key to correctly parameterising breaking dynamics, and the rates of mixing, dissipation and sediment dynamics associated with each breaker type. To most effectively represent the real world, further research should investigate the impacts of complex stratifications, for example the double hyperbolic function (see Manderson *et al.* (2019); Rayson *et al.* (2019)). Furthermore, it is recognised that the field observations of

Jones *et al.* (2020) suggest that background flow can be important in the character of the breaking and shoaling process, and further modelling studies to investigate such effects would be very valuable.

Data availability statement. The data that support the findings of this study openly available at https://doi.org/10.25405/data.ncl.c.5619616

Acknowledgements. YiYi Whitchelo is thanked for carrying out preliminary experiments at the University of Dundee as part of her undergraduate studies at the University of St Andrews. Prof. John Grue is thanked for useful discussions on this topic at the 4th Norway-Scotland Waves Symposium which inspired this study.

3.A. Supplementary Figures

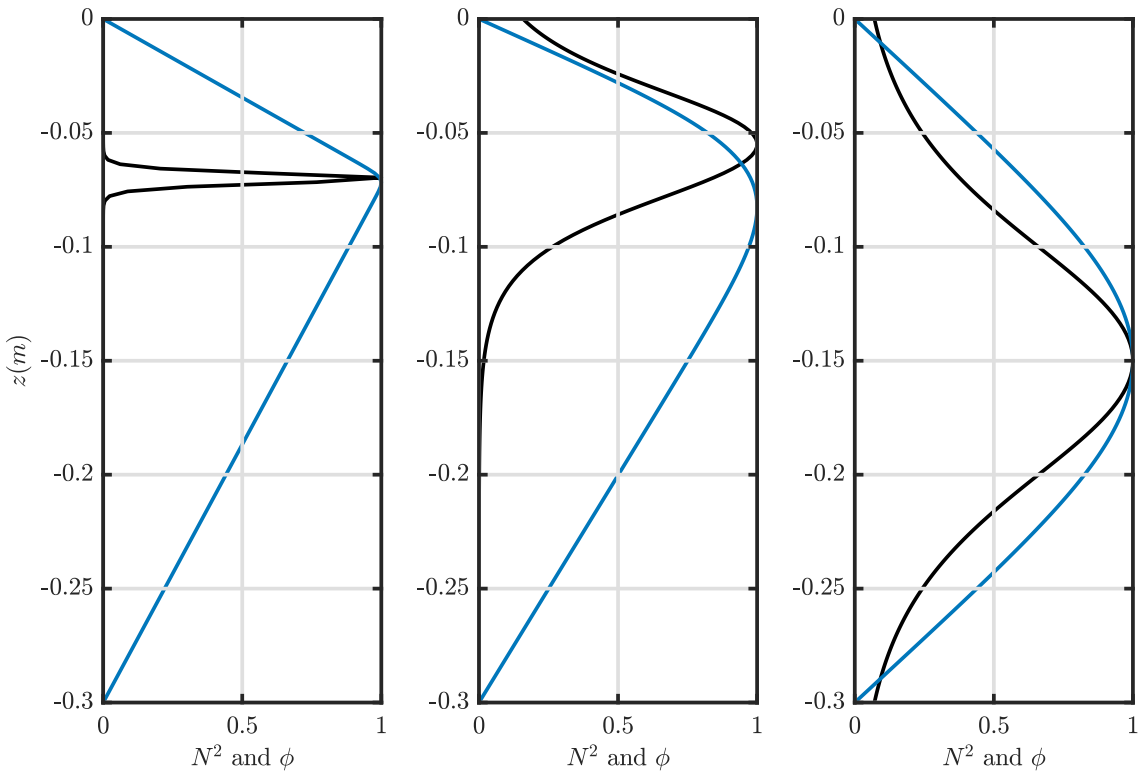


Figure 3.16: Vertical structures of N^2 (black) and ϕ (blue) of each stratification in this chapter, thin tanh (left), surface stratification (centre) and broad tanh stratification (right). Each normalised by the maximum value.

3.B. Supplementary Tables

Table 3.2: Complete table of parameters for simulations presented in and analysed for this study. Classifications denoted as follows, R = Reflected, F = Fission, S = Surging, C = Collapsing, P = Plunging, IS = Surging with instabilities on bolus (bracketed classification indicating some elements of that breaking dynamic present). Exp. Name indicates the experiment number (see caption Figure 3.3) used for cases presented within the text of the article.

Run	Exp. Name	Slope	L_s (m)	a (m)	λ (m)	S_w	c (m/s)	Ir	Classification	Re_w	Re	z_{pyc} (m)	h_{pyc} (m)	L_x (m)
Thin Pycnocline Stratification														
02_090720		0.400	0.75	0.045	0.598	0.076	0.110	1.450	C	5020	33100	0.07	0.003	7.00
03_100720		0.400	0.75	0.083	0.972	0.085	0.112	1.370	C	9780	35400	0.07	0.003	7.00
04_110720		0.067	1.50	0.046	0.598	0.076	0.110	0.242	R	5020	33100	0.07	0.003	7.00
05_120720		0.067	1.50	0.083	0.966	0.086	0.119	0.227	C	9890	35700	0.07	0.003	7.00
07_310720		0.400	0.75	0.081	0.932	0.087	0.118	1.358	C	9540	35400	0.07	0.003	7.00
24_071020	(1)	0.200	1.50	0.076	0.491	0.154	0.111	0.509	P	8100	32800	0.07	0.003	7.00
25_221020		0.200	1.50	0.075	0.791	0.095	0.115	0.650	C	8600	34400	0.07	0.003	7.00
26_091120		0.200	1.50	0.048	0.598	0.080	0.108	0.706	C	5200	32500	0.07	0.003	7.00
27_111120		0.200	1.50	0.009	0.645	0.014	0.096	1.666	S	896	28900	0.07	0.003	7.00
28_121120		0.033	9.00	0.048	0.600	0.080	0.108	0.118	F	5190	32400	0.07	0.003	14.50
29_150321		0.400	0.75	0.009	0.645	0.014	0.096	3.332	C	895	28900	0.07	0.003	7.00
30_160321		0.400	0.75	0.075	0.796	0.094	0.114	1.302	C(P)	8570	34200	0.07	0.003	7.00
31_170321		0.033	9.00	0.009	0.646	0.014	0.095	0.278	F	888	28600	0.07	0.003	14.50
32_180321		0.033	9.00	0.075	0.791	0.095	0.114	0.108	F	8560	34200	0.07	0.003	14.50
Surface Stratification														
200520_02		0.200	1.50	0.078	0.601	0.129	0.098	0.556	C	7600	29300	0.055	0.035	7.00
250520_03		0.200	1.50	0.083	0.630	0.131	0.099	0.552	C	8140	29600	0.055	0.035	7.00
270520_04		0.200	1.50	0.045	0.503	0.090	0.092	0.666	C	4200	27700	0.055	0.035	7.00
280520_05		0.400	0.75	0.091	0.710	0.129	0.100	1.115	C	9160	30100	0.055	0.035	7.00
040620_06		0.067	1.50	0.045	0.503	0.090	0.092	0.222	R	4200	27700	0.055	0.035	7.00
050620_07		0.067	1.50	0.077	0.600	0.129	0.098	0.186	R	7570	29300	0.055	0.035	7.00

Run	Exp. Name	Slope	L_s (m)	a (m)	λ (m)	S_w	c (m/s)	Ir	Classification	Re_w	Re	z_{pyc} (m)	h_{pyc} (m)	L_x (m)
070620_08		0.067	1.50	0.091	0.710	0.129	0.100	0.186	R	9160	30100	0.055	0.035	7.00
080620_09		0.067	1.50	0.061	0.534	0.115	0.097	0.197	R	5940	29000	0.055	0.035	7.00
080620_10		0.067	4.50	0.045	0.504	0.090	0.093	0.222	F(C)	4210	27800	0.055	0.035	10.00
090620_11		0.067	4.50	0.092	0.704	0.130	0.102	0.185	C(F)	9350	30500	0.055	0.035	10.00
110620_12		0.400	0.75	0.045	0.503	0.090	0.092	1.331	C	4200	27700	0.055	0.035	7.00
120620_13		0.400	0.75	0.061	0.534	0.115	0.097	1.180	C	5940	29000	0.055	0.035	7.00
130620_14		0.400	0.75	0.077	0.600	0.129	0.098	1.113	C	7570	29300	0.055	0.035	7.00
140620_15		0.133	1.50	0.091	0.710	0.129	0.100	0.371	C	9160	30100	0.055	0.035	7.00
150620_16		0.133	1.50	0.045	0.503	0.090	0.092	0.443	C(F)	4200	27700	0.055	0.035	7.00
160620_17		0.133	1.50	0.077	0.600	0.129	0.098	0.371	C(F)	7570	29300	0.055	0.035	7.00
170620_18		0.133	1.50	0.061	0.534	0.115	0.097	0.393	C(F)	5940	29000	0.055	0.035	7.00
230620_19		0.133	2.25	0.045	0.504	0.090	0.092	0.444	C(F)	4190	27600	0.055	0.035	7.75
240620_20		0.133	2.25	0.077	0.600	0.129	0.098	0.371	C(F)	7570	29300	0.055	0.035	7.75
250620_21		0.133	2.25	0.091	0.711	0.128	0.100	0.372	C	9150	30100	0.055	0.035	7.75
260620_22		0.200	1.50	0.061	0.534	0.115	0.097	0.590	C	5940	29000	0.055	0.035	7.00
270620_23		0.267	1.50	0.091	0.710	0.129	0.100	0.744	C	9160	30100	0.055	0.035	7.00
280620_24		0.267	1.50	0.045	0.503	0.090	0.092	0.888	C	4200	27700	0.055	0.035	7.00
010720_25		0.267	1.50	0.061	0.534	0.115	0.097	0.786	C	5940	29000	0.055	0.035	7.00
020720_26		0.267	1.50	0.077	0.600	0.129	0.098	0.742	C	7570	29300	0.055	0.035	7.00
030720_27		0.067	4.50	0.061	0.539	0.114	0.095	0.198	F(C)	5800	28400	0.055	0.035	10.00
040720_28		0.067	4.50	0.077	0.600	0.129	0.098	0.186	F(C)	7580	29300	0.055	0.035	10.00
050720_29		0.133	2.25	0.045	0.504	0.090	0.092	0.444	C	4200	27700	0.055	0.035	7.00
250720_31	(2)	0.200	1.50	0.011	0.529	0.022	0.077	1.358	S	879	23000	0.055	0.035	7.00
260720_32		0.400	0.75	0.012	0.529	0.022	0.077	2.712	S	882	23000	0.055	0.035	7.00
270720_33	(4)	0.033	9.00	0.045	0.504	0.090	0.092	0.111	F	4180	27600	0.055	0.035	14.50
300720_36		0.400	0.75	0.095	0.783	0.122	0.108	1.147	C	10300	32300	0.055	0.035	7.00

Run	Exp. Name	Slope	L_s (m)	a (m)	λ (m)	S_w	c (m/s)	Ir	Classification	Re_w	Re	z_{pyc} (m)	h_{pyc} (m)	L_x (m)
081020_44	(6)	0.200	1.50	0.083	0.634	0.131	0.099	0.552	C	8200	29600	0.055	0.035	7.00
Broad Pycnocline Stratification														
091020_45		0.200	1.50	0.031	0.376	0.083	0.081	0.696	IS	2520	24400	0.150	0.075	7.00
101020_46	(8)	0.200	1.50	0.054	0.427	0.126	0.079	0.563	IS	4240	23600	0.150	0.075	7.00
111020_47	(9)	0.033	9.00	0.035	0.386	0.092	0.081	0.110	F	2860	24200	0.150	0.075	14.50
121020_48	(10)	0.200	1.50	0.010	0.356	0.027	0.082	1.212	S	796	24700	0.150	0.075	7.00
101120_49	(11)	0.200	1.50	0.038	0.388	0.097	0.080	0.642	IS	3030	24100	0.150	0.075	7.00
120220_50		0.133	2.25	0.031	0.376	0.082	0.081	0.464	IS	2520	24400	0.150	0.075	7.75
130220_51		0.266	1.13	0.031	0.376	0.083	0.081	0.926	IS	2520	24400	0.150	0.075	7.00
140220_52		0.133	2.25	0.010	0.356	0.027	0.083	0.808	S	806	25000	0.150	0.075	7.75
150220_53		0.266	1.13	0.010	0.356	0.027	0.082	1.612	S	797	24700	0.150	0.075	7.00
160220_54		0.133	2.25	0.021	0.364	0.057	0.082	0.556	IS	1720	24700	0.150	0.075	7.75
170220_55		0.267	1.13	0.021	0.364	0.057	0.082	1.112	S	1710	24500	0.150	0.075	7.00
180220_56		0.200	1.50	0.021	0.364	0.057	0.082	0.834	IS	1710	24500	0.150	0.075	7.00

Table 3.3: As table 3.2, for Laboratory Experiments. Due to practical considerations, measured values of z_{pyc} and h_{pyc} were not available for all experiments.

Run	Exp. Name	Slope	L_s (m)	a (m)	λ (m)	S_w	c (m/s)	Ir	Classification	z_{pyc} (m)	h_{pyc} (m)	ρ_1	ρ_2
Laboratory Experiments													
090120		0.400	0.75	0.074	0.590	0.125	0.099	1.133	C	0.076	0.018	1024.0	1045.0
130120		0.400	0.75	0.101	0.845	0.119	0.106	1.159	C	0.062	0.037	1026.0	1046.0
150120		0.400	0.75	0.066	0.557	0.118	0.098	1.163	C	0.058	0.028	1026.0	1046.0
170120		0.400	0.75	0.049	0.545	0.090	0.090	1.330	C	0.062	0.028	1026.0	1046.0
090320	(7)	0.200	1.50	0.089	0.708	0.126	0.103	0.564	C	0.060	0.034	1025.0	1046.0
110320		0.200	1.50	0.054	0.540	0.101	0.081	0.631	C	–	–	1025.0	1046.0
260820		0.200	1.50	0.036	0.596	0.060	0.075	0.818	C	0.094	0.048	1024.5	1046.0
020920	(5)	0.067	1.50	0.104	0.895	0.117	0.101	0.195	C(F)	–	–	1026.0	1046.0
040920		0.067	1.50	0.027	0.656	0.041	0.083	0.329	C	0.054	0.013	1024.0	1046.0
070920		0.067	1.50	0.060	0.543	0.110	0.099	0.201	C	–	–	1024.0	1046.0
170920		0.067	1.50	0.091	0.732	0.125	0.106	0.189	C	0.060	0.030	1025.0	1045.5
220920		0.200	1.50	0.065	0.554	0.117	0.091	0.584	C	0.090	0.048	1024.5	1046.0
230920	(3)	0.200	1.50	0.024	0.686	0.035	0.075	1.076	S	0.038	0.030	1024.0	1045.5

Chapter 3

References

Aghsaee, P., Boegman, L. & Lamb, K. G. 2010 Breaking of shoaling internal solitary waves. *Journal of Fluid Mechanics* **659**, 289–317, https://doi.org/10.1017/S002211201000248X.

Allshouse, M. R. & Swinney, H. L. 2020 Dependence of Internal Wave Bolus Transport on Pycnocline Thickness. *Geophysical Research Letters* **47** (14), e2020GL086952, https://doi.org/10.1029/2020GL086952.

Arthur, R. S. & Fringer, O. B. 2014 The dynamics of breaking internal solitary waves on slopes. *Journal of Fluid Mechanics* **761** (2), 360–398, https://doi.org/10.1017/jfm.2014.641.

Arthur, R. S., Koseff, J. R. & Fringer, O. B. 2017 Local versus volume-integrated turbulence and mixing in breaking internal waves on slopes. *Journal of Fluid Mechanics* **815**, 169–198, https://doi.org/10.1017/jfm.2017.36.

Barros, R., Choi, W. & Milewski, P. A. 2020 Strongly nonlinear effects on internal solitary waves in three-layer flows. *Journal of Fluid Mechanics* **883**, A16, https://doi.org/10.1017/jfm.2019.795.

Boegman, L. & Ivey, G. N. 2009 Flow separation and resuspension beneath shoaling nonlinear internal waves. *Journal of Geophysical Research: Oceans* **114** (2), 2018, https://doi.org/10.1029/2007JC004411.

Boegman, L., Ivey, G. N. & Imberger, J. 2005 The degeneration of internal waves in lakes with sloping topography. *Limnology and Oceanography* **50** (5), 1620–1637, https://doi.org/10.4319/lo.2005.50.5.1620.

Boegman, L. & Stastna, M. 2019 Sediment Resuspension and Transport by Internal Solitary Waves. *Annual Review of Fluid Mechanics* **51** (1), 129–154, https://doi.org/10.1146/annurev-fluid-122316-045049.

Bogucki, D., Dickey, T. & Redekopp, L. G. 1997 Sediment resuspension and mixing by resonantly generated internal solitary waves. *Journal of Physical Oceanography* **27** (7), 1181–1196, https://doi.org/10.1175/1520-0485(1997)027¡1181:SRAMBR¿2.0.CO;2.

Bogucki, D. J. & Redekopp, L. G. 1999 A mechanism for sediment resuspension by internal solitary waves. *Geophysical Research Letters* **26** (9), 1317–1320, https://doi.org/10.1029/1999GL900234.

Cacchione, D. A., Pratson, L. F. & Ogston, A. S. 2002 The Shaping of Continental Slopes by Internal Tides. *Science* **296** (5568), 724–727, https://doi.org/10.1126/science.1069803.

Carr, M. & Davies, P. A. 2006 The motion of an internal solitary wave of depression over a fixed bottom boundary in a shallow, two-layer fluid. *Physics of Fluids* **18** (1), 016601, https://doi.org/10.1063/1.2162033.

Carr, M., Davies, P. A. & Hoebers, R. P. 2015 Experiments on the structure and stability of mode-2 internal solitary-like waves propagating on an offset pycnocline. *Physics of Fluids* **27** (4), 046602, https://doi.org/10.1063/1.4916881.

Carr, M., Davies, P. A. & Shivaram, P. 2008*a* Experimental evidence of internal solitary wave-induced global instability in shallow water benthic boundary layers. *Physics of Fluids* **20** (6), 066603, https://doi.org/10.1063/1.2931693.

Carr, M., Fructus, D., Grue, J., Jensen, A. & Davies, P. A. 2008*b* Convectively induced shear instability in large amplitude internal solitary waves. *Physics of Fluids* **20** (12), 126601, https://doi.org/10.1063/1.3030947.

Carr, M., Stastna, M., Davies, P. A. & van de Wal, K. J. 2019 Shoaling mode-2 internal solitary-like waves. *Journal of Fluid Mechanics* **879**, 604–632, https://doi.org/10.1017/jfm.2019.671.

da Silva, J. C., Buijsman, M. C. & Magalhaes, J. M. 2015 Internal waves on the upstream side of a large sill of the Mascarene Ridge: A comprehensive view of their generation mechanisms and evolution. *Deep-Sea Research Part I: Oceanographic Research Papers* **99**, 87–104, https://doi.org/10.1016/j.dsr.2015.01.002.

Dalziel, S. B., Carr, M., Sveen, J. K. & Davies, P. A. 2007 Simultaneous synthetic schlieren and PIV measurements for internal solitary waves. *Measurement Science and Technology* **18** (3), 533–547, https://doi.org/10.1088/0957-0233/18/3/001.

Davis, K. A., Arthur, R. S., Reid, E. C., Rogers, J. S., Fringer, O. B., DeCarlo, T. M. & Cohen, A. L. 2020 Fate of Internal Waves on a Shallow Shelf. *Journal of Geophysical Research: Oceans* **125** (5), e2019JC015377, https://doi.org/10.1029/2019JC015377.

Deepwell, D. 2018 High resolution simulations of mode-2 internal waves : Transport , shoaling , and the influence of rotation by. PhD thesis, University of Waterloo.

Deepwell, D., Sapède, R., Buchart, L., Swaters, G. E. & Sutherland, B. R. 2020 Particle transport and resuspension by shoaling internal solitary waves. *Physical Review Fluids* **5** (5), 054303, https://doi.org/10.1103/PhysRevFluids.5.054303.

Diamessis, P. J. & Redekopp, L. G. 2006 Numerical investigation of solitary internal wave-induced global instability in shallow water benthic boundary layers. *Journal of Physical Oceanography* **36** (5), 784–812, https://doi.org/10.1175/JPO2900.1.

Fructus, D., Carr, M., Grue, J., Jensen, A. & Davies, P. A. 2009 Shear-induced breaking of large internal solitary waves. *Journal of Fluid Mechanics* **620**, 1–29, https://doi.org/10.1017/S0022112008004898.

Green, R. H., Jones, N. L., Rayson, M. D., Lowe, R. J., Bluteau, C. E. & Ivey, G. N. 2019 Nutrient fluxes into an isolated coral reef atoll by tidally driven internal bores. *Limnology and Oceanography* **64** (2), 461–473, https://doi.org/10.1002/lno.11051.

Grue, J. 2005 Generation, propagation, and breaking of internal solitary waves. *Chaos* **15** (3), 037110, https://doi.org/10.1063/1.2047907.

Grue, J., Jensen, A., Rusas, P. & Sveen, J. K. 1999 Properties of large-amplitude internal waves. *Journal of Fluid Mechanics* **380**, 257–278, https://doi.org/10.1017/S0022112098003528.

Grue, J., Jensen, A., Rusås, P. O. & Sveen, J. K. 2000 Breaking and broadening of internal solitary waves. *Journal of Fluid Mechanics* **413**, 181–217, https://doi.org/10.1017/S0022112000008648.

Helfrich, K. R. & Melville, W. K. 2006 Long nonlinear internal waves. *Annual Review of Fluid Mechanics* **38** (1), 395–425, https://doi.org/10.1146/annurev.fluid.38.050304.092129.

Horn, D. A., Imberger, J. & Ivey, G. N. 2001 The degeneration of large-scale interfacial gravity waves in lakes. *Journal of Fluid Mechanics* **434**, 181–207, https://doi.org/10.1017/S0022112001003536.

Hosegood, P., Bonnin, J. & van Haren, H. 2004 Solibore-induced sediment resuspension in the Faeroe-Shetland channel. *Geophysical Research Letters* **31** (9), L09301, https://doi.org/10.1029/2004GL019544.

Huang, X., Chen, Z., Zhao, W., Zhang, Z., Zhou, C., Yang, Q. & Tian, J. 2016 An extreme internal solitary wave event observed in the northern South China Sea. *Scientific Reports* **6** (1), 30041, https://doi.org/10.1038/srep30041.

Ivey, G. N., Bluteau, C. E., Gayen, B., Jones, N. L. & Sohail, T. 2021 Roles of Shear and Convection in Driving Mixing in the Ocean. *Geophysical Research Letters* **48** (3), e2020GL089455, https://doi.org/10.1029/2020GL089455.

Jones, N. L., Ivey, G. N., Rayson, M. D. & Kelly, S. M. 2020 Mixing Driven by Breaking Nonlinear Internal Waves. *Geophysical Research Letters* **47** (19), e2020GL089591, https://doi.org/10.1029/2020GL089591.

Lamb, K. G. 2014 Internal Wave Breaking and Dissipation Mechanisms on the Continental Slope/Shelf. *Annual Review of Fluid Mechanics* **46** (1), 231–254, https://doi.org/10.1146/annurev-fluid-011212-140701.

Lamb, K. G. & Nguyen, V. T. 2009 Calculating Energy Flux in Internal Solitary Waves with an Application to Reflectance. *Journal of Physical Oceanography* **39** (3), 559–580, https://doi.org/10.1175/2008JPO3882.1.

Lamb, K. G. & Yan, L. 1996 The evolution of internal wave undular bores: Comparisons of a fully nonlinear numerical model with weakly nonlinear theory. *Journal of Physical Oceanography* **26** (12), 2712–2734, https://doi.org/10.1175/1520-0485(1996)026¡2712:TEOIWU¿2.0.CO;2.

Lien, R. C., Tang, T. Y., Chang, M. H. & D'Asaro, E. A. 2005 Energy of nonlinear internal waves in the South China Sea. *Geophysical Research Letters* **32** (5), 1–5, https://doi.org/10.1029/2004GL022012.

Luzzatto-Fegiz, P. & Helfrich, K. R. 2014 Laboratory experiments and simulations for solitary internal waves with trapped cores. *Journal of Fluid Mechanics* **757**, 354–380, https://doi.org/10.1017/jfm.2014.501.

Ma, X., Yan, J., Hou, Y., Lin, F. & Zheng, X. 2016 Footprints of obliquely incident internal solitary waves and internal tides near the shelf break in the northern South China Sea. *Journal of Geophysical Research: Oceans* **121** (12), 8706–8719, https://doi.org/10.1002/2016JC012009.

Maderich, V. S., Van Heijst, G. J. & Brandt, A. 2001 Laboratory experiments on intrusive flows and internal waves in a pycnocline. *Journal of Fluid Mechanics* **432**, 285–311, https://doi.org/10.1017/s0022112000003323.

Manderson, A., Rayson, M. D., Cripps, E., Girolami, M., Gosling, J. P., Hodkiewicz, M., Ivey, G. N. & Jones, N. L. 2019 Uncertainty quantification of density and stratification estimates with implications for predicting ocean dynamics. *Journal of Atmospheric and Oceanic Technology* **36** (8), 1313–1330, https://doi.org/10.1175/JTECH-D-18-0200.1.

Masunaga, E., Fringer, O. B., Yamazaki, H. & Amakasu, K. 2016 Strong turbulent mixing induced by internal bores interacting with internal tide-driven vertically sheared flow. *Geophysical Research Letters* **43** (5), 2094–2101, https://doi.org/10.1002/2016GL067812.

Michallet, H. & Ivey, G. N. 1999 Experiments on mixing due to internal solitary waves breaking on uniform slopes. *Journal of Geophysical Research: Oceans* **104** (C6), 13467–13477, https://doi.org/10.1029/1999jc900037.

Miles, J. W. 1961 On the stability of heterogeneous shear flows. *Journal of Fluid Mechanics* **10** (4), 496–508, https://doi.org/10.1017/S0022112061000305.

Moum, J. N., Farmer, D. M., Smyth, W. D., Armi, L. & Vagle, S. 2003 Structure and generation of turbulence at interfaces strained by internal solitary waves propagating shoreward over the continental shelf. *Journal of Physical Oceanography* **33** (10), 2093–2112, https://doi.org/10.1175/1520-0485(2003)033¡2093:SAGOTA¿2.0.CO;2.

Munro, R. J. & Davies, P. A. 2006 The flow generated in a continuously stratified rotating fluid by the differential rotation of a plane horizontal disc. *Fluid Dynamics Research* **38** (8), 522–538, https://doi.org/10.1016/j.fluiddyn.2006.03.002.

Nakayama, K., Sato, T., Shimizu, K. & Boegman, L. 2019 Classification of internal solitary wave breaking over a slope. *Physical Review Fluids* **4** (1), 014801, https://doi.org/10.1103/PhysRevFluids.4.014801.

Orr, M. H. & Mignerey, P. C. 2003 Nonlinear internal waves in the South China Sea: Observation of the conversion of depression internal waves to elevation internal waves. *Journal of Geophysical Research* **108** (C3), 3064, https://doi.org/10.1029/2001JC001163.

Rayson, M. D., Jones, N. L. & Ivey, G. N. 2019 Observations of large-amplitude mode-2 nonlinear internal waves on the australian north west shelf. *Journal of Physical Oceanography* **49** (1), 309–328, https://doi.org/10.1175/JPO-D-18-0097.1.

Reeder, D. B., Ma, B. B. & Yang, Y. J. 2011 Very large subaqueous sand dunes on the upper continental slope in the South China Sea generated by episodic, shoaling deep-water internal solitary waves. *Marine Geology* **279** (1-4), 12–18, https://doi.org/10.1016/j.margeo.2010.10.009.

Reid, E. C., DeCarlo, T. M., Cohen, A. L., Wong, G. T., Lentz, S. J., Safaie, A., Hall, A. & Davis, K. A. 2019 Internal waves influence the thermal and nutrient environment on a shallow coral reef. *Limnology and Oceanography* **64** (5), 1949–1965, https://doi.org/10.1002/lno.11162.

Sarkar, S. & Scotti, A. 2017 From Topographic Internal Gravity Waves to Turbulence. *Annual Review of Fluid Mechanics* **49** (1), 195–220, https://doi.org/10.1146/annurev-fluid-010816-060013.

Shroyer, E. L., Moum, J. N. & Nash, J. D. 2009 Observations of polarity reversal in shoaling nonlinear internal waves. *Journal of Physical Oceanography* **39** (3), 691–701, https://doi.org/10.1175/2008JPO3953.1.

St Laurent, L., Simmons, H., Tang, T. Y. & Wang, Y. 2011 Turbulent Properties of Internal Waves in the South China Sea. *Oceanography* **24** (4), 78–87, https://doi.org/10.5670/oceanog.2011.96.

Stastna, M. & Lamb, K. G. 2002 Large fully nonlinear internal solitary waves: The effect of background current. *Physics of Fluids* **14** (9), 2987–2999, https://doi.org/10.1063/1.1496510.

Subich, C. J., Lamb, K. G. & Stastna, M. 2013 Simulation of the Navier-Stokes equations in three dimensions with a spectral collocation method. *International Journal for Numerical Methods in Fluids* **73** (2), 103–129, https://doi.org/10.1002/fld.3788.

Sutherland, B. R., Barrett, K. J. & Ivey, G. N. 2013 Shoaling internal solitary waves. *Journal of Geophysical Research: Oceans* **118** (9), 4111–4124, https://doi.org/10.1002/jgrc.20291.

Venayagamoorthy, S. K. & Fringer, O. B. 2007 On the formation and propagation of nonlinear internal boluses across a shelf break. *Journal of Fluid Mechanics* **577**, 137–159, https://doi.org/10.1017/S0022112007004624.

Vieira, G. S. & Allshouse, M. R. 2020 Internal wave boluses as coherent structures in a continuously stratified fluid. *Journal of Fluid Mechanics* **885**, A35, https://doi.org/10.1017/jfm.2019.993.

Wallace, B. C. & Wilkinson, D. L. 1988 Run-up of internal waves on a gentle slope in a two-layered system. *Journal of Fluid Mechanics* **191**, 419–442, https://doi.org/10.1017/S0022112088001636.

Walter, R. K., Brock Woodson, C., Arthur, R. S., Fringer, O. B. & Monismith, S. G. 2012 Nearshore internal bores and turbulent mixing in southern Monterey Bay. *Journal of Geophysical Research: Oceans* **117** (7), 7017, https://doi.org/10.1029/2012JC008115.

Winters, K. B., Lombard, P. N., Riley, J. J. & D'Asaro, E. A. 1995 Available potential energy and mixing in density-stratified fluids. *Journal of Fluid Mechanics* **289** (C5), 115–128, https://doi.org/10.1017/S002211209500125X.

Xu, C. & Stastna, M. 2020 Instability and cross-boundary-layer transport by shoaling internal waves over realistic slopes. *Journal of Fluid Mechanics* **895**, R6, https://doi.org/10.1017/jfm.2020.389.

Xu, C., Stastna, M. & Deepwell, D. 2019 Spontaneous instability in internal solitary-like waves. *Physical Review Fluids* **4** (1), 014805, https://doi.org/10.1103/PhysRevFluids.4.014805.

Xu, C., Subich, C. & Stastna, M. 2016 Numerical simulations of shoaling internal solitary waves of elevation. *Physics of Fluids* **28** (7), 76601, https://doi.org/10.1063/1.4958899.

Zulberti, A., Jones, N. L. & Ivey, G. N. 2020 Observations of Enhanced Sediment Transport by Nonlinear Internal Waves. *Geophysical Research Letters* **47** (19), e2020GL088499, https://doi.org/10.1029/2020GL088499.

Chapter 4

Dense Pulses formed from fissioning internal waves

4.1. Introduction

In the ocean, vertical variation in seawater temperature and salinity acts to stratify the oceanic water column, producing conditions in which density disturbances can propagate along a pycnocline as internal waves. Internal solitary waves (ISWs) are a particular form of internal waves that have amplitude comparable to the pycnocline thickness, and often the overall depth of the water column (e.g. Grue *et al.*, 1999). Whilst propagating over a flat bottom in deep water, ISWs can travel long distances without change of form. However, as ISWs move into shallower waters, the bed interacts with the flow, and waves propagating over shallowing topography undergo shoaling. During shoaling, the form of ISWs change considerably, and they are known to modify water properties by inducing considerable vertical mixing of cool, nutrient rich waters from depth (McPhee-Shaw *et al.*, 2007; Reid *et al.*, 2019). These changes can benefit benthic ecosystems such as coral reefs and kelp forests (Green *et al.*, 2019), and may increase reef resilience to climate change by increasing high frequency temperature variability (Safaie *et al.*, 2018; Reid *et al.*, 2019).

ISWs are found commonly across the world's oceans, and they maintain high levels of research interest due to their effectiveness in transporting energy and water masses (and their associated heat, nutrients and sediments) (Helfrich & Melville, 2006), and for mixing in the ocean (e.g. Lamb, 2014; Huang *et al.*, 2016; Boegman & Stastna, 2019). Typically, internal waves are generated on density interfaces in stably-stratified fluids by barotropic motion over topography such as sills, slopes and the shelf edge (e.g. Grue, 2005; da Silva *et al.*, 2015; Rayson *et al.*, 2019). They are characterised by a balance of nonlinear

steepening and wave dispersion, and as a result are able to travel large distances without significant change of form or magnitude.

Whilst field observations of ISWs document the complexity of real-world dynamics, practical and technological constraints often limit the spatial and temporal resolution of field observations. Instead, idealised modelling studies at the laboratory scale allow full understanding of the underlying fluid dynamics, and the alteration of various parameters to identify trends and regimes that represent specific dynamical characteristics. Numerous efforts have been made to study the dynamics of shoaling mode-1 ISWs of depression on a range of idealised linear (and mostly steep) slopes in laboratory experiments (e.g Boegman *et al.*, 2005) ($s = 0.1 - 0.15$), (Michallet & Ivey, 1999) ($s = 0.069 - 0.214$), and (Sutherland *et al.*, 2013) ($s = 0.143 - 0.417$), and numerical models (e.g. Aghsaee *et al.*, 2010) ($s = 0.01 - 0.3$), (Nakayama *et al.*, 2019) ($s = 0.03 - 0.3$), (Arthur *et al.*, 2017) ($s = 0.218$) (Xu & Stastna, 2020) ($s = 0.02$) where s is the vertical displacement per unit horizontal displacement. Whilst these studies have investigated shoaling over a range of slopes (up to $s = 0.417$), geophysical slopes are very mild, $s \approx 0.001$ for the coastal ocean, $s \approx 0.01$ for lakes, and $s = 0.03 - 0.07$ for typical continental shelves (Cacchione *et al.*, 2002), milder than the slopes in most previous studies.

Laboratory experiments (e.g. Wallace & Wilkinson, 1988), numerical simulations (e.g. Xu & Stastna, 2020) and field observations (e.g. Orr & Mignerey, 2003; Shroyer *et al.*, 2009; St Laurent *et al.*, 2011) have shown that as ISWs of depression shoal over geophysically representative mild slopes they undergo a process called fission. In fissioning waves, nonlinear steepening is insufficient to cause overturning of the wave (Aghsaee *et al.*, 2010), and instead, as the back of the wave steepens, the leading wave evolves into a train of internal bores (ISWs of elevation with the strongest currents and temperature fronts near the bed) or boluses (Reid *et al.*, 2019; Jones *et al.*, 2020). Whilst Xu & Stastna (2020) recently investigated the role of boundary layer instability in fissioning waves propagating over realistic slopes in a high resolution model, there is very little published research into the bottom boundary layer (BBL) dynamics during fissioning (Boegman & Stastna, 2019). When shoaling, energy transported by ISWs is used to enhance turbulent, irreversible mixing (Moum *et al.*, 2003). This process extends over a large area, in the New Jersey shelf, where it has been observed over a distance of 35 km (Shroyer *et al.*, 2010).

To date, all laboratory scale studies of ISWs shoaling over slopes gentle enough for fission to occur have been for a three-layer stratification with a homogeneous surface and bottom layer, separated by a thin pycnocline, resembling an idealised three-layer ocean (e.g. Aghsaee *et al.*, 2010; Arthur & Fringer, 2014; Nakayama *et al.*, 2019; Xu & Stastna,

2020; Ghassemi *et al.*, 2022). Whilst some ISW shoaling studies have investigated different stratifications (with the pycnocline centre at mid-depth, and varying pycnocline thicknesses (Allshouse & Swinney, 2020; Vieira & Allshouse, 2020)), these have been restricted to steeper slopes, over which fission does not occur. As a result, no studies deviating from a three-layer stratification have investigated wave fission, despite these mild slopes being most representative of the real ocean.

Ocean stratification can be described by the density field, ρ which can be expressed as a function of depth z via a hyperbolic tangent profile, and for this reason is widely used in numerical and laboratory studies (e.g. Maderich *et al.*, 2001; Allshouse & Swinney, 2020; Vieira & Allshouse, 2020),

$$\rho(z) = \rho_1 + \Delta\rho \tanh\left(\frac{z - z_{pyc}}{h_{pyc}}\right), \tag{4.1}$$

where ρ_1 is the density of the upper layer (and reference density), $\Delta\rho$ the change in density through the water column, z_{pyc} the depth of the centre of the pycnocline, and h_{pyc} the pycnocline half thickness.

The thin tanh profile system represents a lower limit of h_{pyc}. Yet, stratification in the real-world ocean varies, with associated variability in h_{pyc}. For example, the Labrador Sea is well represented by the three-layer idealised system, whilst in the Sulu Sea, density varies linearly with depth over the entire upper layer, so a broader pycnocline is more representative (Vlasenko *et al.*, 2005). Focusing on steeper slopes, previous work investigated the role of varying stratification on shoaling dynamics (Hartharn-Evans *et al.*, 2022), identifying that dependent on the location of density gradients in the stratification, different shoaling behaviours were suppressed. Past studies of the field have also identified the role of seasonal variation in offshore stratification (as a result of upwelling) in influencing the behaviour of bores (Moum *et al.*, 2007; Walter & Phelan, 2016). With such a variation in pycnocline thickness in the real ocean, it is reasonable to question what impact stratification form may have on fission dynamics. In this chapter, three stratification types are investigated, namely (i) thin tanh (homogeneous upper and lower layers separated by a thin pycnocline), (ii) surface stratification (linearly stratified layer overlaying a homogeneous lower layer) and (iii) broad tanh (continuous density gradient throughout the water column). For the first time, ISW fissioning is investigated in detail in the surface and broad tanh stratification cases using numerical modelling. During the fission process, pulses of dense fluid are formed that travel upslope, this chapter focuses on investigating changes to these pulses of dense fluid (hereafter referred to simply as 'pulses'), and pulse structure and transport of

lower-layer fluid.

Use of numerical simulations is made to investigate the propagation of a mode-1 ISW of depression propagating over a uniformly sloping solid boundary. Results are presented to aid comparison between field observations such as static temperature loggers, and these numerical simulations.

The chapter is organised as follows. In § 4.2 the numerical methods are described. In § 4.3.1, the formation and structure of pulses are described, followed by a description of the evolution and degeneration in § 4.3.2. Finally, a discussion of these results, and their relevance to the ocean scale, as well as conclusions are given in § 4.4.

4.2. Methods

ISWs were simulated in a rectangular tank with waves initiated using the lock gate technique, with the same simulation setup to the extended tank described in chapter 3. A schematic of the model set-up is given in figure 4.1 (*a*), where the length of the tank $L_x = 14.5$ m, and the depth of the tank $L_z = 0.3$ m. A hyperbolic smoothing function produces a numerical step in density 0.3 m from the left end of the tank, from which an ISW is produced propagating from left to right. Simulations were carried out with the pseudospectral code SPINS described in chapter 1 §2.6.

As in chapter 3, here $\rho_1 = 1026\,\mathrm{kg\,m^{-3}}$). No slip boundary conditions were applied at the flat upper, and mapped lower boundaries to satisfy model requirements. A mapped Chebyshev grid is employed in the vertical, implying a clustering of points near both the upper and lower boundary that scales with the number of points in the vertical squared, and that vertical resolution improves over the slope. Free-slip boundary conditions were applied at the vertically oriented left and right ends of the computational domain, the grid spacing of which was regularly spaced. Grid resolution was 4096 points in the x and 256 grid points in the z coordinate, giving $dx = 3.5$ mm, and away from the slope, dz varies between 0.124 mm in the BBL and 1.8 mm near mid-depth. Sensitivity experiments and double and half resolution indicate flow features are appropriately resolved and robust at this resolution, except in the thin tanh stratification. Following these simulations, the horizontal grid resolution was doubled (to 8192 points in the x) for the four largest amplitude wave thin tanh stratification experiments (Thin-7L, Thin-10L, Thin-20L, Thin-30L).

The hyperbolic tangent profile in equation 4.1 was employed for the three stratification types (figure 4.1*b*), namely, (i) a system like that studied previously in the literature consisting of a thin, linearly stratified pycnocline sandwiched between homogeneous layers,

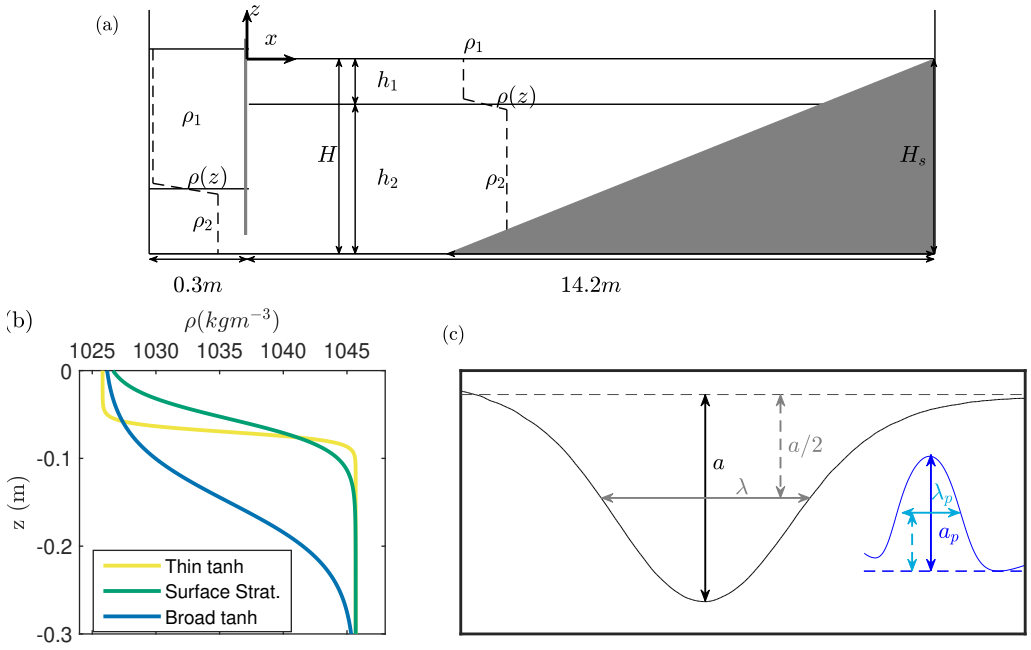


Figure 4.1: (*a*) Schematic diagram of the numerical domain used throughout this study, (*b*) profiles from each of the three stratification types used in the corresponding numerical models (solid lines), and (*c*) the definitions for wave properties a and λ, and pulse properties (blue) a_p and λ_p.

here referred to as 'thin tanh stratification' (ii) a stratification consisting of a homogeneous bottom layer and an approximately linearly stratified top layer, here referred to as 'surface stratification', as the density gradient is close to the surface and (iii) a water column in which the density varies linearly with depth throughout the full water depth, here referred to as 'broad tanh stratification', due to the large value of h_{pyc}. Fourteen model runs are presented in this study (see table 4.1) representing five initial wave amplitudes in each of the three stratification types (except for the Broad tanh stratification, where four different wave amplitudes are simulated). All simulations are carried out for a slope of $s = 0.033$, and the bottom boundary follows the form of Lamb & Nguyen (2009) (see equation 3.2, 3.3). The characteristic transition distance for the slope $d = 0.03L_s$ and the length of the slope $L_s = 9$ m.

Dense pulses formed by the fission process were identified using the Matlab peak fitting function to find peaks in the depth of the $\rho = \rho_1 + \Delta\rho/2$ contour (which represents the centre of the pycnocline in each case). Peaks related to each pulse were identified manually, and the amplitude (a_p), wavelength (λ_p), and propagation speed (c_p) calculated in the same manner as for wave amplitude, wavelength and propagation speed (figure 4.1*a*).

Table 4.1: Summary of simulation parameters. a, λ and c are incident wave amplitude, wavelength and propagation speed respectively (see figure 4.1*c*), h_{adj_pyc} is the location of the centre of the pycnocline behind the gate

Simulation Name	Stratification Type	h_{adj_pyc} (m)	a (m)	λ (m)	c (m/s)
Broad-5L	Broad tanh	0.1682	0.010	0.358	0.083
Broad-10L	Broad tanh	0.2237	0.035	0.386	0.081
Broad-20L	Broad tanh	0.2541	0.046	0.412	0.079
Broad-30L	Broad tanh	0.2926	0.054	0.429	0.079
Surface-5L	Surface	0.0732	0.011	0.541	0.078
Surface-7L	Surface	0.1000	0.028	0.501	0.086
Surface-10L	Surface	0.1287	0.045	0.504	0.092
Surface-20L	Surface	0.1591	0.061	0.533	0.097
Surface-30L	Surface	0.1968	0.077	0.599	0.097
Thin-5L	Thin tanh	0.0855	0.009	0.646	0.095
Thin-7L	Thin tanh	0.1242	0.031	0.573	0.104
Thin-10L	Thin tanh	0.1568	0.048	0.600	0.108
Thin-20L	Thin tanh	0.1908	0.063	0.668	0.110
Thin-30L	Thin tanh	0.2321	0.075	0.791	0.114

4.3. Results

A summary of the dynamics of a fissioning ISW is described in this section. Examples displayed in this section show the surface and broad stratifications, which have not previously been described in the existing literature. Numerical simulations in the thin tanh are qualitatively similar to those in the surface stratification. High resolution simulations of fissioning ISWs in a thin tanh stratification are described in detail in Xu & Stastna (2020). Throughout this text, the features formed by fission are referred to as 'pulses' reflecting the terminology commonly used for field observations.

4.3.1. *Initial pulse formation*

After the initialisation of each simulation in the surface and thin tanh stratification, an ISW of depression is formed after a small sorting distance (of approximately 1 m). The ISW of depression propagates along the flat bed of the tank until it reaches the toe of the slope at $x = 4.9$ m. On reaching the slope, the ISW continues to propagate upslope a distance without significant change of form. However, around halfway up the slope (at 9.5 m), the

wave shape begins to adjust to the evolving water depth, becoming a long wave with a shallow front face that aligns itself to the topographic slope, and a steepening rear face (see figure 4.2*a, f*). During this process, reverse flow at the bed due to BBL separation occurs (Carr & Davies, 2006) (indicated in figure 4.2*a* by a red (positive velocity) region around 9.5 m). The flow reversal begins to grow, as isopycnals at the rear face of the wave rise above the resting pycnocline depth (referred to in other literature Aghsaee *et al.* (e.g. 2010) as a positive tail), indicating the formation of the first wave of elevation (figure 4.2*b, g*). Whilst the propagation of the long wave of depression is almost halted, this wave emerges from the rear face of the long wave with the signal of an internal wave of elevation at the lower boundary in the velocity and vorticity (a smooth bump of positive velocity and negative vorticity, figure 4.2*b*-inset), and continues to propagate upslope as a pulse of dense fluid (figure 4.2*h-j*). These pulses transport dense, lower layer fluid upslope (figure 4.5*d, e*) above its resting height. This role of BBL dynamics in the formation of the ISWs of elevation was previously identified in Xu & Stastna (2020), where the ability of a separation bubble to form in the footprint of the ISW of elevation (which requires an adverse background current) is due to the residual current induced by the leading ISW of depression (figure 4.2*a-c*).

As the rear face of the first pulse clears the trough of the long wave, a second pulse is formed at the rear face in the same process (figure 4.2*c*, inset) and also propagates upslope (figure 4.2*d, i*). Horizontal fluid velocities in the pulse are in the upslope direction (red), which is opposite to flow directly under the leading long wave at the BBL. These results for the surface stratification are qualitatively similar to the thin tanh stratification simulations in this study, as well as prior high resolution simulations of Xu & Stastna (2020) and experimental observations of Ghassemi *et al.* (2022) for the thin tanh stratification. In addition, the dynamics are comparable to an experimental observation of the emergence of fissioning dynamics in the surface stratification (Hartharn-Evans *et al.*, 2022). These similarities are expected, given the similarity of the stratification throughout the lower layer to the thin tanh case, and in particular close to the bottom boundary, where the key dynamics involved in fissioning occur (figure 4.1*b*).

In the surface and thin tanh stratifications, as incident wave amplitude increases, the fission process becomes more unstable. For large incident waves, a global instability (an instability that is strongly coherent in space and time (e.g. Bogucki & Redekopp, 1999; Carr *et al.*, 2008)), forms from the separation bubble. The global instability manifests itself as coherent patches of vorticity which are shed upwards from the separation bubble and follow the wave form as it shoals (figure 4.3*e-g*, blue arrow). This causes turbulent motion

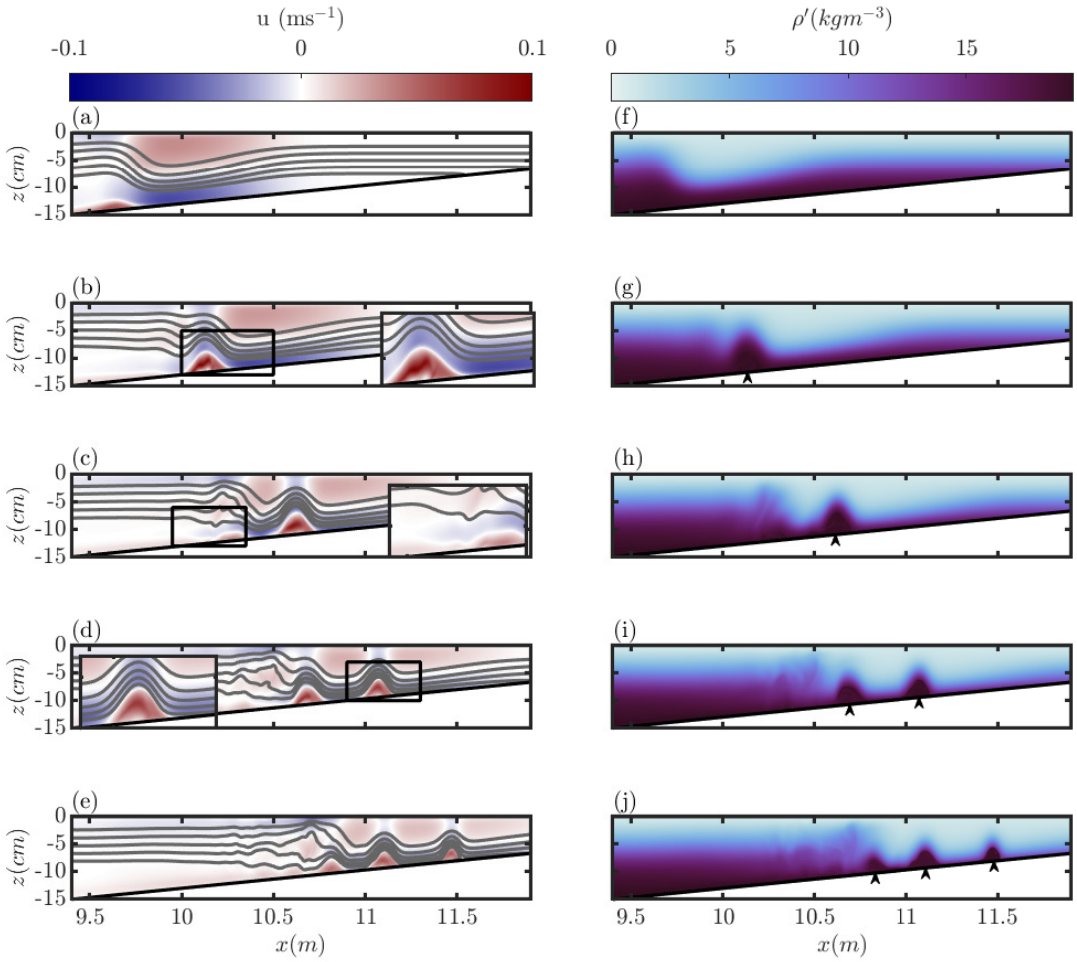


Figure 4.2: Time sequence showing an example fissioning wave in the surface stratification (Exp. Surface-10L). Left panels (*a-e*) showing horizontal velocity, u, overlaid with isopycnals (in black), and right panels (*f-j*) showing density ($\rho' = \rho - \rho_1$). Black arrows indicate the location of the pulse, time interval between images is $\Delta t = 10$ s. Corresponding movie of the experiment is provided in supplementary material as Movie 1

at the pycnocline, and around the pulse (figure 4.3*c-d*). Global instabilities have previously been linked to sediment resuspension and enhanced turbulent kinetic energy under ISWs of depression in field observations (Bogucki *et al.*, 2005). These vortices may not only contribute to loss of energy from the incident ISW of depression, but could also contribute to loss of energy and mass from the pulses (see § 4.3.2, figure 4.9), with large vortices shed from the rear face of the leading pulse (e.g. figure 4.3*c, g*, black arrow).

In the broad tanh stratification, the incident wave approaching the slope is in the form of a train of large amplitude waves, which alternate between waves of elevation and waves

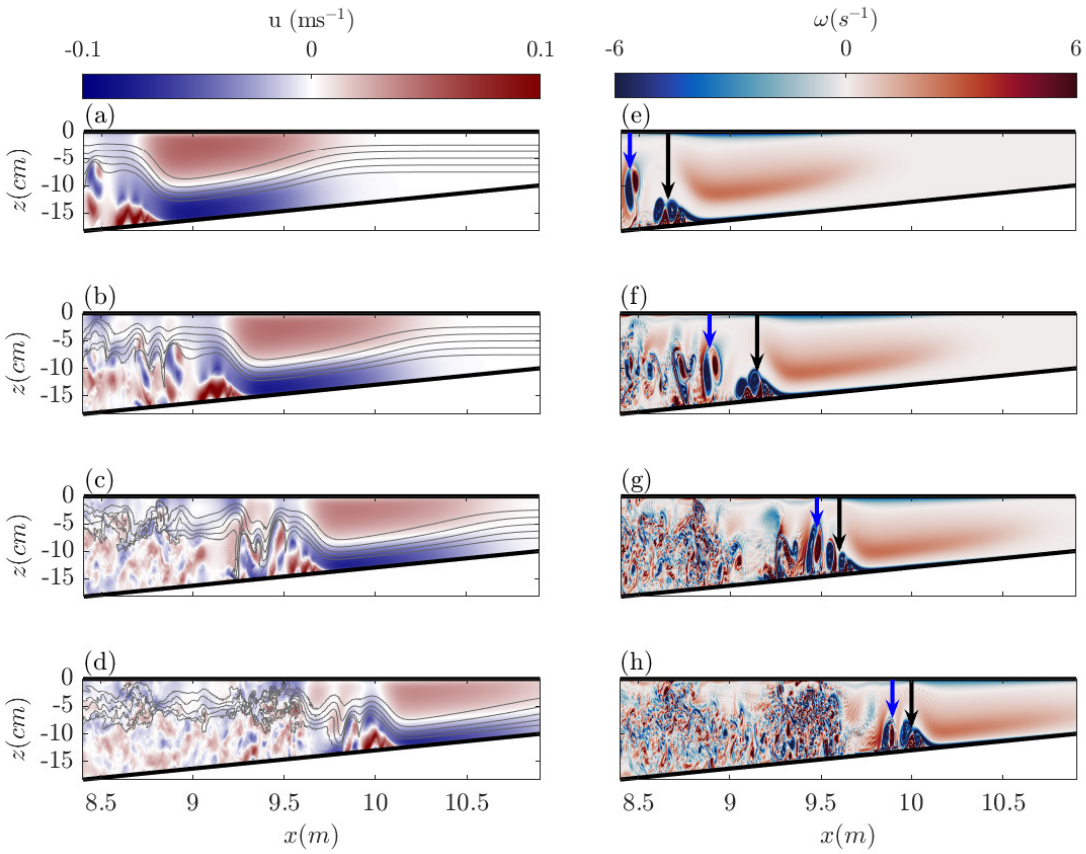


Figure 4.3: Time sequence for a turbulent fissioning wave in the surface stratification (Exp. Surface-30L). Left panels (*a-d*) showing horizontal velocity, u, overlaid with isopycnals (in black), and right panels (*e-h*) showing vorticity. Time interval between images is $\Delta t = 8$ s. In panels (*e-h*), the black and blue arrows indicate the location of the separation bubble and shed vortices, respectively. Corresponding movie of the experiment is provided in supplementary material as Movie 2

of depression (figure 4.4*a, b*), compared to the single incident ISW of depression in the other stratifications (e.g. figure 4.2*a*). As a result, whilst the process of ISW fission is very similar in the surface and thin tanh stratifications (where the pycnocline is vertically offset from the mid-depth of the tank), in the broad tanh stratification, the process of wave fission is considerably different. Whilst separation of the boundary layer still occurs under the rear part of the leading wave of depression, the subsequent flow reversal is enhanced by the wave of elevation directly above it (figure 4.4*b*). In the broad stratification, as the wave propagates upslope, the first incident wave of elevation steepens on both the rear and leading front, until a pulse emerges from this wave, with a velocity structure resembling an ISW of elevation (figure 4.4*c*), leaving behind the leading wave with much reduced amplitude (figure 4.4*d*). In the example simulation, the second and third pulses form

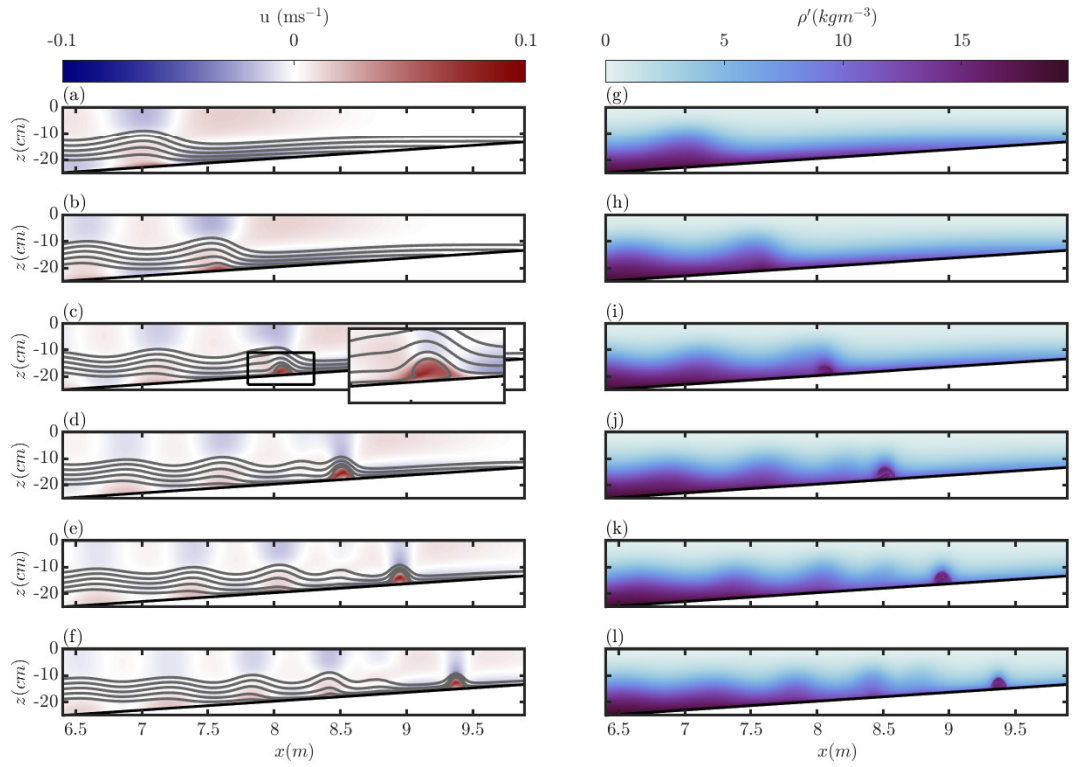


Figure 4.4: Same as figure 4.2, but for a fissioning wave in the broad tanh stratification (Exp. Broad-10L). Time interval between images is $\Delta t = 9$ s. Corresponding movie of the experiment is provided in supplementary material as Movie 3

simultaneously, one emerging from the second approaching wave of elevation, and one emerging from the remnants of the initial incident wave of elevation. Each pulse propagates upslope, bringing a volume of dense fluid far upslope, beyond its undisturbed height (figure 4.4*f*, 4.5*f*). The velocity structure of these pulses resemble closely those in the thin tanh and surface stratifications (figure 4.4*d* c.f. figure 4.2*c*), despite the differences in the incident waves. However, in the broad tanh regime, even the largest pulses (produced by fission of larger amplitude incident waves) remain stable and laminar.

The upslope transport of lower layer fluid may be indicated by the number of dense pulses propagating upslope, along with their size (amplitudes and wavelengths), and so relationships with these quantities are investigated here. For small incident waves, the number of pulses increase as the pycnocline thickness decreases. Meanwhile, as a increases, the number of pulses also increase, due to more energy being available to produce these waves (figure 4.6). However, as a passes the point at which pulses become unstable, the number of pulses produced rapidly decrease with increasing a, as increasing energy is lost

to turbulent mixing and dissipation (figure 4.3). As the leading order control on upslope fluid transport, the number of pulses is affected by both incident amplitude and by the stratification. Upslope fluid transport will also be indicated by the amplitude (a_p) and width (λ_p) of the pulses (figure 4.7). Across all three stratifications, the maximum wave amplitude of the first pulse is directly proportional to the incident wave amplitude (figure 4.7*a*), and this relationship is very similar between stratifications, with the surface stratification producing marginally smaller amplitude pulses. For the broad tanh stratification, the pulse amplitude can be described as $a_p = 0.812a + 0.0087$, whilst for the surface and thin stratifications, the pulse amplitude is $a_p = 0.900a - 0.0038$ and $a_p = 0.9389a + 0.0046$ respectively. Figure 4.9 (*a-c*) shows the role of this relationship, that non-dimensionalised pulse amplitude (a_p/a) in the broad tanh stratification is lower for larger waves in the broad tanh stratification, whilst in the other stratifications, this a_p/a is very similar between simulations. Similar relationships exist between incident wave amplitude and pulse width, λ_p (figure 4.7*c*), which show increasing pulse width with wave amplitude, and also with pulse amplitude a_p. λ_p is larger for the waves in the broad tanh stratification, likely due to small non-linearity parameters in this stratification, but indicative of increased (initial) fluid transport for those waves.

4.3.2. *Pulse Evolution and Degeneration*

Upslope fluid transport in all stratifications is dominated by the passage of dense pulses, which present as red curves (upslope flow) across figure 4.5 (*a-c*) interspersed with slower downslope (blue) regions. Each pulse transports a new parcel of dense fluid upslope, although the volume transported in each decreases (figure 4.5*d-f*). The presence of smaller-scale flow features at higher incident wavelengths is also reflected in the upslope fluid transport signal (figure 4.5).

Leading pulse propagation speed (at the time when a_p is maximum), c_p, appears to scale with a_p (figure 4.7*e*), until (for the surface and thin tanh stratifications) the transition to the more turbulent/unstable regime reduces the propagation speed of the pulse. The negative relationship between c and c_p in the broad tanh stratification (figure 4.7*d*) is explained by the fact that in this stratification, wave speed decreases as a increases. As such, higher c represent smaller amplitude incident waves, which in turn produce smaller amplitude pulses (a_p) (figure 4.7*a*). Therefore, it appears that pulse velocity is more closely determined by a_p (indicating pulses propagate as ISWs of elevation) than by their initial velocity (c). Furthermore, figure 4.7 (*d*) shows that the actual wave propagation speed (c) is slower than the linear long wave speed for the broad tanh stratification, indicating that

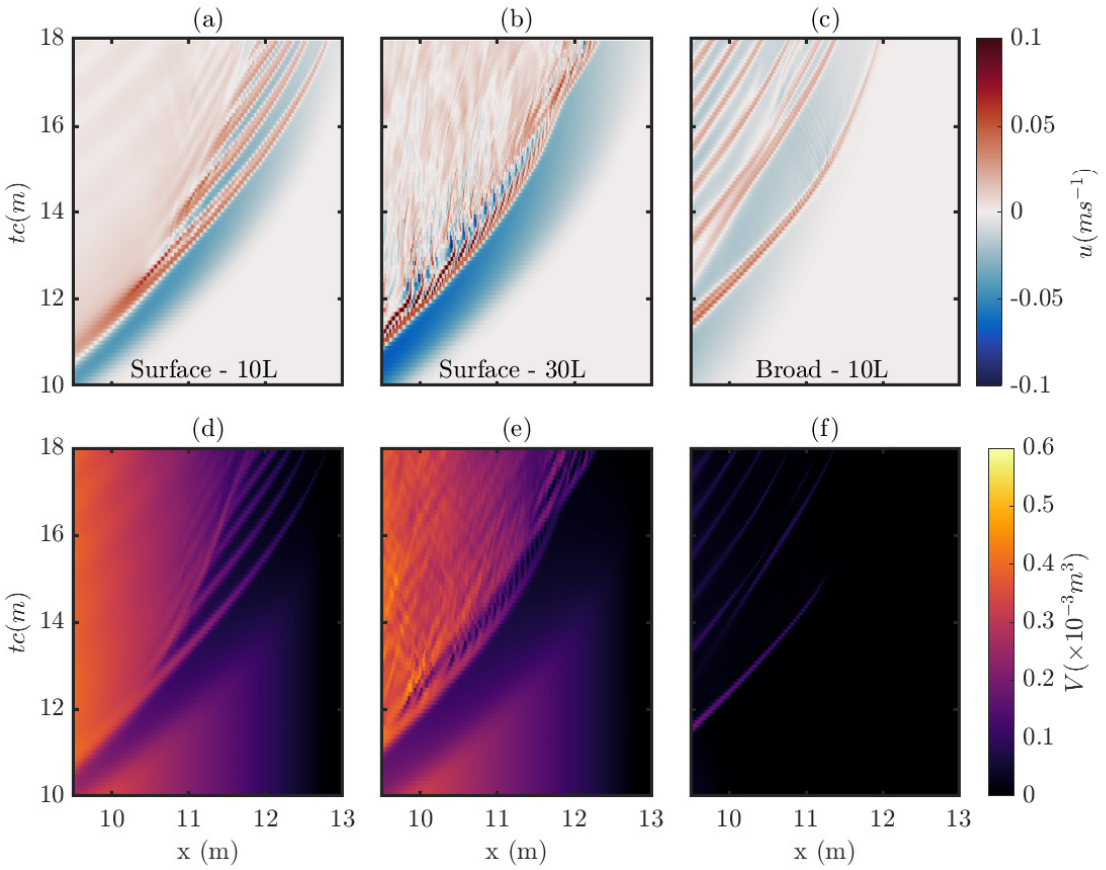


Figure 4.5: Hovmoller plots of near-bed horizontal velocity (*a-c*) and volume of fluid under the $\rho = \rho_1 + \Delta\rho/2$ contour, V, (*d-f*) for the three waves shown in figures 4.2 (left), 4.3 (centre) and 4.4 (right). Time, t is normalised by the wave speed, c. Note the x-scale differs to that used in figures 4.2,4.3 and 4.4 in order to observe longer time and spatial scales required to capture the evolution of the pulses.

waves in this stratification are not ISWs, in part responsible for the different process of pulse formation in this stratification.

As the pulses form, they are initially symmetrical, (figure 4.2*b* - inset), however as they propagate upslope, the front face steepens, and the rear face extends (figures 4.2*d, e, j*, 4.8). This same steepening was previously observed in the thin tanh stratification (Xu *et al.*, 2016). During this process, pulses of dense fluid are carried upslope beyond the undisturbed height (figure 4.2*i, j*). After formation, the pulses in all stratifications slow down, and lose both amplitude and width (figure 4.9). As previously observed by Ghassemi *et al.* (2022), the pulse amplitude decreases linearly across all stratification types (figure 4.9*a-c*). Within stratifications, the rates of the degeneration are very similar between different sized waves 4.9*d-f*), but vary between stratifications, with the amplitude of pulses

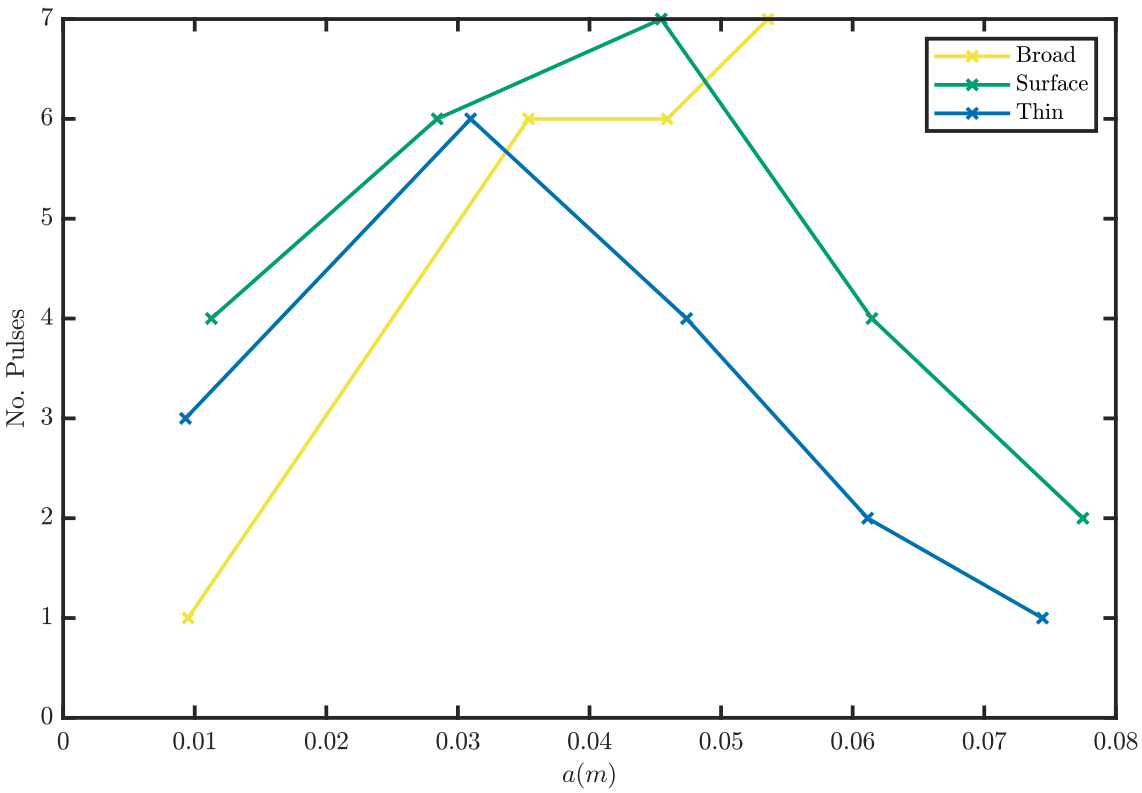


Figure 4.6: Number of pulses identified from an incident wave during the simulation as a function of wave amplitude, a, for each of the three stratification types.

in the broad tanh stratification decreasing faster. Likewise, the pulses lose amplitude and wavelength at similar rates. Whilst the pulses propagate upslope, there is a substantial quasi-trapped core (red areas) but the core is asymmetric in the along slope direction, with clear 'leakiness' (blue) near the back where fluid is continually lost from the rear of the pulse (figure 4.8). This can be seen as the overall volume of dense fluid in the pulse decreasing upslope and through time (figure 4.5*d-f*).

4.4. Discussion & Conclusion

Here, fission of ISWs in stratifications deviating from a three-layer approximation has been investigated, for the first time in detail using a numerical model at the laboratory scale, which allows a full investigation into the time evolution of these structures which is difficult to achieve with field observations. Similar stratifications to those studied here have been investigated in the field (e.g. Richards *et al.*, 2013), highlighting the need for idealised studies to consider different stratifications to simply the three-layer stratification in order to fully understand the dynamics. However, despite the differences between stratification types

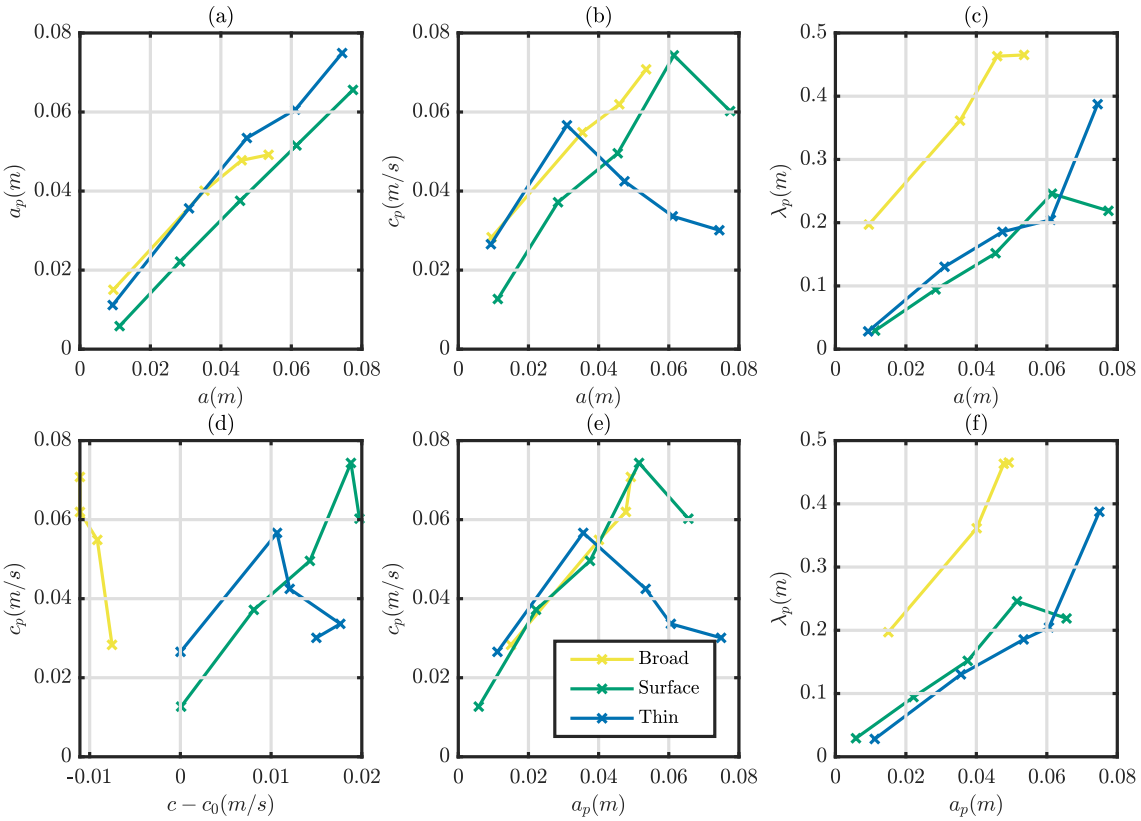


Figure 4.7: Plots to show the relationship between wave amplitude, wavelength, and speed, and the same properties of the leading pulse at the time at which pulse amplitude is maximum for each of the three stratifications. (*a*) Wave Amplitude, a, against Pulse Amplitude, a_p; *b*) a against pulse speed, c_p; (*c*) a against pulse width (wavelength) λ_p; (*d*) Wave speed - linear long wave speed (calculated from KdV solutions), $c - c_0$ against c_p; (*e*) a_p against c_p; and (*f*) a_p against λ_p.

for other wave breaking types, the transition between thin tanh and surface stratifications is found to have minimal impact on the fissioning of ISWs, in terms of pulse formation, structure and evolution. Additionally, the process by which pulses are formed by fission in numerical simulations in this study both for the surface and thin tanh stratifications are very similar to previously published numerical (Xu & Stastna, 2020) and experimental works in the thin tanh stratification (Ghassemi *et al.*, 2022). Shoaling waves in the broad tanh stratification undergo a considerably different process of fissioning, emerging instead from an elevation wave, and remained non-turbulent at all incident wave amplitudes, despite the structure of the pulse being similar to in the other stratifications.

Whilst the use of 3-D simulations in studies of internal wave shoaling would be desirable in order to resolve lobe-cleft instabilities and lateral variability, such simulations over this length of wave tank are too computationally expensive. Furthermore, past studies have

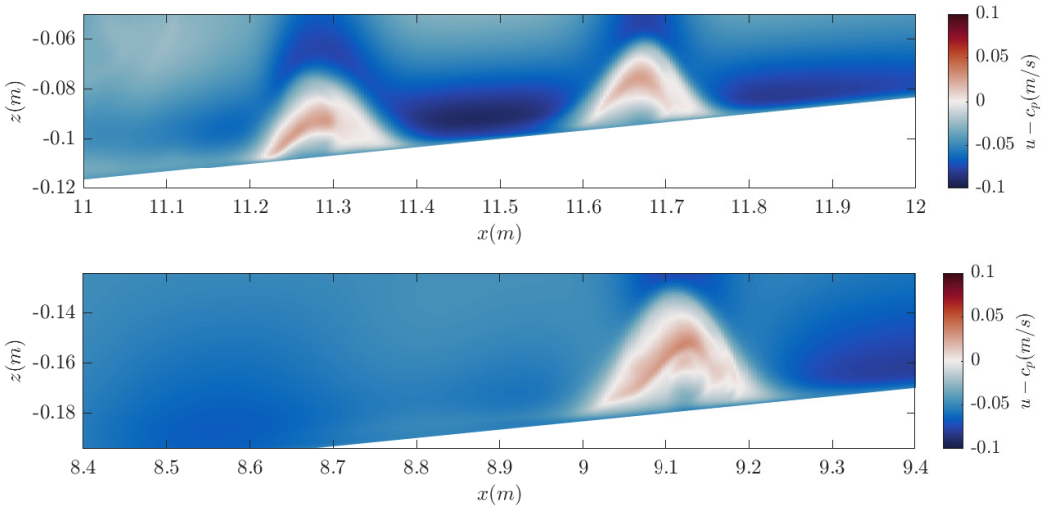


Figure 4.8: Plot of flow velocity u relative to the pulse propagation speed (c_p) for the pulse shown in figure 4.2 (top) at the same time as figure 4.2*d*, and 4.4 (bottom) at same time as figure 4.4*e*.

highlighted the qualitative similarity of wave breaking in 2-D and 3-D simulations during the phases of shoaling studied here (the approach to the slope, breaking event, and start of up-slope propagation) (Arthur & Fringer, 2014; Xu *et al.*, 2019; Hartharn-Evans *et al.*, 2022). Following on from these studies, it is expected that lateral variability and instabilities (which form only in 3-D simulations) would impact on the degeneration process of the pulses formed by fission.

Pulses formed by fission (in all stratification types) are single ISW-like pulses which propagate upslope, in comparison to boluses produced by other wave shoaling types (such as collapsing or surging) as studied by Allshouse & Swinney (2020) and Vieira & Allshouse (2020), which exist as a parcel of fluid which travels in a manner more similar to a gravity current. In particular, Vieira & Allshouse (2020) identified three bolus structures (ball, hook and slivers), which do not appear to correspond to the pulses produced by fission, indicating such features are dynamically different based on the process of shoaling that formed them.

Numerous field observations have detailed the process by which ISWs of depression fission into pulses propagating upslope due to the polarity reversal process (e.g. Orr & Mignerey, 2003; Shroyer *et al.*, 2009). Orr & Mignerey (2003) detail the initial lengthening of the front face of the leading wave (as in figure 4.2*a*), followed by the formation of waves of elevation which advance through the rear of the leading wave of depression (as in figure 4.2*b,c*), in a stratification that is approximated by the surface stratification (see their figure

8). Comparisons between ADCP velocity fields of the pulses propagating upslope (their figure 12) and figure 4.2*d*, show striking similarity in the wave and pulse-induced velocity fields. The present observations are also in strong agreement with the observations of Shroyer *et al.* (2009) as the incident waves pass through the turning point and become internal solitary waves of elevation. The evolution of these pulses has also been documented in the field by Richards *et al.* (2013) and Jones *et al.* (2020). Velocity structures shown by Richards *et al.* (2013) figure 9 are in good agreement with the trains of pulses seen in this study, whilst Jones *et al.* (2020) report very active cores within the pulses, in contrast to this study. Richards *et al.* (2013) reported upslope advection by the wave of turbulent fluid locally produced by fissioning internal waves. In this study, instabilities displayed by larger incident waves upon fissioning in the surface and thin tanh stratifications, and in particular, the vortices shed from the rear of the pulse, also leave behind turbulent fluid, which may form part of the process observed by Richards *et al.* (2013), although difference in scales (with a factor 50-100 difference in Reynolds number) impairs these comparisons. Such a process may be an important source of energy for mixing and dissipation along the slope

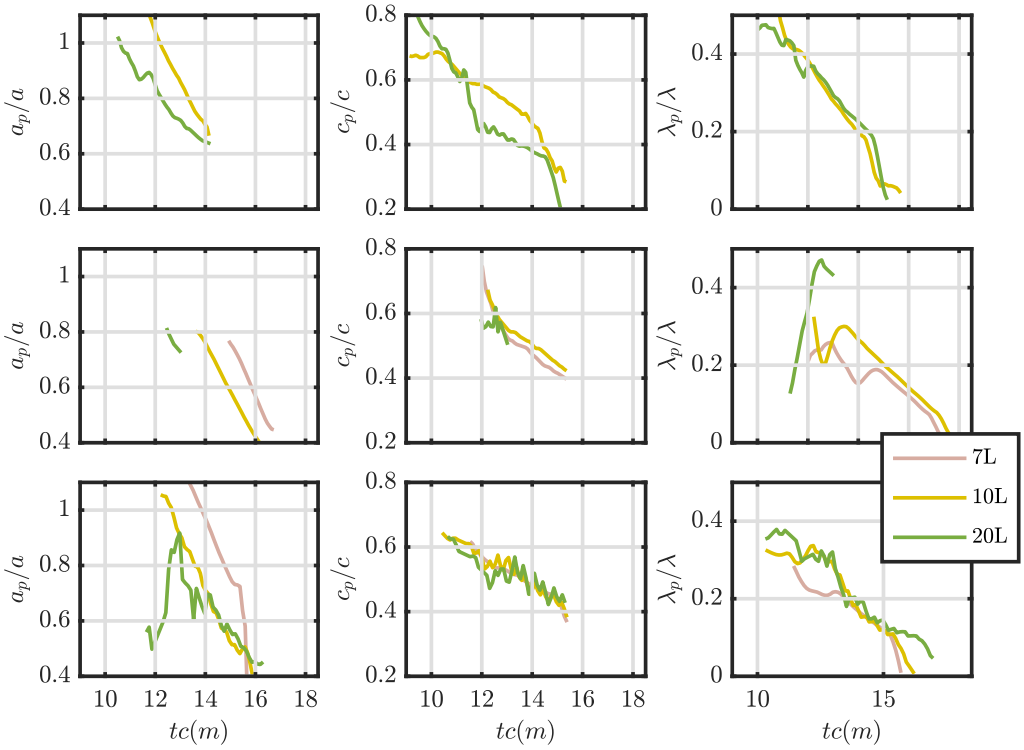


Figure 4.9: Time-evolution of pulse properties a_p (left) c_p (centre) and λ_p (right), each non-dimensionalised by their equivalent wave property (a, c, and λ_w respectively) for the broad tanh (top), surface (middle) and thin tanh (bottom) stratifications.

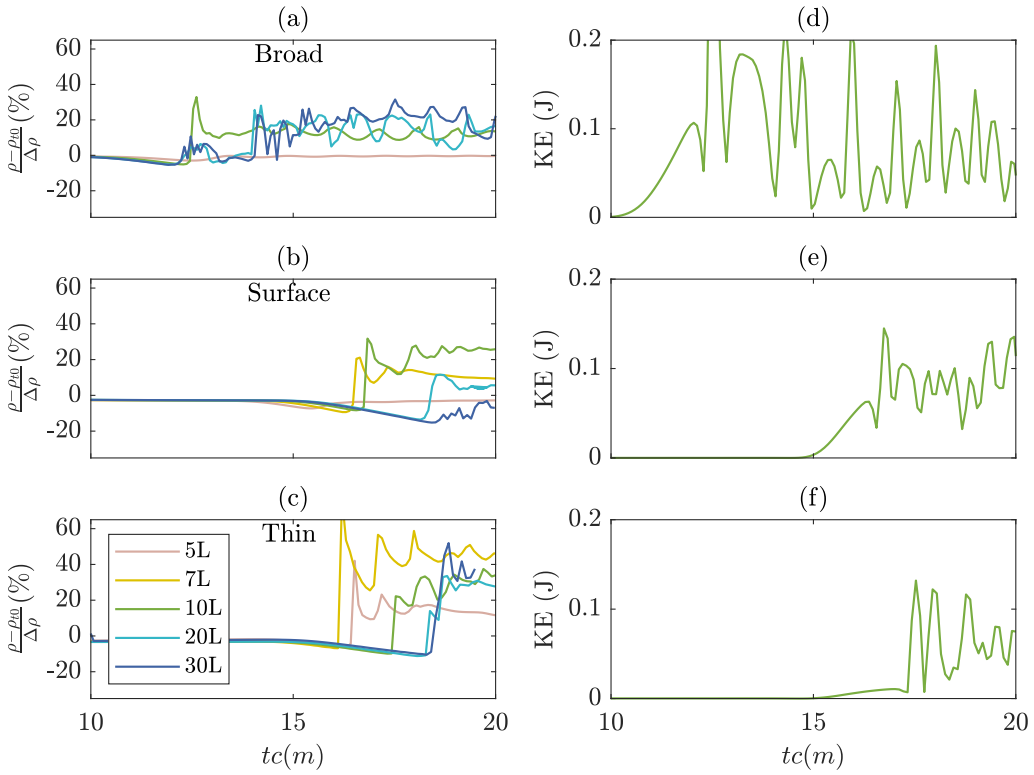


Figure 4.10: Time series of normalised density (left) and kinetic energy (right) at the bottom for the point where the slope intersects with the pycnocline location (left); Shown for each of the stratifications, broad tanh (top), surface (middle) and thin tanh (bottom), with time normalised by wave speed, c. For clarity, only the 10L wave is shown for the KE plots

and shelf.

Confirming that degeneration of pulses remains linear in three different stratifications is indicative that prior results (e.g. Ghassemi *et al.*, 2022) will hold true in a range of real-world situations. As this degeneration occurs by the loss of fluid from the rear of the pulse, the rate at which it occurs has implications for the transport of bottom waters onto the shelf, which in turn, may impact on the benthic ecology. The three-dimensional structure of fissioning waves, in particular lobe-cleft instability was identified by Ghassemi *et al.* (2022), and would alter the mixing of the pulse with surrounding fluid.

Whilst the pulse structure and evolution is similar between the stratifications investigated in this study, the impact of the process of fissioning on ecosystems is still dependent on stratification. Variability in the number of boluses produced by waves in different stratifications (figure 4.6) is an important factor in upslope transport of fluid, and internal-wave derived energy. The time evolution of density (presented here as a 'normalised density') at the bottom boundary for a fixed slope location is used to indicate transport

of lower-layer water, and represent measurements by a virtual mooring (similar to the near-bottom temperature measurements in Richards *et al.* (2013), their figure 9), which in an oceanographic setting is typically cold and nutrient rich. Whilst the upslope transport is not permanent, and the dense fluid moves back downslope (figure 4.5), variability in temperature has previously been identified as an important factor for the health of benthic ecosystems Reid *et al.* (2019). In all stratifications, an initial decrease in normalised density is observed as the incoming wave draws down fluid from the upper layer (figure 4.10). However, the formation of pulses brings dense (lower-layer) water upslope, in doing so modifying the water properties at that location. The overall change in density at the lower boundary is greatest for the largest amplitude waves (figure 4.10*a-c*). Between stratifications, the total change in density (relative $\delta\rho$) increases between broad tanh to surface, and further to thin tanh stratification, due to lower density gradients $\left(\frac{\delta\rho}{\delta z}\right)$. These pulses bring kinetic energy upslope, each pulse associated with a peak in the KE on the slope (figure 4.10). The impact of this is greatest for the broad stratification (figure 4.10*d*).

The fission of internal solitary waves over gentle, and crucially, geophysically realistic slopes forms coherent pulses of dense fluid, which in other contexts are also referred to as cold pulses, or boluses. Such pulses of fluid can be a significant source of nutrients and relief from excess heat to benthic ecosystems (Green *et al.*, 2019; Reid *et al.*, 2019), and understanding the role of stratification (which varies both spatially and seasonally) on the behaviour of these pulses is therefore important. Although the form of the pulse produced by fission is similar across three very different stratifications studied here, for the broad stratification, the pulse formation process does vary. Pulses in the broad stratification propagate slower, and disintegrate faster than in other stratifications. Whilst idealised studies remove the potential impacts of other ocean processes (e.g. the surface tide or eddies), here we show that in such idealised conditions unstable fissioning can also be found, producing pulses of turbulent fluid and advecting this turbulent fluid upslope, inducing mixing and dissipation further upslope than the energy source.

Supplementary information. Supplementary movies for simulations shown in figures 4.2, 4.3 and 4.4 are available online.

Data Availability Statement. All model data for this chapter is available at https://doi.org/10.25405/data.ncl.c.5791673. The SPINS model and processing code is available via https://wiki.math.uwaterloo.ca/fluidswiki/index.php?title=SPINS_User_Guide

Chapter 4

References

Aghsaee, P., Boegman, L. & Lamb, K. G. 2010 Breaking of shoaling internal solitary waves. *Journal of Fluid Mechanics* **659**, 289–317, https://doi.org/10.1017/S002211201000248X.

Allshouse, M. R. & Swinney, H. L. 2020 Dependence of Internal Wave Bolus Transport on Pycnocline Thickness. *Geophysical Research Letters* **47** (14), e2020GL086952, https://doi.org/10.1029/2020GL086952.

Arthur, R. S. & Fringer, O. B. 2014 The dynamics of breaking internal solitary waves on slopes. *Journal of Fluid Mechanics* **761** (2), 360–398, https://doi.org/10.1017/jfm.2014.641.

Arthur, R. S., Koseff, J. R. & Fringer, O. B. 2017 Local versus volume-integrated turbulence and mixing in breaking internal waves on slopes. *Journal of Fluid Mechanics* **815**, 169–198, https://doi.org/10.1017/jfm.2017.36.

Boegman, L., Ivey, G. N. & Imberger, J. 2005 The degeneration of internal waves in lakes with sloping topography. *Limnology and Oceanography* **50** (5), 1620–1637, https://doi.org/10.4319/lo.2005.50.5.1620.

Boegman, L. & Stastna, M. 2019 Sediment Resuspension and Transport by Internal Solitary Waves. *Annual Review of Fluid Mechanics* **51** (1), 129–154, https://doi.org/10.1146/annurev-fluid-122316-045049.

Bogucki, D. J. & Redekopp, L. G. 1999 A mechanism for sediment resuspension by internal solitary waves. *Geophysical Research Letters* **26** (9), 1317–1320, https://doi.org/10.1029/1999GL900234.

Bogucki, D. J., Redekopp, L. G. & Barth, J. 2005 Internal solitary waves in the Coastal Mixing and Optics 1996 experiment: Multimodal structure and resuspension. *Journal of Geophysical Research C: Oceans* **110** (2), 1–19, https://doi.org/10.1029/2003JC002253.

Cacchione, D. A., Pratson, L. F. & Ogston, A. S. 2002 The Shaping of Continental Slopes by Internal Tides. *Science* **296** (5568), 724–727, https://doi.org/10.1126/science.1069803.

Carr, M. & Davies, P. A. 2006 The motion of an internal solitary wave of depression over a fixed bottom boundary in a shallow, two-layer fluid. *Physics of Fluids* **18** (1), 016601, https://doi.org/10.1063/1.2162033.

Carr, M., Fructus, D., Grue, J., Jensen, A. & Davies, P. A. 2008 Convectively induced shear instability in large amplitude internal solitary waves. *Physics of Fluids* **20** (12), 126601, https://doi.org/10.1063/1.3030947.

da Silva, J. C., Buijsman, M. C. & Magalhaes, J. M. 2015 Internal waves on the upstream side of a large sill of the Mascarene Ridge: A comprehensive view of their generation mechanisms and evolution. *Deep-Sea Research Part I: Oceanographic Research Papers* **99**, 87–104, https://doi.org/10.1016/j.dsr.2015.01.002.

Ghassemi, A., Zahedi, S. & Boegman, L. 2022 Bolus formation from fission of nonlinear internal waves over a mild slope. *Journal of Fluid Mechanics* **932**, A50, https://doi.org/10.1017/jfm.2021.1033.

Green, R. H., Jones, N. L., Rayson, M. D., Lowe, R. J., Bluteau, C. E. & Ivey, G. N. 2019 Nutrient fluxes into an isolated coral reef atoll by tidally driven internal bores. *Limnology and Oceanography* **64** (2), 461–473, https://doi.org/10.1002/lno.11051.

Grue, J. 2005 Generation, propagation, and breaking of internal solitary waves. *Chaos* **15** (3), 037110, https://doi.org/10.1063/1.2047907.

Grue, J., Jensen, A., Rusas, P. & Sveen, J. K. 1999 Properties of large-amplitude internal waves. *Journal of Fluid Mechanics* **380**, 257–278, https://doi.org/10.1017/S0022112098003528.

Hartharn-Evans, S. G., Carr, M., Stastna, M. & Davies, P. A. 2022 Stratification effects on shoaling internal solitary waves. *Journal of Fluid Mechanics* **933** (A19), https://doi.org/10.1017/jfm.2021.1049.

Helfrich, K. R. & Melville, W. K. 2006 Long nonlinear internal waves. *Annual Review of Fluid Mechanics* **38** (1), 395–425, https://doi.org/10.1146/annurev.fluid.38.050304.092129.

Huang, X., Chen, Z., Zhao, W., Zhang, Z., Zhou, C., Yang, Q. & Tian, J. 2016 An extreme internal solitary wave event observed in the northern South China Sea. *Scientific Reports* **6** (1), 30041, https://doi.org/10.1038/srep30041.

Jones, N. L., Ivey, G. N., Rayson, M. D. & Kelly, S. M. 2020 Mixing Driven by Breaking Nonlinear Internal Waves. *Geophysical Research Letters* **47** (19), e2020GL089591, https://doi.org/10.1029/2020GL089591.

Lamb, K. G. 2014 Internal Wave Breaking and Dissipation Mechanisms on the Continental Slope/Shelf. *Annual Review of Fluid Mechanics* **46** (1), 231–254, https://doi.org/10.1146/annurev-fluid-011212-140701.

Lamb, K. G. & Nguyen, V. T. 2009 Calculating Energy Flux in Internal Solitary Waves with an Application to Reflectance. *Journal of Physical Oceanography* **39** (3), 559–580, https://doi.org/10.1175/2008JPO3882.1.

Maderich, V. S., Van Heijst, G. J. & Brandt, A. 2001 Laboratory experiments on intrusive flows and internal waves in a pycnocline. *Journal of Fluid Mechanics* **432**, 285–311, https://doi.org/10.1017/s0022112000003323.

McPhee-Shaw, E. E., Siegel, D. A., Washburn, L., Brzezinski, M. A., Jones, J. L., Leydecker, A. & Melack, J. 2007 Mechanisms for nutrient delivery to the inner shelf: Observations from the Santa Barbara Channel. *Limnology and Oceanography* **52** (5), 1748–1766, https://doi.org/10.4319/lo.2007.52.5.1748.

Michallet, H. & Ivey, G. N. 1999 Experiments on mixing due to internal solitary waves breaking on uniform slopes. *Journal of Geophysical Research: Oceans* **104** (C6), 13467–13477, https://doi.org/10.1029/1999jc900037.

Moum, J. N., Farmer, D. M., Smyth, W. D., Armi, L. & Vagle, S. 2003 Structure and generation of turbulence at interfaces strained by internal solitary waves propagating shoreward over the continental shelf. *Journal of Physical Oceanography* **33** (10), 2093–2112, https://doi.org/10.1175/1520-0485(2003)033¡2093:SAGOTA¿2.0.CO;2.

Moum, J. N., Klymak, J. M., Nash, J. D., Perlin, A. & Smyth, W. D. 2007 Energy Transport by Nonlinear Internal Waves. *Journal of Physical Oceanography* **37** (7), 1968–1988, https://doi.org/10.1175/JPO3094.1.

Nakayama, K., Sato, T., Shimizu, K. & Boegman, L. 2019 Classification of internal solitary wave breaking over a slope. *Physical Review Fluids* **4** (1), 014801, https://doi.org/10.1103/PhysRevFluids.4.014801.

Orr, M. H. & Mignerey, P. C. 2003 Nonlinear internal waves in the South China Sea: Observation of the conversion of depression internal waves to elevation internal waves. *Journal of Geophysical Research* **108** (C3), 3064, https://doi.org/10.1029/2001JC001163.

Rayson, M. D., Jones, N. L. & Ivey, G. N. 2019 Observations of large-amplitude mode-2 nonlinear internal waves on the australian north west shelf. *Journal of Physical Oceanography* **49** (1), 309–328, https://doi.org/10.1175/JPO-D-18-0097.1.

Reid, E. C., DeCarlo, T. M., Cohen, A. L., Wong, G. T., Lentz, S. J., Safaie, A., Hall, A. & Davis, K. A. 2019 Internal waves influence the thermal and nutrient environment on a shallow coral reef. *Limnology and Oceanography* **64** (5), 1949–1965, https://doi.org/10.1002/lno.11162.

Richards, C., Bourgault, D., Galbraith, P. S., Hay, A. & Kelley, D. E. 2013 Measurements of shoaling internal waves and turbulence in an estuary. *Journal of Geophysical Research: Oceans* **118** (1), 273–286, https://doi.org/10.1029/2012JC008154.

Safaie, A., Silbiger, N. J., McClanahan, T. R., Pawlak, G., Barshis, D. J., Hench, J. L., Rogers, J. S., Williams, G. J. & Davis, K. A. 2018 High frequency temperature variability reduces the risk of coral bleaching. *Nature Communications* **9** (1), 1–12, https://doi.org/10.1038/s41467-018-04074-2.

Shroyer, E. L., Moum, J. N. & Nash, J. D. 2009 Observations of polarity reversal in shoaling nonlinear internal waves. *Journal of Physical Oceanography* **39** (3), 691–701, https://doi.org/10.1175/2008JPO3953.1.

Shroyer, E. L., Moum, J. N. & Nash, J. D. 2010 Energy transformations and dissipation of nonlinear internal waves over New Jersey's continental shelf. *Nonlinear Processes in Geophysics* **17** (4), 345–360, https://doi.org/10.5194/npg-17-345-2010.

St Laurent, L., Simmons, H., Tang, T. Y. & Wang, Y. 2011 Turbulent Properties of Internal Waves in the South China Sea. *Oceanography* **24** (4), 78–87, https://doi.org/10.5670/oceanog.2011.96.

Sutherland, B. R., Barrett, K. J. & Ivey, G. N. 2013 Shoaling internal solitary waves. *Journal of Geophysical Research: Oceans* **118** (9), 4111–4124, https://doi.org/10.1002/jgrc.20291.

Vieira, G. S. & Allshouse, M. R. 2020 Internal wave boluses as coherent structures in a continuously stratified fluid. *Journal of Fluid Mechanics* **885**, A35, https://doi.org/10.1017/jfm.2019.993.

Vlasenko, V., Stashchuk, N. & Hutter, K. 2005 *Baroclinic Tides*. Cambridge: Cambridge University Press.

Wallace, B. C. & Wilkinson, D. L. 1988 Run-up of internal waves on a gentle slope in a two-layered system. *Journal of Fluid Mechanics* **191**, 419–442, https://doi.org/10.1017/S0022112088001636.

Walter, R. K. & Phelan, P. J. 2016 Internal bore seasonality and tidal pumping of subthermocline waters at the head of the Monterey submarine canyon. *Continental Shelf Research* **116**, 42–53, https://doi.org/10.1016/j.csr.2016.01.015.

Xu, C. & Stastna, M. 2020 Instability and cross-boundary-layer transport by shoaling internal waves over realistic slopes. *Journal of Fluid Mechanics* **895**, R6, https://doi.org/10.1017/jfm.2020.389.

Xu, C., Stastna, M. & Deepwell, D. 2019 Spontaneous instability in internal solitary-like waves. *Physical Review Fluids* **4** (1), 014805, https://doi.org/10.1103/PhysRevFluids.4.014805.

Xu, C., Subich, C. & Stastna, M. 2016 Numerical simulations of shoaling internal solitary waves of elevation. *Physics of Fluids* **28** (7), 76601, https://doi.org/10.1063/1.4958899.

CHAPTER 5

A new approach to understanding fluid mixing in process-study models of stratified fluids

5.1. Introduction

At the largest scales, the ocean is stably stratified, typically with warmer, less dense water overlaying cold, more dense water (although in many locations, such as the polar regions, the stratification is salinity dominated instead and warm water can underlay cold). Similar density stratifications also exist across other geophysical settings, such as lakes, estuaries, and the atmosphere. Thus, the process by which the layers mix is of great interest to a range of disciplines, from biological scientists interested in the distribution of nutrients, plankton, and sediment, to physical oceanographers interested in the global (and local) distribution of heat and buoyancy. Mixing primarily occurs due to flows that induce small-scale motions that stir the fluid and stretch density interfaces. Across the increased surface area, molecular diffusion is effectively sped up in the process of diapycnal mixing (Salmon, 1998). Since they have small scales, mixing processes occur below the grid scale of many oceanic and atmospheric models. Process-scale numerical modelling is thus a useful tool to better understand the routes to mixing, with a view to improving the way that climate-scale and regional models parameterise such processes through turbulent or eddy diffusivity. Large-scale models may use sophisticated parameterisations of eddy diffusivity, dependent on local velocity shear and buoyancy, and examples include the well known $k - \varepsilon$ model for Reynolds-averaged Navier–Stokes (RANS) (Pope, 2000), and the Smagorinsky model for large eddy simulations (LES) (Wyngaard, 2010).

The mechanical process of stirring is a geometric deformation of fluids and does not in

itself imply irreversible mixing. However, the presence of a diffusion term in the equations of motion (equation 2.4) allows mixing (where the concentration of a tracer, or density, of a given fluid parcel is modified) to occur across density gradients that are stretched by stirring. Commonly, mixing in numerical simulations is quantified according to the framework set out by Winters *et al.* (1995). Under this framework, energy is partitioned into various components; kinetic energy (KE), background potential energy (BPE), available potential energy (APE) and internal energy (IE). APE is the potential energy available to be released to kinetic energy and is computed by first adiabatically redistributing the density field to find the lowest possible energy state (this state in turn defines the BPE). The conversion between APE and BPE is considered the energy used to conduct irreversible diapycnal mixing, and is therefore an important concept. Crucially, calculating APE involves sorting the density field in order to identify the lowest energy state achievable by adiabatic redistribution (or under certain formulations, a far-field reference density profile (Lamb, 2008)). Other formulations for measuring mixing have been suggested, such as computing the Thorpe length scales (Thorpe, 1977), which have been applied to both laboratory experiments and numerical simulations (e.g. Carr *et al.*, 2017).

The most widely used APE framework is valuable due to its uses in comparisons to the field and parameterisation in larger-scale models. However, the sorting process by Winters *et al.* (1995) does little to inform us of interesting questions around where and how this mixing is taking place, or what happens to the mixed fluid (Moum *et al.*, 2003; Carr *et al.*, 2017). Exploration of the spatial distribution BPE density, and APE density, or local APE can give us some further information about the flow (e.g. Lamb, 2008; Scotti & White, 2014), but these are rarely considered in comparison with domain integrated, or bulk values. This is in part due to the complexity of calculating these local values.

The diapycnal mixing of passive tracers was considered from a different point of view by Penney *et al.* (2020) using simple two-variable probability density histograms showing the statistical relationship between a tracer and density. Penney *et al* referred to their primary tool as "weighted density-tracer scatter plots"; since we propose a methodology that is more general, we will adopt the acronym USP, for user-controlled scatter plot. The user specifies the two variables chosen, and the manner in which their ranges are set in order to focus on dynamical phenomena of interest. The pair of fields studied in detail in Penney *et al.* (2020) is a subset of our more general methodology.

To demonstrate the efficacy of our methodology we choose two application areas, one in which the geometry is complex (shoaling internal waves) and one in which the equation of state is nonlinear (in water below the 4 °C temperature of maximum density). Grace *et al.*

(2021) simulated the evolution of gravity currents in water below the 4 °C temperature of maximum density. They demonstrated profound asymmetries between cold gravity currents intruding into warm water and warm gravity currents intruding into cold water. They labelled this temperature regime the "weak cabbeling" regime, because two water parcels mixed together yield a different density than the average density of the individual parcels. Grace *et al* found histograms of a single fluid quantity (e.g. temperature) to be a useful analysis tool in characterising the gravity currents.

Here, we bring the methods of Penney *et al.* (2020) and Grace *et al.* (2021) together, investigating the utility of selecting fluid parcels based on the combination of two quantities, for example, asking where the density is within one range, and the kinetic energy (KE) exceeds a threshold value simultaneously. An interactive Matlab tool is developed and applied to two example flows which have previously been studied extensively. Firstly shoaling nonlinear Internal Solitary Waves (ISWs), which result from such waves propagating upslope are studied, a process investigated in numerous process studies for its role in transport and mixing of heat, nutrients, and sediment (e.g. Michallet & Ivey, 1999; Aghsaee *et al.*, 2010; Arthur *et al.*, 2017; Sutherland *et al.*, 2013; Hartharn-Evans *et al.*, 2022). Secondly, the stratified shear flow and its Kelvin-Helmholtz instability, a feature explored in many studies relating to mixing due to its fundamental importance (e.g. Winters *et al.*, 1995; Caulfield & Peltier, 2000; Peltier & Caulfield, 2003; Caulfield, 2021), are applied here in three dimensions to a cold-water setting, where the nonlinear equation of state alters the dynamics. Such features have been observed in a range of environmental settings, from enhancing mixing by ISWs on the Oregon Shelf (Moum *et al.*, 2003), deepening the Arctic Ocean surface mixed layer (Lincoln *et al.*, 2016), and affecting the highly stratified Connecticut River estuary (Geyer *et al.*, 2010).

The joint probability histograms, and specifically the change in their form over time allow identification of fluid quantities that are interesting. Additionally, the method allows us to determine the physical region of fluid where these quantitatively unambiguously identified "interesting things" are happening. Instead of the understanding of how much bulk mixing is taking place (as provided by the sorting algorithm), we can understand where, when and perhaps how mixing is taking place. Using this method of selecting regions based on user-selected paired histograms (USPs) also has advantages over the Winters *et al.* (1995) sorting algorithm in that it is unaffected by small perturbations inherent to numerical methods (e.g. due to uncertainties in bathymetry, or general under resolution), and as there is no assumption of mass (or energy) conservation inside the region to be analysed, the spatial domain for analysis can be restricted to just the physical area we are

interested in.

This chapter is organised as follows. In §5.2.1, the USP methodology is introduced. In §5.2.2 the numerical model SPINS is introduced, with specific model setups for the fissioning ISW and cold shear flows introduced in §§5.2.2 and 5.2.2 respectively. The method is then applied to identify the causes of different mixing regimes according to wave breaking types in §5.3.1, followed by application of the method to understand diapycnal mixing in the cold shear instability in §5.3.2. The results conclude with the introduction of a passive, rather than active tracer to the cold shear instability in §5.3.3, identifying the differences between active and passive tracers with differing diffusivity.

5.2. Methods

5.2.1. *Paired Histograms*

This study employs pseudocolour plots showing the characteristics of fluid parcels in a two-dimensional (2-D) space where the two dimensions, instead of being spatial dimensions, are chosen to be fluid characteristics, similar to the weighted density-tracer scatter plots in Penney *et al.* (2020). Each USP shows the characteristics of fluid parcels in terms of this redefined 2-D space, with two fluid properties as their coordinates, and the colour showing the proportion of the fluid within each discretised coordinate bin. The change of a scatter plot, reminiscent of temperature-salinity plots widely used to trace water masses in oceanography (e.g. Helland-Hansen, 1916; Imasato *et al.*, 1993), to the paired histogram by discretising into bins and applying weightings is shown in figure 5.1 and described in the following.

Following the method of Penney *et al.* (2020), the algorithm employed is applied as follows. For two variables ϕ and θ (which could for example represent density and kinetic energy), the domains are subdivided into N_ϕ and N_θ bins, with sizes:

$$\delta\phi = \frac{\phi_{max} - \phi_{min}}{N_\phi}, \tag{5.1}$$

$$\delta\theta = \frac{\theta_{max} - \theta_{min}}{N_\theta} \tag{5.2}$$

For each grid cell, the nearest bin centre is identified:

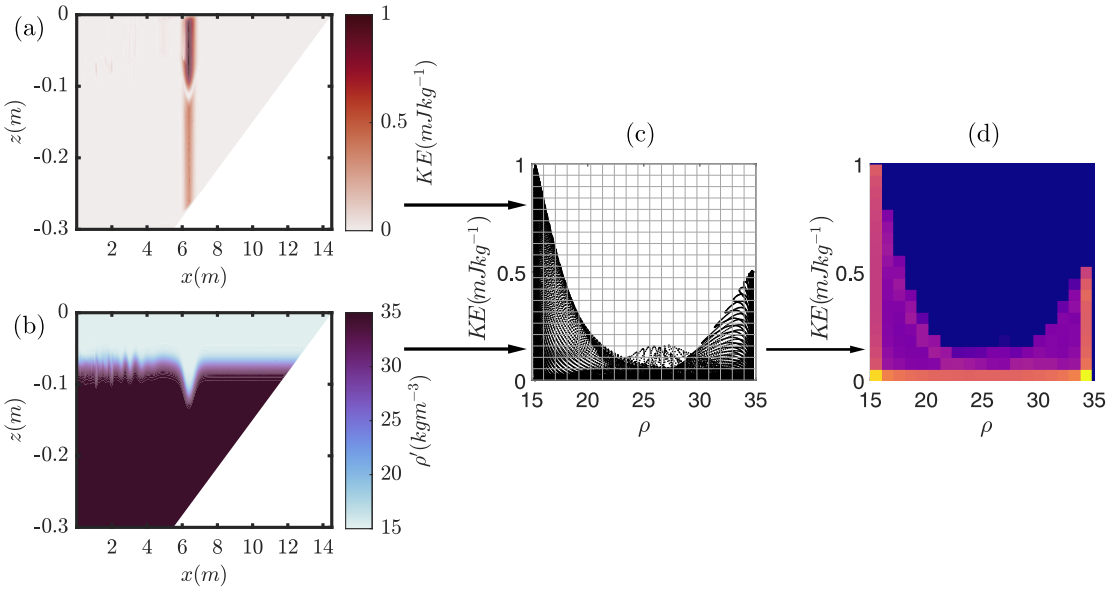


Figure 5.1: Schematic of the creation of USP diagrams. The combination of two fluid properties (left) is represented in variable-variable space (centre), and then summed into discrete bins (right)

$$\phi_i = \phi_{min} + \frac{2i-1}{2}\delta\phi, \quad i = 1, 2, ..., N_\phi, \tag{5.3}$$

$$\theta_j = \theta_{min} + \frac{2j-1}{2}\delta\theta, \quad j = 1, 2, ..., N_\theta \tag{5.4}$$

For each grid cell, the $I_{ij}(\phi, \theta)$ is calculated:

$$I_{ij}(\phi,\theta) = \begin{cases} dxdzdy, & (\phi(x,z) - \phi_i, \theta(x,z) - \theta_i) \in \left[-\frac{1}{2}\delta\rho, \frac{1}{2}\delta\rho\right) \times \left[-\frac{1}{2}\delta\theta, \frac{1}{2}\delta\theta\right) \\ 0, & \text{otherwise,} \end{cases} \tag{5.5}$$

and the total weight for each given bin with centre (ϕ_i, θ_j) is given by:

$$W_{ij} = \frac{1}{V}\sum I_{ij}(\phi,\theta). \tag{5.6}$$

Thus for a given bin the weight W_{ij} is the total volume of grid cells that had $(\phi_i - \frac{1}{2}\delta\phi \leq \phi < \phi_i + \frac{1}{2}\delta\phi)$ and $(\theta_j - \frac{1}{2}\delta\theta \leq \theta < \theta_j + \frac{1}{2}\delta\theta)$. The end result of the process is a bivariate weighted histogram. The weighting ensures that the probability density function (PDF) reflects the probability a volume of fluid has given properties in mapped domain cases.

A code for this applied to the numerical model SPINS (introduced in §5.2.2) can be found at: https://github.com/HartharnSam/SPINS_USP. This code generalises the formulation in Penney *et al.* (2020) to any two fluid variables, and to a non-uniform grid (including mapped grids).

The second new tool introduced herein is the technique of Region of Interest (ROI) plots. Here, the variable is plotted in physical space, but only where conditions identified on the paired histogram are met, for example $1040 < \rho < 1050\,\mathrm{kgm}^{-3}$ and $0.1 < KE < 0.2\,\mathrm{Jkg}^{-1}$. In relation to mixing in the shoaling wave simulations, the kinematic quantity investigated is enstrophy density, $\Omega = \frac{1}{2}|\boldsymbol{\omega}|^2$ (where $\boldsymbol{\omega} = \nabla \times \boldsymbol{u}$) which describes the rotational energy linked to dissipation in 2-D flows and so is a quantity associated with (but not a measure of) mixing. The kinetic energy density, $KE = \frac{1}{2}\boldsymbol{u}^2$, is used as a measure of energy of translation in the flow.

In order to unambiguously identify time periods of interest in the various case studies reported on below we have utilised the methodology of Shaw & Stastna (2019). Briefly, this technique computes the Empirical Orthogonal Functions (EOFs) for a particular physical quantity using the built in *svds* function in Matlab. The EOFs are used to create reconstructions of the original physical field, and the infinity norm of the difference between the reconstruction and original field is plotted as a function of time and the number of modes used in the reconstruction. Time periods for which a jump in the number of EOFs needed to obtain an approximation below a given error tolerance are taken as "periods of interest" and hence selected for detailed examination. This technique is attractive because it builds on a standard technique (EOFs) while addressing its well-known shortcoming (the fact that individual EOFs are not physical quantities).

5.2.2. *Numerical model*

Simulations were carried out with the pseudospectral code SPINS described in chapter 1 §2.6. An additional passive tracer is implemented using the following equation:

$$\frac{\partial \Xi_i}{Dt} + \boldsymbol{u} \cdot \boldsymbol{\nabla \Xi_i} = \kappa_{\Xi_i} \nabla^2 \Xi_i \tag{5.7}$$

Throughout this chapter density is reported using the density perturbation $\rho' = \rho - \rho_1$. Scalar diffusivities are κ_ρ for density and κ_{Ξ_i} for tracer. The boundary conditions, domain dimensions and other varying parameters for each simulation are described for each case in §§5.2.2 and 5.2.2.

Shoaling Internal Solitary Waves

To illustrate the USP method, simulations from previous chapters on ISW shoaling will be utilised, namely simulations 27_111120 (here the surging case), 26_091120 (here the collapsing case), and 24_071020 (here the plunging case) from chapter 3 and the Thin-20L case (here the fissioning case) from chapter 4. Full details of the simulations can be found in the respective chapters. ISWs were simulated in a rectangular tank with waves initiated using the lock gate technique, and a slope at one end of the tank as shown in the schematic of the model set-up in figure 5.2 (a). The length of the tank $L_x = 7$ m (extended to $L_x = 14.5$ m for the fissioning case), and the depth of the tank $L_z = 0.3$ m. A hyperbolic smoothing function produces the gate region by a numerical step in density 0.3 m from the left end of the tank, from which an ISW is produced and propagates from left to right.

The vertical density profile in the main tank was set according to the smoothed two-layer, or hyperbolic tangent profile:

$$\rho(z) = \rho_0 + \frac{\Delta\rho}{2} \tanh\left(\frac{z - z_{pyc}}{h_{pyc}}\right), \tag{5.8}$$

set for a system like that studied previously in the literature consisting of a thin, linearly stratified pycnocline ($h_{pyc} = 0.015$ m) sandwiched between homogeneous layers, here referred to as "thin tanh stratification". The density change, $\Delta\rho = 20\,\mathrm{kgm}^{-3}$, the reference density $\rho_0 = 1026\,\mathrm{kgm}^{-3}$ and the depth of the pycnocline, $z_{pyc} = 0.07$ m. Simulations are carried out for a slope of $s = 0.2$ in all cases except the fission case at $s = 0.033$, and in all cases the slope height is 0.3 m, the full depth of the water column. The bottom boundary follows the form of Lamb & Nguyen (2009) (see equation (3.2)). The surging ($a = 0.009$ m), collapsing ($a = 0.048$ m) and plunging ($a = 0.076$ m) cases represent increasing wave amplitudes (a), and the fissioning ($a = 0.063$ m) case has an intermediate wave amplitude.

Cold shear instability

A Kelvin-Helmholtz instability was produced for a three-dimensional (3-D) simulation in a domain 0.512 m in the x direction, and 0.128 m in the y and z directions by initialising a temperature stratified shear flow perturbed with white noise. Free slip boundary conditions were applied at the upper and lower boundaries, with regular grid spacing in all dimensions, and periodic boundary conditions in the x and y domains. To produce a stratified shear flow,

the temperature field, $T(z)$ and horizontal velocity field, $u(z)$ were initialised as follows:

$$T(z) = T_0 + \frac{\Delta T}{2}\left(1 - \tanh\left(\frac{z - z_{mix}}{h_{mix}}\right)\right), u(z) = \Delta u \tanh\left(\frac{z - z_{mix}}{h_{mix}}\right). \tag{5.9}$$

Where T_0 is the reference temperature (here, $T_0 = 0.5$ °C), ΔT is the temperature difference (here $\Delta T = 3$ °C), and the velocity difference, $\Delta u = 0.01$ ms^{-1} A nonlinear equation of state suitable for cold, fresh water was chosen. The equation of state to calculate densities from temperature and salinity is the polynomial fit from Brydon *et al.* (1999), assuming salinity and excess pressure are 0 everywhere (pressure everywhere is equivalent to the surface pressure). The background temperature and velocity gradient regions are thus in a similar location, but the density stratification is asymmetric (figure 5.2 b). Salinity was set to 0 everywhere, and v and w were set at rest, with small white noise perturbations to initialise the instability. The interface depth, z_{mix} and thickness, h_{mix}, were 0.064 m and 0.01 m respectively. The minimum initial Richardson number, Ri_0 is defined as:

$$Ri_0 \approx \frac{g\Delta\rho h}{\rho_0(\Delta u)^2}. \tag{5.10}$$

The configuration was set such that $Ri_0 \ll 0.25$ (= 0.087). The low value was chosen because $Ri = 0.25$ is the necessary, but not sufficient, criterion for shear instability. For this temperature range, the density range is very small, so for the cold shear instability cases, the density perturbation, ρ', is a useful measure.

Such flows characterise situations where the temperature and momentum are linked, rather than density and momentum, for example, a warm river flow entering a cold lake.

To establish the interplay between passive and active tracers, a passive tracer (i.e. dye in a laboratory setting) was additionally initialised in two further simulations with the same initial conditions as temperature (equation 5.9) but with each case performed at different tracer diffusivity to the temperature tracer, as described in §5.3.3.

5.3. Results

5.3.1. *Fissioning Internal Solitary Waves & the newly-mixed layer*

The evolution of shoaling ISWs in this stratification takes one of four forms: surging, collapsing, plunging, or fissioning (for more details see e.g. Sutherland *et al.*, 2013; Hartharn-Evans *et al.*, 2022) and chapter 3. Each of these manifests different mixing and dissipation characteristics, as identified via bulk mixing measures (Arthur & Fringer, 2014).

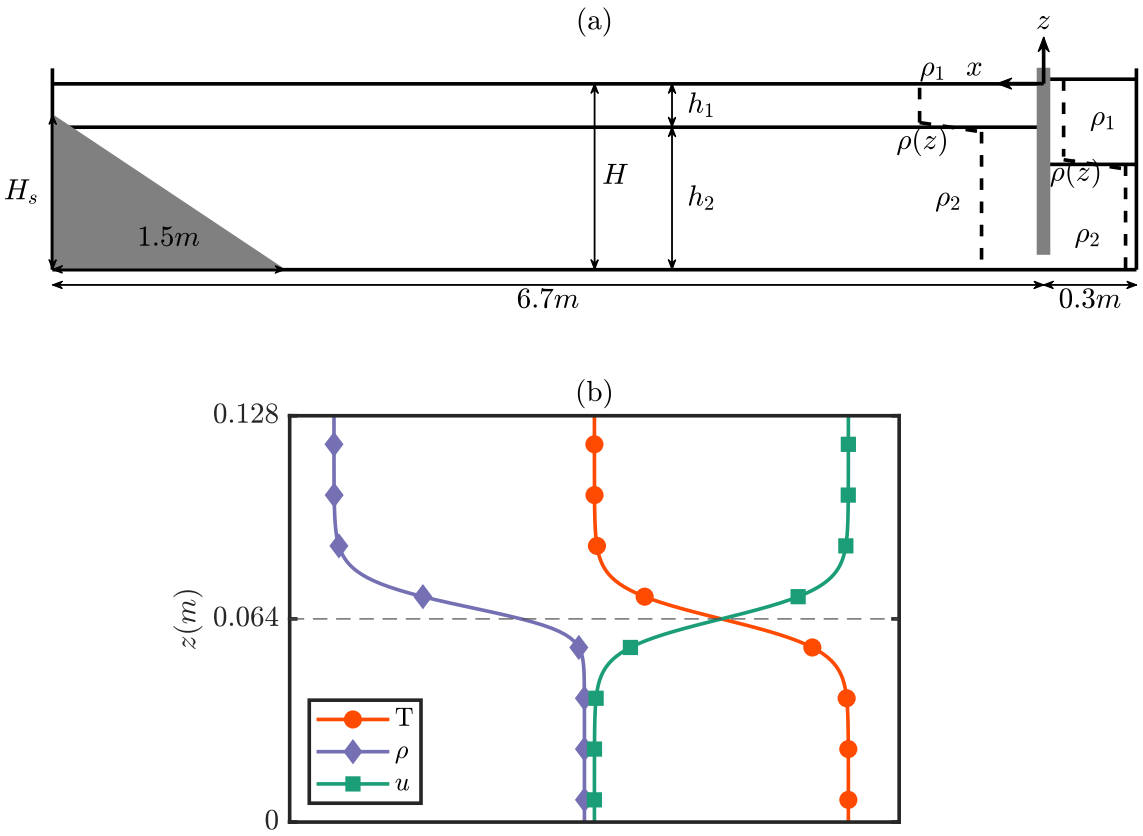


Figure 5.2: (a) Shoaling ISW schematic diagram showing the numerical domain used for the shoaling internal solitary wave simulations in this study. (b) Cold shear instability schematic indicating the initial vertical profiles of the density, temperature, and velocity fields for the cold shear instability simulations (horizontal scales adjusted), the dashed horizontal line indicates the mid-tank and the centre of the interface for T and u.

Figure 5.3 shows the evolution of one of these examples collapsing, which occurs with moderate steepness waves over moderate slopes; this will be explored here in more detail (each of the other examples is presented in Supplementary Figures 1-3). A more complete description of these processes can be found in chapter 3 §4.3, but here the focus is on the evolution of USPs during this process.

First, the reference USP case for an ISW prior to interacting with the slope, as shown in figure 5.1, is explored. At this point, most of the fluid in a three-layer stratification is at either extreme of density (ρ = 1015 or 1035 kgm^{-3}) (figure 5.1*b, d*), with only a small amount of fluid in intermediate densities across a thin pycnocline. Meanwhile, the KE is strong in both the upper and lower layers around the wave itself (figure 5.1*a*), and is small at the centre of the pycnocline due to shear here. The overall result is an arcing pattern in USP space. This pattern is asymmetric, due to the asymmetric stratification (in the vertical),

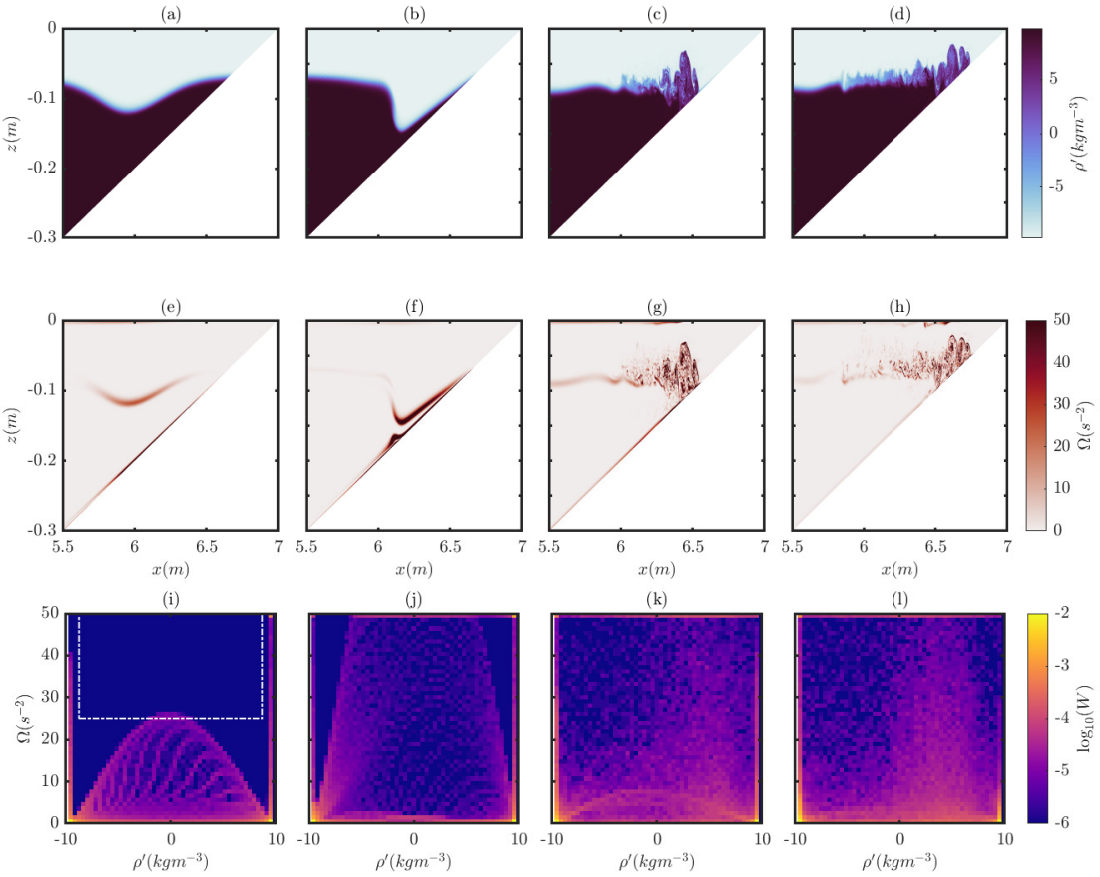


Figure 5.3: Time sequence of collapsing wave shoaling process shown as ρ' (top), Ω (middle), and the USP for the same variables (bottom). t = [55, 60, 70, 75]s

which concentrates the KE in the upper layer. In order to investigate mixing due to the shoaling of this wave, we will now explore how this pattern changes during the shoaling process, and identify the fluid regions which these new fluid properties apply to, instead using enstrophy, Ω as a measure of energy in the flow available for mixing. Almost inverse to the KE USP in figure 5.1, Ω is highest at the highest shear region across the pycnocline in the wave, and at the upper and lower boundaries around the wave (figure 5.3*i*).

As the wave begins to interact with the slope and steepen (figure 5.3*a, b, e, f*), a separation bubble forms on the slope due to boundary layer separation (Carr *et al.*, 2008; Boegman & Ivey, 2009), meanwhile enstrophy remains constrained to the pycnocline (now extended), and the separation bubble is reflected in much higher enstrophy across mid-densities (figure 5.3*f, j*). As the wave continues to propagate upslope and concentrate into a shallower region, the separation bubble strengthens and produces a global instability (figure 5.3*c, g*). The USP reveals higher enstrophy primarily associated with higher

densities, with remnants of the high enstrophy at the upper and lower boundaries still visible in the USP as the high enstrophy at high and low density limits (figure 5.3*g, k*). This evolves into a bolus of fluid moving upslope (figure 5.3*d, h*). Although plots of enstrophy and density indicate mixing is occurring around the pycnocline at the head of the bolus (figure 5.3*d, h*), the USP is informative of where mixing is occurring. As the bolus propagates upslope, the skew of high enstrophy fluid towards higher densities (lower-layer fluid) becomes clearer in the USP diagram (figure 5.3*l*).

A region of USP space can be identified at early output times, which includes only Ω higher than that associated with a stable ISW, and intermediate densities, and therefore is here taken to represent active mixing regions (white box figure 5.3*i*). The fluid that has the properties contained within such a region can be identified, and is plotted in figure 5.4 (*e-h*), for each type of wave shoaling. For a collapsing wave at a late time step, this shows a large continuous patch of actively mixing fluid, extending over around 0.7 m (figure 5.4*f*), concentrated at intermediate densities (the pycnocline), although slightly skewed towards higher densities (figure 5.4*j*).

Following this same process for four example waves across the four breaking regimes reveals their mixing properties. Surging is observed for small amplitude waves, and the resulting process is a non-turbulent surge of dense fluid propagating upslope (figure 5.4*a*). A single region of high enstrophy forms as the combination of that at the pycnocline and the lower boundary (figure 5.4*e*), and this is advected upslope. Little mixing occurs during this process (figure 5.4*i*), and the small active mixing region is advected upslope in the pulse of dense fluid. Plunging, which takes place at high slope and wave steepness values, results in an anvil-shaped instability plunging forward from the rear steepening face of the wave. As a result, overturning occurs, and this process has been associated with high levels of mixing. Although this process produces high enstrophy across the density range, indicating a lot of mixing (figure 5.4*k*), the actively mixing fluid is less continuous, and stretches over a smaller horizontal extent than a collapsing wave (figure 5.4*c, g*). The active mixing region is vertically extensive, reflected in the USP with high enstrophy across all densities, but a slight skew in the USP diagram indicates mixing is associated with lower densities mixing to intermediate densities rather than higher densities to intermediate densities. The final wave shoaling behaviour, fissioning, is shown in the right column of figure 5.4, and occurs over gentle slopes. The formation of multiple dense pulses of fluid (figure 5.4*d*), which in this example are quasi-turbulent, produces actively mixing fluid over a long horizontal extent (figure 5.4*h*), with active mixing occurring as the pulses propagate upslope. A strong skew in the USP indicates mixing is primarily associated with

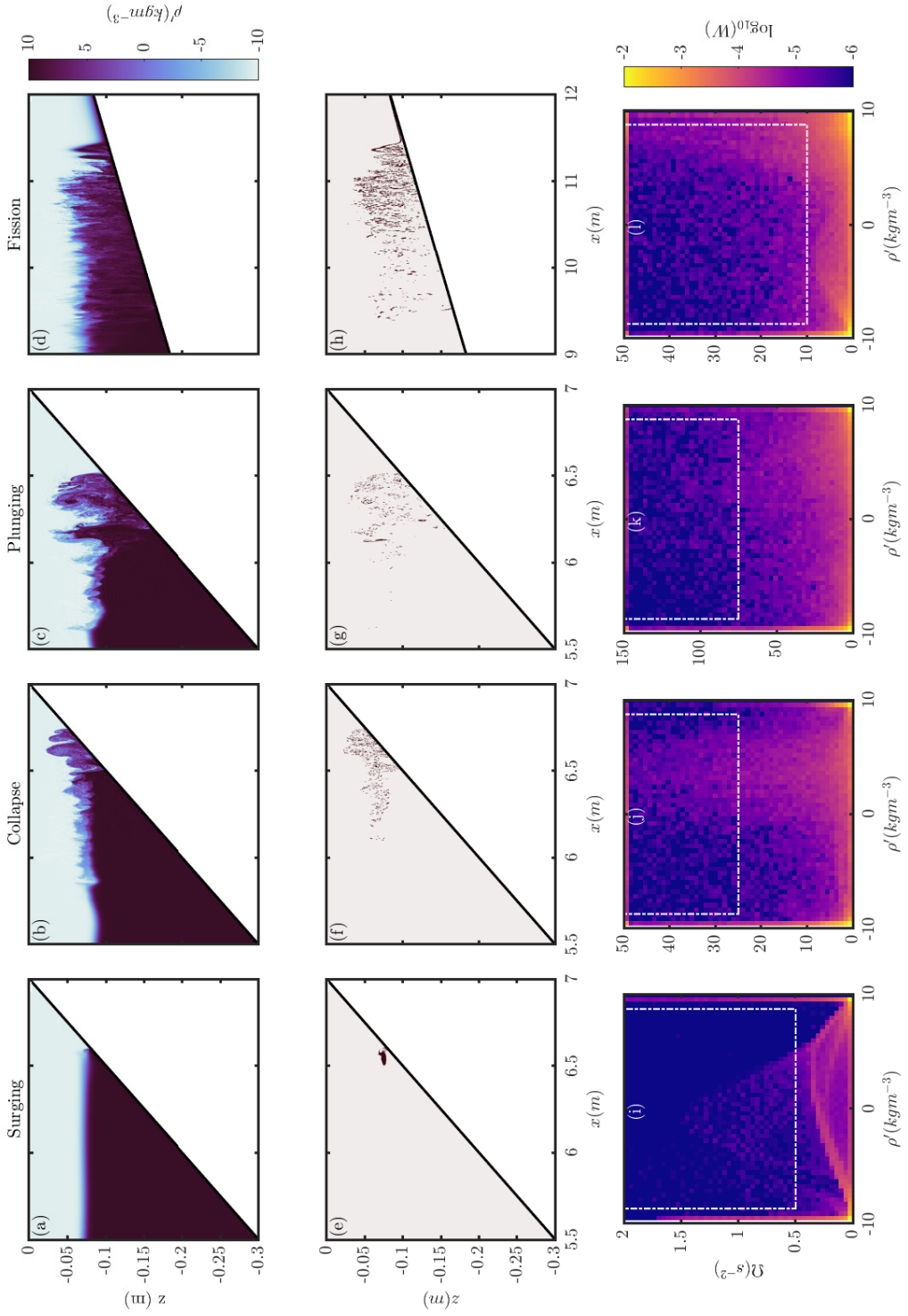


Figure 5.4: Four example waves representing different breaking regimes at a late time step, showing density (top); region of interest (ROI; middle), where the fluid meeting the criteria is marked in dark red; and the USP (bottom). The white box in the lower panels indicate the ROI selected, based on USP at earlier time steps.

high densities, and therefore the lower layer (figure 5.4*l*). This follows with the concept of dense pulses propagating upslope and mixing as they do so.

As an overview of this pattern, as the wave steepness increases, and therefore the wave breaking regime moves from surging through collapsing to plunging, the region of actively mixing fluid increases. Fissioning takes this a step further, with a similar input wave to the collapsing case, the gentle slope allows the wave to mix over a longer distance.

5.3.2. *Cold shear instability*

The unstable shear flow undergoes the typical evolution through the formation of Kelvin-Helmholtz (K-H) instability, as follows. Initially, the flow is a shear flow in stably stratified fluid (figure 5.5*a, e*), where the kinetic energy (KE) is high in both the upper and lower layers, but at the interface of the layers is zero, at the inflection point of the horizontal velocity (figure 5.2*b*). As the fluid is a two layered shear flow, one would expect the ρ'/KE USP to be a symmetrical curve, where the highest kinetic energy is associated with the highest- and lowest- density anomalies away from the interface (which is also where most of the fluid resides), whilst intermediate densities represent the shear layer where KE is lower. Here, the ρ'/KE USP shows a "crooked smiley face", with most of the fluid concentrated at the extremes of density, but due to the temperature stratification and non-linear equation of state, the curve is shifted towards higher densities (figure 5.5*i*). Despite kinetic energy being high at this stage in the other directions, there is very little kinetic energy in the y direction ($\mathrm{KE}_v = \frac{1}{2}v^2$), indicating the flow features at this stage are not dependent upon 3-D elements of the flow (figure 5.5*i, m*).

It is worth noting that while the evolution of the shear instability is generic, the nonlinearity of the equation of state means that the symmetry across the centre of the co-located shear and density layers is broken. The visual manifestation of the billows is effectively slightly biased toward one side.

Small fluctuations in the flow result in stationary waves growing on the interface, which, due to the shear, grow and roll up, forming braids and billows (figure 5.5*b, f*). As the billows form and stretch, an increasing amount of the flow's KE builds around the billows and is therefore associated with the intermediate densities (figure 5.5*f, j*). Until now, the flow is two-dimensional, with negligible kinetic energy in the transverse direction (figure 5.5*m, n*) and little transverse variability. During the braiding and billow growth, the pycnocline is stretched thin (figure 5.5*b*), enhancing the potential for mixing by stretching density gradients. The roll up of these billows is such that alternating layers of high and low density form, with the density now statically unstable, leading to turbulence (and in

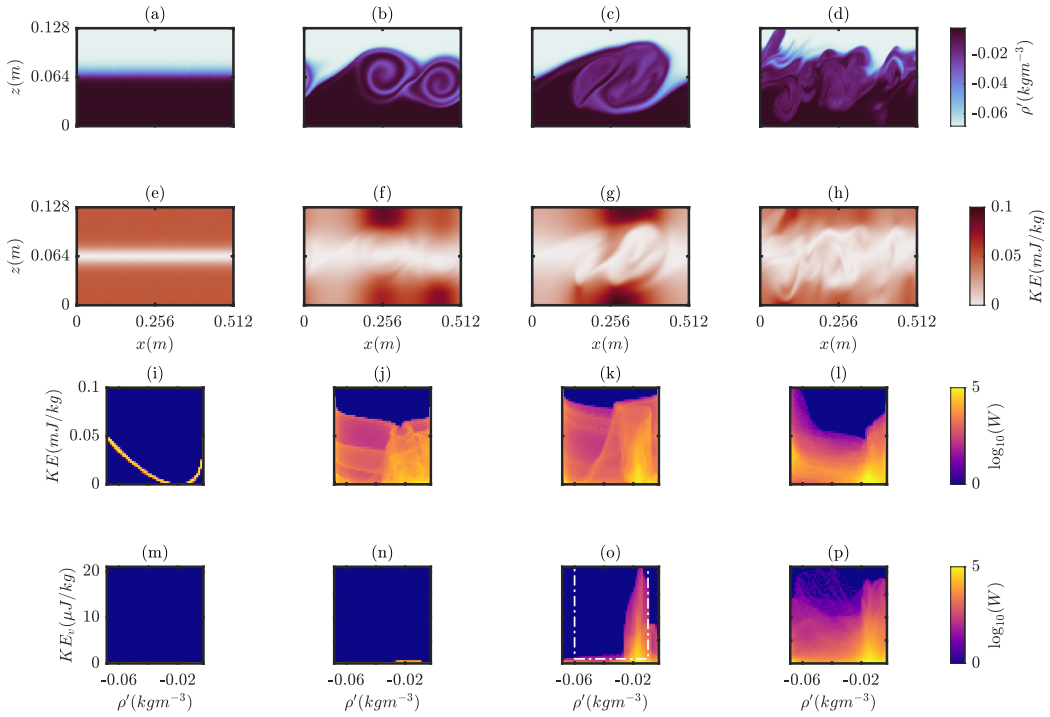


Figure 5.5: Time sequence of the cold shear instability, shown as density (*a-d*) and Kinetic Energy density (*e-h*) fields, and the USP for density vs KE density (*i-l*) and for density vs KE_v (the KE density for just the v component) (*m-p*). t =[5, 170, 225, 275]s.

turn spanwise instability) and mixing. These billows pair and coalesce by $t = 225$ s (figure 5.5*c*). The kinetic energy associated with intermediate densities continues to build as the billows coalesce, but by this stage, an increased volume of fluid that represents fluid in the $\rho' = -0.03\,\mathrm{kgm}^{-3}$ to $-0.01\,\mathrm{kgm}^{-3}$ range is evident (figure 5.5*k*), indicating that mixing has occurred in the fluid. When the billows coalesce, KE_v is high, and almost all of this is associated with the same density range as that of the newly mixed fluid layer at late stages (figure 5.5*o*). This indicates the importance of these transverse flow features in the mixing produced by billows formed from a K-H instability. The skew in the density of newly mixed fluid, as a result of the cold temperature nonlinearity in density, is to some extent visible (but easily missed) in the ρ' plots (figure 5.5*c*) but is only truly apparent in USP space (figure 5.5*k, l, o, p*).

Beyond this time, mixing across the braids continues and leads to a new state (figure 5.5*d*) where a quasi-turbulent intermediate density layer forms, which represents a new steady state, where the *Ri* is reduced by a smoothed density gradient. As the flow begins to settle back towards the new steady state, kinetic energy at the intermediate densities falls,

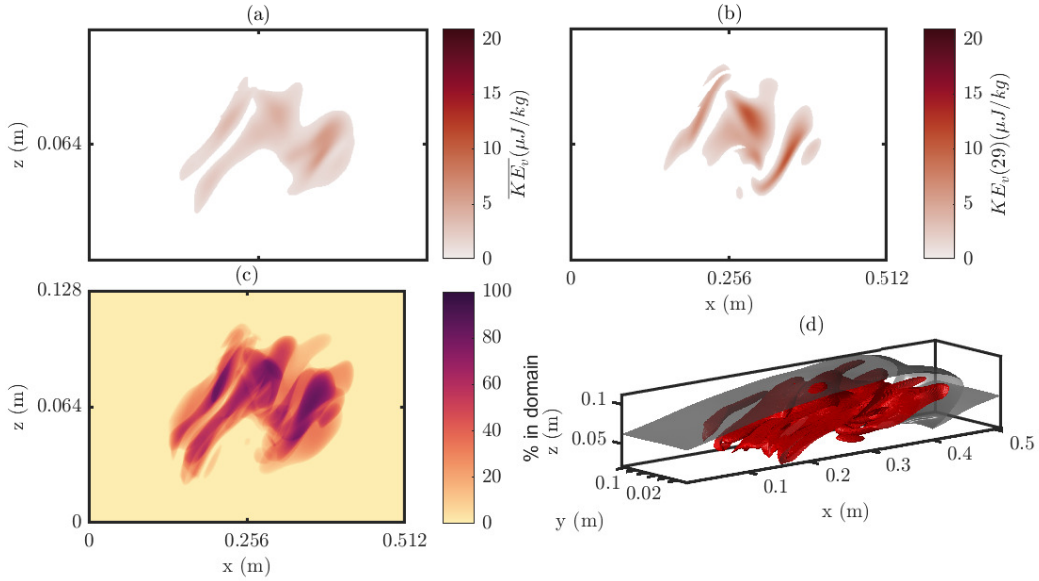


Figure 5.6: Regions of interest of the cold shear instability case at $t = 225$ s, based on the region indicated in the white box of figure 5.5 (*o*). Shown as the ROI in the transverse mean KE_v field (*a*), the KE_v x, z slice most representative of the mean (*b*), the proportion of the y domain within the ROI for the (x, z) plane (*c*), and the boundaries of the ROI (red) with the $\rho' = -0.0454\,\mathrm{kgm}^{-3}$ isopycnal for reference (black) (*d*).

with the presence of the layer of intermediate density evident at $\rho' \approx -0.02\,\mathrm{kgm}^{-3}$.

The USP region in which active mixing is related to 3-D processes is identified in figure 5.5 (*o*). This is where KE_v is higher than any of the flow in early time steps and with intermediate density. This region of the flow for $t = 225$ s is isolated in figure 5.6. The transverse average KE_v (figure 5.6*a*) shows that this active 3-D mixing is occurring right at the core of the K-H billow, whilst there is considerable variability throughout the y direction (figure 5.6*c, d*). Peaks in KE_v are particularly localised (figure 5.6*b*), indicating the small-scale processes at play responsible for the mixing. Such results are indicative of the importance of 3-D simulations for understanding these mixing processes. By isolating the fluid undergoing these processes, we can identify regions of the flow worthy of future study.

5.3.3. *Cold shear instability with passive tracers*

Two additional simulations were carried out with a passive tracer, Ξ_i, with different prescribed diffusivities. A less diffusive case (case K-H Dye 1) had $\kappa_{\Xi_1} = 10^{-8}\,\mathrm{m^2 s^{-1}}$ (case K-H Dye 1), and a more diffusive case (case K-H Dye 2) had $\kappa_{\Xi_2} = 10^{-6}\,\mathrm{m^2 s^{-1}}$.

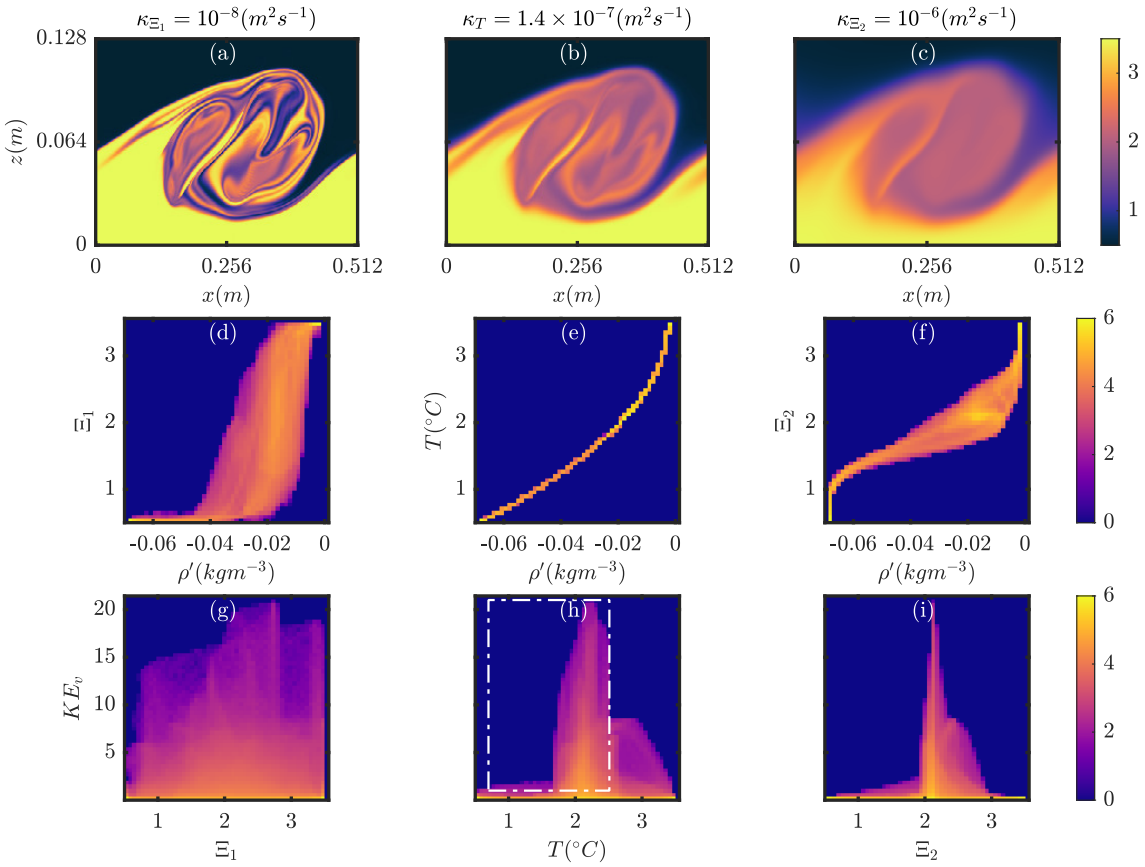


Figure 5.7: Late time step (t = 225 s) plots for the K-H Dye 1 case (left, *a, d, g*), the base case (centre, *b, e, h*) and the K-H Dye 2 case (right, *c, f, i*). Top panels (*a, b* and *c*) show a single slice of the tracer field (tracer for the cases K-H Dye case 1 and 2, temperature for base case); centre panels (*d, e* and *f*) show the ρ' vs tracer USP; and bottom panels (*d, e* and *f*) show tracer vs KE_v.

These represent diffusivity approximately one order of magnitude lower and greater than the active temperature field, $\kappa_T = 1.4 \times 10^{-7}\,\mathrm{m^2 s^{-1}}$. A snapshot taken of the time step at which billows coalesce (t = 225 s) reveals the emergence of fine structures in the K-H Dye 1 case within the billow core, and with sharp interfaces (figure 5.7*a*), a much more diffuse core, with blurred interfaces in the K-H Dye 2 case (figure 5.7*c*). Such features manifest in the USP of the tracer against density (figure 5.7 mid-row). A control with the active temperature tracer is presented (figure 5.7*e*), indicating the nonlinear relationship between density and temperature. The skew of this figure to the K-H Dye 1 case (figure 5.8*d*) shows which gradient is diffused faster, here indicating that the density gradient is diffusing faster than the tracer, that is that the extremes of salinity, associated with the upper- and lower-layer fluids initially, now map onto a range of densities. Meanwhile, the skew of this figure to the K-H Dye 2 case (figure 5.7*f*) shows that the tracer gradient is

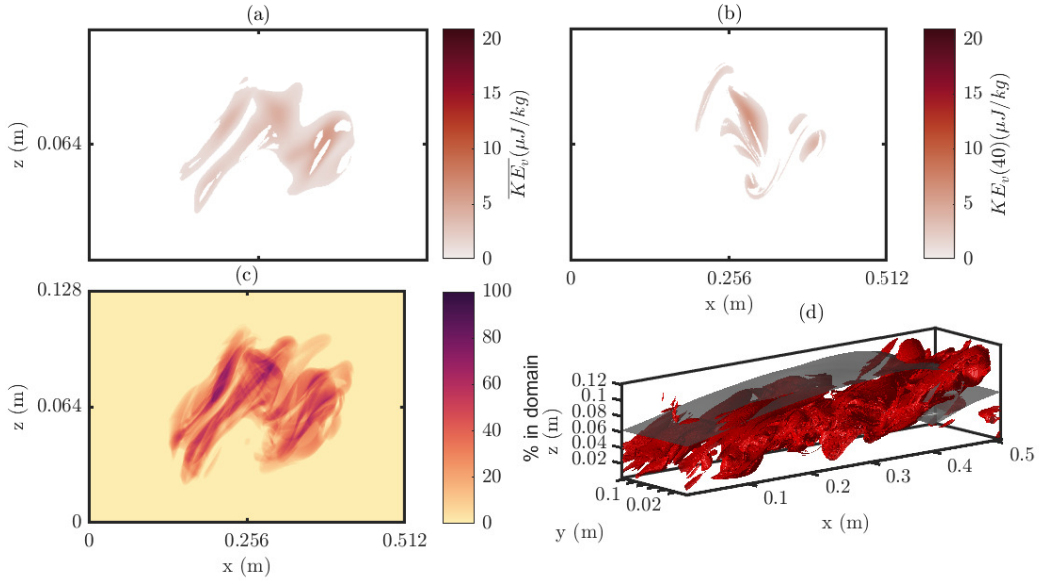


Figure 5.8: ROI plots as in figure 5.6 but for the K-H Dye 1 case, for the ROI indicated by the white box in figure 5.7 (*h*)

diffusing faster than the density, that is that the extremes of density, associated with the upper- and lower-layer fluids, now map onto a range of densities, and indicate that if the fluids were sorted again by density, each layer would contain varying levels of the tracer (that is to say, the tracer has mixed).

Applying the same region of active 3-D mixing (based on the density of that fluid at the initiation of the simulation), as in figure 5.6 (see region in figure 5.7*h*), produces figures 5.8 and 5.9. The mixing of the less diffusive passive dye indicates a pattern of highly localised, filamentous structures that are regions of active dye mixing (figure 5.8*b-d*). In contrast, the diffusive passive dye is mixing in broader-scale structures (figure 5.9*c*). However, the large-scale regions in which this passive dye is mixing is similar across both simulations (figure 5.8*a, c* 5.9*a, c*), indicating that there is an important interplay between the large-scale flow structures (the K-H billow, and overturn of the isopycnals shown as the black isosurface) and filamentous fine-scale structures, across which the diffusive dye is able to diffuse. This result highlights the small scales at which diffusion plays an important role, only once the fluid and associated gradients are stretched to fine scales does the difference in diffusivity between dyes (and indeed the active tracer in figure 5.6) play any role.

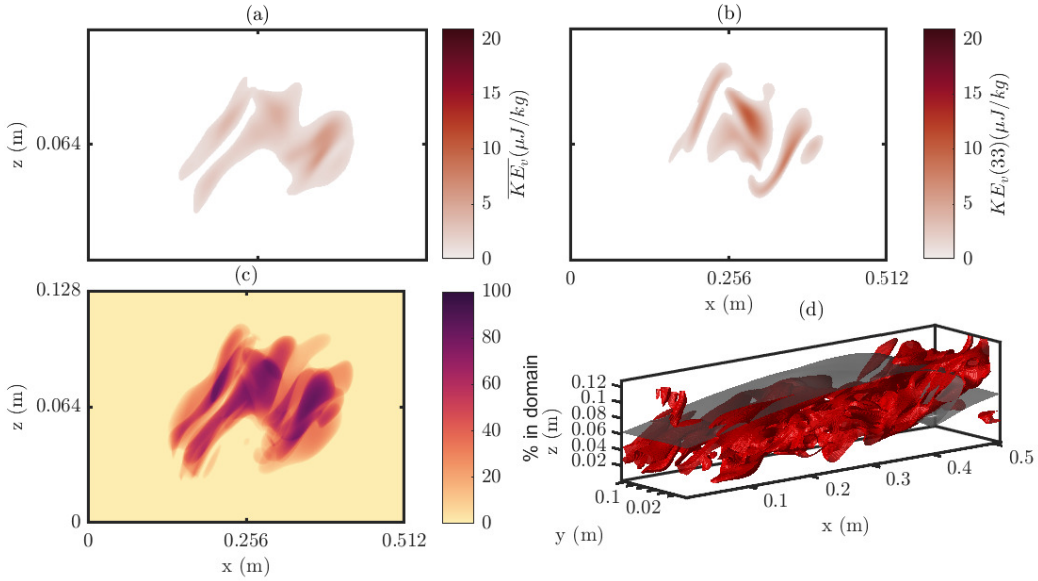


Figure 5.9: ROI plots as in figure 5.6 but for the K-H Dye 2 case, for the ROI indicated by the white box in figure 5.7 (*h*)

5.4. Discussion

By pairing a kinematic measure (KE, KE_v, or Ω) with a conserved tracer (density, temperature, or passive dye), the role of both turbulence in stirring the fluid and diffusive processes in irreversibly blurring density gradients is shown for several example stratified flows. This process has also been used to identify which fluid constituents are being mixed more effectively by a given process, whether the low density, upper layer fluid is being mixed into the pycnocline, or higher density, lower layer fluid is being mixed upwards, and the eventual fate of these fluids. In the case of the shoaling ISWs, it is used to evidence whether mixed fluids are retained locally to the site of mixing, advected upslope, or advected away from the slope as an intermediate layer. Each of these questions is difficult to answer using existing bulk energetics models. The USP method has an additional advantage over existing methods for understanding in its ease of implementation, and its reliability, in cases where the model is under-resolved, or has non-trivial bathymetry.

The results from shoaling ISWs reveal considerably different mixing regimes between breaking types, for example the horizontal extents of mixing between collapsing and plunging, where past studies have identified similar results between breaking types based on the energetics-based mixing measures alone. However, whilst it may be the bulk measure that is most useful in parameterising global-scale models, the locality of mixing, and

transport of this fluid, which may carry with it nutrients, heat (or thermal refuge), and sediment (depending on the local geomorphological setting), is crucial to understand the effects of such processes on ecosystems. The features outlined by ROI in some shoaling ISW examples (e.g. figure 5.3*h*) have a striking similarity to the intermediate nepheloid layers identified by Bourgault *et al.* (2014), formed due to the shoaling of ISWs, and the interaction of sediment resuspension and mixing. Similar features have been observed in various locations, but due to their episodic nature, their formation mechanisms can be unclear (Schulz *et al.*, 2021). Understanding how these features form and evolve may help understand how such features may contribute to larger-scale sediment fluxes, and as a result carbon exports (Schulz *et al.*, 2021). To investigate these processes, the USP method could be applied with an active sediment tracer.

For the cold shear instability, these results also reveal new insights into the dynamics of shear flows at low temperatures (below the density maximum). The shear flow presented could represent a cold river flow into a lake, and as such the position of the velocity gradient and temperature gradient are linked, whilst the density gradient position is offset. The result of this in the shear flow is to produce asymmetric K-H features (e.g. figure 5.5*b*), and mixing bias towards one density (figure 5.5*o*). These asymmetric stratified shear flows have attracted recent attention following field observations in estuarine environments (e.g. Tu *et al.*, 2020; Olsthoorn *et al.*, 2023). Previous work on K-H billows has highlighted the role of 3-D instabilities beyond the point at which billows coalesce. Here, isolating the fluid where these 3-D (v) flows are playing an active part in mixing, shows not only that 3-D processes are important at this stage, but also that they remain within the coalesced billow region, and at small scale (figure 5.6). Beyond that stage, this v component of the KE remains high around the active mixing region, but also increasingly across the entire flow. Furthermore, investigating the mixing of passive tracers is also not possible using energetics models, and has been presented here, identifying which densities the mixing of passive tracers is associated with, and the role of 3-D instabilities in the passive tracer mixing processes.

5.5. Conclusions

The USP method identifies how the different regimes of mixing associated with different breaking types (and therefore with differing wave and slope characteristics) manifest themselves. ISWs breaking with surging behaviour produce a small mixing region, which is advected upslope, indicating transport of the mixed fluids, potentially to regions of

high biological activity. In contrast, collapsing ISWs produce a large patch of actively mixing fluid over a long horizontal area, particularly with lower layer fluid mixed up into the pycnocline. Plunging ISWs, which initially appear to have similarities to collapsing ISWs, are instead dominated by upper layers mixed down into the pycnocline, and are more horizontally constrained. Finally, ISWs undergoing fissioning produce active mixing over a long horizontal region, advected upslope in the form of quasi-turbulent dense pulses (i.e. boluses).

Temperature-stratified shear flow simulations in the cold, nonlinear equation of state regime reveal important differences with a density-stratified shear flow. The USPs at early time steps immediately reveals the asymmetry of the distribution of density and kinetic energy, an asymmetry which goes on to play an important role in the mixing induced by the shear instability. Once density gradients have been stretched, and transverse flow at medium-high densities forms, mixing occurs in an asymmetric manner, producing a late stage state with the layer of newly mixed fluid skewed towards medium-high densities. Simulations of the shear flow with passive tracers of varying diffusivity highlight the nature of flow structures associated with mixing fluid. At low diffusivities, filamentous structures in the tracer are observed, heavily associated with 3-D elements of the flow, whilst at high diffusivity, tracer gradients are blurred. Both scenarios show interplay between the dynamic drivers in large-scale flow features and diffusive effects at filamentous fine-scales once gradients are stretched. Such fine-scale structures are revealed by the new ROI plots based on the USP double histograms. Overall, the new USP method provides valuable insights into the evolution and dynamics of sheared flows, and the role of temperature-based stratification within the nonlinear equation of state regime and diffusivity in mixing processes in particular.

The USP method provides a method of interpreting and investigating mixing that is not blind, i.e. it invites the researcher to understand the ongoing processes in a way that is ignored by the relative black box of typical (bulk) mixing methods. The tagging of particles based on variables provides a methodology that lies somewhere between a strictly Eulerian and strictly Lagrangian approach to understanding mixing. In the case of the passive tracer the method has been used to trace the motion of specific parcels of fluid. This could be further refined by introducing tracer at different times in the simulation into localized regions of interest. Future work could also set up higher dimensional histograms (although these become increasingly difficult to visualise), and/or more complex selection criteria based on multiple quantities; effectively a language to classify aspects of the fluid motion.

Code Data Availability. The interactive Matlab tool presented in this study can be found at https://github.com/HartharnSam/SPINS_USP. Data available from https://doi.org/10.25405/data.ncl.c.6704289.

Acknowlegements. Exploratory computations/code related to the USP mixing diagnostics and discussions of these with Karem Abdul-Samad and Chris Subich are gratefully acknowledged.

5.A. Supplementary Figures

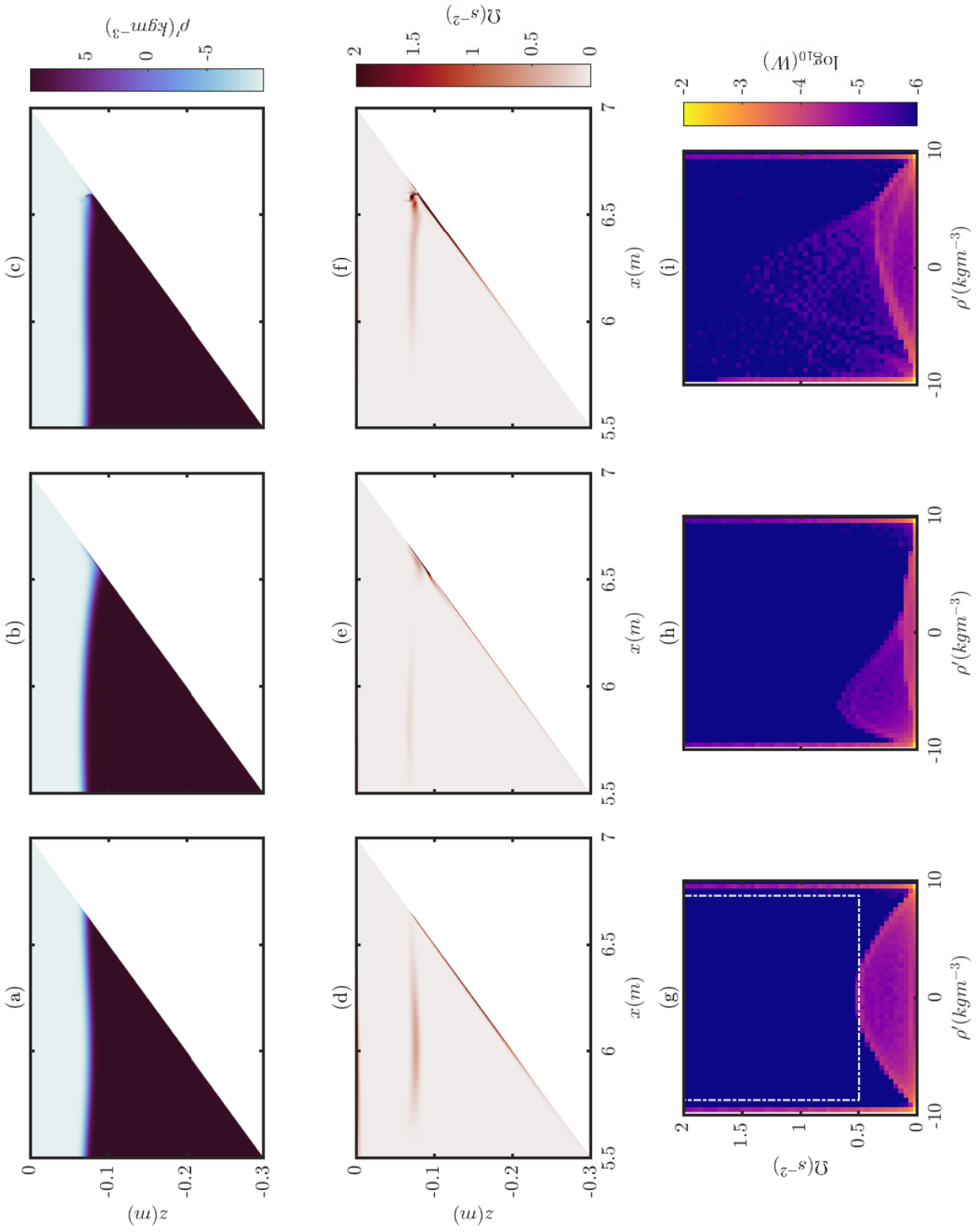


Figure 5.10: Supplementary Material 1: Time sequence of surging wave shoaling process shown as ρ' (top), Ω (middle), and USP for the same variables (bottom). t = [62, 70, 75] s

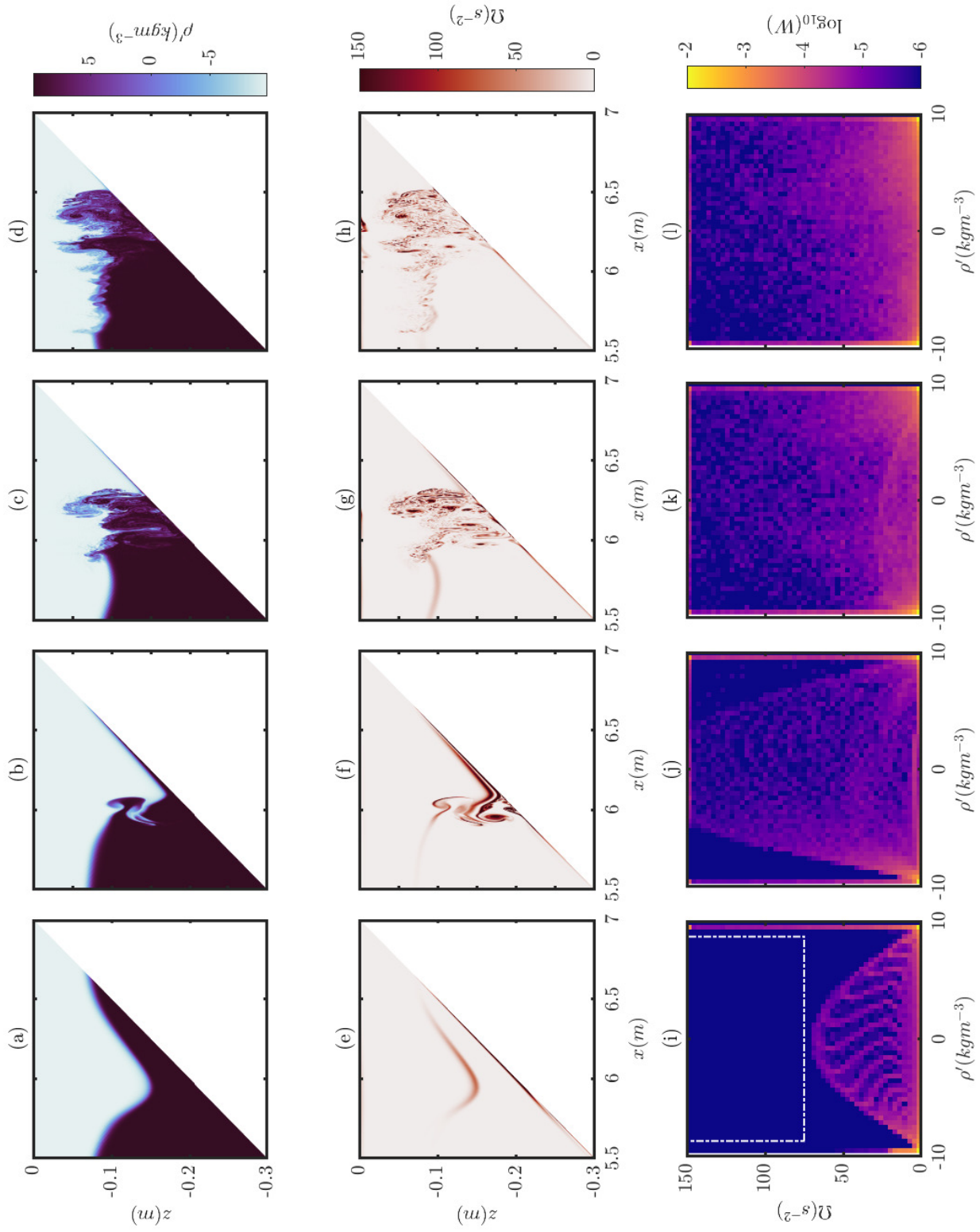


Figure 5.11: Supplementary Material 2: Time sequence of plunging wave shoaling process shown as ρ' (top), Ω (middle), and USP for the same variables (bottom). t = [55, 60, 65, 70] s

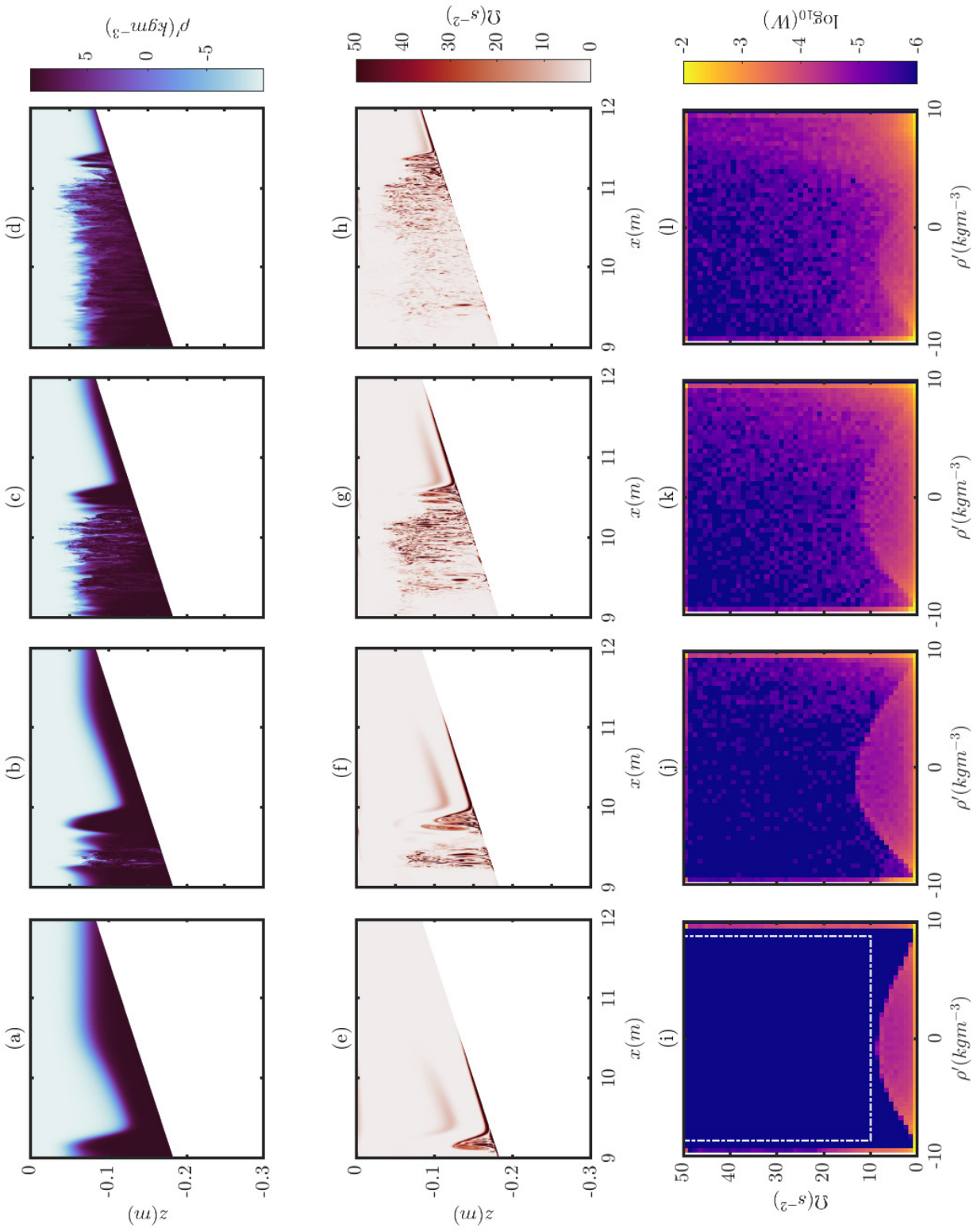


Figure 5.12: Supplementary Material 3: Time sequence of fissioning wave shoaling process shown as ρ' (top), Ω (middle), and USP for the same variables (bottom). t = [100, 108, 120, 136] s

Chapter 5

References

Aghsaee, P., Boegman, L. & Lamb, K. G. 2010 Breaking of shoaling internal solitary waves. *Journal of Fluid Mechanics* **659**, 289–317, https://doi.org/10.1017/S002211201000248X.

Arthur, R. S. & Fringer, O. B. 2014 The dynamics of breaking internal solitary waves on slopes. *Journal of Fluid Mechanics* **761** (2), 360–398, https://doi.org/10.1017/jfm.2014.641.

Arthur, R. S., Koseff, J. R. & Fringer, O. B. 2017 Local versus volume-integrated turbulence and mixing in breaking internal waves on slopes. *Journal of Fluid Mechanics* **815**, 169–198, https://doi.org/10.1017/jfm.2017.36.

Boegman, L. & Ivey, G. N. 2009 Flow separation and resuspension beneath shoaling nonlinear internal waves. *Journal of Geophysical Research: Oceans* **114** (2), 2018, https://doi.org/10.1029/2007JC004411.

Bourgault, D., Morsilli, M., Richards, C., Neumeier, U. & Kelley, D. E. 2014 Sediment resuspension and nepheloid layers induced by long internal solitary waves shoaling orthogonally on uniform slopes. *Continental Shelf Research* **72**, 21–33, https://doi.org/10.1016/j.csr.2013.10.019.

Brydon, D., Sun, S. & Bleck, R. 1999 A new approximation of the equation of state for seawater, suitable for numerical ocean models. *Journal of Geophysical Research: Oceans* **104** (C1), 1537–1540, https://doi.org/10.1029/1998JC900059.

Carr, M., Davies, P. A. & Shivaram, P. 2008 Experimental evidence of internal solitary wave-induced global instability in shallow water benthic boundary layers. *Physics of Fluids* **20** (6), 066603, https://doi.org/10.1063/1.2931693.

Carr, M., Franklin, J., King, S. E., Davies, P. A., Grue, J. & Dritschel, D. G. 2017 The characteristics of billows generated by internal solitary waves. *Journal of Fluid Mechanics* **812**, 541–577, https://doi.org/10.1017/jfm.2016.823.

Caulfield, C. 2021 Layering, Instabilities, and Mixing in Turbulent Stratified Flows. *Annual Review of Fluid Mechanics* **53** (1), 113–145, https://doi.org/10.1146/annurev-fluid-042320-100458.

Caulfield, C. P. & Peltier, W. R. 2000 The anatomy of the mixing transition in homogeneous and stratified free shear layers. *Journal of Fluid Mechanics* **413**, 1–47, https://doi.org/10.1017/S0022112000008284.

Geyer, W. R., Lavery, A. C., Scully, M. E. & Trowbridge, J. H. 2010 Mixing by shear instability at high Reynolds number. *Geophysical Research Letters* **37** (22), https://doi.org/10.1029/2010GL045272.

Grace, A. P., Stastna, M., Lamb, K. G. & Andrea Scott, K. 2021 Asymmetries in gravity currents attributed to the nonlinear equation of state. *Journal of Fluid Mechanics* **915**, A18, https://doi.org/10.1017/jfm.2021.87.

Hartharn-Evans, S. G., Carr, M., Stastna, M. & Davies, P. A. 2022 Stratification effects on shoaling internal solitary waves. *Journal of Fluid Mechanics* **933** (A19), https://doi.org/10.1017/jfm.2021.1049.

Helland-Hansen, B. 1916 Nogen hydrografiske metoder. *Forh Skand Naturf Mote* **16**, 357–359.

Imasato, N., Nagashima, H., Takeoka, H. & Fujio, S. 1993 Diagnostic approaches on deep ocean circulation. In *Deep Ocean Circulation* (ed. T. Teramoto), *Elsevier Oceanography Series*, vol. 59, pp. 307–331. Elsevier.

Lamb, K. G. 2008 On the calculation of the available potential energy of an isolated perturbation in a density-stratified fluid. *Journal of Fluid Mechanics* **597**, 415–427, https://doi.org/10.1017/S0022112007009743.

Lamb, K. G. & Nguyen, V. T. 2009 Calculating Energy Flux in Internal Solitary Waves with an Application to Reflectance. *Journal of Physical Oceanography* **39** (3), 559–580, https://doi.org/10.1175/2008JPO3882.1.

Lincoln, B. J., Rippeth, T. P. & Simpson, J. H. 2016 Surface mixed layer deepening through wind shear alignment in a seasonally stratified shallow sea. *Journal of Geophysical Research: Oceans* **121** (8), 6021–6034, https://doi.org/10.1002/2015JC011382.

Michallet, H. & Ivey, G. N. 1999 Experiments on mixing due to internal solitary waves breaking on uniform slopes. *Journal of Geophysical Research: Oceans* **104** (C6), 13467–13477, https://doi.org/10.1029/1999jc900037.

Moum, J. N., Farmer, D. M., Smyth, W. D., Armi, L. & Vagle, S. 2003 Structure and generation of turbulence at interfaces strained by internal solitary waves propagating shoreward over the continental shelf. *Journal of Physical Oceanography* **33** (10), 2093–2112, https://doi.org/10.1175/1520-0485(2003)033¡2093:SAGOTA¿2.0.CO;2.

Olsthoorn, J., Kaminski, A. K. & Robb, D. M. 2023 Dynamics of asymmetric stratified shear instabilities. *Phys. Rev. Fluids* **8** (2), 024501, https://doi.org/10.1103/PhysRevFluids.8.024501.

Peltier, W. R. & Caulfield, C. P. 2003 Mixing Efficiency in Stratified Shear Flows. *Annual Review of Fluid Mechanics* **35** (1), 135–167, https://doi.org/10.1146/annurev.fluid.35.101101.161144.

Penney, J., Morel, Y., Haynes, P., Auclair, F. & Nguyen, C. 2020 Diapycnal mixing of passive tracers by Kelvin-Helmholtz instabilities. *Journal of Fluid Mechanics* **900**, 26–26, https://doi.org/10.1017/jfm.2020.483.

Pope, S. B. 2000 Turbulent-viscosity models. In *Turbulent Flows*. Cambridge: Cambridge University Press.

Salmon, R. 1998 *Lectures on Geophysical Fluid Dynamics*. Oxford, New York: Oxford University Press.

Schulz, K., Büttner, S., Rogge, A., Janout, M., Hölemann, J. & Rippeth, T. P. 2021 Turbulent Mixing and the Formation of an Intermediate Nepheloid Layer Above the Siberian Continental Shelf Break. *Geophysical Research Letters* **48** (9), e2021GL092988, https://doi.org/10.1029/2021GL092988.

Scotti, A. & White, B. 2014 Diagnosing mixing in stratified turbulent flows with a locally defined available potential energy. *Journal of Fluid Mechanics* **740**, 114–135, https://doi.org/10.1017/jfm.2013.643.

Shaw, J. & Stastna, M. 2019 Feature identification in time-indexed model output. *PLOS ONE* **14** (12), e0225439, https://doi.org/10.1371/journal.pone.0225439.

Sutherland, B. R., Barrett, K. J. & Ivey, G. N. 2013 Shoaling internal solitary waves. *Journal of Geophysical Research: Oceans* **118** (9), 4111–4124, https://doi.org/10.1002/jgrc.20291.

Thorpe, S. A. 1977 Turbulence and mixing in a Scottish Loch. *Philosophical Transactions of the Royal Society of London. Series A, Mathematical and Physical Sciences* **286** (1334), 125–181, https://doi.org/10.1098/rsta.1977.0112.

Tu, J., Fan, D., Lian, Q., Liu, Z., Liu, W., Kaminski, A. & Smyth, W. 2020 Acoustic Observations of Kelvin-Helmholtz Billows on an Estuarine Lutocline. *Journal of Geophysical Research: Oceans* **125** (4), e2019JC015383, https://doi.org/10.1029/2019JC015383.

Winters, K. B., Lombard, P. N., Riley, J. J. & D'Asaro, E. A. 1995 Available potential energy and mixing in density-stratified fluids. *Journal of Fluid Mechanics* **289** (C5), 115–128, https://doi.org/10.1017/S002211209500125X.

Wyngaard, J. 2010 *Turbulence in the Atmosphere*. Cambridge : Cambridge University Press.

CHAPTER 6

Interactions between Internal Solitary Waves and Sea Ice

6.1. Introduction

Across the world's oceans, variations in seawater temperature and salinity stratify the water column, producing conditions where density disturbances can propagate as internal waves (IWs). One manifestation of these internal waves are Internal Solitary Waves (ISWs). Such waves, are able to transport energy and fluid properties (such as heat, salinity, nutrients, or sediment) long distances without considerable change of form or magnitude as they exist due to a balance of nonlinear steepening and linear wave dispersion (e.g. Apel *et al.*, 1985; Boegman & Stastna, 2019). Typically, ISWs are generated on density interfaces in stably-stratified fluids by barotropic motion over topography, internal tides interacting with localised stratifications, or by nonlinear steepening of the internal tide.

The Arctic Ocean is a unique oceanographic environment for such IWs. Firstly, the Arctic Ocean stratification is salinity-driven, with the Arctic halocline insulating the surface cold, fresh water from the deep, warmer salty water. If it erodes the consequences for sea ice maintenance are profound, with sufficient heat contained within this layer to melt all Arctic sea ice within a few years (Turner, 2010). Therefore, the mixing that can be driven by IWs is crucial for the heat distribution across the Arctic Ocean. Secondly, poleward of the critical latitude (which for the M2 tide is much of the central Arctic), linear internal tides are unable to propagate (Vlasenko *et al.*, 2003; Rippeth *et al.*, 2017), and as a result, short-scale (including nonlinear/solitary) IWs are proposed as being a key agent for the transfer of energy from tidal to turbulent scales (Rippeth *et al.*, 2017). Finally, the presence of an ever-changing sea ice cap across most of the ocean modulates exchange of heat and

momentum with the atmosphere. In some cases, this acts as a cap, preventing wind energy being converted to surface and internal waves. In other cases, the motion of the ice relative to the surface waters can also act as a generation mechanism for IWs in itself (Martin *et al.*, 2014; Zhang *et al.*, 2022*a*). Despite the presence of sea ice being assumed to be at least partially responsible for the low internal wave energy in the Arctic (due to a combination of reducing energy input, and damping of IWs), recent studies have not found evidence of a significant rise in internal wave energy in response to rapidly declining sea ice extent (Guthrie *et al.*, 2013; Guthrie & Morison, 2021).

Remote sensing (SAR imagery) of ISWs at high latitudes has confirmed the prevalence of these features in ice-free regions (Zimin *et al.*, 2016; Kozlov *et al.*, 2017). The retreat of sea ice over past decades allows these studies to highlight their prevalence in the presence of ice. Recently, direct observations have confirmed properties of these ISWs in proximity to the ice edge, with onshore propagating ISWs of 20 m–30 m amplitude, up to a maximum of 50 m (Marchenko *et al.*, 2021), and field-scale numerical modelling has provided further details of their behaviour (Morozov & Pisarev, 2002; Kurkina & Talipova, 2011). Such nonlinear IWs are thought to be formed from internal lee waves, a mechanism where the barotropic tide over topography forms steep IWs with strong nonlinearity able to overcome the rotational damping effects that prevent linear internal tide propagation at the high latitudes (Vlasenko *et al.*, 2003; Rippeth *et al.*, 2017; Guthrie & Morison, 2021; Urbancic *et al.*, 2022). Upon encountering sea ice, the evolution of IWs under ice has been shown in direct observations to be dependent on ice concentration, roughness, and the stratification (Cole *et al.*, 2018).

The ongoing declines in sea ice thickness provide a positive ice–ocean-heat feedback (Polyakov *et al.*, 2020). By increasing the rate of atmospheric momentum flux into the ocean, and in turn inducing IW-driven mixing, the heat content of the upper ocean may increase, melting more ice, and further increasing the mixing and melting. Many observational studies have linked ISWs in the Arctic to mixing processes (e.g. Rippeth *et al.*, 2017; Fer *et al.*, 2020), however, there has so far been little identification of the processes that lead to this conversion of energy between the ISW interactions with ice and mixing.

As well as driving mixing, ISWs have long been known to be an agent for mass transport in the ocean. Lamb (1997) used weakly nonlinear ISW models to analyse how small particles ($L_f \ll \lambda$, where L_f is float length, and λ is wavelength) at the surface would be transported by ISWs. At larger scales relevant to sea ice, horizontal gradients in ISW-induced vertical velocity has been observed causing the flexure of sea ice in the field

(Czipott *et al.*, 1991; Marchenko *et al.*, 2010) and the ice banding effect in the marginal ice zone has also been theoretically attributed to IW activity (Muench *et al.*, 1983; Saiki & Mitsudera, 2016). This indicates that ISWs are capable of inducing movement of sea ice on the order of the ice floe length scales, and here, laboratory experiments are used alongside fully nonlinear models to investigate both small and much larger floating structures.

Whilst there has been considerable attention to the interaction of surface ocean waves interacting with sea ice (e.g. Squire & Moore, 1980; Li *et al.*, 2015; Squire, 2020), relatively little is understood about the interactions of IWs and sea ice. Theoretical understanding of the evolution of internal (solitary) waves propagating beneath sea ice have primarily generalised the problem to a two-fluid problem under a flexible elastic sheet (e.g. Wang *et al.*, 2014). Such analytical studies can provide valuable insight of expected behaviours, such as changes to the wave form at low computational or experimental cost. However, field observations show the problem as more complex, with Pinkel (2005) showing the attenuation of IWs through scatter and dissipation under ice due to under-ice topography, bringing about instabilities formed from the interactions. To properly model these, numerical modelling or experiments are required, of which there have only been two process-scale studies. Carr *et al.* (2019*b*) conducted experiments with different surface ice types, identifying not only considerable turbulent kinetic energy dissipation at the ice-fluid interface, but also finding interaction with the ice edge can cause the ISW to break or even be destroyed by the process. Meanwhile, Zhang *et al.* (2022*b*,*a*) used numerical simulations to investigate the impact of a fixed ice keel on IW propagation and generation respectively.

Therefore, here we explore the interrelationship between ISW-induced flow and freely floating bodies representing sea ice at the surface. Whilst the work is focused on sea ice, the effects of ISW-induced currents at the surface (and therefore the phenomena identified in this study) are also of interest for SAR imagery (Jackson *et al.*, 2013), ship motion (for example, the dead water effect (Nansen, 1897; Ekman, 1904)), oil rigs (Osborne *et al.*, 1978), and floating offshore wind farms (Dorrell *et al.*, 2022).

In §6.2 the experimental methodology is presented, firstly the laboratory methods (§6.2.1), and the quantification of the flow and float motion (§6.2.2), followed by the formulation of a Float Motion Model (FMM) for the motion of a float under ISW-induced flow (§6.2.3). The results are presented in two parts, §6.3.1 presents how the floats move under the influence of an ISW, including comparisons with the FMM and relationships between float motion and known parameters; and is followed by §6.3.2 on how the flow is changed by the presence of floats. A discussion of these results follows in §6.4.

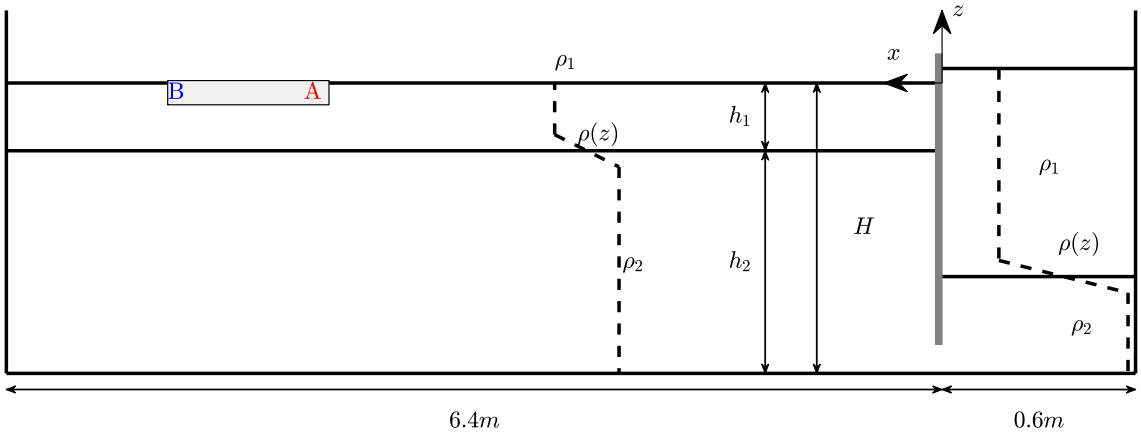


Figure 6.1: Schematic diagram of laboratory experiment used throughout this study, indicating the fluid densities and layer depths.

6.2. Methods

6.2.1. *Laboratory Experiments*

The experiments were carried out at Newcastle University in a wave tank 7 m long, 0.4 m wide and 0.6 m high, described within a Cartesian coordinate system (x, y, z) (hereafter the World Coordinate System, WCS). The x and z directions denote the horizontal direction of wave propagation (from right to left) and vertical direction against gravity, respectively. A removable vertical gate was situated 0.6 m from one end of the flume, separating it into two sections (see figure 6.1). This gate when inserted sat 0.03 m from the base of the tank, at the WCS origin $x = 0$, separating the main flume ($x > 0$) and the wave generating region ($x < 0$). $z = 0$ was at the surface of the water column (as indicated in figure 6.1).

The background stratification of the main part of the flume consisted of two homogeneous layers of miscible brine solution, separated by a thin layer (known as the pycnocline) in which the density varied linearly with depth. The lower layer was a homogeneous layer of prescribed density $\rho_2 = 1049.5 \pm 0.5\ \mathrm{kg\,m^{-3}}$ with a target depth (once the tank was fully filled) of $h_2 = 0.23\ \mathrm{m}$, whilst the upper layer was a homogeneous layer of density $\rho_1 = 1029 \pm 1\ \mathrm{kg\,m^{-3}}$, and target thickness of $h_1 = 0.07\ \mathrm{m}$ (such that $\Delta\rho = \rho_2 - \rho_1 = 20 \pm 1\ \mathrm{kg\,m^{-3}}$ in all cases). Due to practical constraints, the densities ρ_2 and ρ_1 differed slightly from prescribed values between runs, but the values were measured before the initiation of each run using a hydrometer. This stratification was set up through the initial filling of the lower layer with ρ_2 density brine, and filling the top layer using a floating sponge system. Brine was slowly drained from a reservoir above the tank through

an array of sponges to ensure laminar flow into the main tank, and therefore prevent mixing into the lower layer. The tank was filled to a prescribed depth in this manner.

Once filled, the density profile of the main tank was measured using high precision micro-conductivity probes (Munro & Davies, 2006), from which the depths of each layer could be identified. The surface and bottom densities were fixed to match the measurements of the lower layer and head reservoir, respectively (see Carr *et al.* (2015) for further details). These sensors were moved vertically through the water column and measurements taken at 1 cm intervals, and at 0.5 cm intervals close to the pycnocline. Density profiles were measured for the downcast only. A hyperbolic tangent profile was fitted to the laboratory measurements as follows:

$$\rho(z) = \rho_2 + \frac{\Delta\rho}{2}\left(1 - \tanh\left(\frac{z + z_{pyc}}{h_{pyc}}\right)\right), \tag{6.1}$$

where z_{pyc} is the distance of the centre of the pycnocline measured from the surface, and h_{pyc} the pycnocline half thickness. For these experiments, measured z_{pyc} and h_{pyc} were 0.068 ± 0.010 m and 0.010 ± 0.006 m respectively.

Polystyrene floats, with lead weights embedded such that their density matched that of sea ice ($\rho_f = 910 \pm 6$ kg m^{-3}), were added to the surface of the water at around $x = 3.5$ m–5 m. This location was chosen to allow visualisation of the interactions of the ice and wave fully, prior to any interaction with the end wall, whilst also far enough from the gate that waves have passed through their sorting distance. Previous experiments of Carr *et al.* (2019*b*), in which real ice was used in a similar laboratory setting, have shown that the dominant properties of the ISW-ice interactions were due to the flow-structure interactions, rather than the material properties of the ice (such as temperature or elasticity). Hence weighted floats are deemed an appropriate substitute for real ice in this study, although it is acknowledged that real sea ice has rough bottom topography (e.g. Wadhams *et al.*, 2006), and multi-year ice (which is increasingly rare) can have large keels in its underside. The rough underside of sea ice could lead to enhanced wave dissipation and also lead to possible wave generation as the barotropic tide interacts with the underside of the sea ice (Zhang *et al.*, 2022*b*,*a*). Two reference locations A and B are identified at the right and left ends of the float respectively (figure 6.1), which are used to aid explaination of the dynamics later in the results.

To generate a mode-1 ISW, the gate was inserted at $x = 0$ m, and through a single sponge behind the gate, a further volume of ρ_1 density brine added, causing a downwards displacement of the pycnocline behind the gate. The volume of brine added behind the gate

was varied to alter wave amplitude, and was determined by the change in total fluid depth, measured before and after filling behind the gate. The total fluid depth after filling behind the gate was fixed at $H = 0.3$ m throughout the study. Whilst the generating volume, V is reported in table 6.1 as an indicative measure of wave size, it should be noted that the relationship between V and amplitude is not linear, in particular at very large amplitudes the wave passes the conjugate limit and further increases in volume manifest only as broadening of the wave (Grue *et al.*, 2000; Turner & Vanden-Broeck, 1988; Lamb & Wan, 1998; Lamb & Warn-Varnas, 2015).

The experiment was initiated by the vertical removal of the gate, which by producing a discontinuity and displacement of the pycnocline resulted in the generation of a mode-1 ISW. To enable the transition from ice-free to ice-covered waters, these experiments were performed without a lid, and therefore much of the tank had a free surface. Sixteen experiments are presented here with differing combinations of float sizes and wave generating volumes, summarised in table 6.1. Due to practical considerations, the shape of float was different for $L_f > 0.15$ m (where floats were rectangular) than for floats $L_f \leq 0.15$ m (where floats were circular).

Table 6.1: Table of experimental parameters for experiments presented in this chapter, showing experiment name, float length, L_f, wave amplitude, a, initial wave generating volume, V, float shape, wavelength, λ, and wave propagation speed, c.

Experiment Name	L_f (m)	Shape	a (m)	V (L)	λ (m)	c (m s^{-1})
100mm_Circ_20L	0.10	Circle	0.053	20	1.63 ± 0.08	0.118
100mm_Circ_30L	0.10	Circle	0.065	30	1.99 ± 0.08	0.128
100mm_Circ_40L	0.10	Circle	0.074	40	2.54 ± 0.03	0.125
150mm_Circ_20L	0.15	Circle	0.053	20	1.60 ± 0.13	0.113
150mm_Circ_30L	0.15	Circle	0.079	30	2.41 ± 0.46	0.130
150mm_Circ_40L	0.15	Circle	0.077	40	3.07 ± 0.50	0.111
350mm_Squ_10L	0.35	Square	0.031	10	1.55 ± 0.13	0.120
350mm_Squ_20L	0.35	Square	0.052	20	1.61 ± 0.06	0.107
350mm_Squ_30L	0.35	Square	0.072	30	2.12 ± 0.24	0.106
350mm_Squ_40L	0.35	Square	0.070	40	2.24 ± 0.08	0.114
2.4m_Rect_20L	2.40	Rectangle	0.053	20	1.67 ± 0.05	0.137
2.4m_Rect_40L	2.40	Rectangle	0.079	40	2.61 ± 0.05	0.131
1.2m_Rect_20L	1.20	Rectangle	0.052	20	1.65 ± 0.26	0.128
1.2m_Rect_40L	1.20	Rectangle	0.070	40	2.51 ± 0.49	0.136
350mm_Squ_20L_Rounded	0.35	Square	0.036	20	1.65 ± 0.07	0.140
350mm_Squ_30L_Rounded	0.35	Square	0.068	30	2.00 ± 0.21	0.115

6.2.2. *Flow and Float Quantification*

Fluid motion was viewed through the movement of light-reflecting neutrally-buoyant tracer particles within a vertical light sheet. These tracer particles were made of inert "pliolite" 150 µm–300 µm in diameter, and and by using two types with different densities had neutral buoyancy over the density range throughout the water column. A vertical section in the mid-plane of the tank was illuminated by a continuous collimated light sheet from an array of light boxes placed beneath the transparent base of the tank. Fixed digital video cameras recorded the particle motions within the light sheet. The cameras (UNIQ UP-1830CL-12B) were set up outside the tank, synchronised in time and positioned to have overlapping fields of view. They were centred in the vertical direction on the pycnocline to avoid distortion and perspective errors in the upper layer (including the pycnocline and float interactions). The cameras recorded at 30 f.p.s at 1024×1024 pixels resolution. Past experiments found the settling velocities of the seeding particles to be two orders of magnitude lower than the wave induced vertical velocities (Dalziel *et al.*, 2007). The continuous synoptic velocity, (u, w), and vorticity, ω, fields, in a given two-dimensional vertical slice (x, z) of the flow were quantified using Particle Image Velocimetry (PIV) in the DigiFlow software package (Dalziel *et al.*, 2007) using the most recent algorithm (2017a) with window size and spacing of 19×19, and 16×16 pixels squared respectively.

Wave properties were measured using the method described in Carr *et al.* (2019*a*) (their figure 2). The time series function of DigiFlow, which tracks changes of pixel values in a given column, row or defined line over time, was used to measure wave speed, c, and amplitudes, a. Tracing of the streamline coinciding with the pycnocline is possible through these time series due to the high concentration of seeding particles that collects at the density interface. It was not always possible to trace the exact same streamline based on height between runs, however, the closest available streamline to the pycnocline centre was always chosen. To calculate c, the time at which the interface reached maximum displacement was measured from vertical time series (constructed from a given column of pixels from each frame), and the wave speed calculated from the slope of these times, and the fixed x locations at which the time series were produced. Vertical time series were also used to measure wave amplitude; the maximum displacement of a chosen streamline, with this process repeated at three vertical cross-sections in order to measure variance. Finally, wave length, λ, was measured as twice the time interval between the streamline crossing half the maximal displacement ($z = -(z_{pyc} + (a/2))$), multiplied by c. Due to the combining of measurement errors in this approach, wavelengths reported in table 6.1

are an average of the measured wavelengths and DJL wavelengths, as described in §3.2.2, with uncertainty from the extremes of these four measurements. Fully non-linear DJL solutions have previously been shown to be in good agreement with laboratory waves (Luzzatto-Fegiz & Helfrich, 2014). The package (described in §2.1)was used to calculate a solution for each experiment with matching density profiles and wave amplitudes.

Dependent on the size of the floats, two techniques for visualising float motion were used. For floats with $L_f \leq 0.15$ m, the Particle Tracking Velocimetry (PTV) function in DigiFlow (Dalziel *et al.*, 2007) was used on videos from a downward looking camera, with the floats illuminated from above using an array of LED lights. This algorithm was employed using a blobs policy, using blob validation parameters that matched specific float sizes and shapes.

For floats with $L_f > 0.15$ m, due to the scale of the float in relation to the cameras' field of view, the PTV method was not suitable. Instead, float location was computed using videos from the side on cameras, employing an algorithm described as follows. The lower edge of the ice floats were identified in raw images from the videos by a combination of identifying peaks in light intensity which exceeded a prescribed threshold, and where those peaks were within a depth range that the float bottom would be expected to reside. Peaks in brightness intensity are expected to be found from the reflection and scattering of the vertical light sheet on the white underside of the float. For each column of pixels, pixels above the peak in intensity were masked. Hovmoller time series (horizontal time series constructed from a given column of pixels from each frame) of the movies from a row of pixels between the bottom of the float and the surface were taken, and the edges of the floats identified as the boundary of the mask, therefore providing a location for the float edge at each time step. The centre of the float (the float track) could easily then be calculated, and float velocities at each time step calculated by a Finite Differencing scheme. Whichever of these methods are used, throughout this chapter the observed floats from the laboratory experiments will be referred to as (Obsv.). The float tracks from multiple cameras were collated, and smoothing was applied to remove small errors that could arise due to this collation.

6.2.3. *Float Motion Model (FMM)*

In this section, a Float Motion Model (FMM) is developed and described in order to estimate float position from hydrodynamic data, whether that is theory, simulations, or measured. The robustness of the model will be compared to experimental measurements in section 6.3.1. The FMM assumes that the float moves at the average speed of the fluid

beneath it by solving the equation:

$$\frac{dx_f}{dt} = U(t) = \frac{\iint u(x_f(t), t)\, dx\, dy}{\iint dx\, dy}, \tag{6.2}$$

where $x_f(t)$ is the horizontal position of the centre of the float at time, t, U is the horizontal velocity of the float, and integration is performed over the spatial extent of the float. The reference surface velocity is defined as:

$$u(x,t) = u_{PIV}(x,z,t), \quad or \tag{6.3}$$

$$u(x,t) = u_{DJL}(x - ct, z) \tag{6.4}$$

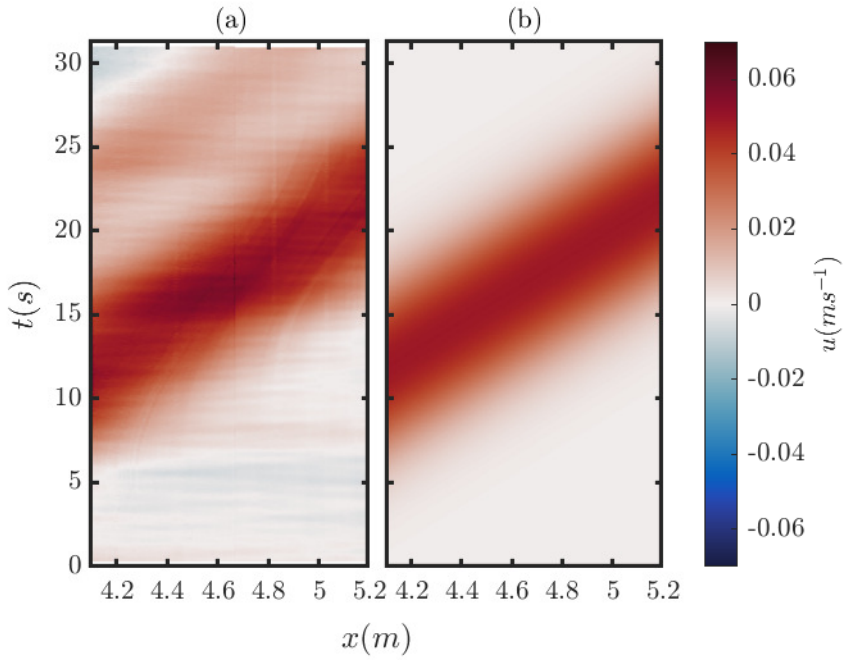


Figure 6.2: Hovmoller time series of the horizontal velocity for PIV laboratory measurements just below the lower surface of the floats (*a*) and for a DJL solution at the upper surface (*b*), as given by equations (6.3) and (6.4) respectively.

where u_{PIV} is the horizontal velocity field measured in the laboratory just beneath the base of teh float ($z = z_b$) and u_{DJL} is the horizontal velocity field computed from the fully nonlinear Dubreil-Jacotin-Long (DJL) equation (2.3) at the surface ($z = 0$). The DJL solution is transformed from a stationary frame of reference to a time-varying one as shown in equation (6.4). There is no physical float present in the DJL model, therefore solutions

of the FMM (equation (6.2)) with DJL velocities as input (equation (6.4)) provide reference states which can be compared with laboratory observations in which a float is present to assess the impact of the float on the flow. Examples of u_{PIV} and u_{DJL} are shown in figures 6.2*a* and 6.2*b* respectively. Note that other input signals could also be employed (e.g. a numerical model).

The FMM equation (6.2) is solved in the following way. Given the velocity field and float position at $t = t_n$, along with the updated velocity field at $t = t_{n+1}$ the float's position, x_f, is updated using a fourth-order Runga-Kutta time integrator. The grid points containing the float at time t are identified, and an average (weighted by the width of the float at each x position) velocity is calculated where the fluid velocity is assumed to be constant in the y direction, to account for the shape of the float. The model is a version of Lamb (1997) adapted for float lengths longer than the grid spacing. Throughout, when the experimental PIV velocity, u_{PIV}, is utilised in the FMM it will be referred to as FMM/PIV, and when DJL solutions, u_{DJL}, are used it will be referred to as FMM/DJL.

6.3. Results

6.3.1. *Motion of floats*

The wave-induced horizontal flow in the upper layer is oriented in the same direction as wave propagation. As the wave approaches the fluid is accelerated in the same direction as the wave. After this point the fluid decelerates as the wave passes (see figure 6.2 for example).

Consequently, as a result of this wave-induced flow, floats (Obsv.) travel in the same horizontal direction as the wave, accelerating as the wave approaches and decelerating once it passes. The observed floats never quite reach the same speed as the wave, and so the float moves backwards in a frame of reference moving with the wave, and after passing through the mid-point of the wave, slows (in a stationary frame of reference) (figure 6.3). Figure 6.3 shows experimentally measured float motion for three different float sizes, where the initial generating volume is held constant ($a = 0.0525 \pm 0.0005$ m), and so only the float changes (within experimental variability). In experiments, due to reflection of the wave from the end wall of the tank, the tracks of floats follow a bell shape, indicating transport of the float by the reflected wave. The bell shape seen in figure 6.3 is due to the wave being reflected off the end wall of the flume and subsequently transporting the float back upstream. With increasing float length, L_f, the total travel by the float decreases, seen in the difference between the 2.4 m float, which moves 0.1 m and the 0.1 m floats, which

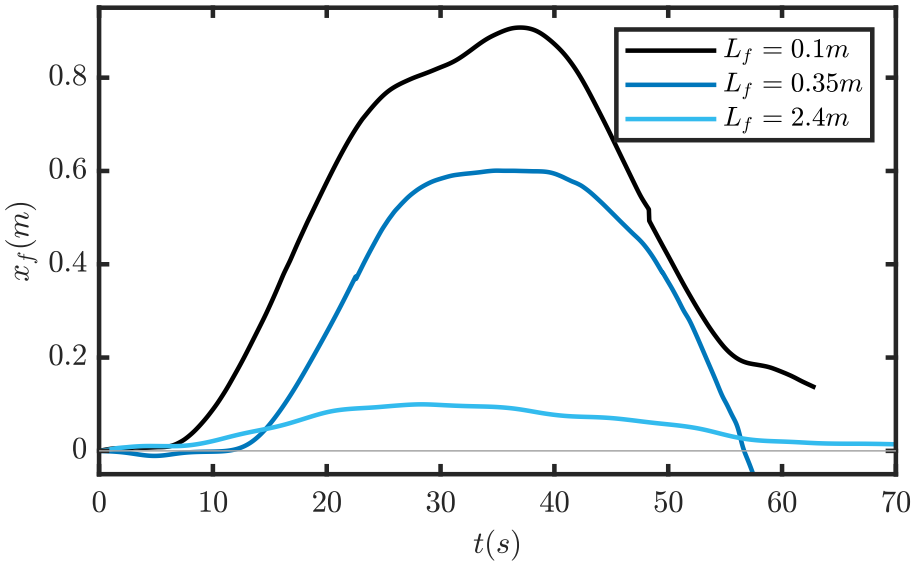


Figure 6.3: Time series of experimentally measured float location during the passage of an ISW for three floats of varying lengths, experiments 100mm_Circ_20L, 350mm_Squ_20L and 2.4m_Rect_20L. x location is relative to the initial position of the float.

move 0.9 m in figure 6.3.

To demonstrate the efficacy of the FMM in predicting the actual motion of the float, the motion of the Observed floats is compared with the FMM applied to PIV observations (FMM/PIV) in figure 6.4. Positions A and B on the float are hereafter defined as the edge of the float which is first impacted by the wave, and the opposite edge respectively (figure 6.1). The velocities at these points (i.e. $u(A) = u(x_f - \frac{L_f}{2}, t), u(B) = (x_f + \frac{L_f}{2}, t)$ are shown to indicate the range of fluid velocities influencing the float at any given time. The float velocity over time, as well as the fluid velocities at the endpoints of the float (A and B) are shown (figure 6.4). Firstly considering FMM/DJL, for small floats (figure 6.4*a*), the floats essentially act like buoyant tracer particles, and the float velocity closely follows a sech^2-like profile. U peaks at almost the same height as $u(A)$ and $u(B)$. This float velocity profile is situated between the similar shaped curves at point A and point B. To explore the impact of differing float sizes and wave amplitudes, following the results of Carr *et al.* (2019*b*), L_f/λ is used here as a nondimensionalised float length, the full nature of this relationship will be explored later. As L_f/λ increases, the float velocity profiles undergo two changes. Firstly, the maximum float velocity falls, and the curve widens, and by $L_f/\lambda = 1.6$ (figure 6.4*g*), a clear flat top to the curve is present. Secondly, a slight asymmetry of the peak, such that the rising limb is longer than the falling limb can be observed (figure 6.4*d, g*). For smaller L_f/λ, the $u(A)$ and $u(B)$ curves are broader, due to

the length of interaction with the wave at these points being increased by the float moving with the wave.

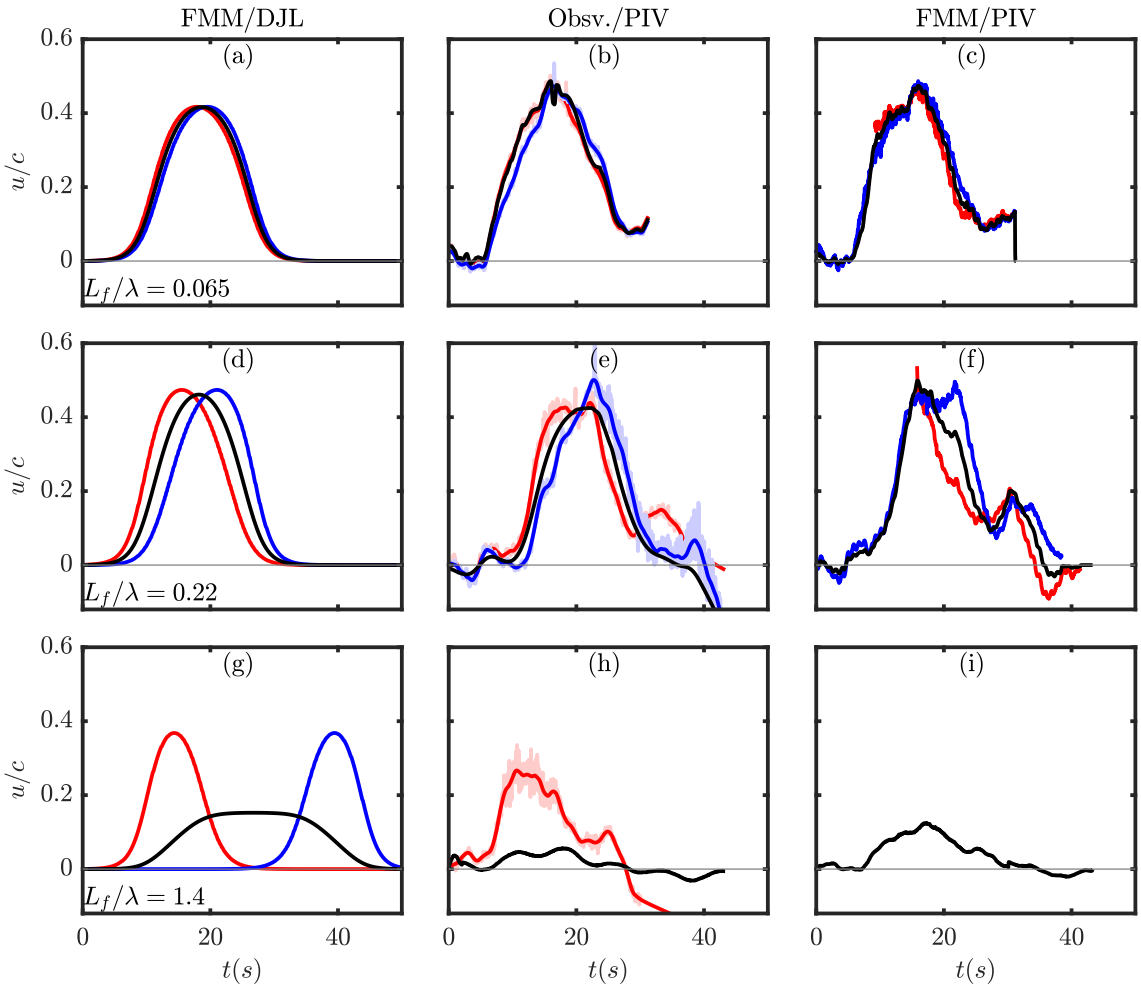


Figure 6.4: Time series of float velocity (black) during the passage of an internal solitary wave for three floats of varying lengths (*a-c* representing $L_f = 0.1$ m, *d-f* representing $L_f = 0.35$ m and *g-i* representing $L_f = 2.4$ m), and the horizontal fluid velocity at points A (red) and B (blue) on the float. Note that the y axis label u/c is actually U/c for all black traces. Left column (*a, d, g*) shows the FMM applied to DJL velocity data, the central column (*b, e, h*) shows the observed float motion, and right column (*c, f, i*) showing the FMM applied to observed PIV velocities. All velocities normalised by the internal wave propagation speed, c, and smoothed PIV velocities shown in the central column (smoothed lines in dark colours, faded colours the original).

The measured U, and u at points A and B from PIV (Obsv./PIV) are in good agreement with the FMM/DJL solutions, albeit with experimental noise/error (figure 6.4*a,d,g* compared to *b, e, h*). The changes in velocity profiles as L_f/λ increase match those for the FMM/DJL, as do the overall shapes of profiles, indicating the suitability of this model. Figure 6.4*g* and *h* show that U_{max} for the longer floats were overestimated by the FMM/DJL solutions.

This discrepancy can be explained by the fact that FMM/DJL does not contain a real float, and so does not capture the flow features documented for longer floats in section 6.3.2. Differences between the FMM/DJL and laboratory observations are to be expected as the float size becomes non-negligible. Some interactions with the tank side wall were observed for the longest floats, which may have further slowed the float movement. When further comparing to FMM/PIV (modelled float velocity based on PIV measurements), the signal is considerably noisier, indicative of amplification of observational error and noise by the model. However, broad patterns can still be identified as being in good agreement (figure 6.4*c, e, h*) with both the FMM/DJL solutions, and Obsv./PIV. Any interactions between the float and the flow will also be reflected in those models, in a way that DJL cannot reflect. Note that for the largest floats, the width of the experimental viewing window is insufficient to measure $u(B)$.

These results show that a DJL wave applied to the model (FMM/DJL) gives a good understanding of float motion, despite no real float being present in the model. The good agreement between FMM/DJL and laboratory float motions indicate that the background ISW-induced flow is the main parameter controlling the float transport.

Figure 6.5 are a representation of the FMM, showing distribution of wave-induced velocities influencing a float for each timestep, explaining observed behaviours. For small floats (figure 6.5*a*), the range of wave-induced velocities being experienced by a float at a given time are small, and as a result U closely matches the motion of fluid parcels, similar to Lamb (1997). As the float size increases, at any given time, the float is under the influence of fluid travelling at a range of spatially varying wave-induced velocities. This results in the float propagation speed being slower than the maximum wave-induced fluid velocity, influenced by the fluid either side of the wave centre, which has lower velocities. Extended yet further, once $L_f \gg \lambda$ (figure 6.5*c*), the entire wave can be under the float, and much of the float is influenced by the non-moving fluid (the PDF is dominated by $u/c = 0$). As a result U (as the average of this distribution) is much slower than the fastest wave-induced fluid speeds (e.g. the red and blue lines), and interaction time increases. This model therefore explains the relationship of faster U_{max} with smaller values of L_f/λ.

Given the good agreement between the FMM/DJL model and the laboratory observations, the relationship between float size, wave size and the motion of the float can be explored using FMM/DJL. Figure 6.6 (*a*) shows the relationship between float length, L_f, and maximum float velocity, U_{max}, for a small ($a = 0.0351$ m) DJL wave. Figure 5 (*a*) shows that $U_{max}/c \propto \text{sech}^2(L_f)$, and maximum float speed decreases with increasing float length, his sech^2 relationship arising entirely empirically. The effect of increasing the wave

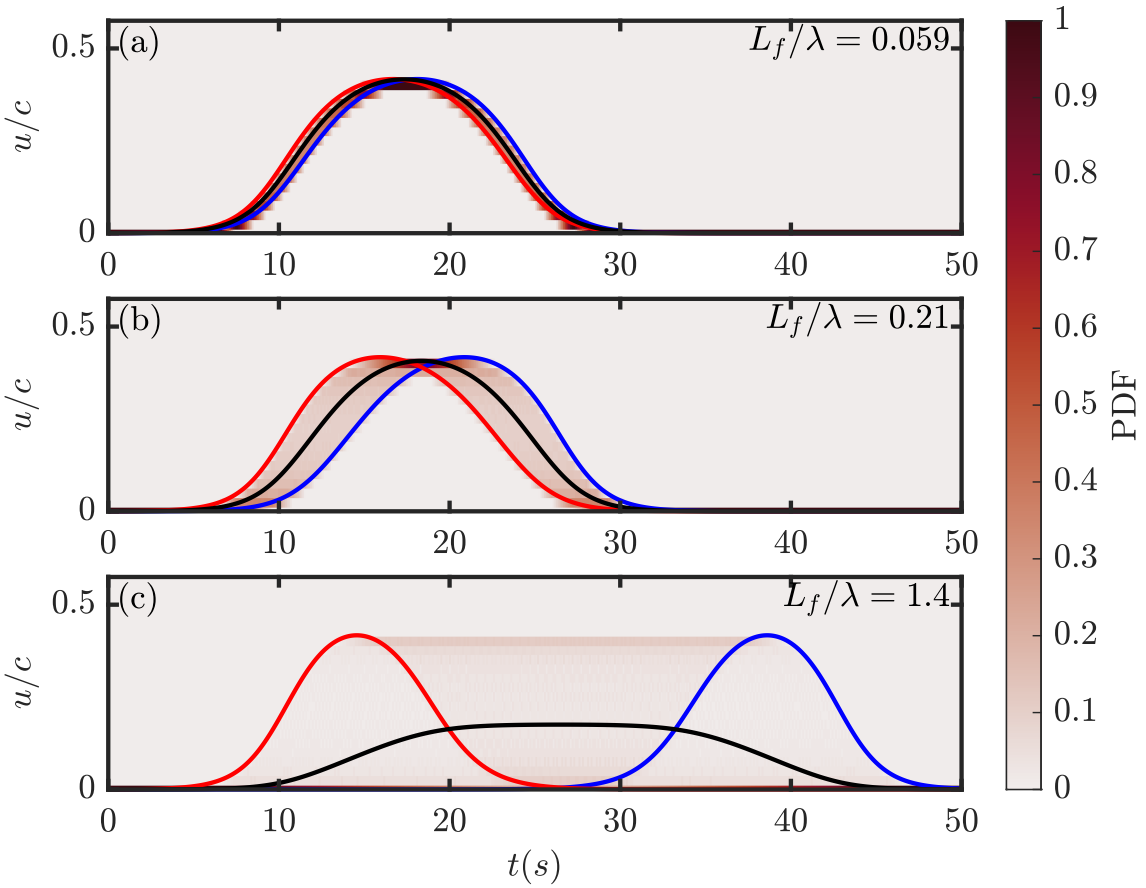


Figure 6.5:]
Histogram time series of fluid velocities between Point A (red trace) and Point B (blue trace) (i.e. under the float) for the FMM applied to DJL waves (FMM/DJL), showing the probability density function (PDF) of fluid velocity. The same DJL wave is used for each simulation, with only float size varying from $L_f = 0.1$ m (a), $L_f = 0.35$ m (b) and $L_f = 2.4$ m (c). All velocities normalised by the internal wave propagation speed, c.

amplitude, a, is to increase the maximum float speed, although the effect is stronger for a very small float ($L_f = 0.1$ m, figure 6.6*b*, blue line) than for larger floats (red line, figure 6.6*b*). To capture these behaviours, a parameterisation of the wave-induced float motion is captured by the following relationship:

$$\frac{U_{max}}{c} = \left(b_0 \frac{a}{H} + b_1\right)\left(\text{sech}^2\left(\frac{L_f}{b_2\lambda + b_3}\right) + b_4\right) \tag{6.5}$$

where $b_0 = 1.2458, b_1 = 0.1538, b_2 = 0.6681, b_3 = -0.1870$, and $b_4 = 0.2233$, are calculated empirically using a Matlab least squares fit. The goodness of fit measure between this parameterisation and observations is $R^2 = 0.9969$ when ($n = 2940$) FMM/DJL

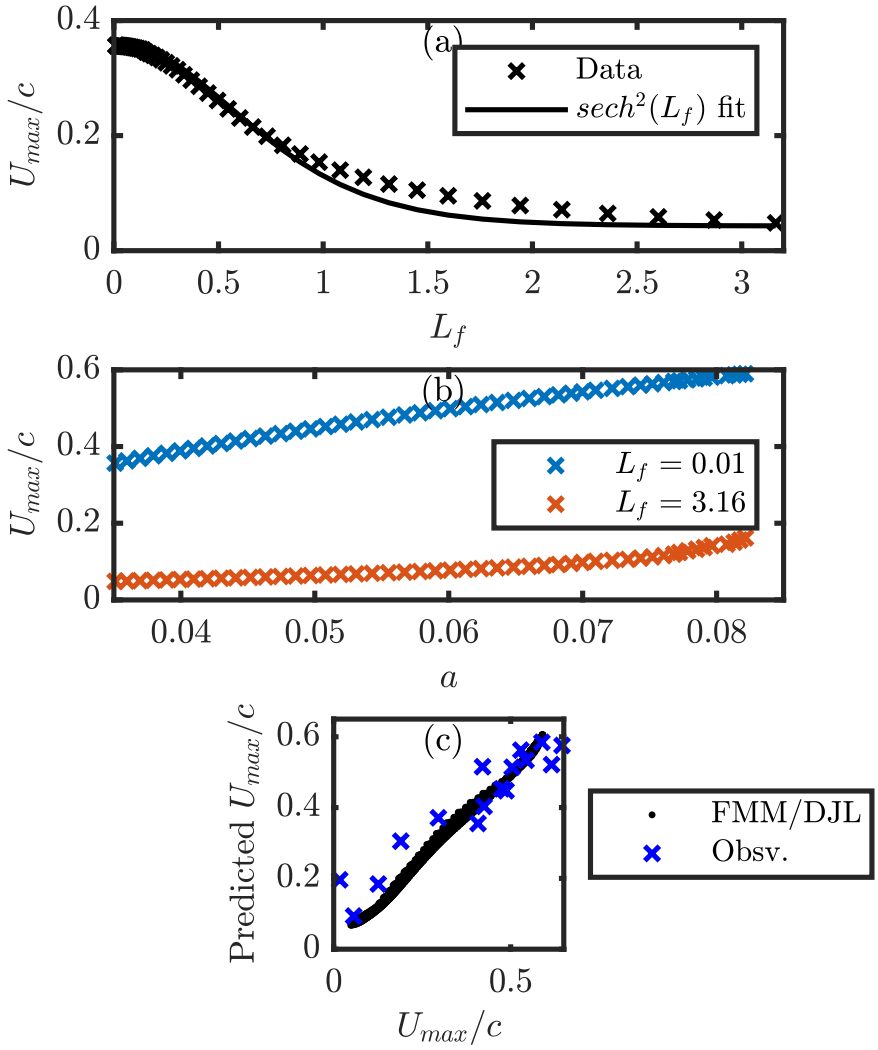


Figure 6.6: Indicative illustrations of the relationship between (a) float length, L_f, and maximum float speed, U_{max}/c, from FMM/DJL, (b) wave amplitude, a, and U_{max}/c, and (c) goodness of fit of equation (6.5) to observations for the FMM/DJL (black dots) and direct measurements from the laboratory experiments (blue x), with R^2 indicated for the FMM/DJL solution.

solutions are used, and $R^2 = 0.8579$ when Obsv./PIV measures are utilised (figure 6.6c). Given the large uncertainty in some experimental wavelengths (table 6.1), this is still a particularly good result.

6.3.2. *Observations of float interactions with internal wave-induced flow*

For smaller floats, flow does not deviate from the baseline of an ISW with no floats. However, as floats become larger (observed for $L_f \geq 0.35$ m), they begin to interact with the flow, resulting in new flow features being seen. In particular, when the float accelerates

as the ISW approaches, a separation bubble, evolving into a clockwise vortex forms attached to the float at point A (figure 6.7*a-d*, blue region of vorticity). As the float starts to move, a jet initially forms down under the float at point B (figure 6.7*b, g*, red region of vorticity), which as the float speed increases, evolves into a counter-clockwise vortex at point B (figure 6.7*c*, red region of vorticity). As the mid-point of the wave passes point A, the vortex there stagnates and declines (figure 6.7*d, e*). Once the mid-point of the wave passes point B, the float begins to slow, and the vortex at point B detaches from the float, initially forming a vortex of opposite polarity in the lee of the float (figure 6.7*d*, blue vorticity). Then, as the wave continues to overtake the float, the vortex is transported in the same direction as the wave (figure 6.7*e*). At larger wave amplitudes (figure 6.7*f-j*), the size of these vortex structures increase. Additionally, the clockwise vortex formed at point A is advected forward under the float, whilst remaining attached (in positive x direction, figure 6.7*h, i*). An additional vortex forms at point A again.

At larger L_f, (figure 6.8), the overall structures formed in the flow are the same, but at point A there is a further tendency for the vortices to be transported upstream (figure 6.8*c, d*), and for multiple clockwise vortices to be formed along the base of the float (indicated by black arrows in figure 6.8*c, d, g*). Due to the length of the float, features at B were not visualised, but were observed to resemble those for smaller L_f floats.

To investigate the role of the shape of the float edge on these dynamics, a pair of experiments:
350mm_Squ_20L_Rounded and 350mm_Squ_30L_Rounded were carried out with a rounded edge to the floats (figure 6.9). For the larger wave, a similar set of dynamics are observed to the comparable experiment with a sharp corner, but the vortex formed at A was smaller (figure 6.9*h*). Whilst the jet forms at B, no vortex forms here (figure 6.9*h*). The smaller wave extends this trend further, with no vortex forming at A either (figure 6.9*b, c*), although the other similar flow features continue to evolve in a similar manner, including the formation of a small detached vortex at point B as the wave passes (figure 6.9*d*).

6.4. Discussion

6.4.1. *Application of theory to understand the flow and floats*

The motion of the floats is here modelled using a simple model, which, without using energetic arguments, assumes the float moves at the average velocity of the fluid in contact with the float. The model gives strong agreement with past work (e.g. Carr *et al.*, 2019*b*), and with experimental results presented here, and so can further be used to understand the

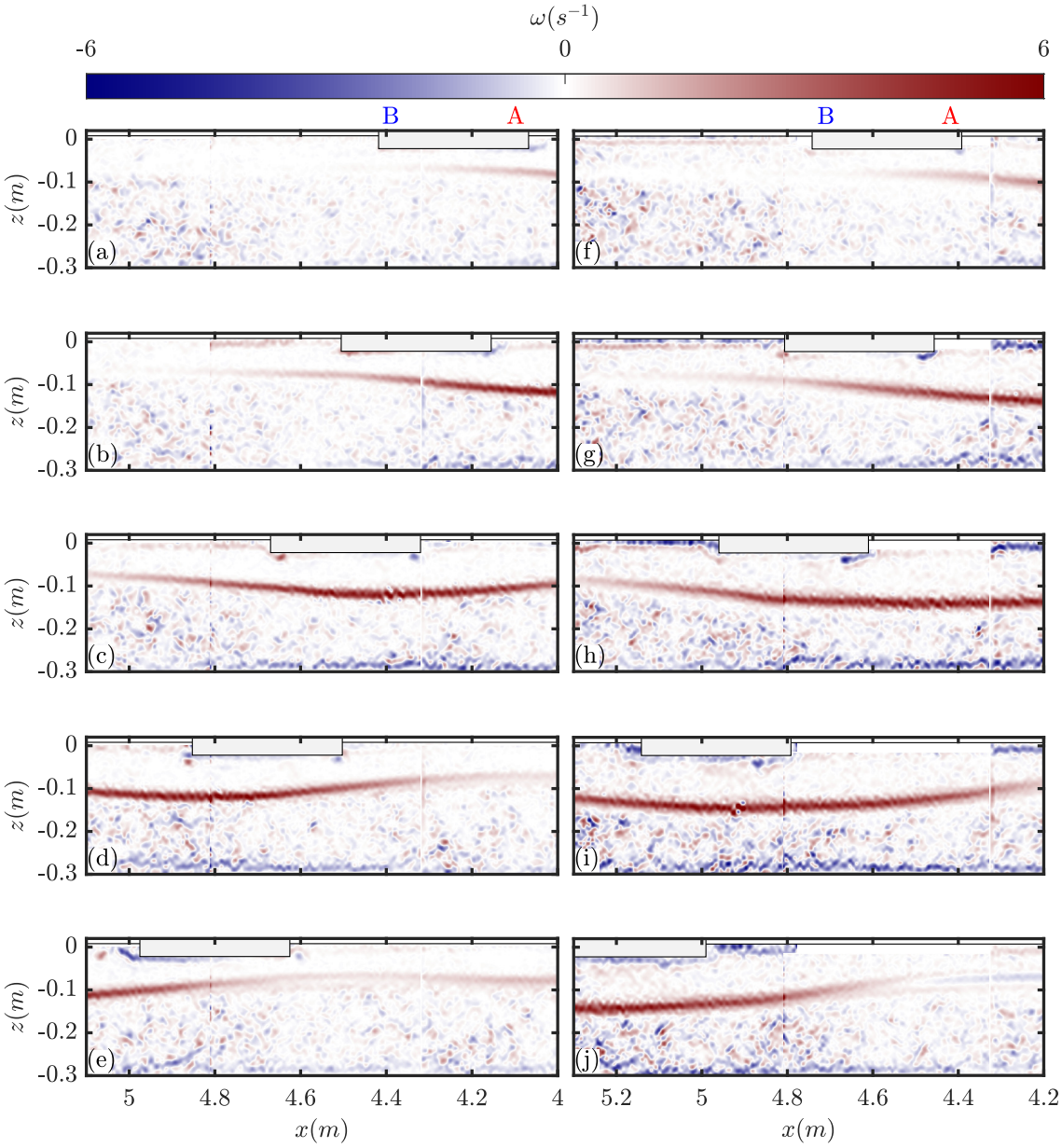


Figure 6.7: Time sequences showing medium float experiments for a small amplitude wave (350mm_squ_20L, left) and large amplitude wave (350mm_squ_40L, right). The colour scheme displays vorticity. The observed location of the float is overlaid to aid visualisation. Time interval between images is Δt = 4 s. Note that images are made up of images from three cameras merged to form a single image. Corresponding movies of the experiments (supplementary Movie 1 & Movie 2) are provided for additional clarity.

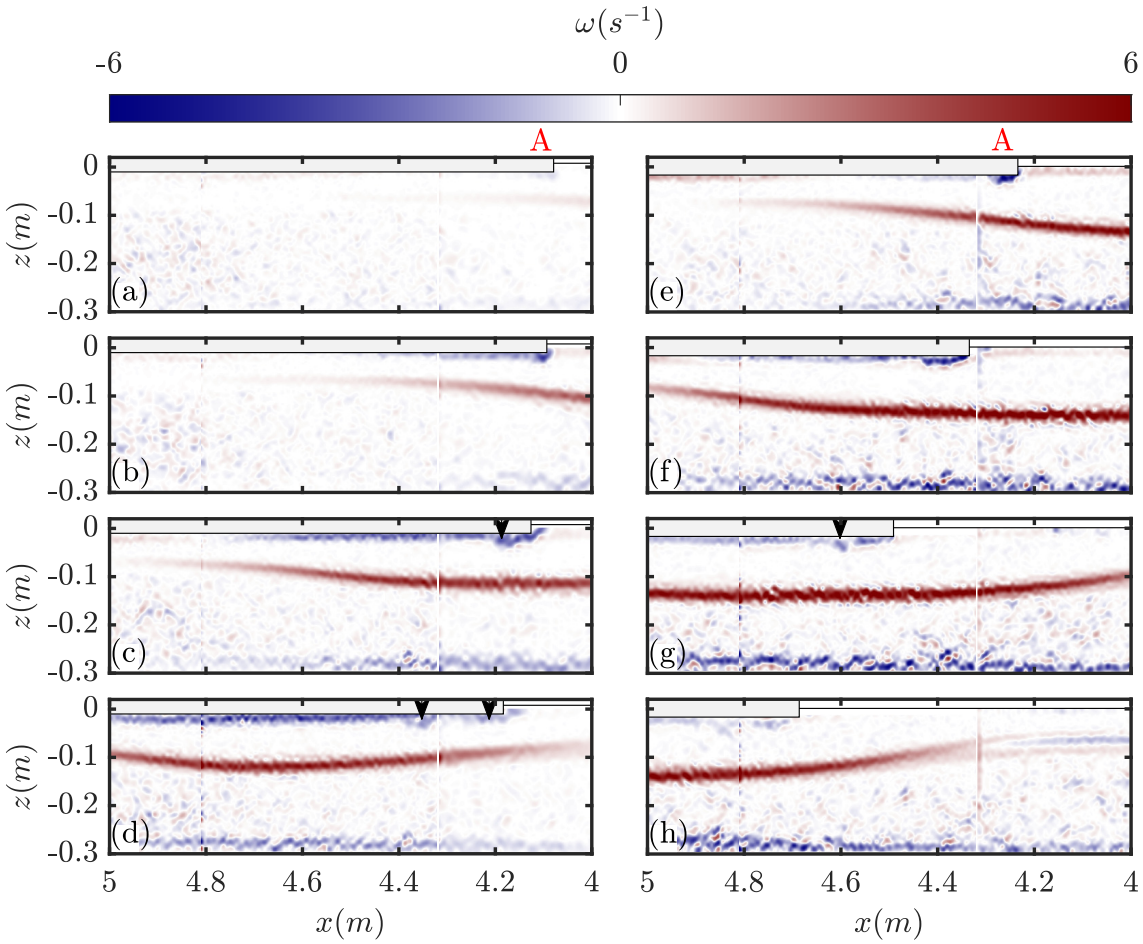


Figure 6.8: Time sequences as in figure 6.7, but showing long float experiments for a small amplitude wave (1.2m_rect_20L, left) and large amplitude wave (1.2m_rect_40L, right). Time interval between images is $\Delta t = 4$ s. Corresponding movies of the experiments (supplementary Movie 3 & Movie 4) are provided for additional clarity.

patterns of flows described in §6.3.1. Past work has applied a full calculation of the forces invoked on floating structures under the influence of ISWs through an adapted Morison formula (e.g. Song *et al.*, 2011; Wang *et al.*, 2018), but such complexity has not been necessary here, providing a more intuitive result for the motion pattern of ice, and similar floating bodies. Intuitively, the result of larger floats travelling less fast would appear to be due to the increased mass relative to the wave, and to reach the same speeds the force exerted on the float by the wave would need to increase accordingly. However, the good fit between the FMM (which does not take into account these forces, or any energy transfer) and laboratory observations indicates that this relationship is in fact a more simple outcome of the basic behaviour of the ISW-induced flow, and increasing influence of the still water either side of the wave as float size increases. Estimating the efficiency of energy transfer

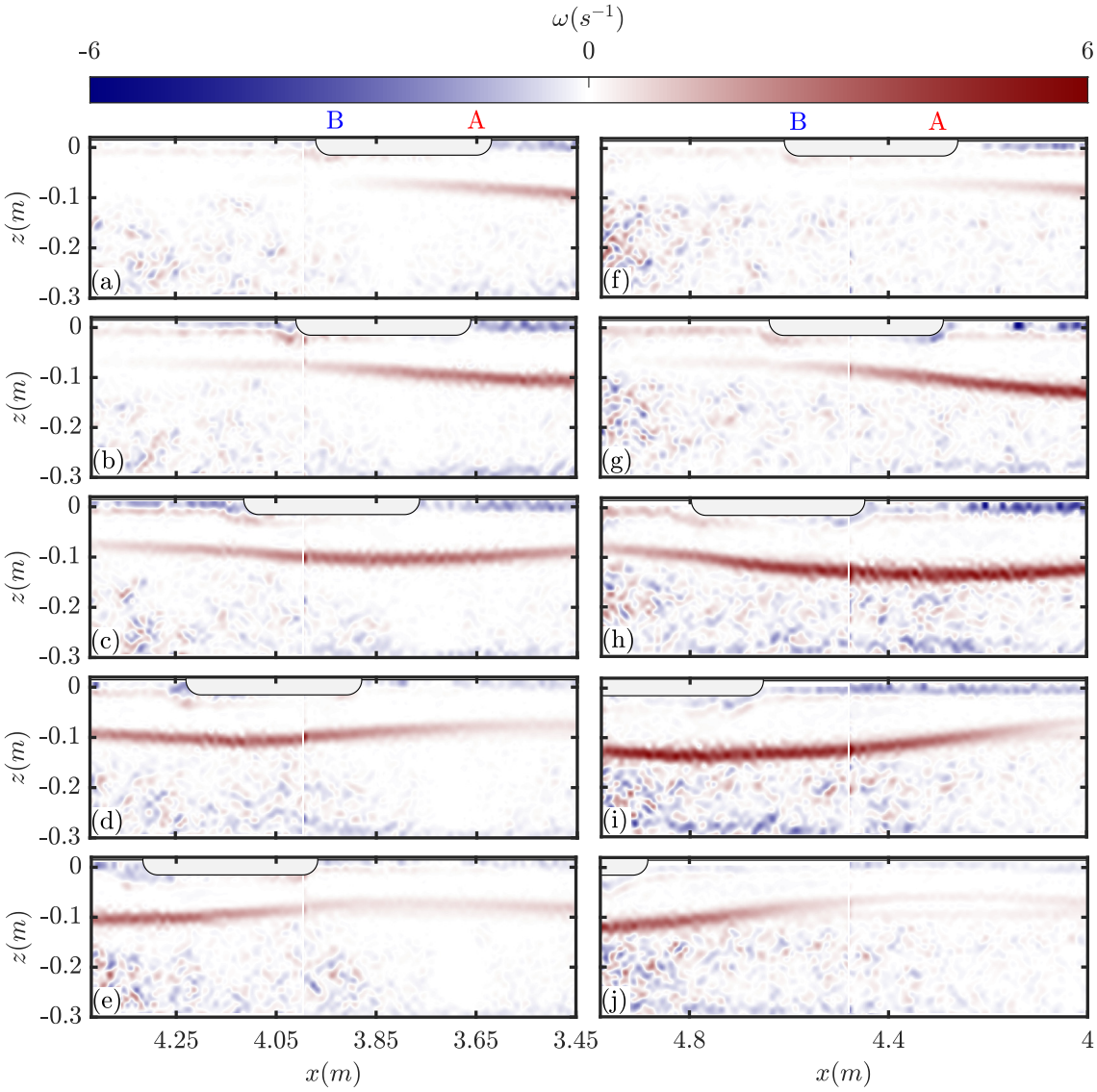


Figure 6.9: Time sequences as in figure 6.7, but showing curved float experiments for a small amplitude wave (350mm_squ_20L_C, left) and large amplitude wave (350mm_squ_30L_C, right). Time interval between images is Δt = 2.8 s and 4 s for the left and right sides, respectively. Corresponding movies of the experiments (supplementary Movies 5 & Movie 6) are provided for additional clarity.

between the wave's Available Energy (AE) and float's maximum Kinetic Energy (KE_f, at the point at which $U = U_{max}$) as:

$$KE_f = 0.5 M_f U_{max}^2, \tag{6.6}$$

$$AE = APE_{DJL} + KE_{DJL} \tag{6.7}$$

where M_f is the mass of the float, U_{max} is taken from experimental observations, APE_{DJL} and $KE_{DJL} = u^2 + v^2$ are the estimates of Available Potential Energy and Kinetic Energy from the DJL solution of the experimental waves. The efficiency of transfer is defined to be KE_f/AE. Over all experiments studied the maximum efficiency of energy transfer was between 0.06 % and 2.8 %, indicating the float takes a very small proportion of the available energy from the wave system in each case. The efficiency in energy transfer was seen to increase slightly as float size increased.

To understand the features observed in §6.3.2, the vortex features formed by the ISW-ice interaction are here discussed in the context of boundary layer flows, and specifically theory developed for elongated bluff body aerodynamics (e.g. van der Kindere & Ganapathisubramani, 2018; Aleyasin *et al.*, 2021). To understand such features, it is the velocity relative to the boundary layer that matters. Usually in internal wave studies, a fixed boundary layer means this is simply the flow field in a fixed frame of reference, but in this case it is valuable to consider the boundary layer flow using an adjusted horizontal velocity, so that we are considering the PIV velocities of wave-induced flow relative to the float's measured motion.

In a stationary reference frame, the initial formation of the vortex at point A can be understood as a separation bubble and instability resulting from the reverse flow, similar to Aleyasin *et al.* (2021) (their figure 5e). At point A, as the wave approaches, a flow in the same direction as the wave is found in the upper layer (figure 6.10*a, b*). As the flow approaches point A, it decelerates due to the obstacle, and stagnates. This deflects and concentrates the flow under the float, such that there forms a separation bubble (figure 6.10*c, d*). A similar vortex feature was previously observed in an ISW context by Talipova *et al.* (2013) (their figure 8) over a fixed step, but the formation and evolution was not discussed in detail.

However, the vortex at point B forms whilst the velocity (in a stationary reference frame) is approximately equal to zero (figure 6.10*a*). When the reference frame of the float is considered ($u - U$), the horizontal velocity becomes negative at point B (figure 6.10*b*). This builds up a region of pressure ahead of point B, which manifests as a jet of fluid towards $x = 0$. Simultaneously at point A, the flow velocity induced by the wave is always faster than the floats ($u - U > 0$), causing a deceleration and stagnation of the flow behind the float (figure 6.10*h*, as seen in the non-adjusted flow). As a result, there is deflection of the flow below the float, producing a separated and recirculating region at the corner, manifesting as a vortex with opposite vorticity to the surrounding fluid. By the point the wave is mid-way across the float, $u - U > 0$, and the vortex at B is advected,

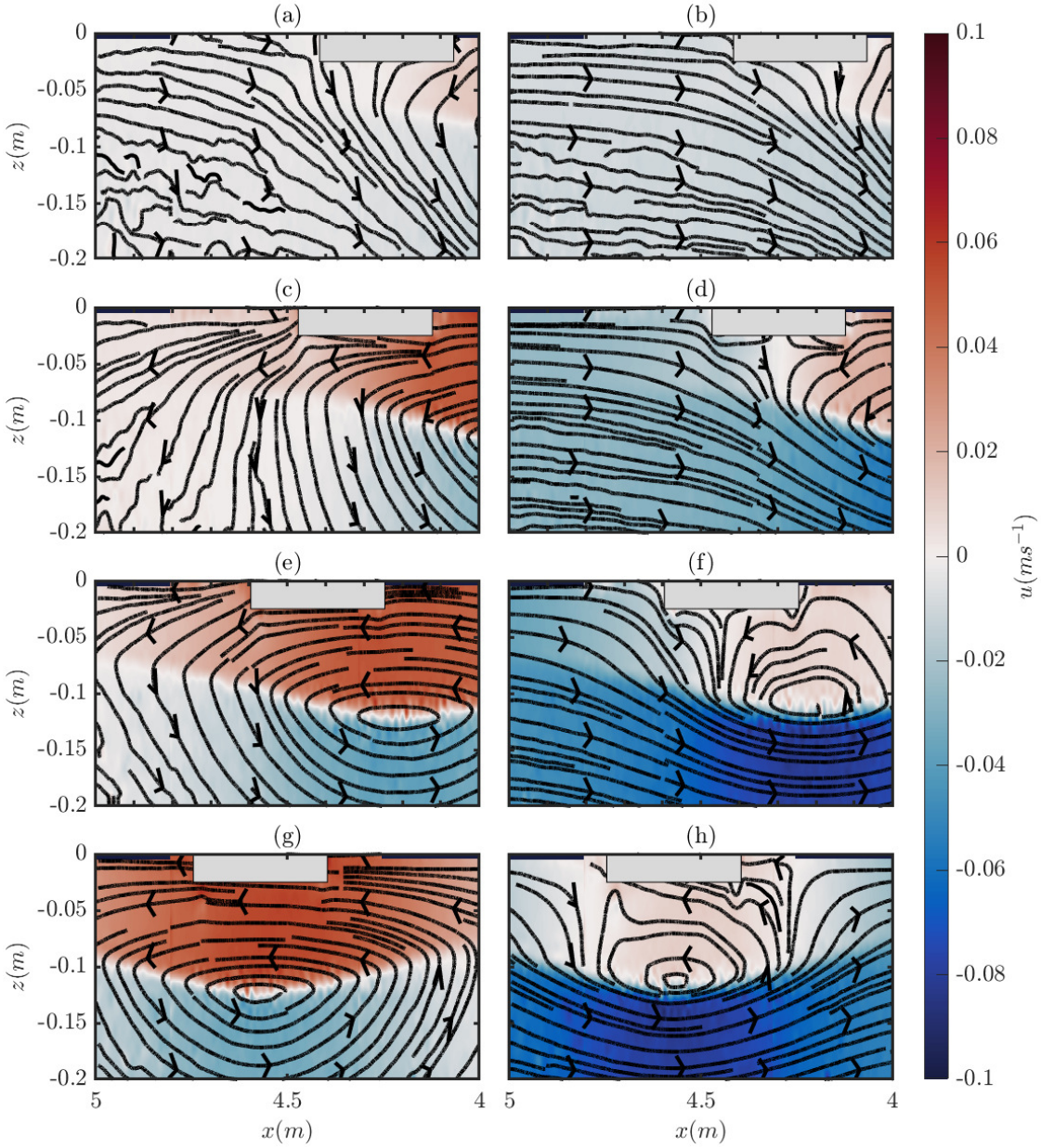


Figure 6.10: Time sequences showing the medium float experiment 0.35m_squ_20L, for a stationary frame of reference (left) and a frame of reference relative to the float velocity (right). The colour scheme displays horizontal velocity, and overlaid are streamlines. The location of the float is indicated. Note that images are made up of images from three cameras merged to form a single image.

leading to an attached vortex in the lee of the float (figure 6.10*h*), similar to Aleyasin *et al.* (2021) (their figure 5a, c, e).

As the float continues to travel at $U < c$ the wave begins to overtake the float, during which process, the vortices at points A and B persist (figure 6.10*f*), before $u(A) - U$ approaches 0 (as U reaches U_{max}, and u decreases at the tail of the wave), and the flow becomes unfavourable for the vortex. Simultaneously, the vortex at point B are shed towards positive x, since $u(B) - U > 0$. The presence of these features has the effect of reducing the wave-induced velocities at the wave-float interface, and therefore also the float velocity, as seen by the difference between both $u(A)$ and U in figure 6.4 (*g, h*).

The identification here of a relationship between L_f, λ and a (equation 6.5) further simplifies the understanding of the motion induced by ISWs. However, the surprising result that this relationship takes the sech^2 form is as yet unexplained.

6.4.2. *Field Scale*

Past studies on the interactions between waves and ice have indicated the ratio between L_f and λ is critical for understanding the different flow regimes involved (e.g. Bennetts & Williams, 2015; Carr *et al.*, 2019*b*) for surface and internal waves, respectively. Therefore, the overall approach here to scaling to the field scale is studying the ISW-ice interactions at a complete range of ratios of L_f/λ. Figure 6.4 indicates the success in moving through a range of regimes, implying results are applicable to float sizes of all scales studied, with the expectation that these trends will continue as L_f becomes very small or large.

Following Timco (1980); Bennetts *et al.* (2015); Bennetts & Williams (2015), the density difference between the floats and surface fluid is comparable to that in the field, which allows the results to be scaled effectively between laboratory and field scales. Whilst the surface fluid density was chosen primarily to optimise visualisation with the pliolite seeding, this also coincided with the surface water density of the ocean, so that both the surface and float densities also match those in the field.

Various other scales can be applied to scale flows, the most commonly used are the Reynolds number, $Re = UL/\nu = cH/\nu$ where U, L are indicative velocity (not float velocity as elsewhere in this chapter) and length scales, here taken to be c and H respectively (formulation from Hartharn-Evans *et al.* (2022)). The Froude number, $Fr = U/\sqrt{gL}$ is also a useful scaling term. Assuming $\nu = 10^{-6}\text{m}^2\text{s}^{-1}$, typical values for the field are $Re \approx 10^6 - 10^8$ and $Fr \approx 0.001 - 0.01$. Typical values for these experiments are $Re \approx 3\times10^4$ and $Fr \approx 0.06$. The density of the fluid in the bottom layer ($\rho_2 = 1049\,\text{kg}\,\text{m}^{-3}$) was chosen to make $\Delta\rho$ as large as practically possible. The impact of a higher $\Delta\rho$ in these experiments

is to increase the wave speed, acting to counter the effect of smaller length scales in the wave speed, and therefore Froude number. Differences in *Re* are unavoidable at these small scales, but are in line with previous laboratory studies.

6.4.3. *Roughness and Shape of floats*

Experimentally, sweeping all possible parameters related to this interaction problem is practically not possible, but existing literature can indicate how the interactions may occur for other parameters.

The flow features induced by the presence of floats in an ISW are a special case of flow over elongated bluff bodies, a phenomenon well studied due to it's application in aerodynamics in engineering (e.g. automotive vehicles) (e.g. van der Kindere & Ganapathisubramani, 2018; Aleyasin *et al.*, 2021). However, spatio-temporally varying flow and motion of the float complicate the situation in comparison to a fixed body in constant flow. Such studies identify the edge roundness of the body as a key factor in the formation of vortices associated with separation, and for this reason a pair of experiments were carried out with rounded edges. Whilst some reduction in the strength and extent of these features was identified (most notably in the smaller wave experiment), the pair of counter-rotating vortices at each end of the float could still be formed, albeit at larger wave amplitudes than for a sharp corner.

An aspect of the interaction of particular oceanographic interest is diapycnal mixing induced by the interaction. Here this is not measured, due to experimental difficulties in doing so. Past results of Carr *et al.* (2019*b*) are indicative of enhanced Turbulent Kinetic Energy dissipation at the ice-water interface, associated with the ISW-ice interaction, indicating enhanced energy loss from the wave due to the interaction, but not necessarily diaypycnal mixing. However, in that study, the formation of Kelvin-Helmholtz (K-H) instability on the pycnocline in experiments with a deep ice in comparison to the pycnocline depth were indicative of enhanced diapycnal mixing in that case. Although the vortex features in these experiments at times reached depths comparable to the pycnocline depth, z_{pyc}, these only occur at times when the pycnocline is displaced by the wave, and so do not interact significantly with the pycnocline. It is assumed that in the present experiments, mixing was not significantly enhanced. Such changes can be captured based on a blocking ratio, for example, the one used for a stationary step in Talipova *et al.* (2013). The ratio compares the pycnocline depth, amplitude, and depth of the float, as $B = \frac{h_1 - h_f}{a}$, where h_f is the height of the step, and is used to identify five regimes of interaction. The level of interaction with the step increased with increasing B, from the formation of

K-H instability on the pycnocline, through to total reflection of the incident wave. The interactions identified here align with those for a weak interaction in Talipova *et al.* (2013)'s experiments, with the motion of the float here becoming an important factor in reducing the intensity of these interactions. Carr *et al.* (2019*b*) also identified changes to the shape of the pycnocline in experiments where the pycnocline distance from the base of the float were much less, corresponding to Moderate-Strong interactions in the Talipova *et al.* (2013) system of regimes, overall indicating an applicability of these regimes even to a moving obstacle, as in the case of ice.

In applying to the field, the interaction between pressure gradients induced by surface waves, and wind, would also need consideration in conjunction with the ISWs, both in terms of the motion of ice, and the flow features induced by the relative motions of the ice and fluid. A final aspect that is likely to be important in a real-ocean system is the interaction of multiple floats, where field observations indicate effects linked to the concentration, where dissipation of the IWs under ice is maximum at intermediate concentrations (Cole *et al.*, 2018), and which should be considered in future work.

6.5. Conclusion

Here, the interactions between laboratory ISWs and free-floating objects representing sea ice are investigated to a simple system of a single float. Reducing the system to this single-float system interacting with a single ISW has allowed isolation of the processes and behaviours for the first time. Applying a simple model of float motion based only on the average fluid velocity in contact with the float helps to understand the behaviours that are observed in the laboratory. The development of this model makes it possible to predict the motion of a floating parcel associated with any near-surface ISW-driven velocity field, and is validated by the use of laboratory experiments. Not only is the FMM itself simple, but it can easily be applied to analytic models which take seconds to solve, rather than hours or days as required by full Navier-Stokes solving numerical models. Float velocity was dependent on both the amplitude of the wave and the length of the float, with larger waves inducing stronger motion. For larger floats, the length of interaction increases, but with a reduction in maximum velocity. Carr *et al.* (2019*b*) initially investigated this dependency on L_f and λ, but the exact nature of the relationship is now captured in equation (6.5), which can only be identified using the larger dataset enabled by this FMM and DJL solutions. The exact nature of the flow and float dynamics exists as a result of non-stationary nature of both the flow, and the float. The good fit with an energy-less model (and with DJL waves)

indicates energy transfer was low, in particular for small floats, and despite an intuitive explanation for the relationship between L_f/λ and U_{max}/c based around the increasing mass/inertia of the float, such a relationship is here explained by the form of the solitary wave velocity profile alone - that is the effect on the float's velocity of the still water either side of the wave.

As sea ice in the Arctic Ocean thins and retreats, moving to an Arctic dominated by seasonal, rather than multi-year sea ice, the state of the upper ocean stratification is changing, and relationships not yet fully understood are changing. This study employs a simple process experimental approach to understanding ISW-ice interactions, removing a number of real-world complexities to focus specifically on the impacts of wave size (measured as the amplitude) and float size (measured as the L_f). Future work on ISW-ice interactions could further investigate more complex (and realistic) float geometries including roughness and increased ice depth, or multiple float systems, where collisions, and cohesion play a role. Now that fundamental dynamics have been explored, a better understanding of the energetics, specifically diapycnal mixing induced by the ice, and attenuation of the wave under ice is needed. Whilst these are difficult to achieve with the present setup, various laboratory and numerical methods are available (e.g. Zahedi *et al.*, 2021, 2023), and would be valuable for understanding grand Arctic Ocean challenges. These include the transport and mixing of heat (Lenn *et al.*, 2009), the fate of energy in the region (Polyakov *et al.*, 2019) and improving understanding of how ongoing seasonal sea ice declines may impact internal wave energy levels in the Arctic (Guthrie *et al.*, 2013).

Open Research Section. The experimental data used in the study are available at Newcastle University's data repository via https://doi.org/10.25405/data.ncl.c.6693927 with CC-BY 4.0 Licence.

Acknowledgements. We thank Dunphy *et al.* (2011) for their DJLES code used in this project, which is freely available at https://github.com/mdunphy/DJLES.

Chapter 6

References

Aleyasin, S. S., Tachie, M. F. & Balachandar, R. 2021 Characteristics of flow past elongated bluff bodies with underbody gaps due to varying inflow turbulence. *Physics of Fluids* **33** (12), 125106, https://doi.org/10.1063/5.0072390.

Apel, J., Holbrook, J., Liu, A. & Tsai, J. 1985 The Sulu Sea Internal Soliton Experiment. *Journal of Physical Oceanography* **15** (12), 1625–1651, https://doi.org/10.1175/1520-0485(1985)015¡1625:TSSISE¿2.0.CO;2.

Bennetts, L. G., Alberello, A., Meylan, M. H., Cavaliere, C., Babanin, A. V. & Toffoli, A. 2015 An idealised experimental model of ocean surface wave transmission by an ice floe. *Ocean Modelling* **96**, 85–92, https://doi.org/10.1016/j.ocemod.2015.03.001, arXiv: 1502.07010.

Bennetts, L. G. & Williams, T. D. 2015 Water wave transmission by an array of floating discs. *Proceedings of the Royal Society A: Mathematical, Physical and Engineering Sciences* **471** (2173), https://doi.org/10.1098/rspa.2014.0698.

Boegman, L. & Stastna, M. 2019 Sediment Resuspension and Transport by Internal Solitary Waves. *Annual Review of Fluid Mechanics* **51** (1), 129–154, https://doi.org/10.1146/annurev-fluid-122316-045049.

Carr, M., Davies, P. A. & Hoebers, R. P. 2015 Experiments on the structure and stability of mode-2 internal solitary-like waves propagating on an offset pycnocline. *Physics of Fluids* **27** (4), 046602, https://doi.org/10.1063/1.4916881.

Carr, M., Stastna, M., Davies, P. A. & van de Wal, K. J. 2019*a* Shoaling mode-2 internal solitary-like waves. *Journal of Fluid Mechanics* **879**, 604–632, https://doi.org/10.1017/jfm.2019.671.

Carr, M., Sutherland, P., Haase, A., Evers, K. U., Fer, I., Jensen, A., Kalisch, H., Berntsen, J., Parau, E., Thiem, O. & Davies, P. A. 2019*b* Laboratory Experiments on Internal Solitary Waves in Ice-Covered Waters. *Geophysical Research Letters* https://doi.org/10.1029/2019GL084710.

Cole, S. T., Toole, J. M., Rainville, L. & Lee, C. M. 2018 Internal Waves in the Arctic: Influence of Ice Concentration, Ice Roughness, and Surface Layer Stratification. *Journal of Geophysical Research: Oceans* **123** (8), 5571–5586, https://doi.org/10.1029/2018JC014096.

Czipott, P. V., Levine, M. D., Paulson, C. A., Menemenlis, D., Farmer, D. M. & Williams, R. G. 1991 Ice flexure forced by internal wave packets in the Arctic Ocean. *Science* **254** (5033), 832–835, https://doi.org/10.1126/science.254.5033.832.

Dalziel, S. B., Carr, M., Sveen, J. K. & Davies, P. A. 2007 Simultaneous synthetic schlieren and PIV measurements for internal solitary waves. *Measurement Science and Technology* **18** (3), 533–547, https://doi.org/10.1088/0957-0233/18/3/001.

Dorrell, R. M., Lloyd, C. J., Lincoln, B. J., Rippeth, T. P., Taylor, J. R., Caulfield, C. c. P., Sharples, J., Polton, J. A., Scannell, B. D., Greaves, D. M., Hall, R. A. & Simpson, J. H. 2022 Anthropogenic Mixing in Seasonally Stratified Shelf Seas by Offshore Wind Farm Infrastructure. *Frontiers in Marine Science* **9**, 124, https://doi.org/10.3389/fmars.2022.830927, arXiv: 2112.12571.

Dunphy, M., Subich, C. & Stastna, M. 2011 Spectral methods for internal waves: Indistinguishable density profiles and double-humped solitary waves. *Nonlinear Processes in Geophysics* **18** (3), 351–358, https://doi.org/10.5194/npg-18-351-2011.

Ekman, V. W. 1904 On Dead-Water: Being a description of the so-called phenomenon often hindering the headway and navigation of ships in Norwgian Fjords and elsewhere, and an experimental investigation of its causes etc. In *The Norwegian North Polar Expedition 1893-1896: Scientific Results* (ed. F. Nansen), , vol. 5, pp. 1–150. London: Fridtjof Nansen Fund for the Advancement of Science, Longmans, Green, and Co.

Fer, I., Koenig, Z., Kozlov, I. E., Ostrowski, M., Rippeth, T. P., Padman, L., Bosse, A. & Kolås, E. 2020 Tidally Forced Lee Waves Drive Turbulent Mixing Along the Arctic Ocean Margins. *Geophysical Research Letters* **47** (16), e2020GL088083, https://doi.org/10.1029/2020GL088083.

Grue, J., Jensen, A., Rusås, P. O. & Sveen, J. K. 2000 Breaking and broadening of internal solitary waves. *Journal of Fluid Mechanics* **413**, 181–217, https://doi.org/10.1017/S0022112000008648.

Guthrie, J. D. & Morison, J. H. 2021 Not Just Sea Ice: Other Factors Important to Near-inertial Wave Generation in the Arctic Ocean. *Geophysical Research Letters* **48** (3), e2020GL090508, https://doi.org/10.1029/2020GL090508.

Guthrie, J. D., Morison, J. H. & Fer, I. 2013 Revisiting internal waves and mixing in the Arctic Ocean. *Journal of Geophysical Research: Oceans* **118** (8), 3966–3977, https://doi.org/10.1002/jgrc.20294.

Hartharn-Evans, S. G., Carr, M., Stastna, M. & Davies, P. A. 2022 Stratification effects on shoaling internal solitary waves. *Journal of Fluid Mechanics* **933** (A19), https://doi.org/10.1017/jfm.2021.1049.

Jackson, C., da Silva, J., Jeans, G., Alpers, W. & Caruso, M. 2013 Nonlinear Internal Waves in Synthetic Aperture Radar Imagery. *oceanog* **26** (2), 68–79, https://doi.org/10.5670/oceanog.2013.32.

Kozlov, I. E., Zubkova, E. V. & Kudryavtsev, V. N. 2017 Internal Solitary Waves in the Laptev Sea: First Results of Spaceborne SAR Observations. *IEEE Geoscience and Remote Sensing Letters* **14** (11), 2047–2051, https://doi.org/10.1109/LGRS.2017.2749681.

Kurkina, O. E. & Talipova, T. G. 2011 Huge internal waves in the vicinity of the Spitsbergen Island (Barents Sea). *Natural Hazards and Earth System Sciences* **11** (3), 981–986, https://doi.org/10.5194/nhess-11-981-2011.

Lamb, K. G. 1997 Particle transport by nonbreaking, solitary internal waves. *Journal of Geophysical Research: Oceans* **102** (C8), 18641–18660, https://doi.org/10.1029/97JC00441.

Lamb, K. G. & Wan, B. 1998 Conjugate flows and flat solitary waves for a continuously stratified fluid. *Physics of Fluids* **10** (8), 2061–2079, https://doi.org/10.1063/1.869721.

Lamb, K. G. & Warn-Varnas, A. 2015 Two-dimensional numerical simulations of shoaling internal solitary waves at the ASIAEX site in the South China Sea. *Nonlin. Processes Geophys.* **22** (3), 289–312, https://doi.org/10.5194/npg-22-289-2015.

Lenn, Y. D., Wiles, P. J., Torres-Valdes, S., Abrahamsen, E. P., Rippeth, T. P., Simpson, J. H., Bacon, S., Laxon, S. W., Polyakov, I. V., Ivanov, V. & Kirillov, S. 2009 Vertical mixing at intermediate depths in the Arctic boundary current. *Geophysical Research Letters* **36** (5), L05601, https://doi.org/10.1029/2008GL036792.

Li, J., Kohout, A. L. & Shen, H. H. 2015 Comparison of wave propagation through ice covers in calm and storm conditions. *Geophysical Research Letters* **42** (14), 5935–5941, https://doi.org/10.1002/2015GL064715.

Luzzatto-Fegiz, P. & Helfrich, K. R. 2014 Laboratory experiments and simulations for solitary internal waves with trapped cores. *Journal of Fluid Mechanics* **757**, 354–380, https://doi.org/10.1017/jfm.2014.501.

Marchenko, A. V., Morozov, E. G., Kozlov, I. E. & Frey, D. I. 2021 High-amplitude internal waves southeast of Spitsbergen. *Continental Shelf Research* **227**, 104523, https://doi.org/10.1016/j.csr.2021.104523.

Marchenko, A. V., Morozov, E. G., Muzylev, S. V. & Shestov, A. S. 2010 Interaction of short internal waves with the ice cover in an Arctic fjord. *Oceanology* **50** (1), 18–27, https://doi.org/10.1134/S0001437010010029.

Martin, T., Steele, M. & Zhang, J. 2014 Seasonality and long-term trend of Arctic Ocean surface stress in a model. *Journal of Geophysical Research: Oceans* **119** (3), 1723–1738, https://doi.org/10.1002/2013JC009425.

Morozov, E. & Pisarev, S. 2002 Internal tides at the arctic latitudes (Numerical experiments). *Oceanology* **42**, 153–161.

Muench, R. D., LeBlond, P. H. & Hachmeister, L. E. 1983 On some possible interactions between internal waves and sea ice in the marginal ice zone. *Journal of Geophysical Research: Oceans* **88** (C5), 2819–2826, https://doi.org/10.1029/JC088iC05p02819.

Munro, R. J. & Davies, P. A. 2006 The flow generated in a continuously stratified rotating fluid by the differential rotation of a plane horizontal disc. *Fluid Dynamics Research* **38** (8), 522–538, https://doi.org/10.1016/j.fluiddyn.2006.03.002.

Nansen, F. 1897 *Farthest North: Being the Record of a Voyage of Exploration of the Ship "Fram" 1893-96 and of a Fifteen Months' Sleigh Journey by Dr. Nansen and Lieut. Johansen*, , vol. 1. London, UK: Constable.

Osborne, A., Burch, T. & Scarlet, R. 1978 The Influence of Internal Waves on Deep-Water Drilling. *Journal of Petroleum Technology* **30** (10), 1497–1504, https://doi.org/10.2118/6913-PA.

Pinkel, R. 2005 Near-inertial wave propagation in the western Arctic. *Journal of Physical Oceanography* **35** (5), 645–665, https://doi.org/10.1175/JPO2715.1.

Polyakov, I. V., Padman, L., Lenn, Y. D., Pnyushkov, A., Rember, R. & Ivanov, V. V. 2019 Eastern arctic ocean diapycnal heat fluxes through large double-diffusive steps. *Journal of Physical Oceanography* **49** (1), 227–246, https://doi.org/10.1175/JPO-D-18-0080.1.

Polyakov, I. V., Rippeth, T. P., Fer, I., Alkire, M. B., Baumann, T. M., Carmack, E. C., Ingvaldsen, R., Ivanov, V. V., Janout, M., Lind, S., Padman, L., Pnyushkov, A. V. & Rember, R. 2020 Weakening of cold halocline layer exposes sea ice to oceanic heat in the eastern arctic ocean. *Journal of Climate* **33** (18), 8107–8123, https://doi.org/10.1175/JCLI-D-19-0976.1.

Rippeth, T. P., Vlasenko, V., Stashchuk, N., Scannell, B. D., Green, J. A. M., Lincoln, B. J. & Bacon, S. 2017 Tidal Conversion and Mixing Poleward of the Critical Latitude (an Arctic Case Study). *Geophysical Research Letters* **44** (24), 12,349–12,357, https://doi.org/10.1002/2017GL075310.

Saiki, R. & Mitsudera, H. 2016 A mechanism of ice-band pattern formation caused by resonant interaction between sea ice and internal waves: A theory. *Journal of Physical Oceanography* **46** (2), 583–600, https://doi.org/10.1175/JPO-D-14-0162.1.

Song, Z. J., Teng, B., Gou, Y., Lu, L., Shi, Z. M., Xiao, Y. & Qu, Y. 2011 Comparisons of internal solitary wave and surface wave actions on marine structures and their responses. *Applied Ocean Research* **33** (2), 120–129, https://doi.org/10.1016/j.apor.2011.01.003.

Squire, V. A. 2020 Ocean Wave Interactions with Sea Ice: A Reappraisal. *Annual Review of Fluid Mechanics* **52** (1), 37–60, https://doi.org/10.1146/annurev-fluid-010719-060301.

Squire, V. A. & Moore, S. C. 1980 Direct measurement of the attenuation of ocean waves by pack ice. *Nature* **283** (5745), 365–368, https://doi.org/10.1038/283365a0.

Talipova, T., Terletska, K., Maderich, V., Brovchenko, I., Jung, K. T., Pelinovsky, E. & Grimshaw, R. 2013 Internal solitary wave transformation over a bottom step: Loss of energy. *Physics of Fluids* **25** (3), 032110, https://doi.org/10.1063/1.4797455.

Timco, G. W. 1980 The mechanical properties of saline-doped and carbamide (urea)-doped model ice. *Cold Regions Science and Technology* **3** (1), 45–56, https://doi.org/10.1016/0165-232X(80)90006-3.

Turner, J. S. 2010 The Melting of Ice in the Arctic Ocean: The Influence of Double-Diffusive Transport of Heat from Below. *Journal of Physical Oceanography* **40** (1), 249–256, https://doi.org/10.1175/2009JPO4279.1.

Turner, R. E. L. & Vanden-Broeck, J.-M. 1988 Broadening of interfacial solitary waves. *The Physics of Fluids* **31** (9), 2486–2490, https://doi.org/10.1063/1.866602.

Urbancic, G. H., Lamb, K. G., Fer, I. & Padman, L. 2022 The Generation of Linear and Nonlinear Internal Waves Forced by Subinertial Tides over the Yermak Plateau, Arctic Ocean. *Journal of Physical Oceanography* **52** (9), 2183–2203, https://doi.org/10.1175/JPO-D-21-0264.1.

van der Kindere, J. & Ganapathisubramani, B. 2018 Effect of length of two-dimensional obstacles on characteristics of separation and reattachment. *Journal of Wind Engineering and Industrial Aerodynamics* **178**, 38–48, https://doi.org/10.1016/j.jweia.2018.04.018.

Vlasenko, V., Stashchuk, N., Hutter, K. & Sabinin, K. 2003 Nonlinear internal waves forced by tides near the critical latitude. *Deep Sea Research Part I: Oceanographic Research Papers* **50** (3), 317–338, https://doi.org/10.1016/S0967-0637(03)00018-9.

Wadhams, P., Wilkinson, J. P. & McPhail, S. D. 2006 A new view of the underside of Arctic sea ice. *Geophysical Research Letters* **33** (4), L04501, https://doi.org/10.1029/2005GL025131.

Wang, X., Zhou, J.-F., Wang, Z. & You, Y.-X. 2018 A numerical and experimental study of internal solitary wave loads on semi-submersible platforms. *Ocean Engineering* **150**, 298–308, https://doi.org/10.1016/j.oceaneng.2017.12.042.

Wang, Z., Pãrãu, E. I., Milewski, P. A. & Vanden-Broeck, J. M. 2014 Numerical study of interfacial solitary waves propagating under an elastic sheet. *Proceedings of the Royal Society A: Mathematical, Physical and Engineering Sciences* **470** (2168), https://doi.org/10.1098/rspa.2014.0111.

Zahedi, S., Aghsaee, P. & Boegman, L. 2021 Internal solitary wave bottom boundary layer dissipation. *Phys. Rev. Fluids* **6** (7), 074802, https://doi.org/10.1103/PhysRevFluids.6.074802.

Zahedi, S., Ghassemi, A. & Boegman, L. 2023 Bolus degeneration on uniform slopes. *Estuarine, Coastal and Shelf Science* **280**, 108190, https://doi.org/10.1016/j.ecss.2022.108190.

Zhang, P., Li, Q., Xu, Z. & Yin, B. 2022*a* Internal solitary wave generation by the tidal flows beneath ice keel in the Arctic Ocean. *J. Ocean. Limnol.* **40** (3), 831–845, https://doi.org/10.1007/s00343-021-1052-7.

Zhang, P., Xu, Z., Li, Q., You, J., Yin, B., Robertson, R. & Zheng, Q. 2022*b* Numerical Simulations of Internal Solitary Wave Evolution Beneath an Ice Keel. *Journal of Geophysical Research: Oceans* **127** (2), e2020JC017068, https://doi.org/10.1029/2020JC017068.

Zimin, A. V., Kozlov, I. E., Atadzhanova, O. A. & Chapron, B. 2016 Monitoring short-period internal waves in the White Sea. *Izvestiya - Atmospheric and Ocean Physics* **52** (9), 951–960, https://doi.org/10.1134/S0001433816090309.

CHAPTER 7

Conclusions

7.1. Summary of Key Findings

Through a series of 63 laboratory experiments and 79 numerical simulations, this thesis explores how ISWs interact with obstacles both submerged and on the surface. The specific scenarios studied were shoaling ISWs both over steep and gentle uniform slopes, and the interaction with sea-ice-like floating bodies.

The first of these studies identified the importance of considering the form of stratification in the dynamical features that occur when an ISW propagates upslope. Whilst it was found that the previous classification scheme for a thin tanh stratification broadly holds, this was not the case for different stratification forms. The presence of a density gradient in the upper layer (as in the surface stratification) suppresses the overturning of the pycnocline that produces plunging dynamics. In their place collapsing dynamics occur instead in the surface stratification, but it is further found that having a density gradient in the lower layer (as in the broad tanh stratification) suppresses the boundary layer instability that produces collapsing dynamics. In this broad stratification, surging replaces these dynamics, which can be unstable to shear due to the large energy input. These key differences are found to impact on dissipation, mixing, and stress on the bottom boundary, each of which has implications for the fate of heat, nutrients and sediment in the marine environment. For example, collapsing and plunging ISWs in the surface stratification regime were associated with high rates of mixing, which depending upon the oceanographic setting could provide thermal refuge and/or nutrients to benthic ecosystems upslope, whilst the enhanced bed shear stress in the surface stratification surging breaker could be associated with high

sediment re-suspension and transport up-slope.

In chapter 4 the impact of these different stratifications on the breaking type most relevant to geophysical settings, namely fission, is explored further. Although other breaker types differ considerably between different stratification types, in the fissioning regime thin tanh and surface stratifications show very similar formation, structure and evolution of dense pulses. In the broad tanh stratification, the process of fissioning differs, emerging instead from an elevation wave, and is unable to become unstable, but the pulse formed by this process remains similar to pulses formed in the other stratifications.

This thesis introduces a new diagnostic tool based on paired histograms of user selected variables for mixing induced by internal waves, and other stratified flows in chapter 5. Unlike existing tools to measure mixing, USP allows the user to identify the spatial location and extent of mixing, and the fate of the mixed fluid. USP and it's associated region of interest plots are used to further explore the mixing regimes discussed in §3.6. Each breaking regime is associated with a unique combination of mixing extent and advection of this mixed fluid. The method is further demonstrated for temperature-stratified shear flow simulations in the cold, nonlinear Equation of State regime, which reveal important differences with a density-stratified shear flow, namely that the non-linearity drives asymmetry in the mixing.

In chapter 6, it is identified for the first time that the motion of sea ice under the influence of ISWs can be modelled simply as the average velocity of fluid in contact with the object. Furthermore, the transport of large floating structures decreases as L_f/λ increase, a result first identified by Carr *et al.* (2019), is found to be due only to the form of the wave's horizontal surface velocity. That is, the effect on the float's velocity of the still water either side of the wave, and not due to any energy based arguments despite an intuitive explanation for the relationship between L_f/λ and U_{max}/c based around the increasing mass/inertia of the float. In fact, only a small proportion of the wave's available energy is transferred to the float, even in the extremes of cases investigated here. Although here applied to the timely and relevant example of sea ice, such interactions are equally applicable to other free-floating objects in the ocean such as rigs, floating wind farms, ships and other engineered structures.

The laboratory and numerical methods used in this thesis are time intensive, and theoretical work (such as KdV, DJL or MCC) offer an attractive alternative to study some problems. One interesting application of this work arising from this thesis would be further study of theoretical fissioning internal waves, and comparison of these solutions with numerical works to further identify the comparative roles of various processes.

7.2. Future work

Here, idealised process studies have been used to improve understanding of how ISWs interact with obstacles at the boundaries of the fluid. Following on from these results, a few key future research areas that would further improve our understanding of ISWs in real-world settings emerge.

First and foremost is that of diapycnal mixing induced by and attenuation of ISW passing under more complex ice cover, such as rough ice floes and multiple floe systems. Such results are required to address key outstanding questions around the fate of internal waves and mixing as sea ice reduces (e.g. Rippeth *et al.*, 2017; Guthrie & Morison, 2021), and require a laboratory investigation considering the energetics of the wave before, during and after it's interaction with the float. It is unlikely that the motion of multiple float systems can be as well understood by the Float Motion Model (FMM), due to the interactions between floats, but the flow features beneath remain important, and would lead to greater understanding of the field observations of Cole *et al.* (2018).

Another question emerging from the work on ice-covered waters is an investigation as to what extent the FMM, and associated relationships presented here can be applied to other floating structures. This question is of particular relevance to marine engineering if specific structures, including tethered structures are considered. In a similar vein, understanding the impact of roughness, and other non-uniform smooth slopes on shoaling ISWs would improve applicability of the shoaling waves to the field. The new diagnostic tool for understanding mixing in stratified fluids presented here should be applied to other applications, and whilst some suggestions are presented in the conclusions of that chapter, these problems may also find utility in applying the USP and Region of Interest tools. As questions remain as to how sediment and nutrients may be transported by shoaling ISWs on realistic slopes, this mixing diagnostic may prove useful in applications with representation of sediment resuspension and transport processes. Finally, an interesting intersection of all the chapters to explore would be the interaction of NLIWs with wavelengths comparable to the bottom topography with the rough slopes, relevant to lee waves in the Arctic Ocean (Vlasenko *et al.*, 2003; Musgrave *et al.*, 2016).

Chapter 7

References

Carr, M., Sutherland, P., Haase, A., Evers, K. U., Fer, I., Jensen, A., Kalisch, H., Berntsen, J., Parau, E., Thiem, O. & Davies, P. A. 2019 Laboratory Experiments on Internal Solitary Waves in Ice-Covered Waters. *Geophysical Research Letters* https://doi.org/10.1029/2019GL084710.

Cole, S. T., Toole, J. M., Rainville, L. & Lee, C. M. 2018 Internal Waves in the Arctic: Influence of Ice Concentration, Ice Roughness, and Surface Layer Stratification. *Journal of Geophysical Research: Oceans* **123** (8), 5571–5586, https://doi.org/10.1029/2018JC014096.

Guthrie, J. D. & Morison, J. H. 2021 Not Just Sea Ice: Other Factors Important to Near-inertial Wave Generation in the Arctic Ocean. *Geophysical Research Letters* **48** (3), e2020GL090508, https://doi.org/10.1029/2020GL090508.

Musgrave, R. C., Pinkel, R., MacKinnon, J. A., Mazloff, M. R. & Young, W. R. 2016 Stratified tidal flow over a tall ridge above and below the turning latitude. *Journal of Fluid Mechanics* **793**, 933–957, https://doi.org/10.1017/jfm.2016.150.

Rippeth, T. P., Vlasenko, V., Stashchuk, N., Scannell, B. D., Green, J. A. M., Lincoln, B. J. & Bacon, S. 2017 Tidal Conversion and Mixing Poleward of the Critical Latitude (an Arctic Case Study). *Geophysical Research Letters* **44** (24), 12,349–12,357, https://doi.org/10.1002/2017GL075310.

Vlasenko, V., Stashchuk, N., Hutter, K. & Sabinin, K. 2003 Nonlinear internal waves forced by tides near the critical latitude. *Deep Sea Research Part I: Oceanographic Research Papers* **50** (3), 317–338, https://doi.org/10.1016/S0967-0637(03)00018-9.